

2019

## ANNUAL REPORT JAHRESBERICHT

 Paul-Drude-Institut  
für Festkörperelektronik  
Leibniz-Institut im Forschungsverbund Berlin e. V.



# Table of Contents

## Inhaltsverzeichnis

Preface	
<a href="#">Vorwort</a>	5
Scientific Advisory Board	
<a href="#">Wissenschaftlicher Beirat</a>	8
Research Highlights	
<a href="#">Forschungshighlights</a>	11
Core Research Areas	
<a href="#">Forschungsschwerpunkte</a>	33
Brief Reports	
<a href="#">Kurzberichte</a>	59
Departments	
<a href="#">Abteilungen</a>	119
Facts & Figures	
<a href="#">Zahlen &amp; Fakten</a>	145
Contact	
<a href="#">Kontakt</a>	168
Imprint	
<a href="#">Impressum</a>	172



1m

Scale  
Child  
1 m  
(1 x 100 m)

m 2:1

# Preface

## Vorwort

This annual report presents the activities that date from the time between the meetings of our Scientific Advisory Board in October 2018 and 2019. As always, it is our intention to give insight to our work not only to academic colleagues but also to the interested public. We therefore first present easy-to-read introductions into our major research areas and into the fields of expertise of our departments.

Selected scientific highlights are presented in three extended reports. They are complemented by a selection of short contributions from all our research areas.

In the past years, PDI has synthesized and investigated an increasingly large spectrum of new materials and nanostructures. For these activities, the technique of molecular

Der vor Ihnen liegende Jahresbericht präsentiert die Arbeit unseres Instituts aus dem Jahreszeitraum, der zwischen den jährlichen Treffen unseres wissenschaftlichen Beirats im Oktober 2018 und 2019 liegt.

Nicht nur den Fachkollegen unseres Arbeitsgebietes, sondern auch der wissenschaftlich interessierten Öffentlichkeit möchten wir einen Einblick in unsere Arbeit vermitteln. Daher geben wir zunächst allgemein-verständliche Einführungen in unsere großen Forschungsgebiete und in die Expertise unserer Abteilungen. Ausgewählte wissenschaftliche Erfolge präsentieren wir ausführlich in drei Highlight-Berichten. Sie werden ergänzt durch eine Selektion von Kurzbeiträgen aus allen Bereichen des Instituts.



beam epitaxy with its thickness control on the scale of single atomic layers and multiple possibilities for in-situ control is our workhorse. A radically different approach to the realization of semiconductor nanostructures, which is uniquely performed at PDI, utilizes the controlled positioning of single atoms on semiconductor surfaces. In this way, prototypical quantum structures can be constructed and spectroscopically investigated in the same setup. The contribution by Van Dong Pham and Stefan Fölsch illustrates that this technique is now capable of constructing almost arbitrary structures consisting of dozens of atoms. Thus, periodic structures can be realized with tailored electronic properties, supporting the vision of producing novel quantum materials on the basis of artificial atomic lattices.

Parallel to the synthesis of nanostructures, PDI conducts comprehensive experiments to fundamentally analyze their physical properties. The close interaction between synthesis and analysis allows a far-reaching understanding of both the growth process and the physics of our nanostructures. A logical next step is shown in the second highlight by Vladimir Kaganer and colleagues. They show how the combination of physical analysis with modeling and simulation can break new ground in our physical methods. In this case, deeper understanding leads to a new and more comprehensive interpretation of the application of cathodoluminescence in the important field of group-III nitrides, at the same time correcting old interpretation routines.

The third highlight by Alberto Hernández-Mínguez and colleagues illustrates how PDI utilizes new materials produced here – in this case layers of hexagonal boron nitride – to realize and investigate prototypical device functionalities. The authors show how the luminescence from such layers can be modulated by electroacoustic fields at GHz frequencies. Since such layers lend themselves well to heterogeneous integration, e.g. into silicon

Das PDI hat in den letzten Jahren ein immer breiteres Spektrum von neuen Materialien und Nanostrukturen hergestellt, wobei wir die Technik der Molekularstrahlepitaxie mit ihrer Schichtdickenkontrolle auf der Skala von einzelnen Atomlagen ausnutzen. Ein radikal anderer Ansatz für die Herstellung von Halbleiternanostrukturen, der weltweit ausschließlich am PDI beherrscht wird, verwendet die gezielte Positionierung einzelner Atome auf Halbleiteroberflächen. So lassen sich exemplarische Quantenstrukturen aufbauen und gleichzeitig spektroskopisch untersuchen. Der Beitrag von Van Dong Pham und Stefan Fölsch zeigt, dass mit dieser Technik mittlerweile fast beliebige Strukturen aus mehreren Dutzend Atomen gezielt aufgebaut werden können und er erläutert wie sich hieraus periodische Strukturen herstellen lassen, deren elektronische Eigenschaften gezielt einstellbar sind. Die Vision dieser Arbeiten besteht darin, mit derartigen künstlichen Atomgittern neuartige, sogenannte Quantenmaterialien mit gezielt einstellbaren Eigenschaften zu realisieren.

Parallel zur Synthese von Nanostrukturen betreibt das PDI umfassende Experimente, um deren physikalische Eigenschaften grundlegend zu analysieren. So erreichen wir durch das Wechselspiel von Synthese und Analyse ein tiefgehendes Verständnis von Herstellung und Eigenschaften unserer Nanostrukturen. Das zweite Highlight von Vladimir Kaganer und Kollegen illustriert, wie sich darüber hinaus durch Kombination von Analytik mit physikalischer Simulation methodisches Neuland erreichen lässt. In diesem Fall führt das vertiefte Verständnis dazu, dass der Einsatz der Kathodolumineszenz an Gruppe-III Nitriden neue und weitergehende Aussagen ermöglicht, und er revidiert damit langjährig praktizierte Routinen.

Das dritte Highlight von Alberto Hernández-Mínguez und Kollegen illustriert, wie am PDI aus den hergestellten Materialien – in diesem Fall aus hexagona-

technology, and they hold high technological promise as room temperature – single photon sources for quantum technologies.

At this time, which marks the end of my term as director of PDI, I would like to thank all members of PDI for their creative and committed work. I consider it a great privilege to have directed and experienced the research and the evolution of our unique institute together with you. I associate my time at PDI with many wonderful, often surprising and in some cases fascinatingly elegant scientific results. With the same joy I look back on the personal collaborations with many quite different characters and talents, both with younger and experienced members of PDI and with scientists and supporting staff alike. I am personally most grateful for this experience of the past 12 years. At the same time, I would like to extend my gratitude to all scientific partners of our Institute, to the funding agencies in the federal and the state government who have relentlessly supported us over the past years. Last but not least, I thank the members of our Scientific Advisory Board for accompanying PDI in a dedicated and critical manner.

Finally, I extend my best wishes to PDI on the exciting path to the horizons of our science and technology.

len Bornitrid-Schichten (h-BN) – auf prototypische Weise Bauelementfunktionalitäten realisiert und untersucht werden. In diesem Fall wird gezeigt, wie die Lumineszenz von Schichten aus h-BN, die sich prinzipiell als Raumtemperatur-Einzelphotonenquellen zum Beispiel in die Silizium-Technologie integrieren lassen, mittels elektro-akustischen Feldern im GHz-Bereich modulieren lassen.

An dieser Stelle und zu diesem Zeitpunkt, der das Ende meiner Amtszeit am PDI markiert, möchte ich allen Mitarbeiterinnen und Mitarbeitern nochmals für ihre kreative und engagierte Arbeit danken. Ich empfinde es als großes Privileg, mit Ihnen zusammen die Forschung und die Geschicke unseres einzigartigen Instituts gesteuert und erlebt zu haben. Ich verbinde meine Zeit am PDI mit vielen wunderbaren, oft überraschenden und zum Teil faszinierend eleganten, wissenschaftlichen Ergebnissen. Ebenso freudig denke ich an die menschlichen Zusammenarbeiten mit vielen oft ganz unterschiedlichen Charakteren und Talenten, bei jüngeren wie bei älteren MitarbeiterInnen, gleichermaßen im Wissenschaftsbereich und beim unterstützenden Personal. Hierfür bin ich außerordentlich dankbar. Mein Dank richtet sich in gleicher Weise an alle wissenschaftlichen Kooperationspartner im Umfeld unseres Instituts, an die Fördergelder beim Bund und Land, die uns in den letzten Jahren verlässlich unterstützt haben, und nicht zuletzt an die Mitglieder unseres wissenschaftlichen Beirats für ihre engagiert kritische Begleitung unserer Arbeit.

Ich wünsche Ihnen viel Freude bei der Lektüre und dem PDI weiterhin viel Erfolg auf dem spannenden Weg zu den Horizonten unserer Wissenschaft und Technologie.

Henning Riechert

**Prof. Dr. Manfred Bayer**

Fakultät Physik, Experimentelle Physik 2,  
Technische Universität Dortmund  
Deutschland

**Dr. Martin Behringer**

OSRAM Opto Semiconductors GmbH,  
OS CTO TLED R  
Regensburg, Deutschland

**Prof. Dr. Oscar Dubon**

University of California  
Berkeley, CA, USA

**Prof. Nicolas Grandjean**

Ecole Polytechnique Federale de Lausanne  
Schweiz

**Dr. Michelle Johannes**

Center for Computational Materials Science,  
Naval Research Laboratory  
Washington DC, USA

**Prof. Dr. Jochen Mannhart**

Max-Planck-Institut für Festkörperforschung  
Stuttgart, Deutschland

**Dr. Heike Riel**

IBM Research – Zürich  
Rüschlikon, Schweiz

**Prof. Dr. James S. Speck**

Materials Department, University of California  
Santa Barbara, CA, USA

**Prof. Dr. Werner Wegscheider**

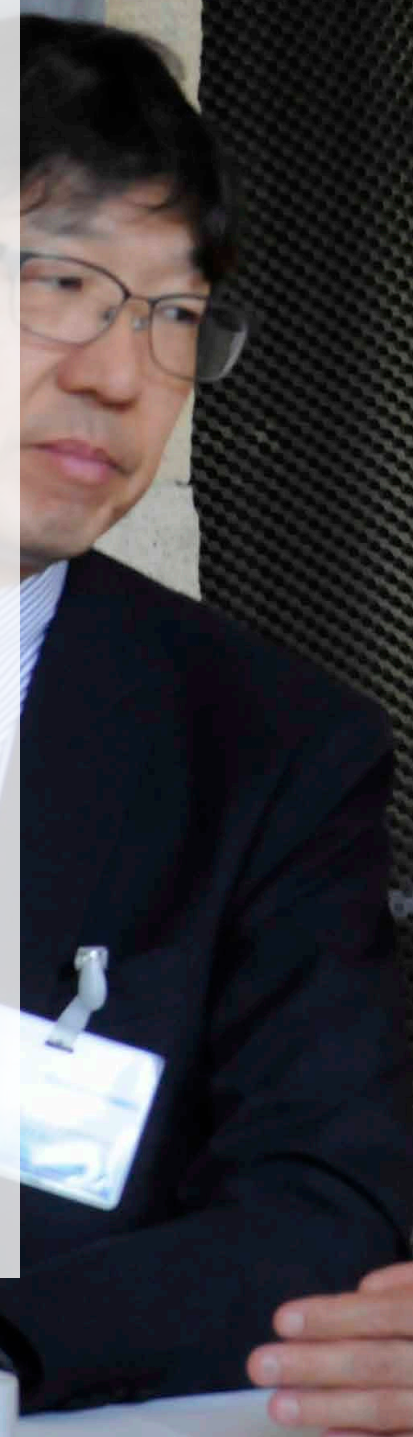
Advanced Semiconductor Quantum Materials  
Laboratory for Solid State Physics, ETH Zürich,  
Schweiz

**Prof. Dr. Matthias Wuttig**

Rheinisch-Westfälische Technische Hochschule Aachen,  
Physikalisches Institut  
Aachen, Deutschland

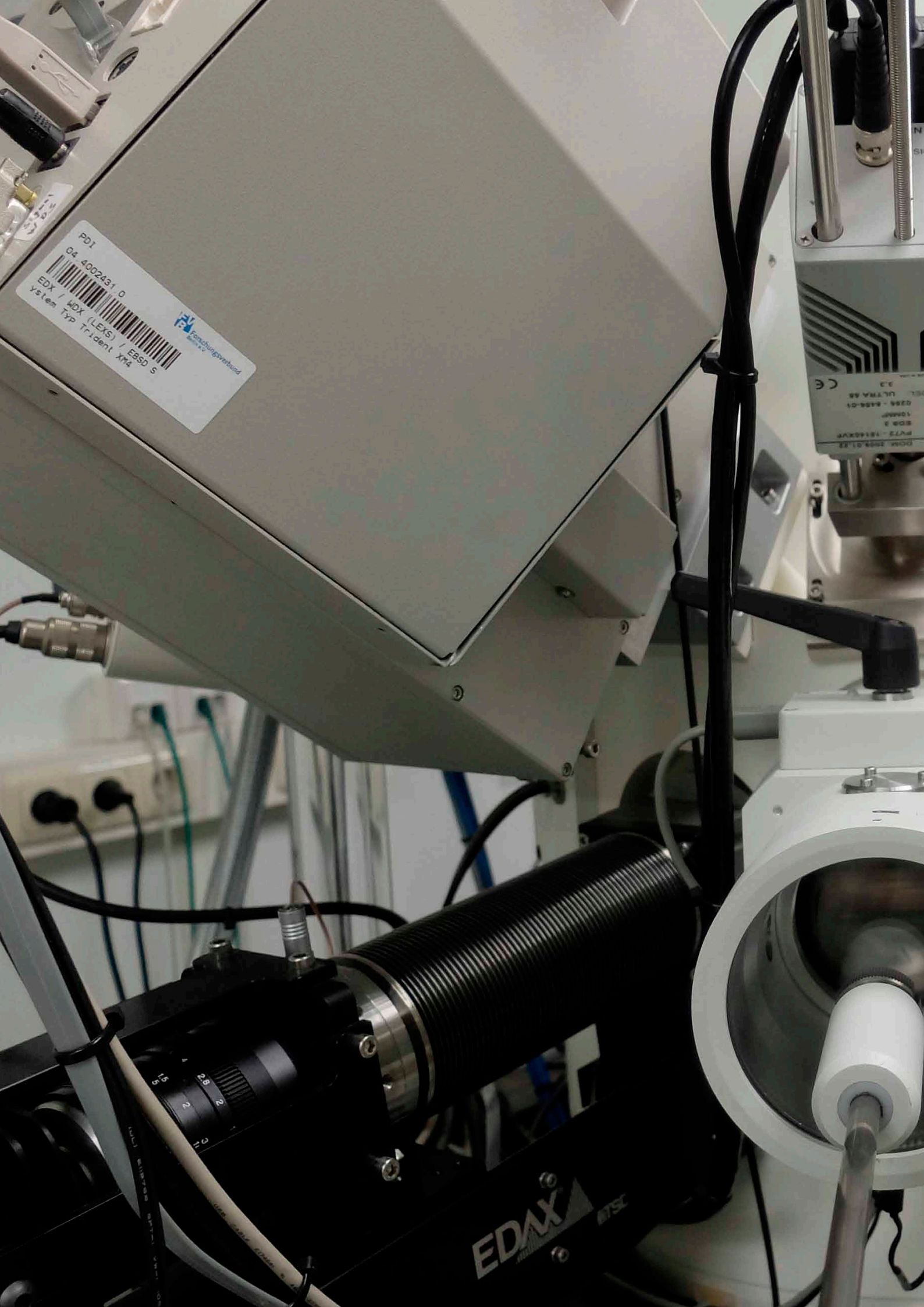
**Dr. Hiroshi Yamaguchi**

NTT Basic Research Laboratories  
Nippon Telegraph and Telephone Corporation  
Kanagawa, Japan



# Scientific Advisory Board Wissenschaftlicher Beirat







# Research Highlights Forschungs-Highlights

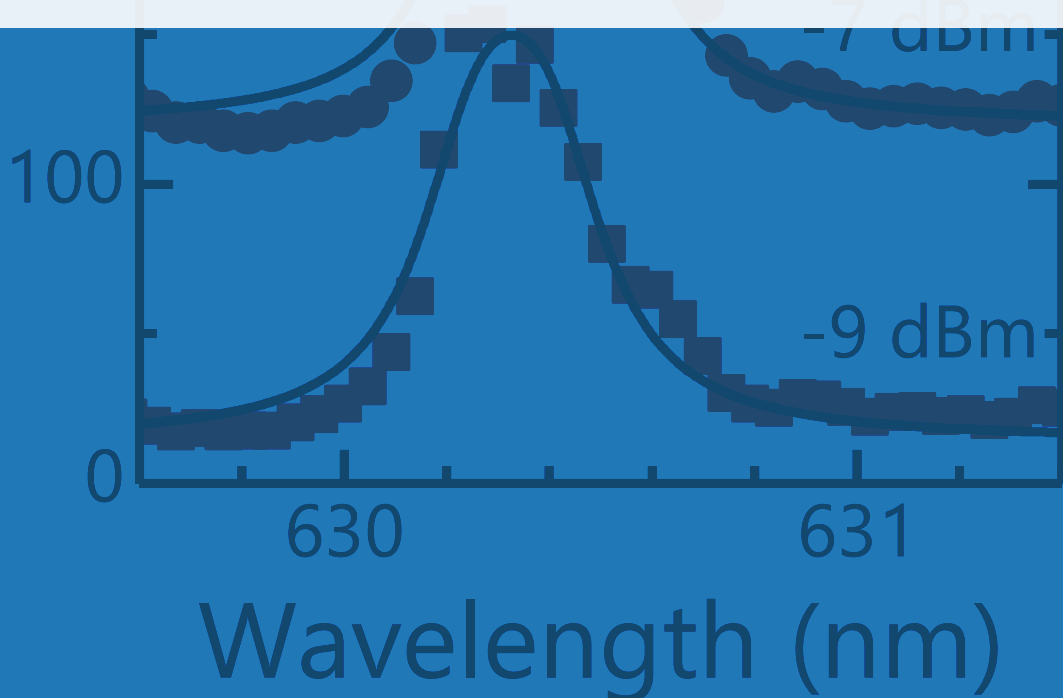
Kopplung von hexagonalen Bornitrid-Lichtemissionszentren an akustische Oberflächenwellen .....	12
Coupling of h-BN light emission centers to surface acoustic waves .....	13
Bestimmung der Ladungsträgerdiffusionslänge in GaN aus Kathodolumineszenz-Rasterbildern: Trugschlüsse und Möglichkeiten .....	18
Determination of the carrier diffusion length in GaN from cathodoluminescence maps: fallacies and opportunities .....	19
Das Verhalten von Elektronen in künstlich erzeugten periodischen Potentialen .....	26
Electron behavior in artificial periodic potentials .....	27

# Kopplung von hexagonalen Bornitrid-Lichtemissionszentren an akustische Oberflächenwellen

Lumineszenzzentren in Festkörpern haben aufgrund ihrer atomartigen optischen Emission, die durch scharfe Linien mit nicht klassischer Photonenstatistik gekennzeichnet ist, viel Aufmerksamkeit auf sich gezogen. Eine der Herausforderungen im Zusammenhang mit diesen Quantenlichtquellen besteht darin, Methoden zur effizienten Steuerung ihrer optoelektronischen Eigenschaften zu finden. Es wurde vor einigen Jahren gezeigt, dass hexagonales Bornitrid (h-BN), ein zweidimensionaler Kristall mit einem graphenartigen Wabengitter, Lumineszenzzentren beherbergen kann, die selbst bei Raumtemperatur als Einzelphotonenemitter wirken. Diese Eigenschaft macht dieses Material vielversprechend für Anwendungen in der Quanteninformationsverarbeitung. In diesem Beitrag zeigen wir, dass akustische Oberflächenwellen (SAW) die optischen Eigenschaften von Lichtemissionszentren in hexagonalem Bornitrid modulieren können.

Wir haben das optische Verhalten von zwei Arten von h-BN-Proben analysiert, nämlich handelsübliche Mehrschichtflocken und Filme mit wenigen Schichten, die durch Molekularstrahlepitaxie gezüchtet wurden. Beide Proben wurden auf der Oberfläche eines starken piezoelektrischen Substrats abgelegt, und die SAWs wurden erzeugt, indem Hochfrequenzsignale an auf dem Substrat strukturierte Interdigitalwandler angelegt wurden. Wir zeigen, dass die Lichtemissionswellenlänge der Defektzentren durch das oszillierende elastische Spannungsfeld der SAW periodisch moduliert wird, was zu einer Ausbreitung ihrer Emissionslinie führt. Aus der linearen Abhängigkeit der Modulationsamplitude von der von der SAW erzeugten Dehnung haben wir ein Verformungspotential von etwa 40 meV per % elastischer Spannung aufgerechnet.

Wegen der relativ geringen Dicke der h-BN-Proben (von einem bis zu einigen hundert Nanometern) können die Lichtemissionszentren aufgrund ihrer Wechselwirkung mit Ladungen, die an den Grenzflächen sowie in Verunreinigungen eingeschlossen sind, Energie- und Intensitätsschwankungen erfahren. Wir zeigen auch, dass das dynamische piezoelektrische Feld der SAW zur Stabilisierung der optischen Eigenschaften der Lichtzentren in den Epitaxiefilmen beiträgt, indem der Ionisationszustand der nahe gelegenen Ladungsfallen gesteuert wird.



# Coupling of h-BN light emission centers to surface acoustic waves

A. Hernández-Mínguez, F. Iikawa<sup>1</sup>, I. Aharonovich<sup>2</sup>, S. Nakhaie, Y.-T. Liou, J. M. J. Lopes, P. V. Santos

Luminescence centers in solids have attracted much attention due to their atomic-like optical emission characterized by sharp lines with non-classical photon statistics. Recently, it has been demonstrated that hexagonal boron nitride (h-BN), a two-dimensional crystal with a graphene-like honeycomb lattice, can host luminescence centers acting as single photon emitters even at room temperature, thus making this material promising for applications in quantum information processing. One of the challenges related to these solid-state luminescence centers is to find mechanisms for the efficient control of their optoelectronic properties. To this end, surface acoustic waves (SAW) are an interesting approach, because their strain and piezoelectric fields oscillating with frequencies from hundreds of MHz up to a few GHz can couple efficiently to light emission centers placed close to the surface of the vibrating substrate.

In this report, we show that optically active centers in h-BN can be dynamically modulated using SAWs. In our study, we analyzed the coupling of SAWs to luminescence centers contained in two kinds of h-BN samples, namely flakes containing multiple h-BN layers and films with just a few h-BN layers. The multilayer h-BN flakes with a thickness of about 200 nm and a lateral size of about 1  $\mu\text{m}$  (obtained from Graphene Supermarket) were drop-casted on a 127°Y-cut LiNbO<sub>3</sub> substrate and then annealed at 850 °C for 30 min. in an Argon atmosphere (1 Torr) to activate their emission properties. Next, SAW delay lines consisting of pairs of inter-digital transducers (IDT) were patterned on

the LiNbO<sub>3</sub> by optical lithography and lift-off metallization, cf. Fig. 1(a). The few-layer-thick h-BN films (about 1 nm thick) were grown on nickel films by molecular beam epitaxy (MBE). Then, an area of about 7  $\times$  6 mm<sup>2</sup> was transferred to a LiNbO<sub>3</sub> SAW delay line using a wet transfer technique.

The luminescence centers were optically excited at low temperature (5 K) using a 532 nm solid-state laser beam focused onto the sample by an objective with large numerical aperture. The emitted light was collected by the same objective, coupled into a single-mode optical fiber, and sent into a monochromator equipped with a Si-based charge-coupled device (CCD) camera. We excited the SAWs by applying a radio-frequency (rf) signal of the appropriate frequency to one of the IDTs. In our experiment, both rf source and laser are amplitude-modulated at the same reference frequency. For each experimental conditions, we first record the spectrum with rf and laser excitation modulated out of phase, i.e. the sample is exposed to the laser during the half-period when the rf signal is switched off (SAW-OFF spectrum,  $I_{\text{off}}$ ). Then, we change the relative phase between the laser and rf modulations to expose the sample to the laser during the half-period when the rf signal is on (SAW-ON spectrum,  $I_{\text{on}}$ ). By repeating ON/OFF accumulation sequences and averaging the corresponding SAW-ON and SAW-OFF measurements, we increase the signal/noise ratio due to the long accumulation times and, most important, we minimize the effects of temperature and laser power fluctuations, as well as those related to

<sup>1</sup> Institute of Physics, State University of Campinas, Brazil

<sup>2</sup> School of Mathematical and Physical Sciences, University of Technology Sydney, Ultimo, Australia

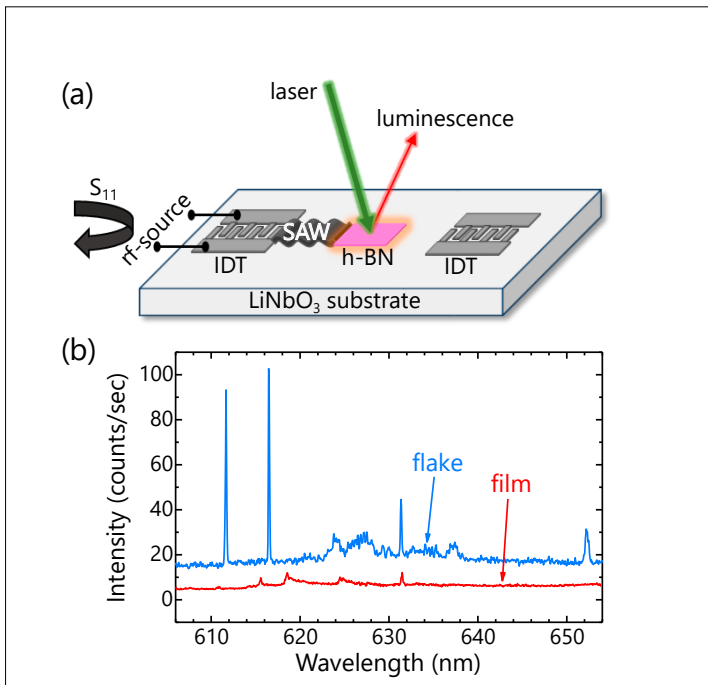


**Fig. 1.** (a) Schematic diagram of the sample. An rf signal applied to one of the interdigital transducers (IDT) excites a SAW in the  $\text{LiNbO}_3$  substrate that propagates along the region containing the h-BN. (b) Low temperature (5 K) luminescence spectrum of defect centers in a multilayer-thick h-BN flake (blue curve) and in a few-layer-thick film (red curve).

spectral fluctuations typically observed in h-BN emission centers.

The blue curve in Fig. 1(b) shows a typical photoluminescence spectrum of an h-BN flake. It consists of several sharp lines distributed along the visible spectral range (between 550 and 800 nm). The transferred h-BN films showed similar sharp lines, cf. red curve in Fig. 1(b), but with a much weaker emission intensity. There are several possible reasons for this weaker emission. First, the flakes contain much more layers than the film, and therefore the chance of finding centers with bright light emission is larger in the flakes than in the film. Second, the flakes were annealed to activate luminescent defects, while the films did not undergo such a process. Third, the proximity of the luminescence centers

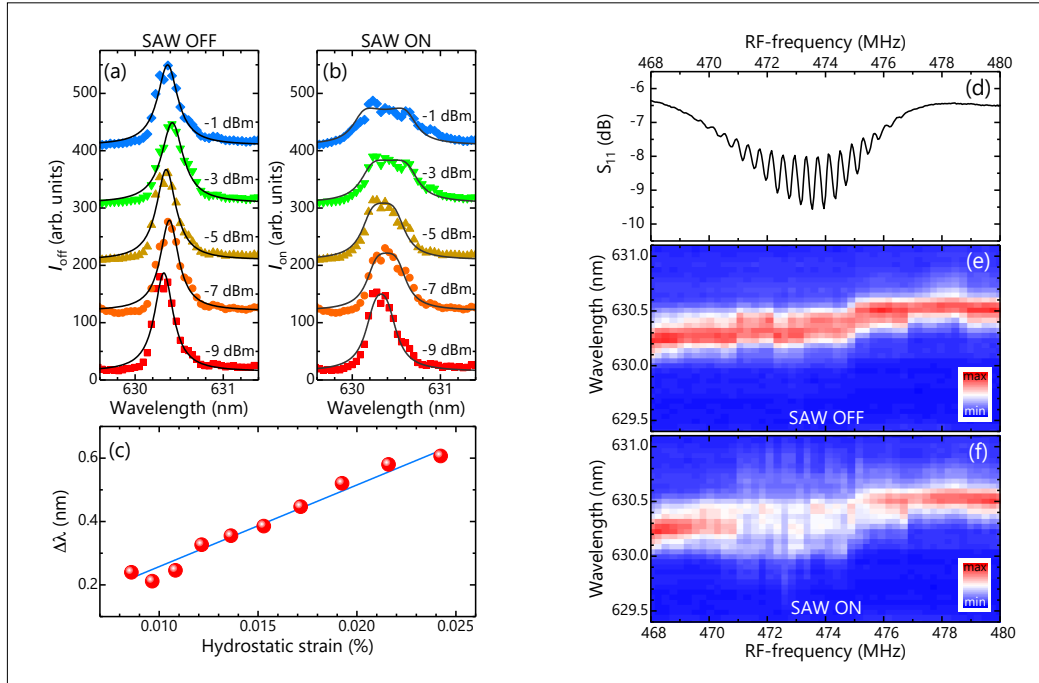
to the  $\text{LiNbO}_3$  substrate may also play a detrimental role in the luminescence intensity. This effect is expected to impact the thin films more significantly than the thicker flakes, since the latter contain also defects in larger distance from the  $\text{LiNbO}_3$ , which are therefore optically brighter.

Figure 2 compares the photoluminescence spectra of one of the emission lines in the h-BN flake recorded in the absence (Fig. 2(a), SAW OFF) and in the presence of SAW excitation (Fig. 2(b), SAW ON). The measurements were performed under a fixed SAW frequency  $f_{\text{SAW}} = 473.3$  MHz for different nominal powers applied by the rf generator. As the  $I_{\text{off}}$  spectra are recorded with the exciting laser and rf signal out of phase, we do not expect any effect of the SAW on the emission properties. We have fitted the  $I_{\text{off}}$  spectra using the following Lorentzian function [black curves in Fig. 2(a)]:

$$I_{\text{off}}(\lambda) = I_0 + \frac{2A}{\pi} \frac{w}{4(\lambda - \lambda_c)^2 + w^2}, \quad (1)$$

where A, w and  $\lambda_c$  are the area, width and center of the emission line, respectively, and  $I_0$  accounts for the background signal. While the width remains at an average value of  $0.28 \pm 0.03$  nm independent of SAW power, the peak center fluctuates around 630.4 nm during the experiment. Spectra measured as a function of time indicate that these shifts are due to spectral and intensity fluctuations (spectral diffusion), which are probably caused by aleatory changes in the ionization state of nearby charge traps like shallow impurities or defects. These fluctuations are also responsible for the relatively broad emission line and for the partial deviation of the line shape from that of a single peak.

The corresponding  $I_{\text{on}}$  spectra, in contrast, show a broad emission line with a line width that increases with the nominal rf power applied to the IDT. We interpret this change in the emission line shape as caused by the dynamic strain of the SAW: the oscillating tensile and compressive strain modu-



**Fig. 2.** Photoluminescence spectra recorded in the (a) absence ( $I_{\text{off}}$ ) and (b) presence ( $I_{\text{on}}$ ) of a SAW, as a function of nominal rf power applied to the IDT. The black curves are fits according to Eqs. 1 and 2. The data are vertically shifted for clarity. (c) Amplitude of the spectral oscillation,  $\Delta\lambda$ , with respect to the amplitude of the SAW-induced hydrostatic strain at the surface of the  $\text{LiNbO}_3$  substrate. The blue line is a linear fit to the data. (d) RF-power reflection coefficient spectrum,  $S_{11}$ , of the IDT at the range of rf frequencies for efficient SAW excitation. (e)  $I_{\text{off}}$  and (f)  $I_{\text{on}}$  spectra measured for the same range of rf frequencies as in panel (d).

lates periodically the crystal structure of the luminescent center, thus leading to the oscillation of its optical transition energy around the equilibrium value. As the acquisition time of the luminescence spectra is much larger than the SAW period, the energy oscillation manifests as a broadening of the emission line and a reduction of its maximum intensity, as shown in Fig. 2(b).

To quantify the strength of the optomechanical coupling, we have fitted the  $I_{\text{on}}$  spectra according to the formula:

$$I_{\text{on}}(\lambda) = I_0 + f_{\text{SAW}} \int_0^{1/f_{\text{SAW}}} \frac{2A}{\pi} \frac{w}{4\{\lambda - [\lambda_c + \Delta\lambda \sin(2\pi f_{\text{SAW}} t)]\}^2 + w^2} dt. \quad (2)$$

Here, the integrand is the Lorentzian function with the values for  $A$ ,  $w$  and  $\lambda_c$  obtained from the fitting of the corresponding

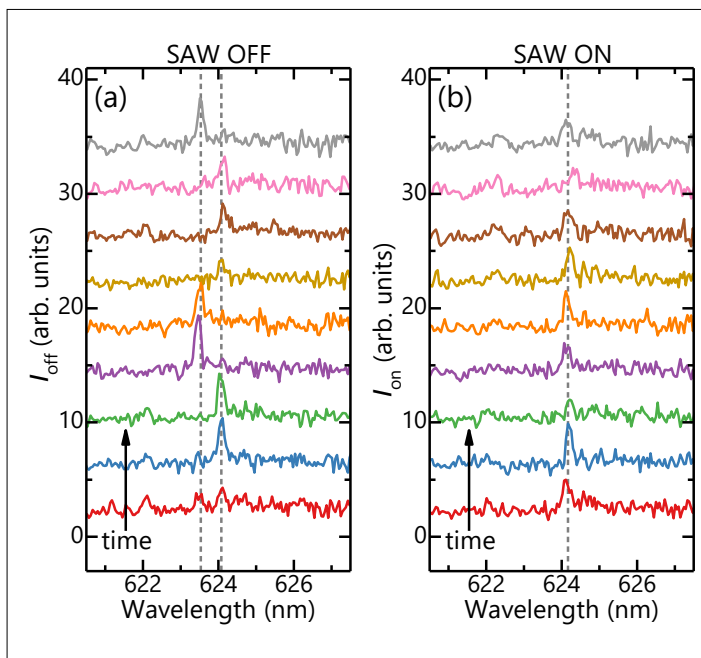
$I_{\text{off}}$  spectra in Fig. 2(a). The amplitude of the SAW-induced spectral oscillation is given by  $\Delta\lambda$ , which is the only free parameter in the fitting procedure. Figure 2(c) displays the fitted values of  $\Delta\lambda$  as a function of the amplitude of the hydrostatic strain,  $\varepsilon_0$ , at the surface of the  $\text{LiNbO}_3$  for the different nominal rf powers. To determine the values of  $\varepsilon_0$ , we first calculated the SAW power density from the nominal rf power applied to the IDT and its power reflection coefficient,  $S_{11}$ , of Fig. 2(d). We then related the SAW power density to  $\varepsilon_0$  by solving numerically the coupled elastic and electromagnetic equations for the  $\text{LiNbO}_3$  substrate. As expected,  $\Delta\lambda$  increases linearly with  $\varepsilon_0$ . From the wavelength rate of  $12.9 \pm 0.2$  nm per % of strain, we estimate a deformation potential of about 40 meV/%.

To verify that the observed modulation is effectively caused by the SAW, we have measured a series of  $I_{\text{off}}$  and  $I_{\text{on}}$  spectra under a constant nominal rf power of -1 dB, while scanning the frequency of the rf signal applied to the IDT. The dip around 473 MHz in the  $S_{11}$  spectrum of Fig. 2(d) identifies the range of rf frequencies for efficient SAW excitation by the transducer. In the  $I_{\text{off}}$  spectra of Fig. 2(e), apart from the luminescence fluctuations related to the previously mentioned spectral diffusion, we do not observe any dependence of the emission line on the rf frequency. The  $I_{\text{on}}$  spectra of Fig. 2(f), in contrast, show an additional line broadening and intensity suppression of about 50 % when the rf frequency crosses the resonance frequency of the IDT, thus confirming the acoustic nature of the luminescence modulation observed in Fig. 2(b).

Finally, we discuss the effect of the SAW on the h-BN films grown by MBE. As mentioned

before, the emission lines of these samples are very weak. In addition, they undergo significant spectral diffusion. These features masked the observation of the acoustic broadening reported above for the flakes. Under the application of the SAW, however, we observed a stabilization of the optical emission for some luminescence centers. Figure 3(a) shows a series of consecutive luminescence spectra (integration time of 20 s per spectrum) recorded for a sharp peak emitting at 624 nm in the absence of SAWs. The emission line jumps in time between two well-defined values at 623.5 and 624.1 nm, marked as vertical gray dashed lines. The intensity of the emission line also fluctuates, even though laser excitation density and sample temperature were kept constant during the experiment. Figure 3(b) shows the same sequence of spectra in the presence of a SAW of  $f_{\text{SAW}} = 513.50$  MHz and nominal rf power of 0 dBm (the IDTs in this sample were designed to launch SAWs with a different frequency than the ones for the flakes). Under the application of SAWs, the peak at 623.5 nm disappears. This effect was reproducible every time that we switched the acoustic waves on.

**Fig. 3.** Time evolution of the light emitted by a center in the MBE-grown film (a) in the absence of SAW and (b) when the SAW is on. The data are vertically shifted for clarity. The spectra were recorded sequentially starting from the bottom. The vertical dashed lines mark the spectral positions of the peaks.



As discussed above for the flakes, the spectral fluctuations in absence of SAWs suggest a coupling of the luminescent center to the ionization state of a nearby shallow charge trap. It is known that the piezoelectric fields of SAWs can dynamically control the charge population of shallow charge-trap centers. Therefore, we interpret the stabilization of the luminescence as caused by the interaction of the SAW with the nearby charge trap.

Following this model, we attribute the quenching of the 623.5 nm peak in Fig. 3(b) to the fact that the dynamic SAW piezoelectric field favors a particular ionization state of the nearby shallow trap. This can happen either by continuously injecting charge carriers into the trap, or by extracting the charge carriers as soon as they are trapped. Supposing that the high and low

energy peaks in Fig. 3(a) reflect the interaction of the luminescence center with a nearby shallow trap in its negative and neutral charge states, respectively, then the suppression of the high energy peak in Fig. 3(b) indicates that charge carrier extraction is the dominant mechanism in this case. Although a more comprehensive understanding of this mechanism requires additional experiments that go beyond the scope of this contribution, these results suggest that SAWs could be a helpful tool to reduce the energy fluctuation of the emission lines in the case of unstable emitters, as in our MBE-grown h-BN film.

In conclusion, we have demonstrated the interaction of SAWs with luminescence cen-

ters in h-BN flakes and films transferred to the surface of LiNbO<sub>3</sub> crystals. In the case of the flakes, the alternating acoustic field can modulate the shape and intensity of the emission lines. From the dependence of this modulation on the SAW power, we have estimated a deformation potential for the centers in h-BN of about 40 meV%. For the MBE-grown film, we have shown that the SAW fields can suppress the spectral fluctuations, thus leading to a more stable optical emission of the centers. We attribute this stabilization to the control of the ionization states of nearby charge traps by the piezoelectric field of the SAW. Our results show that SAWs are a powerful tool to modulate and control the electronic states of two-dimensional materials.

# Bestimmung der Ladungsträgerdiffusionslänge in GaN aus Kathodolumineszenz-Rasterbildern: Trugschlüsse und Möglichkeiten

Die Kathodolumineszenz (CL)-Spektroskopie ermöglicht es, die Emission von Halbleitern mit hoher räumlicher Auflösung abzubilden und ist daher gut geeignet, um Ladungsträger- oder Exziton-Diffusionslängen zu bestimmen. Die Ortsauflösung ist durch das Volumen definiert, in dem Elektronen-Loch-Paare durch den einfallenden Elektronenstrahl erzeugt werden. Eine genaue Bestimmung der Diffusionslänge erfordert die quantitative Kenntnis dieses Generationsvolumens, von dem häufig angenommen wird, daß es durch die Energieverlustverteilung im Halbleiter gegeben ist. In der vorliegenden Arbeit bestimmen wir das Generationsvolumen experimentell, indem wir die CL-Emission eines einzelnen  $(\text{In},\text{Ga})\text{N}/(\text{Al},\text{Ga})\text{N}$ -Quantentopfs messen, der in einer GaN-Matrix eingebettet ist. Die dünnen  $(\text{Al},\text{Ga})\text{N}$ -Barrieren verhindern das Einfangen von Ladungsträgern durch Diffusion in der GaN-Matrix, so dass die Emission ausschließlich durch direkte Ladungsträgergeneration erzeugt wird. Die gemessenen CL-Intensitätsprofile sind breiter als die berechnete Energieverlustverteilung, und ihre Breite nimmt mit abnehmender Temperatur monoton zu. Dieser Effekt erklärt sich aus der Notwendigkeit, dass die angeregten heißen Ladungsträger vor der strahlenden Rekombination bis an die Bandkanten abkühlen müssen, ein Prozess, der durch Elektron-Phonon-Streuung geschieht und zu einer räumlichen Ausdehnung des initialen Generationsvolumens führt.

Nachdem wir somit das Generationsvolumen der Ladungsträger quantifiziert haben, bestimmen wir deren Diffusionslänge, indem wir einen einzelnen  $(\text{In},\text{Ga})\text{N}/\text{GaN}$ -Quantentopf ohne zusätzliche Barrieren als Ladungsträgerkollektor verwenden, und CL-Profilen am Probenquerschnitt als Funktion der Temperatur aufzeichnen. Ein klassisches Diffusionsmodell erklärt die zwischen 120 und 300 K erfassten Profile, während unterhalb von 120 K ein zusätzlicher Quanteneinfangprozess berücksichtigt werden muss. Es zeigt sich, dass die Diffusionslänge zwischen 300 und 10 K um den Faktor 5 zunimmt. Die Kombination dieser Ergebnisse mit der effektiven Ladungsträgerlebensdauer, die mittels zeitaufgelöster Photolumineszenz-Spektroskopie gemessen wird, ermöglicht uns die Bestimmung der Ladungsträgerdiffusivität. Wir zeigen, dass die Temperaturabhängigkeit der Diffusivität quantitativ verstanden werden kann, wenn man die Diffusion gekoppelter Populationen von freien Trägern und Exzitonen berücksichtigt.

Die Ladungsträgerdiffusionslänge in GaN wurde häufig aus der Breite des CL-Intensitätskontrastes um den Austritt von Fadenversetzungen an der Oberfläche bestimmt. Dieser Kontrast hängt jedoch nicht von der Temperatur ab, im scheinbaren Widerspruch zu der starken Variation der Diffusionslänge, die in den oben beschriebenen Quantentopf-Messungen beobachtet wurde. Unser neues Verständnis des CL-Intensitätskontrasts von Versetzungen basiert auf der Erkenntnis, dass der Versetzungsaustritt an der  $\text{GaN}(0001)$ -Oberfläche mit einem piezoelektrischen Feld assoziiert ist, was in keiner früheren Studie berücksichtigt wurde. Dieses Feld dissoziert Exzitonen (und unterbindet damit die strahlende Rekombination) noch in einem Abstand, der mit der Breite der experimentell beobachteten CL-Intensitätsprofile vergleichbar ist. Für ein vollständiges Verständnis dieser Ergebnisse führen wir Monte-Carlo-Simulationen der CL-Bilder von Versetzungen durch, die zusätzlich zur Exzitonendiffusion die Auswirkungen der dreidimensionalen Spannungsverteilung um den Versetzungsaustritt berücksichtigen, nämlich die Exxitondrift aufgrund der lokalen Bandlückenvariation im Versetzungsspannungsfeld und die Exxitondissoziation im piezoelektrischen Feld, das durch die Spannungsänderungen induziert wird. Als sehr empfindliches Maß für die Diffusionslänge erweist sich der Energiekontrast, den wir daher als eine neue experimentelle Beobachtungsmöglichkeit für die Bestimmung der gekoppelten Ladungsträger-Exziton-Diffusionslänge in GaN vorschlagen.

# Determination of the carrier diffusion length in GaN from cathodoluminescence maps: fallacies and opportunities

V. Kaganer, U. Jahn, J. Lähnemann, K. Sabelfeld<sup>1</sup>, A. Kireeva<sup>1</sup>, C. Pfüller, T. Flissikowski, C. Chèze, K. Biermann, H. T. Grahn, R. Calarco, O. Brandt

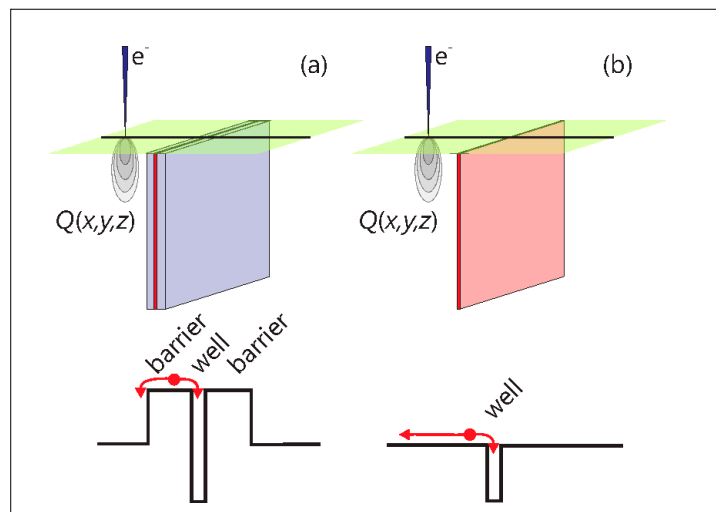
The minority carrier, ambipolar, or exciton diffusion length is the quantity that governs all scenarios where electrons and holes or excitons diffuse and recombine and is as such one of the crucial parameters that controls the behavior of semiconductor devices. A popular method to experimentally determine the diffusion length in GaN(0001) is based on cathodoluminescence (CL) maps that reveal threading dislocations as dark spots, directly demonstrating that dislocations act as centers of nonradiative recombination. It is commonly believed that (i) the initial spatial distribution of carriers generated by the primary high-energy electrons (the generation volume) coincides with the electron energy loss distribution calculated by empirical expressions, (ii) threading dislocations are lines that act as nonradiative sinks for minority charge carriers, and (iii) the size of the zone of reduced luminescence intensity around the dislocation provides, after correction for the generation volume, the carrier or exciton diffusion length. Our work presents a radically different view and constitutes a paradigm shift for the understanding of CL measurements on GaN and their application for the determination of the exciton diffusion length.

To experimentally determine the generation volume relevant for CL spectroscopy, we use the CL emission from a single (In,Ga)N quantum well (QW) clad by thin (Al,Ga)N barriers embedded in a GaN matrix. The barriers prevent carrier capture by diffu-

sion, as sketched in Fig. 1(a). In other words, the QW emission is produced exclusively by direct carrier generation within the QW and the barriers, while thermalized carriers in the GaN matrix cannot contribute to it. With the generation volume thus determined, we study the temperature dependence of the carrier diffusion length using an analogous sample without the (Al,Ga)N barriers so that carriers in the GaN matrix can diffuse to the QW, as shown in Fig. 1(b).

These single QW structures were synthesized by molecular beam epitaxy. A 3-nm-thick  $\text{In}_{0.16}\text{Ga}_{0.84}\text{N}$  well clad by 15-nm-thick

**Fig. 1.** Configuration of the CL experiments, with the electron beam scanning across the QW (a) sandwiched between barriers or (b) without the barriers, and sketches of the corresponding conduction band profiles.



<sup>1</sup> Institute of Computational Mathematics and Mathematical Geophysics, Russian Academy of Sciences, Novosibirsk, Russia

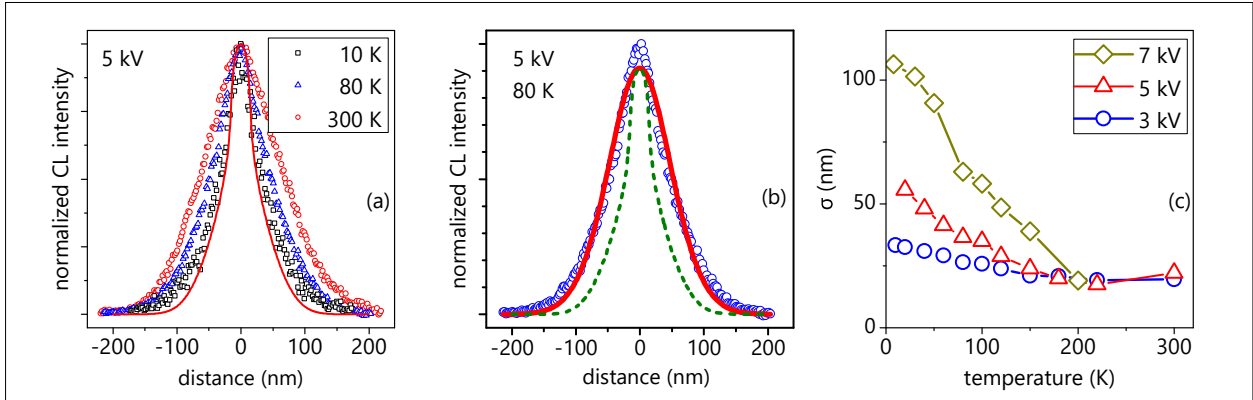


**Fig. 2.** (a) Experimental CL intensity profiles across the  $\text{In}_{0.16}\text{Ga}_{0.84}\text{N}$  QW clad by  $\text{Al}_{0.11}\text{Ga}_{0.89}\text{N}$  barriers taken with an acceleration voltage of 5 kV and at different temperatures (symbols). The line represents the electron energy loss distribution with the maximum possible width, calculated assuming that all carriers excited in the barriers reach the QW. (b) An example of the fit (solid line) of the experimental CL intensity profile (symbols) with a convolution of the energy loss distribution (dashed line) with a Gaussian. (c) Standard deviation  $\sigma$  of the Gaussian broadening of the energy loss distribution obtained by fits of experimental CL profiles as a function of temperature for various acceleration voltages of the primary electrons.

$\text{Al}_{0.11}\text{Ga}_{0.89}\text{N}$  barriers was embedded in a 1.4- $\mu\text{m}$ -thick GaN layer. This structure was deposited on top of a GaN(0001) template prepared by metal-organic chemical vapor deposition on a sapphire substrate. A second sample, containing the QW without the barriers, was synthesized in otherwise exactly the same way.

It is commonly assumed that the initial distribution of carriers generated by the electron beam is given by the energy loss distribution of the incident electrons. Here, we calculate this loss distribution using the free software CASINO [D. Drouin *et al.*, *Scanning* **29**, 92 (2007)]. The line in Fig. 2(a) shows the corresponding CL intensity at an acceleration voltage of 5 kV. This profile has the maximum possible width, since we assume that all carriers generated within the barriers reach the QW. The experimental CL intensity profiles, measured at the same acceleration voltage at different temperatures, are shown in Fig. 2(a) by symbols. The measured CL intensity profiles are broader than the calculated one and become progressively broader with decreasing temperature.

We explain this effect by considering that radiative recombination of charge carriers takes place only between thermalized electron-hole populations in the vicinity of  $\mathbf{k} = 0$ . The mean free path of carriers relaxing to their respective band edges is controlled by carrier-phonon scattering and thus increases with decreasing temperature. We have performed Monte Carlo simulations of this energy relaxation process, explicitly taking into account the Fröhlich interaction of electrons with longitudinal optical phonons, which qualitatively confirm this effect (not shown here). In addition, we have found this phenomenon to be more pronounced for higher electron beam energies, which we attribute to a marked slow-down of carrier relaxation due to the non-equilibrium phonon population (hot phonons) building up with increasing carrier density. In view of the considerable complexity of the thermalization and energy relaxation of carriers in semiconductors, we do not attempt to develop a unified framework embracing the initial high-energy loss processes and the subsequent thermalization, but have opted for a phenomenological approach capable of approximating the tempera-

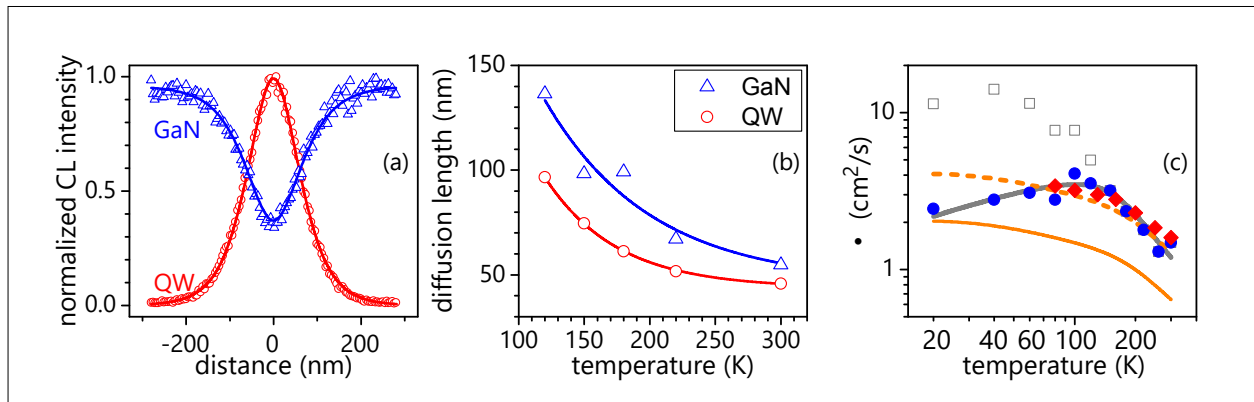


**Fig. 3.** (a) Experimental CL intensity profiles across the QW recorded at the wavelengths of GaN and the  $(\text{In},\text{Ga})\text{N}$  QW at 300 K and an electron acceleration voltage of 5 kV (symbols). The solid lines show fits using the diffusion length as a fit parameter. (b) Temperature dependence of the diffusion length obtained from the GaN and the QW intensity profiles. (c) Diffusivity  $D$  derived from the diffusion length assuming a pure diffusive process (squares) and after correction with regard to the impact of a quantum capture effect as a function of temperature (circles). Diffusivities obtained by the light-induced transient grating technique (diamonds) are shown for comparison. The solid and dashed lines show the theoretical hole and ambipolar diffusivities, respectively. The thick solid line represents a fit of the corrected diffusivity values taking into account the temperature-dependent coupling between free carriers and excitons.

ture- and voltage-dependent lateral generation profiles reasonably well. This goal can be achieved by convoluting the energy loss profile computed by CASINO with a Gaussian of variable standard deviation  $\sigma$ , as presented in Figs. 2(b) and 2(c).

Having thus quantified the generation volume of the carriers, we can proceed to the determination of the carrier diffusion length using the single QW without barriers, as depicted in Fig. 1(b). Figure 3(a) shows the CL intensity profiles measured at 300 K recorded at the wavelengths of GaN and the  $\text{In}_{0.16}\text{Ga}_{0.84}\text{N}$  QW. The CL profiles are simulated by a classical diffusion model using the generation volume profiles determined experimentally as described above and the diffusion length as a fit parameter. Figure 3(b) presents the temperature dependence of the diffusion length drawn from both kinds of profiles between 120 and 300 K. The GaN- and QW-related profiles differ in the diffusing carrier species contributing to the respective CL intensity profiles. Within the considered temperature range, excitons and free carriers co-exist. Due to the higher quantum efficiency

of excitonic compared to band-to-band transitions, the optical emission of GaN is dominated by exciton recombination. Consequently, the GaN CL profiles reflect dominantly exciton diffusion even at room temperature. The QW CL profiles contain, however, contributions from all diffusing species due to the nonselective carrier capture into the QW. Thus, the values deduced from QW-related CL profiles are diffusion lengths averaged over all contributing carrier species. It turns out that the utilized classical diffusion model cannot describe CL profiles measured at temperatures lower than 120 K, where fast quantum capture by the well contributes significantly to the shape of the experimental CL profiles.

In order to obtain the diffusivity  $D$  as a function of temperature from the diffusion length, we have measured the temperature dependence of the carrier lifetime by time-resolved photoluminescence experiments. The diffusivity derived from these lifetimes and the diffusion length assuming a purely diffusive process is shown in Fig. 3(c) by squares. The circles present the diffusivity obtained after correction for

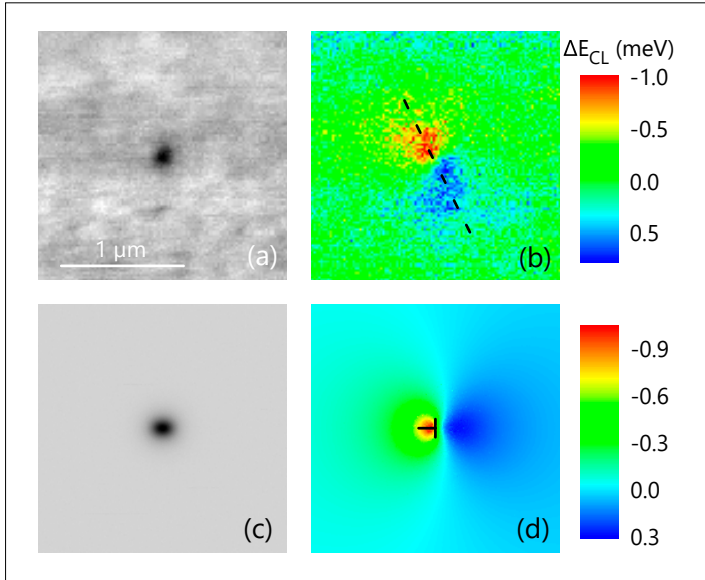


**Fig. 4.** Experimental [(a), (b)] and simulated [(c), (d)] two-dimensional spatial maps of the spectrally integrated CL intensity [(a), (c)] and CL spectral line positions [(b), (d)] for a temperature of 120 K around a threading dislocation. The dashed line in (b) indicates the direction of the line scans shown in Fig. 5. The scale bar in (a) applies to all maps. The extra half-plane of the dislocation is indicated in (d).

quantum capture. These latter values are in good agreement with those obtained from light-induced transient grating measurements [P. Ščajev *et al.*, *J. Appl. Phys.* **111**, 023702 (2012)] shown by diamonds. The experimental data are compared to results of calculations considering deformation potential, piezoelectric, and polar optical phonon scattering. The hole and ambipolar diffusivity are obtained without free parameters. Between 150 and 300 K, the data are seen to follow the ambipolar diffusivity, but they deviate significantly at lower temperatures. Taking into account the temperature-dependent coupling between free carriers and excitons allows us to obtain a satisfactory fit of the corrected diffusivity values.

Having obtained reliable insight into the temperature-dependent diffusivity and diffusion length in GaN, we proceed to the analysis of the CL images of dislocations. Figures 4(a) and 4(b) present hyperspec-

tral maps around the outcrop of a threading dislocation in a free-standing GaN layer grown by hydride vapor phase epitaxy. A full CL spectrum was recorded at each point in the energy range from 3.2 to 3.8 eV, covering all free- and bound-exciton transitions of GaN. The maps of the spectrally integrated intensity of the dominant exciton transition and its spectral position, shown in Figs. 4(a) and 4(b), are obtained by fits to the spectra. The maps clearly reveal the reduced CL intensity and the shift of the transition energy at the outcrop of the threading dislocation.

For a quantitative analysis, Figs. 5(a) and 5(b) show the integrated intensity and the spectral position of the exciton transition obtained by line scans across the strain dipole of the dislocation [dashed line in Fig. 4(b)] in the temperature range from 10 to 200 K. The width of the CL intensity curves does not notably depend on temperature, although the diffusion length is known to vary strongly with temperature, such as depicted in Fig. 3(b). This result cannot be understood within the common perception of a threading dislocation as a nonradiative line defect acting as a sink for carriers.

Our new understanding of the CL intensity contrast from dislocations is based on the recognition that the dislocation outcrop in GaN(0001) is associated with a piezoelectric field, which was not taken into account in any previous study. Wurtzite GaN is a pyroelectric (and thus piezoelectric) crystal. Uniform strain produces a piezoelectric polarization, and strain gradients such as around a dislocation generate a piezoelectric field that may dissociate excitons. In bulk GaN, neither *a*-type edge nor *c*-type screw dislocations with the line direction along  $\langle 0001 \rangle$  cause piezoelectric fields, in contrast to dislocations with other line directions. However, when these dislocations reach a surface, a polarization charge is created due to the relaxation of the elastic strain of the dislocation at the free surface.

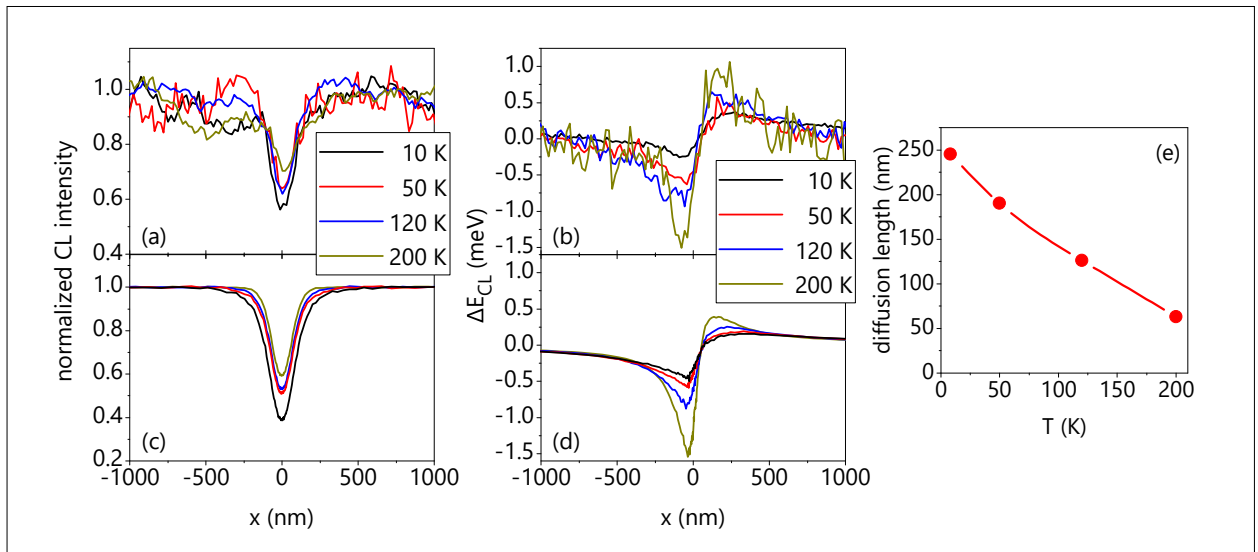


**Fig. 5.** (a) Experimental and (c) simulated spectrally integrated CL intensity, (b) experimental and (d) simulated spectral position of the dominant exciton line in scans along the strain dipole of the dislocation [dashed line in Fig. 4(b)]. (e) Temperature dependence of the exciton diffusion length obtained from the simulations in (c) and (d).

Figure 6(a) shows the calculated distribution of the piezoelectric field that arises from elastic strain relaxation at the surface around the outcrops of threading dislocations in GaN{0001}. This field drastically reduces the exciton lifetime close to the dislocation outcrop. Figure 6(b) presents the calculated CL image of the dislocation in the absence of exciton diffusion, with exciton dissociation as the only reason for a variation of the CL signal near the dislocation. The width of the CL intensity profile thus obtained is comparable with the width of the profile observed experimentally.

For a full understanding of these results, we perform Monte Carlo simulations of the CL images of dislocations that take into account, in addition to exciton diffusion, the effects of the three-dimensional strain distribution associated with the dislocation, namely, exciton drift due to the local band-gap variation in the dislocation strain field and exciton dissociation in the piezoelectric field induced by the changes in strain.

Figures 4(c), 4(d), 5(c), and 5(d) present the results of these Monte Carlo simulations. The temperature dependence of the diffusion length employed in the simulations, chosen such as to reproduce the experimental trends, is shown in Fig. 5(e). Evidently, varying the diffusion length by a factor of 5 has very little effect on the CL intensity profile. The key for understanding this insensitivity is the fact that excitons generated within the reach of the piezoelectric field have no chance to escape its influence, since their lifetime (and hence diffusion length) is reduced to effectively zero regardless of their diffusion length far from the dislocation. In fact, the finite contrast observed for excitation within the *lateral* reach of the piezoelectric field stems from excitons generated beneath its *vertical* reach. This fraction of excitons excited deeper in the crystal also dominates the spectral position of the exciton transition close to the dislocation line. For short diffusion lengths, excitons decay radiatively close to their point of excitation and thus

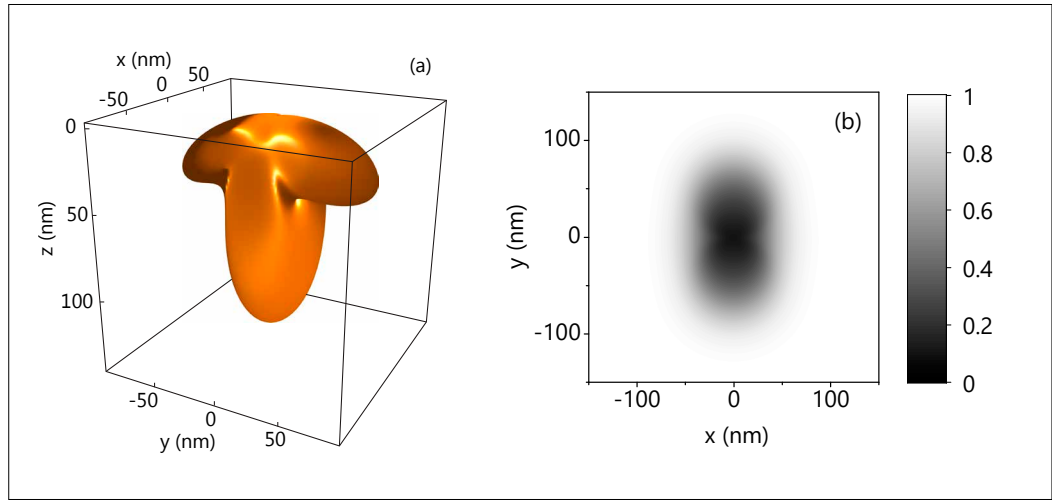


**Fig. 6.** (a) Electric field distribution  $E = |\mathbf{E}|$  around the outcrop of an edge threading dislocation. The figure shows an iso-field surface at  $E = 10 \text{ kV/cm}$ . The  $xy$  plane at  $z = 0$  corresponds to the GaN{0001} surface. (b) Calculated CL intensity map around an edge threading dislocation in the absence of carrier diffusion.

probe the high strain close to the dislocation line. In contrast, long diffusion lengths lead to a spatial redistribution of excitons, the majority of which will then decay far from the dislocation line with transition energies close to the bulk value, hence smoothing out the characteristic variation of the energy position in the vicinity of a dislocation. Energy profiles across edge dislocation outcrops at the GaN{0001} surface are thus a sensitive means to access the exciton or carrier diffusion length in GaN [cf. Figs. 5(b) and 5(d)].

Our results show that the common understanding of a diffusion-controlled intensity contrast around threading dislocations in GaN{0001} is a misconception. The mechanism dominating the intensity contrast is the piezoelectric field around the dislocation outcrop, and exciton diffusion changes this contrast only marginally. However, the energy contrast turns out to be highly sensitive to the diffusion length, which we thus propose as a new experimental observable for the actual determination of the coupled carrier-exciton diffusion length in GaN.

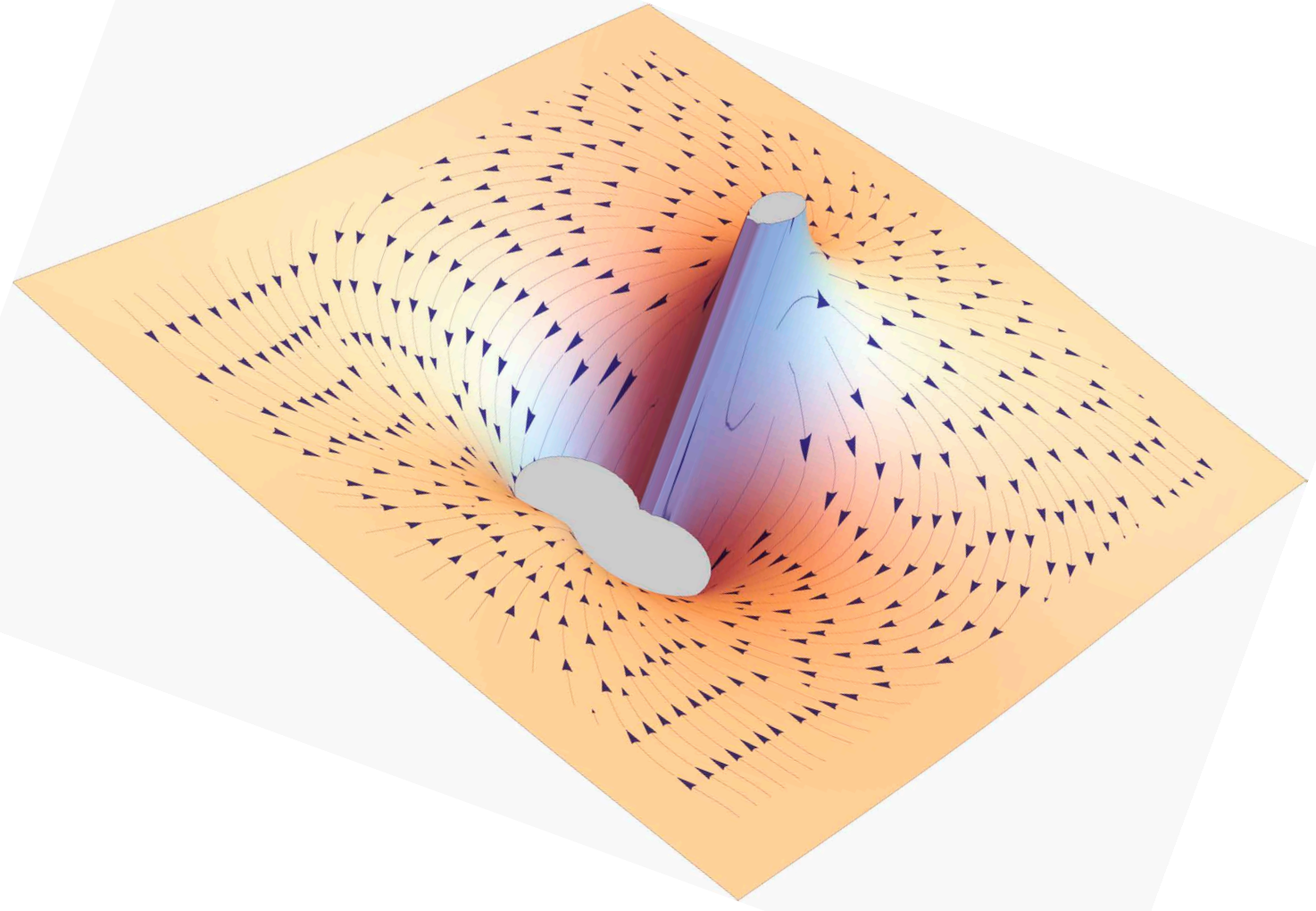


**Fig. 7.** Band-gap variation around the line of an  $\alpha$ -type edge dislocation in GaN at room temperature and the drift velocity field caused by this variation. The length of the arrowheads is proportional to the drift velocity.

# Das Verhalten von Elektronen in künstlich erzeugten periodischen Potentialen

Künstliche zwei-dimensionale Gitter sind aktuell von großem Interesse weil sie exotische Bandstruktureffekte zugänglich machen, zum Beispiel Energiebänder mit linearer Dispersion und extrem hoher Ladungsträgerbeweglichkeit oder auch flache Energiebänder, die zu Elektronenkorrelation führen können. Künstliche Gitter könnten sogenannte Quanten-Materialien mit vielseitigen und präzise einstellbaren Eigenschaften Wirklichkeit werden lassen. Experimentelle Methoden wie die Lithographie, ultrakalte Atome in optischen Fallen, Atom-Manipulation mittels Rastertunnelmikroskopie (STM) und photonische Kristalle wurden bis dato erfolgreich eingesetzt, um künstliche Gitter zu erzeugen. Durch Atom-Manipulation mittels STM konnten sie bisher lediglich auf Metallocberflächen aufgebaut werden. Demgegenüber hätte ihre Realisierung auf Halbleiteroberflächen entscheidende Vorteile, weil elektrostatische Abschirmungseffekte hier deutlich geringer sind als bei Metallen. Dies würde es erlauben, Ladungsträger gezielt und atomar genau durch geladene (und umpositionierbare) Punktdefekte zu beeinflussen. Darüber hinaus könnten aufgebaute atomare Strukturen durch externe Elektroden elektrostatisch angesteuert werden, was ein langfristiges Ziel unserer Arbeit darstellt.

Kürzlich haben wir gezeigt, daß sich periodische atomare Strukturen auf einer Halbleiteroberfläche mittels Atom-Manipulation aufbauen lassen, um die Zustände von Ladungsträgern gezielt zu beeinflussen [1]. Im Einzelnen haben wir hexagonale Ringstrukturen erzeugt, welche die typischen Energieniveaus eines Quantenrings aufweisen – einem geschlossenen Pfad, auf dem sich die Elektronen phasenkohärent bewegen können. Die Niveaustuktur entspricht einem einfachen Grundzustand und zweifach entarteten angeregten Zuständen. Die hexagonale Ringform bewirkt eine periodische Modulation des Ringpotentials und damit eine Störung der Energieniveaus. Als Folge wird die Energieentartung für bestimmte Zustände aufhoben; ganz analog zum Fall der Ausbildung von Energielücken in der Bandstruktur eines ein-dimensionalen linearen Gitters. Durch Hinzufügen oder Entfernen einzelner Atome mit der STM-Spitze kann die Modulation verstärkt oder auch invertiert werden. Unsere Ergebnisse zeigen, daß sich Ladungsträgerdynamik in einem maßgeschneiderten periodischen Potential gezielt einstellen und verändern lässt. Dieser Ansatz könnte es zukünftig ermöglichen, ausgedehnte künstliche Gitter auf Halbleiteroberflächen atomar genau herzustellen.

# Electron behavior in artificial periodic potentials

V. D. Pham, K. Kanisawa<sup>1</sup>, S. Fölsch

Artificial two-dimensional lattices currently attract broad interest because they make it possible to explore exotic band structure features like linear band dispersion hosting massless Dirac fermions or flat bands supporting electron correlation. They could pave the way towards the realization of "quantum materials" with broadly variable and precisely controlled properties. To create these artificial lattices experimental approaches like lithography, ultracold atoms in optical traps, atom manipulation by scanning tunneling microscopy (STM), and photonic crystals have been used. So far, it was shown that atom manipulation by STM is capable of creating artificial lattices on metal surfaces. In contrast, constructing them on a semiconductor has obvious advantages because screening effects are reduced as compared to metals. This allows for a tunable electrostatic confinement of carriers by charged (and repositionable) point defects. It also enables to address assembled structures by external gate electrodes, which is a long-term goal of our work.

We recently demonstrated that electrons can be confined in an artificial periodic potential created by atom manipulation on a semiconductor surface [1]. Specifically, hexagonal atomic rings were assembled that reveal the generic energy level structure of a quantum ring including its single ground state and doubly degenerate excited states. The hexagonal ring shape leads to a periodic potential modulation and thereby a perturbation of the level structure that can be understood in analogy to band gap formation in a one-dimensional (1D) periodic potential. The modulation can be enhanced or inverted by further adding or removing atoms with the STM tip. Our results demonstrate the possibility of de-

signing and controlling electron dynamics in a tunable periodic potential, holding promise for the construction of extended artificial lattices on a semiconductor surface.

Our experiment takes advantage of positively charged adatoms on an InAs surface that can be repositioned by the STM tip. This allows us to engineer the electrostatic surface potential landscape and thereby induce carrier confinement with atomic-scale precision [2]. In detail, we employ the InAs(111)A surface which is In-terminated and exhibits a  $2\times 2$  In-vacancy reconstruction as illustrated in Fig. 1(a). The surface hosts a low concentration (roughly 0.005 monolayer) of native In adatoms residing on the vacancy sites. An adatom of choice can be transferred to the tip by current-assisted bond breaking and subsequently transferred back to another desired surface vacancy site by forming a tip-surface point contact [3]. This so-called vertical atom manipulation of In adatoms on InAs(111)A can be performed in a highly reliable way. The STM topography images in Figs. 1(b-h) show the successive build-up of a hexagonal  $\text{In}_{30}$  ring with an adatom spacing of  $\sqrt{3}a' = 14.84 \text{ \AA}$ , where  $a' = 8.57 \text{ \AA}$  is the lattice constant of the  $2\times 2$  In-vacancy reconstruction. The increased apparent height around the charged adatoms is due to the screened electrostatic potential which locally increases the density of states available for the tunnel process.

Our earlier work revealed that the positively charged In adatoms confine electrons belonging to surface states of pristine InAs(111)A [2]. The resulting confined states can be probed by scanning tunneling spectroscopy measurements of the differential tunnel conductance  $dI/dV$ . Consider, for example, the  $\text{In}_{30}$  ring shown in Fig. 2(a) which

<sup>1</sup> NTT Corporation, Atsugi, Japan

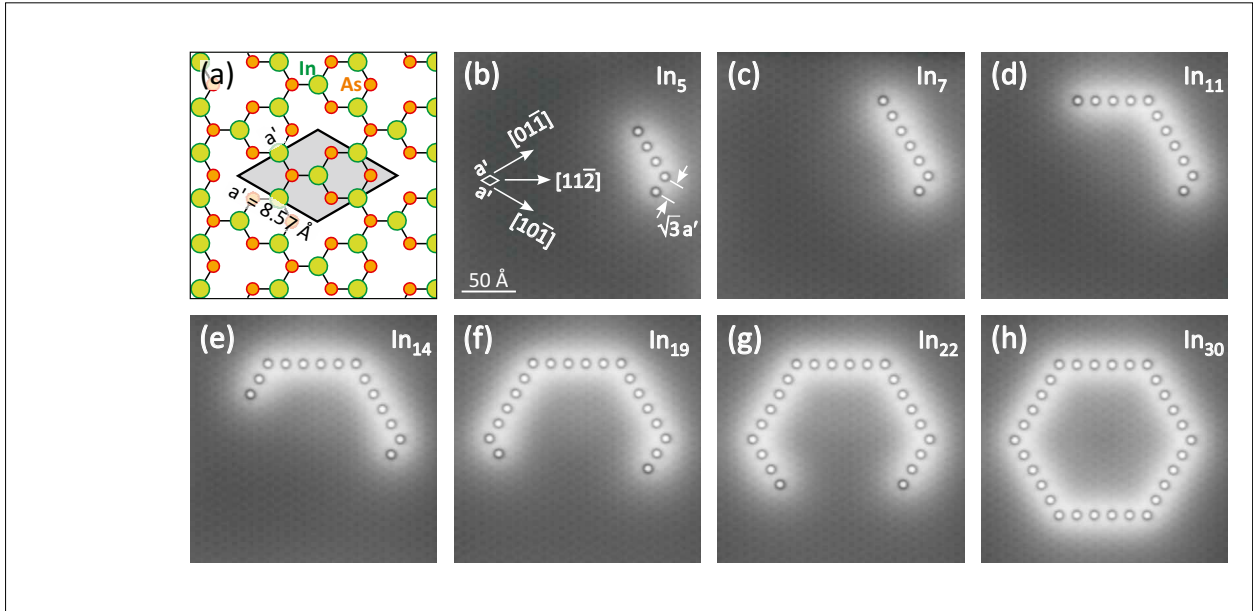


**Fig. 1.** (a) Stick-and-ball model of the first two atomic layers of the InAs(111)A surface with topmost In surface atoms (large green spheres) and As atoms in the second layer (smaller orange spheres); the nearest-neighbor spacing of the In vacancy sites of the  $2 \times 2$ -reconstructed surface is  $a' = 8.57 \text{ \AA}$ . (b-h) STM topography images (0.1 nA, 0.1 V) illustrating the stepwise assembly of a hexagonal ring composed of 30 In adatoms with an interatomic spacing of  $\sqrt{3}a' = 14.84 \text{ \AA}$ .

has a slightly larger adatom spacing of  $2a'$  as compared to that in Fig. 1. Recording the tunnel conductance at the tip positions marked in Fig. 2(a) yields the spectra in Fig. 2(b). The observed  $dI/dV$  peaks signify the emergence of quantized states. These states can be readily understood within the picture of free-electron motion along a closed path. Neglecting the effect of the hexagonal shape and treating the problem, to a first approximation, as a circular ring of circumference  $L = 2\pi R$ , the eigenstate energies are

$$E_l = \frac{\hbar^2}{2m^*} \frac{l^2}{R^2}, l = 0, \pm 1, \pm 2, \pm 3, \dots \quad (1)$$

with  $R$  the radius and  $l$  the quantum number of angular momentum. The ground state with  $l = 0$  is a singlet whereas excited states with finite angular momentum are doubly-degenerate. Following this level assignment, we observe the ground state with  $l = 0$  and the excited states with  $l = \pm 1, \pm 2$ , and  $\pm 3$  within the energy window covered

by the spectra in Fig. 2(b). Nevertheless, of particular interest is the 13 mV splitting of the eigenstate with  $l = \pm 3$  which clearly goes beyond the first-order approximation of confinement in a circular ring. The splitting highlights the effect of the corner sites: the wave functions associated with  $l = \pm 3$  have  $2l/l = 6$  lobes so that their positions can be in registry either with the corners or the sides of the hexagon. This circumstance lifts the degeneracy of the  $l = \pm 3$  state because the confining potential is enhanced at the corners compared to the sides (due to the locally enlarged charge density at the corners). As a consequence, the component localized at the corners is lower in energy (blue spectrum) than that localized at the sides (red spectrum). These observations illustrate the general principle of quantum mechanics that symmetry lowering causes degeneracy lifting.

Figures 2(c,d) add STM images of rings with the same adatom spacing as in pan-

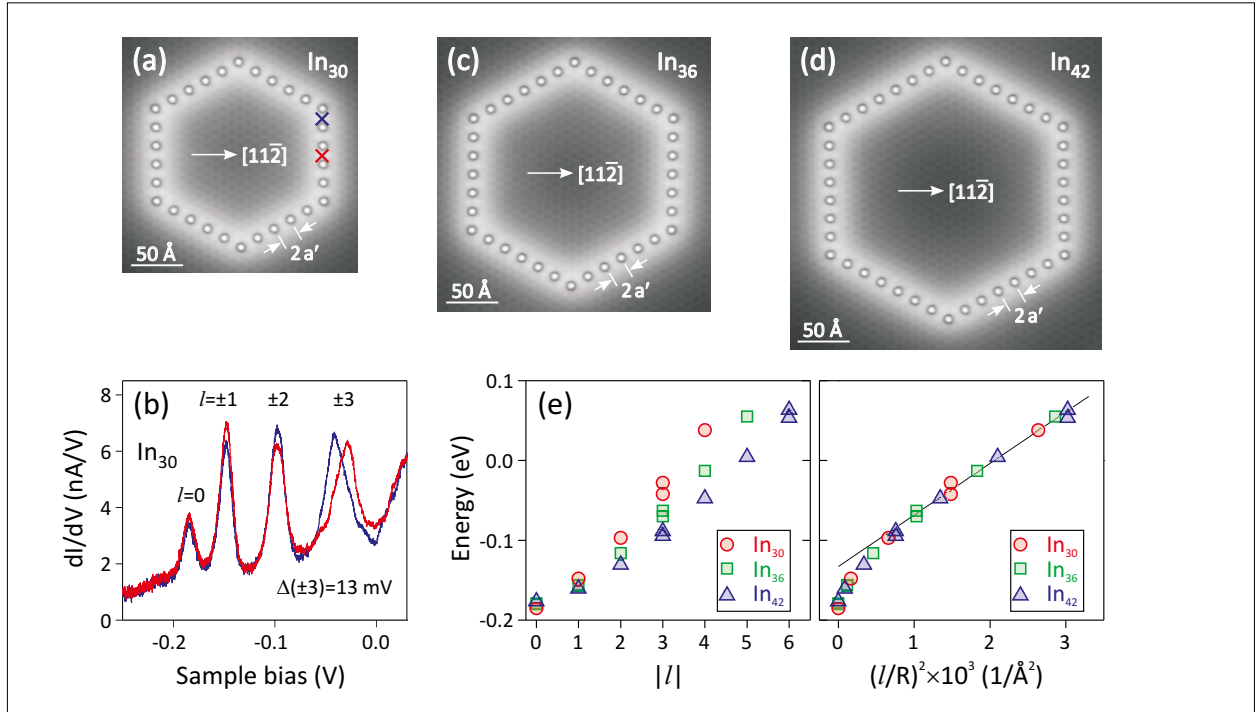


**Fig. 2.** (a) STM topography image (0.1 nA, 0.1 V) of an  $In_{30}$  ring with an interatomic spacing of  $2a' = 1714$  Å. (b) Conductance spectra taken along the  $In_{30}$  ring at the tip positions indicated in (a) revealing  $dI/dV$  peaks that signify the ring-confined states with quantum number of angular momentum  $l = 0, \pm 1, \pm 2$ , and  $\pm 3$ . The  $l = \pm 3$  degeneracy is lifted as a result of the hexagonal ring shape. (c,d) STM topography images (0.1 nA, 0.1 V) of rings composed of  $N = 36$  and 42 atoms with the same interatomic spacing as in (a). (e) Left panel: energies of the quantized states as a function of  $|l|$  observed for the rings with  $N = 30$  (red spheres),  $N = 36$  (green squares), and  $N = 42$  (blue triangles). The degeneracy of the states with  $l = \pm 3$  and  $\pm 6$  is lifted, in line with the discussion in the text. Right panel: the same energies plotted versus  $(I/R)^2$ , where the effective radius is  $R = sN/(2\pi)$  with  $s = 2a'$  the interatomic spacing and  $N$  the number of atoms. The linear dependence predicted by Eq. (1) is confirmed for energies at moderate bias voltages whereas the deviation at larger negative bias is likely due to the tip-induced electric field.

el (a) but composed of  $N = 36$  [panel (c)] and  $N = 42$  adatoms [panel (d)]. The spectra found for these larger rings (not shown in Fig. 2) are qualitatively similar to those displayed in panel (b). The left panel of Fig. 2(e) summarizes the energies of the quantized states depending on  $|l|$  as observed for all three rings of different size. The right panel of Fig. 2(e) shows the same energies plotted versus  $(I/R)^2$ , where the effective radius is  $R = sN/(2\pi)$  with  $s = 2a'$  the interatomic spacing and  $N$  the number of atoms. Clearly, all data points in the E-versus- $(I/R)^2$  plot collapse on a single curve. The linear dependence expected from Eq. (1) is fulfilled for confined-state ener-

gies detected at moderate bias voltages whereas a deviation from the linear trend is observable at negative biases exceeding a magnitude of about 100 mV. This behavior is likely due to the tip-induced electric field causing a notable local band bending at sufficiently large bias magnitude. The data in Fig. 2(e) confirm that Eq. (1) captures the qualitative features of the level structure in our assembled rings.

The observed level splitting (degeneracy lifting) can be understood in analogy to the occurrence of an energy gap predicted for electrons in a 1D periodic potential. The effect becomes more obvious when the po-

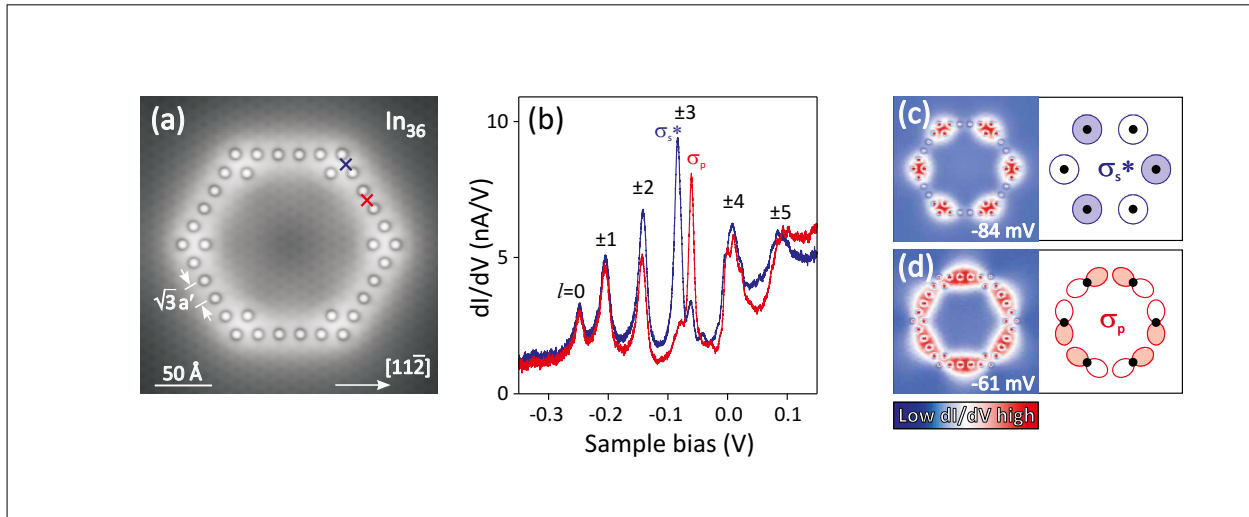


**Fig. 3.** (a) STM image (0.1 nA, 0.1 V) of a In<sub>36</sub> hexagonal ring with 6 auxiliary adatoms to enhance the confinement at the corners. (b) Conductance spectra taken at the tip positions shown in (a) revealing the confined states with  $l = 0$  to  $\pm 5$ ; the  $l = \pm 3$  degeneracy is lifted as a result of the enhanced confinement at the corners. (c) Spatial conductance map (left) recorded for the  $l = \pm 3$  component at lower energy revealing that the confined wave function symmetry is equivalent to an antibonding state of s orbital character ( $\sigma_s^*$ ), see scheme on the right. (d) As (c) but for the component at higher energy, the lobe structure is equivalent to a bonding state of p orbital character ( $\sigma_p$ ).

tential modulation is further enhanced by adding auxiliary adatoms at the corners, see Fig. 3(a). The obtained conductance spectra in Fig. 3(b) are qualitatively similar to those of the bare In<sub>30</sub> ring in Fig. 2(b), however, they indicate a significantly larger splitting of the  $l = \pm 3$  state,  $\Delta(\pm 3) = 23$  mV. The relative intensities within the doublet show that the  $l = \pm 3$  component at lower (higher) energy is detected at the corners (sides) of the hexagon. Consistently, the corresponding spatial conductance maps [Figs. 3(c) and (d)] reveal that the lobes of the confined wave function are centered at the corners for the component at lower energy (implying stronger binding), while they are centered in between of the corners for the component at higher energy (weaker binding). The corners can be viewed as artificial atoms (sites of enhanced confinement) coupled through the straight sides of the hexagonal ring structure.

To further rationalize the observed energy splitting and the confined wave functions we draw an analogy to the case of elec-

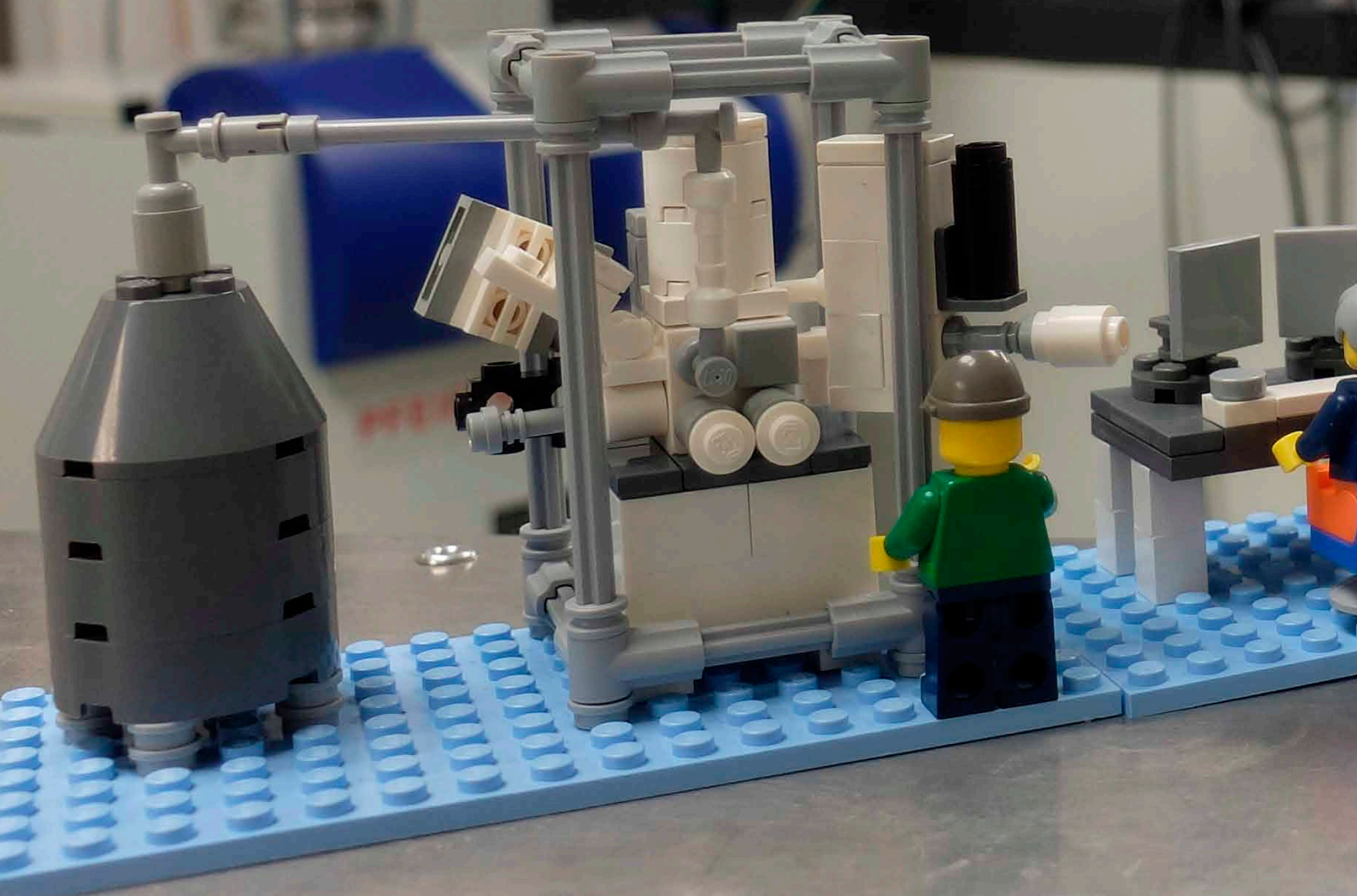
trons in a 1D periodic potential where energy gaps occur for wave vectors equal to half a reciprocal lattice vector: first considering the lowest-lying energy gap, the state at the lower band gap edge is of fully antibonding s orbital character ( $\sigma_s^*$ ), whereas the state at the upper band gap edge is of fully bonding p orbital character ( $\sigma_p$ ). Indeed, the spatial conductance maps at  $l = \pm 3$  are consistent with the expected wave function symmetry because the state at lower energy [Fig. 3(c)] is centered at the artificial atoms and has nodes in between ( $\sigma_s^*$ ) while the state at higher energy [Fig. 3(d)] has nodes at the atomic positions and lobes in between ( $\sigma_p$ ). Returning to the 1D potential case, higher-lying energy gaps occur at wave vectors associated with larger reciprocal lattice vectors. Likewise, we expect energy splittings in our rings also for states with  $l = \pm 6, \pm 9, \pm 12, \dots$  for which the number of wave function lobes (nodes) is a multiple of 6. States of all other quantum numbers are expected to show no splitting. This can be readily shown by a simple model considering the matching between the probability

density of a confined state and a perturbation potential of hexagonal symmetry. Access to states of higher quantum number  $l$  can be expected for rings of enlarged size and enhanced confinement, leading to a reduced level spacing. By assembling larger rings, we indeed observed states of quantum numbers up to  $l = \pm 9$  and a total of three splittings (energy gaps) at  $l = \pm 3, \pm 6$ , and  $\pm 9$  [1].

In conclusion, the results discussed here show that atom manipulation on the InAs(111)A surface allows one to engineer atomically precise quantum rings which exhibit an energy spectrum that is consistent with 1D confinement along a closed loop. Their hexagonal shape (predefined by the surface symmetry) leads to a periodic potential modulation that perturbs the states. As a result of this perturbation, states as-

sociated with a wave function that shares the hexagonal symmetry of the ring potential experience are lifting of their degeneracy – in analogy to band gap opening at the Brillouin zone boundaries for electrons in a 1D periodic potential. Our results are a proof of principle that artificial lattices can be created on the InAs(111)A surface, offering a test ground for exotic band structure features of lattice structures that can be designed with atomic-scale perfection.

- [1] V. D. Pham, K. Kanisawa, and S. Fölsch, Phys. Rev. Lett. **123**, 066801 (2019).
- [2] S. Fölsch, J. Martínez-Blanco, J. Yang, K. Kanisawa, and S. C. Erwin, Nat. Nanotechnol. **9**, 505 (2014).
- [3] J. Yang, C. Nacci, J. Martínez-Blanco, K. Kanisawa, and S. Fölsch, J. Phys. Condens. Matter **24**, 354008 (2012).





# Core Research Areas Forschungsschwerpunkte

Nanofabrication

[Nanofabrikation](#) ..... 35

Nanoanalytics

[Nanoanalytik](#) ..... 40

Control of Elementary Excitations by Acoustic Fields

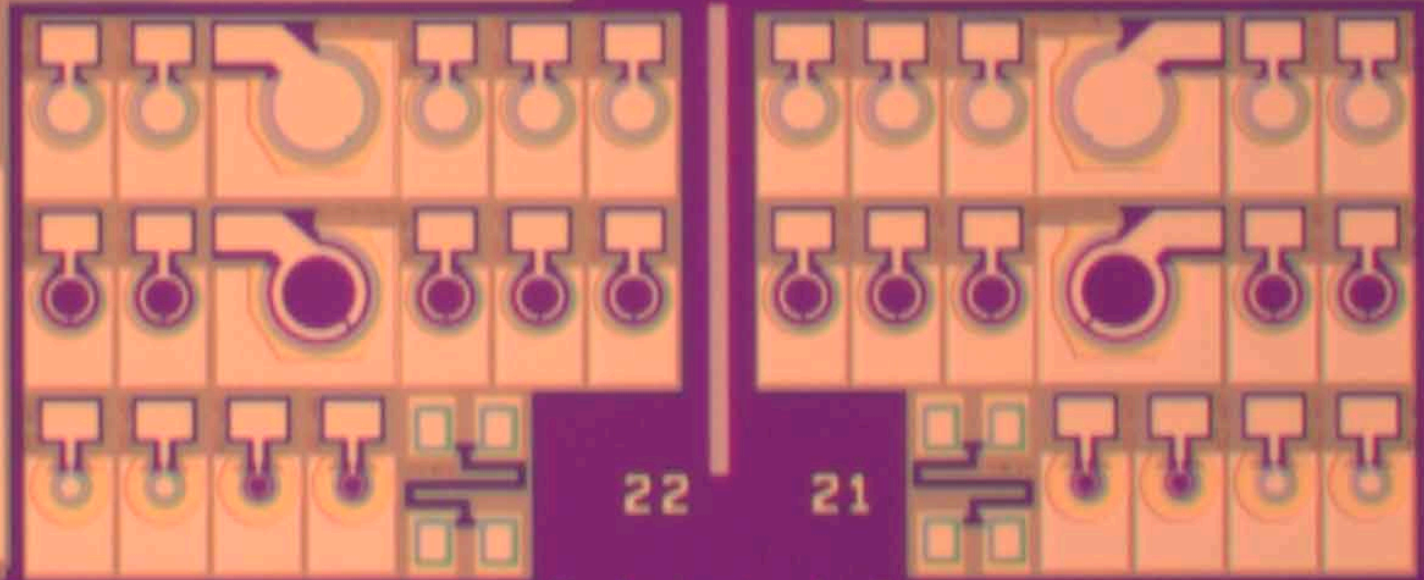
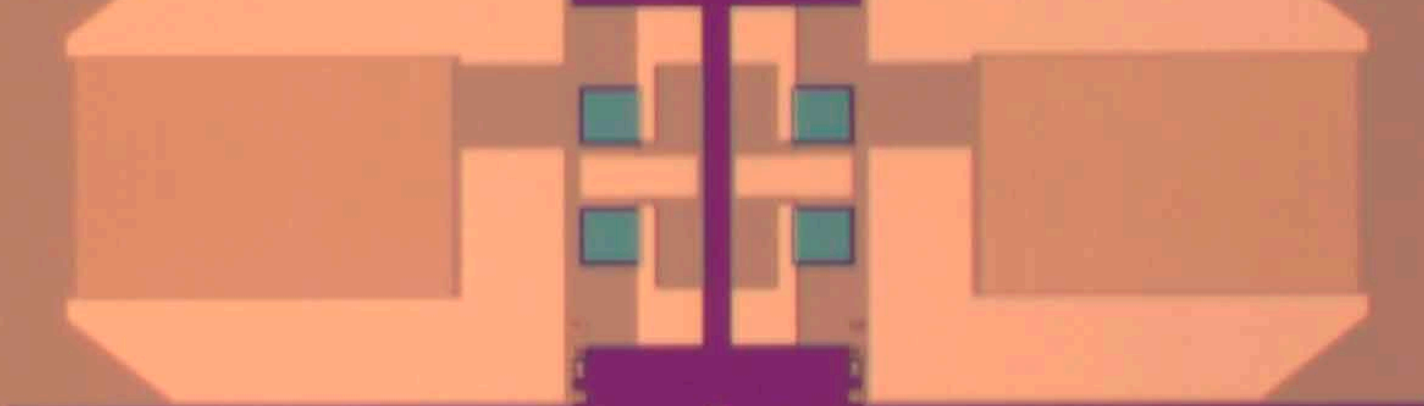
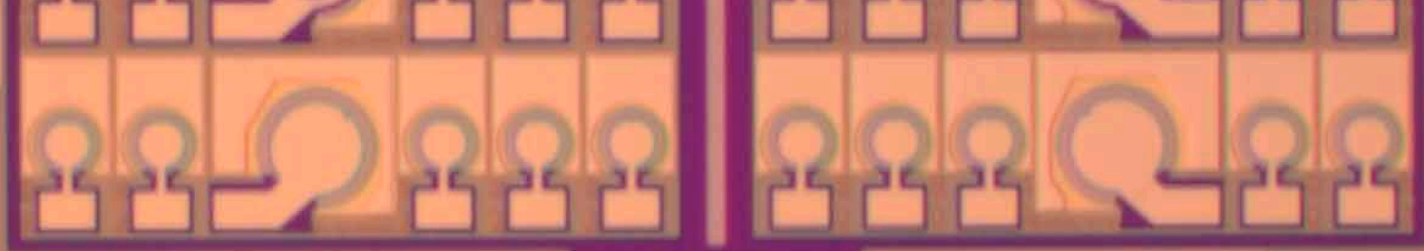
[Die Kontrolle von elektrischen Anregungen in Halbleiter-Nanostrukturen](#) ..... 44

III-V Nanowires for Optoelectronics

[III-V-Nanodrähte und deren Anwendung in der Optoelektronik](#) ..... 47

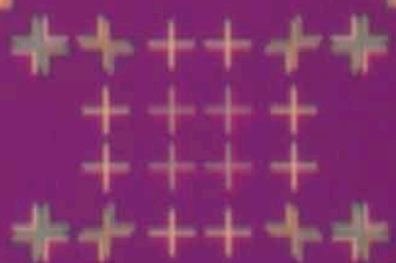
Intersubband Emitters: GaAs-based Quantum-Cascade Lasers

[Intersubbandemitter: GaAs-basierte Quantenkaskadenlaser](#) ..... 52

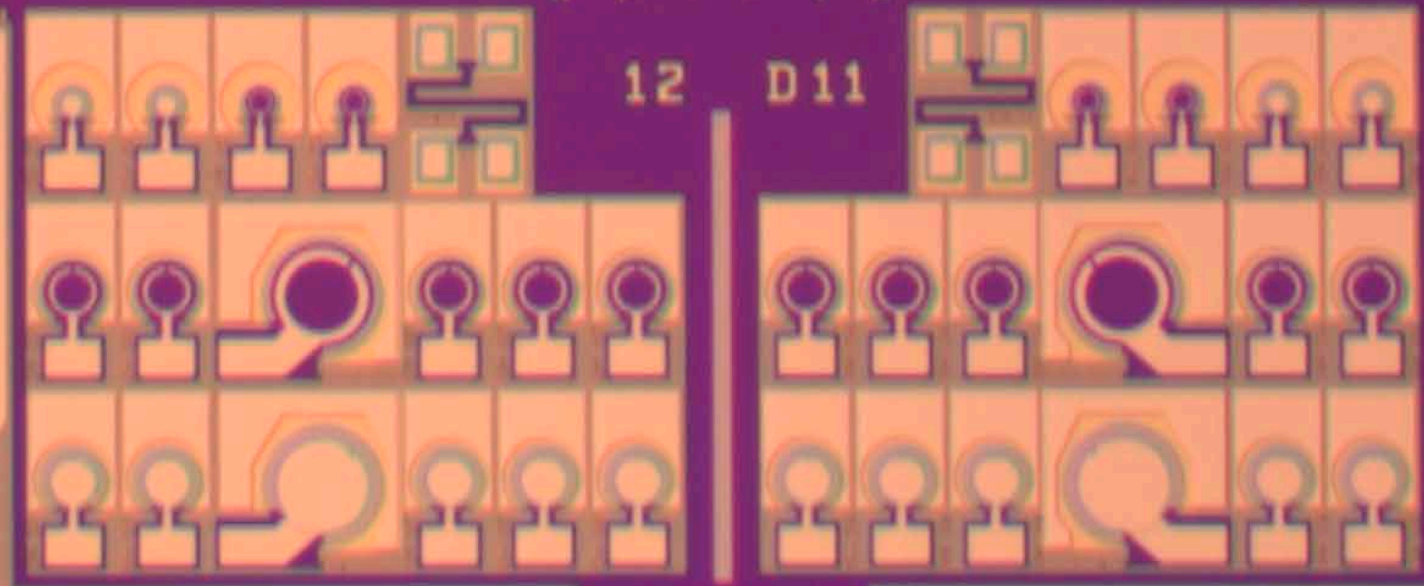


22

21



12 D11



# Nanofabrication / Nanofabrikation

Dr. Lutz Geelhaar

Dr. Klaus Biermann – Group-III arsenides

Dr. Oliver Bierwagen – Oxides

Dr. Raffaella Calarco – Group-III nitrides, GeTe-Sb<sub>2</sub>Te<sub>3</sub> phase-change materials

Dr. Jens Herfort – Ferromagnet semiconductor hybrid structures

Dr. Joao Marcelo J. Lopes – Graphene, hexagonal BN

The subject of this core research area is the fabrication of novel types of nano-structured crystals and the investigation of fundamental growth mechanisms. The perspective of such samples is to enable the investigation of exciting physical phenomena or to offer new tailored functionalities that may inspire innovative devices. In general, we fabricate our samples in the bottom-up approach, i.e. in a process of adding material by growth in contrast to removing material by etching. Thus, for the desirable high level of control over fabrication it is mandatory to understand the underlying growth mechanisms. Moreover, these mechanisms are often highly fascinating by themselves. The standard technique for the fabrication of samples at PDI is molecular beam epitaxy (MBE). Hence, our samples are usually grown as epitaxial thin films on crystalline substrates, and different materials may be stacked on top of each other to form heterostructures of considerable complexity. In addition, we also grow on substrates whose surface has been pre-patterned by lithography to induce lateral variations in growth, and self-organization phenomena can be employed for the deliberate formation of three-dimensional structures like quantum wires instead of two-dimensional planar films. The samples that we aim to fabricate are novel in at least one of the following aspects:

- A material of this chemical composition has not been synthesized before, or at least not in this crystalline quality and/or chemical purity.
- Different materials are monolithically integrated to form an unprecedented hybrid structure.

Das Thema dieses Forschungsschwerpunktes ist die Herstellung neuartiger nanostrukturierter Kristalle und die Untersuchung fundamentaler Wachstumsmechanismen. Solche Proben dienen dazu, spannende physikalische Phänomene zu untersuchen oder aber neue, maßgeschneiderte Funktionalitäten zu ermöglichen, die innovative Anwendungen inspirieren können. Generell werden die Proben in einem sogenannten ‚bottom-up‘-Ansatz (englisch für ‚von unten nach oben‘) hergestellt. Dies bedeutet, dass während des Herstellungsprozesses Material durch Wachstum hinzugefügt wird – im Unterschied zu Verfahren, bei denen aus einer größeren Probe Material durch Ätzprozesse abgetragen wird. Daher ist es für das angestrebte hohe Maß an Kontrolle bei der Probenherstellung unabdingbar, die zugrundeliegenden Wachstumsmechanismen genau zu verstehen – ganz abgesehen davon, dass diese Mechanismen per se faszinierend sind.

Die Standardmethode, die wir am PDI für die Probenherstellung verwenden, ist die Molekularstrahlepitaxie (englisch molecular beam epitaxy, MBE). Infolgedessen werden unsere Proben gewöhnlich als epitaktische dünne Schichten auf kristallinen Substraten gezüchtet. Hierbei können unterschiedliche Materialien als Schichtsystem übereinander gewachsen werden und bilden dann Heterostrukturen von hoher Komplexität. Darüber hinaus wird auf Substraten gewachsen, deren Oberflächen mittels lithographischer Techniken vorstrukturiert sind. Somit können laterale Änderungen im Wachstum induziert werden. Außerdem werden Phänomene der Selbstorganisation ausgenutzt, um die Ausbildung dreidi-

- A known material or combination of materials is structured on the nanoscale in a new way, i.e. the sample is shaped in at least one dimension to a new type of geometry, or a heterostructure of exceptional complexity or precision is created.

Typical examples are extending the range of compositions over which films can be grown in high quality, the use of novel substrates, and the heteroepitaxy of dissimilar materials.

In general, all growth mechanisms are governed by the interplay between thermodynamics and kinetics. At the nanoscale, the role of surface and interface effects is often crucial. In heterostructures, differences between the crystal lattices induce strain which affects crystal growth and is often accommodated by the formation of defects. Hence, the elucidation of growth mechanisms is inextricably linked to the investigation of surface structure, interface formation, and in general the microstructure of the sample. Therefore, the close collaboration with the core research area *Nanoanalytics* is indispensable for the understanding of growth mechanisms and the successful fabrication of nanostructures. Where needed, experiments are complemented by theoretical calculations.

Our research is based on the longstanding expertise of PDI in the MBE of III-As and III-N compound semiconductors, but more and more we study the growth of other materials. One general objective is the monolithic integration of various materials on silicon. In the following, the material systems that are currently under investigation will be presented.

The epitaxial growth of *group-III-arsenide* heterostructures serves as the backbone of various internal and external research projects, due to the unique structural quality of the (Al,Ga)As material system and its very abrupt interfaces even in complex heterostructures — like quantum cascade la-

mensionaler Strukturen – wie zum Beispiel Quantendrähten – anstelle von planaren Schichten zu ermöglichen.

Die Proben, deren Herstellung wir anstreben, sind unter mindestens einem der folgenden Gesichtspunkte neuartig:

- Ein Material dieser chemischen Zusammensetzung wurde zuvor noch nicht synthetisiert – zumindest nicht in dieser kristallinen Qualität oder chemischen Reinheit.
- Unterschiedliche Materialien werden monolithisch integriert, um eine bislang nicht existierende Hybrid-Struktur zu erzeugen.
- Ein bekanntes Material oder eine Materialkombination wird auf der Nanoskala auf neuartige Weise strukturiert – d.h. die Probe wird entlang zumindest einer Raumrichtung zu einer neuartigen Geometrie geformt, oder eine Heterostruktur von außergewöhnlicher Komplexität oder Präzision wird erschaffen.

Typische Beispiele sind die Verwendung neuartiger Substrate, die Erweiterung des Zusammensetzungsbereichs, in dem Schichten in hoher Qualität gezüchtet werden können, und die Heteroepitaxie von sich stark unterscheidenden Materialien.

sters for the THz emission frequency range, which consist of up to some thousands of single thin layers with nominal thicknesses down to one monolayer. A second focus of this activity are microcavity structures for acoustically driven charge and spin transport experiments, for phonon and photon coupling and for exciton-polaritons with and without intra-cavity shallow patterning. Some of these structures are used for spatially resolved photoluminescence measurements to investigate the interaction of polaritons confined to arrayed traps. This year, we have continued our efforts to reach lateral trap dimensions on the order of  $0.5\text{ }\mu\text{m}$  as needed for trapping single polaritons. The anisotropic elongation of square mesas observed during overgrowth at standard growth temperatures could be suppressed by substantially lowering the temperature during the overgrowth of the intra-cavity patterned samples. Thus, well-defined arrays of  $1 \times 1\text{ }\mu\text{m}^2$  sized polariton traps were fabricated. A further reduction to  $0.5 \times 0.5\text{ }\mu\text{m}^2$  trap dimensions will be approached by using e-beam lithography instead of conventional photolithography. Samples for internal and external partners include heterostructures grown on GaAs substrates of various orientations for experiments like studying optical generation of THz radiation, random generators working at room temperature, open microcavities, sources of entangled photons, acoustically driven single photon sources, and biased dipolariton structures.

In the field of group-*III* nitride epitaxy, our work focuses on In-rich (In,Ga)N. For the development of efficient light emitting and laser diodes in the green spectral range, the growth of (In,Ga)N alloys with high In content as required to access the higher wavelength range of the emission spectrum is still challenging. In this context, short period super-lattices (SPSL) made of alternating binary InN and GaN layers, have been proposed as an ordered alternative to (In,Ga)N layers. Yet, the growth of such SPSLs has yielded instead (In,Ga)N/GaN

SPSLs with In content not higher than 0.3 in the quantum sheets with self-limited thickness of 1 monolayer (ML), and the intermixing with Ga has been attributed to strain related issues. This year, we have investigated the growth of (1 ML InN/2 MLs GaN) short period superlattices on Zn-(0001) and O-(0001̄) polar ZnO substrates, intercalating a coherent InN monolayer to prevent the strong chemical reaction of Ga with ZnO. ZnO is an attractive substrate as it is isomorphic to GaN and InN, and lattice-matched to  $\text{In}_{0.18}\text{Ga}_{0.82}\text{N}$ . We have monitored the growth of these SPSLs *in situ* by reflection high-energy electron diffraction. After few MLs, the growth mode becomes three-dimensional, and an (In,Ga)N alloy forms instead of a SL, as revealed by X-ray diffraction and by Raman spectroscopy. Thus, further efforts are needed for the growth of the desired SPSLs.

The fabrication of *ferromagnet semiconductor hybrid structures* in high crystal perfection is a prerequisite for the investigation of spin transport phenomena relevant for spintronic device concepts. Our focus is on the growth of half-metallic Heusler alloys on GaAs-related structures. The preparation of fully crystalline thin film stacks consisting of a semiconducting channel sandwiched between two ferromagnetic layers constitutes a prerequisite for a new vertical device type. In order to overcome the challenges associated with the growth of a semiconductor on a metal, we have continued to develop solid-phase epitaxy as an approach where an amorphous film of Ge is deposited on  $\text{Fe}_3\text{Si}$  and then crystallized slowly by thermal annealing. Previous comprehensive structural analysis of  $\text{Fe}_3\text{Si} / \text{Ge}(\text{Fe},\text{Si}) / \text{Fe}_3\text{Si}$  thin-film stacks grown this way showed that the  $\text{Ge}(\text{Fe},\text{Si})$  films crystallize in the well-oriented, layered tetragonal structure  $\text{FeGe}_2$ . This kind of structure does not exist as a bulk material and is stabilized by the solid-phase epitaxy of Ge on  $\text{Fe}_3\text{Si}$ . In a close collaboration with the core research area *Nanoanalytics*, we have studied the potential and the

characteristics of such  $\text{FeGe}_2$  interlayers in vertical spin valves. Furthermore, in order to characterize this new material individually, eliminating the underlying  $\text{Fe}_3\text{Si}$  film is essential, otherwise transport and magnetometry measurements would be dominated by metallic features. We have managed to do so using the same solid phase epitaxy approach by first growing a few monolayers of crystalline  $\text{Fe}_3\text{Si}$ , and then thicker amorphous Ge with a thickness ratio such as to obtain the right stoichiometry for layered  $\text{FeGe}_2$ . An 8-nm-thick  $\text{FeGe}_2$  film shows a drastic increase of the resistance by over 400% as the temperature is lowered. We can reasonably assert that this nonmetallic behavior is a characteristic of  $\text{FeGe}_2$  alone. In addition, magnetotransport at low temperature reveals a strong anomalous Hall effect, which suggests the presence of ferromagnetism. Hence,  $\text{FeGe}_2$  provides an interesting framework to study the interplay between chemical bonding and magnetism, and could open new ways for applications involving ferromagnetic layered materials.

Transparent (semi)conducting oxides are widely used in devices. For example, n-type  $\text{In}_2\text{O}_3$ ,  $\text{Ga}_2\text{O}_3$ ,  $\text{SnO}_2$ , and  $\text{NiO}$  traditionally serve as active material in conductometric gas sensors and—highly doped—as transparent contact layers in solar cells, displays, and LEDs. The requirements on material quality for these traditional applications are low, and usually met by polycrystalline, sputtered material. During the last decade, however, transparent semiconducting oxides have been re-discovered as true wide-band-gap semiconductors by virtue of their synthesis to semiconductor standards (single crystalline, highly pure with well-defined doping). This development enables the investigation of the underlying physics of these materials and their applications. It further opens up the possibility for novel and improved conventional oxide-semiconductor-based devices by rational design. For example, based on its large band gap of  $E_g=4.5$  eV, single crystalline  $\text{Ga}_2\text{O}_3$  is a promising material for next generation power

electronics as well as solar-blind ultra violet sensors. Combined with  $\text{In}_2\text{O}_3$  ( $E_g=2.7$  eV) and  $\text{Al}_2\text{O}_3$  ( $E_g=8.8$  eV), band gap engineering and heterostructures with large band offsets are foreseeable. Compared to traditional compound semiconductors, semiconducting oxides are at an early stage of development with many open fundamental questions. Our efforts to answer these questions are embedded in the Leibniz ScienceCampus GraFOx, lead by PDI. The main contribution of our core research area in this context is the growth of semiconducting oxides by MBE, a proven tool to synthesize high-quality semiconductor thin films, and to investigate their properties.

With crystalline  $\text{SnO}$  we have added a new, p-type semiconducting oxide to our materials portfolio, that is characterized by a high hole mobility. Based on our previous understanding of the growth kinetics of  $\text{SnO}_2$  we have been able to rationally determine the growth conditions for  $\text{SnO}$  that have allowed us to grow epitaxial, phase-pure  $\text{SnO}(001)$  layers having a hole mobility as high as  $3 \text{ cm}^2/\text{Vs}$ .  $\text{SnO}$  as gaseous species, created by heating  $\text{SnO}_2$  in an effusion cell to temperatures above  $1000$  °C, is typically used for the growth of the perovskite oxide  $\text{BaSnO}_3$ . This year we have demonstrated that a mixture of  $\text{SnO}_2$  and Sn can form gaseous  $\text{SnO}$  at significantly lower temperatures, resulting in a more efficient  $\text{SnO}$  source. In collaboration with the graphene activity we have also investigated the heteroepitaxy of  $\text{NiO}$  and  $\text{In}_2\text{O}_3$  on graphene with the purpose of functionalizing graphene for gas sensing applications. The comparison to the growth of  $\text{NiO}$  and  $\text{In}_2\text{O}_3$  on  $\text{SiC}$ , which is structurally similar to graphene but has stronger bonds, has shown a significant influence of the weak bonds of graphene on the epitaxial relation and morphology of the oxide film.

*Phase change materials* (PCM) are unique compounds employed in non-volatile random access memory thanks to the rapid and reversible transformation between the

amorphous and crystalline states that display large differences in electrical and optical properties. Our unique approach in this field is the use of MBE for the fabrication of epitaxial PCM, which makes possible advanced studies on the properties of these materials. The epitaxial growth of GeSbTe alloys is quite demanding as an interplay between composition, phase and ordering occurs. Control over those three parameters is mandatory to obtain material with well defined physical properties. Starting from this year, in the framework of the EU project BeforeHand we are actively involved in the development of high temperature and long data retention PCMs complying with the requirements of automotive applications. In this context, epitaxial Ge-rich GeSbTe alloys and heterostructures are currently under investigation. Finally, we have established the epitaxial growth of the metastable phase of GaTe on Si(111). GaTe belongs to the class of monochalcogenides that have emerged as a new class of layered materials beyond graphene and transition metal dichalcogenides.

*Graphene* is promising for several applications, and is thus anticipated to play a major role in future technologies. The practical utilization of this material in nanoelectronics will require the development of scalable processes enabling its controlled synthesis on various substrates. For this purpose we have systematically studied MBE large-area synthesis of graphene on different metallic and insulating substrates. While on metals state-of-the-art graphene could be realized, achieving the same degree of crystalline perfection for graphene grown on insulators has proven challenging. Nevertheless, we have demonstrated that MBE synthesis of graphene on dielectrics offers specific potential beyond other synthesis techniques, such as control over the number of grown layers. In addition, the precision offered by MBE has allowed us to obtain insights into the fundamental growth behavior of graphene as a prototypical two-dimensional (2D) material. Most re-

cently, the focus of our growth studies has shifted to another 2D material: hexagonal boron nitride (h-BN). H-BN is a layered dielectric with great technological potential, in particular when combined with graphene to form so-called van der Waals (vdW) heterostructures. We have demonstrated with plasma-assisted MBE large-area growth of few-layer thick h-BN films which exhibit structural quality comparable to that of state-of-the-art h-BN single crystals and have established a route for a scalable and technologically relevant fabrication of h-BN/graphene heterosystems. Furthermore, we have obtained an in-depth understanding of the defect-mediated vdW epitaxy of h-BN on graphene, and have elucidated how surface modification of epitaxial graphene can be used to tailor nucleation and growth of h-BN. Interestingly, we have observed that this approach also promotes the formation of unconventional BN nanostructures on the graphene surface, whose phase has so far only been predicted to be stable at high pressures. In collaboration with external and internal partners, we have also shown that atomically thin h-BN grown by MBE can be successfully employed as encapsulation layers for other 2D materials such as transition metal dichalcogenides, as well as large-area templates hosting luminescent defects acting as single photon emitters.

Parallel to MBE, we operate a furnace in which Si is desorbed from SiC to induce epitaxial graphene formation. This is an established method which enables us to fabricate continuous or nanostructured graphene (single layer to multi-layer thick) on SiC. Recently, we have employed this type of samples as templates to perform fundamental growth studies of different materials on graphene such as h-BN (as mentioned above), GaN nanowires, and thin films of the semiconducting oxides NiO and  $In_2O_3$ . The high crystalline quality, inertness, and atomic flatness of epitaxial graphene on SiC make it an ideal substrate for the development of growth protocols for vdW epitaxy.

# Nanoanalytics / Nanoanalytik

Dr. Achim Trampert

Dr. Stefan Fölsch – Scanning tunneling microscopy and spectroscopy

Dr. Michael Hanke – Synchrotron studies

The ongoing miniaturization in semiconductor technology increases the demand for precise information on the structural and compositional quality of low-dimensional systems and nanomaterial-based devices. The mission of this Core Research Area is the development and combination of sophisticated experimental and theoretical tools for materials analysis on the nanometer scale. For this purpose synchrotron X-ray diffraction is carried out to investigate surfaces and interfaces in epitaxial layers and three-dimensional nanostructures during growth. The structural and electronic properties of as-grown materials are investigated by various electron microscopy techniques including imaging, diffraction and spectroscopy with high spatial resolution. Low-temperature scanning tunneling microscopy is applied to build and analyze individual nanostructures.

The research addresses the following topics:

- Interfaces in hetero-structures and nanosystems
- Order-disorder phenomena and phase transitions
- Microstructure and mechanical properties of metastable and nanostructured systems
- Manipulation and spectroscopy of materials at the single-atom scale

A central goal in preparing modern artificial heterostructures and nanomaterials is the control of *interfaces* and the understanding of their building principles. Interfaces have a crucial effect on both, physical properties and device performance, in particular as structure sizes become smaller. Epitaxial

Die stetige Miniaturisierung in der Halbleitertechnologie erhöht den Bedarf an präziser Information über die strukturelle Qualität und chemische Zusammensetzung niedrig-dimensionaler HalbleiterSysteme und Nanomaterialien. Das Ziel dieser Core Research Area ist die Entwicklung und Kombination ausgefeilter experimenteller und theoretischer Untersuchungswerzeuge zur Materialanalyse auf der Nanometerskala. Hier wird Synchrotron Röntgenbeugung für die Untersuchung von Oberflächen und Grenzschichten in epitaktisch gewachsenen Schichtsystemen und dreidimensionalen Nanostrukturen während des Wachstums eingesetzt. Nach der Schichtaufbringung werden die strukturellen und optischen Eigenschaften des gewachsenen Materials mit unterschiedlichen elektronenmikroskopischen Methoden – einschließlich der mikroskopischen Abbildung, der Elektronenbeugung, sowie der energiedispersiven Röntgenspektroskopie und der Elektronenenergieverlustspektroskopie – mit höchster räumlicher Auflösung untersucht. Darüber hinaus erlaubt die Tieftemperatur-Rastertunnelmikroskopie individuelle Nanostrukturen gezielt herzustellen und strukturell und spektroskopisch zu analysieren.

Nanoanalytik behandelt folgende Themen:

- Grenzflächen in Heterostrukturen und Nano-Systemen
- Ordnungs-Unordnungsphänomene und Phasenübergänge
- Mikrostruktur und mechanische Eigenschaften von metastabilen und nanostrukturierten Systemen
- Manipulation und Spektroskopie von Materialien auf der Skala von Einzel-Atomen

hetero-interfaces are generally classified as coherent or semi-coherent, depending on the epitaxial strain state. We are studying the character of epitaxial strain and strain relieving mechanisms as well as the atomic configuration and translation state of coherent interfaces between dissimilar materials. In addition, interfaces in III-V semiconductor heterostructures are quantitatively analyzed with respect to structural roughness and chemical intermixing as defined by compositional profiles.

For some time, we have continuously improved our understanding of interfaces in axial and radial III-V nanowires, two-dimensional layered materials, and, especially, in planar III-V heterostructures and quantum wells. Accordingly, we have used our analytical tools to study the structure of coaxial GaAs/(In,Ga)As dot-in-a-well nanowire heterosystem and were able to prove the presence of quantum dots in this complex geometry by scanning transmission electron microscopy (STEM). Quantitative analysis of high-angle annular dark-field STEM intensity profiles along the wells clearly demonstrate composition fluctuations, which are unambiguously attributed to the embedded quantum dots.

Investigations have been further carried out on non-common-atom heterovalent interfaces. The selective combination of closely lattice-matched group II-VI / group III-V semiconductors offers potential benefits due to the wide range of band-gap energies achievable and novel effects at the interface arising from the valence-mismatch. The combination of, for example, CdTe and InSb implies the existence of such a heterovalent non-common-atom interface, which must contain mixtures of II-V and/or III-VI bonds. Besides the atomic resolved STEM imaging mode, we have used the 002 dark-field (DF) TEM technique to emphasize the interface location by comparing differences in structure factors between the two materials. It is also remarkable that a detailed analysis of the DF images

allows the quantification of the interface width: the comparison of experimental and simulated contrast profiles across the interface by assuming a sigmoidal function for the atomic species reveals that the Cd-Te-on-InSb interface is structurally abrupt to within about 1.5 nm (10-to-90%-criterion). Further investigations on heterovalent and non-common-atom interfaces will be carried out.

Interfaces in semiconductor heterostructures are almost never atomically abrupt and perfectly flat and consequently have a certain degree of three-dimensional (3D) extension. Therefore, the interpretation of two-dimensional (2D) projections of those interfaces can be very challenging. Most recently, we have demonstrated that electron tomography allows an accurate and quantitative determination of the structural and chemical roughness of buried interfaces in III-V multi-layer samples. For the tomography experiment, well-defined needle-shaped specimens have to be fabricated by focused ion-beam (FIB) techniques allowing full 180° rotation for tilt series acquisition of 2D STEM images. The reconstructed volume is used to create an isosurface for each interface describing its position in 3D space. The isosurfaces are then prepared to create topographic height maps of the interfaces enabling new approaches for quantitative analysis of the buried interfaces. Applying this novel method to the (Al,Ga)As/GaAs as well as (Al,Ga)N/GaN multi-layer system the root mean square (RMS) roughness could be determined for interface areas larger than 200 nm × 200 nm. Furthermore, it is verified that for both material systems, the direct and inverse interfaces show different RMS roughness values and anisotropic features like atomic steps along crystallographic directions, respectively.

The physical properties of ferromagnetic Heusler alloys or semiconducting oxide layers depend on their *structural order* and *phase stability*. The stability limitations and

phase transformation processes are studied in dependence on internal parameters like chemical composition and strain state as well as external parameters given by temperature and growth kinetics. The degree of order/disorder and their spatial distribution in thin films are determined quantitatively by X-ray diffraction and electron microscopy – in-situ and ex-situ.

We have continued our work on Schottky-Barrier-Tunneling-Transistors structures. The crystal lattices of epitaxial Ge and Fe<sub>3</sub>Si films on GaAs substrates match well to the known structures of their bulk materials. However, when the Fe<sub>3</sub>Si film is used as a substrate for solid phase epitaxy of amorphous Ge, the influence of the Fe<sub>3</sub>Si structure on the epitaxially growing Ge film unexpectedly turns out to be strong and ordering phenomena occur resulting in a superlattice-like structure of FeGe<sub>2</sub> type on the basis of Fe interdiffusion. In-situ TEM has been used to observe the amorphous/crystalline phase transition with high spatial resolution and time dependence. The study demonstrated that heterogeneous nucleation starts at the amorphous/crystalline interface evolving a layer-by-layer growth of epitaxial aligned Ge. The transition to the superlattice FeGe<sub>2</sub> structure will only take place in a second phase. The time dependent measurements are used to analyze the crystallization kinetics following a square root characteristic.

Apart from this study, we continued our research on semiconducting oxides, a work which has been performed at the PHARO end station at Berlin synchrotron BESSYII (HZB). Monoclinic  $\beta$ -Ga<sub>2</sub>O<sub>3</sub> became one prominent representative of transparent semiconducting oxides (TSO), and although there is a rapidly increasing interest in this material only a few of the fundamental thermal properties are known so far. We have applied synchrotron-based in-situ X-ray diffraction to obtain detailed information on the anisotropic coefficient of thermal expansion  $\alpha$  in the temperature window rel-

evant for most growth scenarios between room temperature and 1200 K. This study is going to be completed by measuring the expansion coefficient and the Poisson ratio in Ga<sub>2</sub>O<sub>3</sub>/Al<sub>2</sub>O<sub>3</sub> heterostructures.

In the last years, nanofocus synchrotron radiation has developed into a powerful technique for characterizing *local strain and chemical composition* as well as morphological properties of individual low-dimensional objects. As a direct result of a steadily improved x-ray optics, beam foci as small as 100 nm or below with high photon flux ( $10^{10}$  photons/sec) at hard X-ray energies (10–30 keV) are nowadays available at third-generation synchrotron facilities like PETRAIII at DESY in Hamburg or the European Synchrotron Radiation Facility (ESRF) in Grenoble. This year, the Diamond Light Source in UK has been used to study the elastic strain field of individual Ge/Si nanowires (NWs) in dependence of shell thickness. Towards thermoelectric applications of NWs strain engineering is of fundamental interest as it allows to increase the charge carrier mobility and thus their thermoelectric figure of merit. The experimental results are interpreted by means of finite element method. Furthermore, the very same NW will be investigated in terms of electrical and thermal transport properties, which can then be linked to the strain field revealed by the nanofocused x-ray diffraction.

The complete three-dimensional knowledge of the *microstructure* is essential for the quality improvement of monolithically integrated optoelectronic components. In this light, electron tomography in conjunction with sophisticated focused ion beam based sample preparation is applied to gain insight into the 3D defect arrangement and defect interaction process. Epitaxial III-(Sb,As) layers were grown on Si(001) substrates. This materials system is exemplary for the challenges of monolithically integrating III-V compound semiconductors with Si. Threading dislocations and

anti-phase boundaries occur as extended defects through the epilayers due to the lattice misfit between the dissimilar materials and due to the growth of polar on nonpolar materials, respectively. Based on an annular bright-field STEM image series dislocation tomography is obtained which gives access not only to an accurate determination of dislocation lines but also slip planes, which again helps to analyze the mechanism of the dislocation movement in more detail. In addition, the STEM imaging mode enables the reconstruction of the displacement field around the dislocation and thus can give in principle access to a complete analysis of its 3D property.

A popular method to experimentally determine the diffusion length of excitons in semiconductors relies on the perception that threading dislocations act as nonradiative sinks for carriers. The zone of reduced luminescence intensity around the dislocation is thus related to the exciton diffusion length. It is shown experimentally and explained theoretically that, contrary to common belief, the cathodoluminescence (CL) intensity contrast of dislocations is only weakly affected by exciton diffusion but is caused primarily by exciton dissociation in the piezoelectric field at the dislocation outcrop. Hence, the extension of the dark

spots around dislocations in the luminescence maps cannot be used to determine the exciton diffusion length. However, the CL energy contrast, which reflects the local band-gap variation in the dislocation strain field, does sensitively depend on the exciton diffusion length and hence enables its experimental determination.

As a further topic of our Core Research Area we employ *atom manipulation* by low-temperature scanning tunneling microscopy (LTSTM) to investigate the quantum properties of artificial nanostructures on III-V semiconductor surfaces. Understanding and controlling these properties is essential for future device concepts based on quantum effects. State-of-the-art LTSTM is used to create individual nanostructures atom-by-atom and subsequently analyze their electronic structure and elementary excitations by local tunneling spectroscopy. We found that positively charged adatoms on an InAs surface can be positioned with atomic precision to form perfectly defined quantum dots. We use this approach to create regular quantum dot assemblies with tunable electronic properties. In addition, we study epitaxially grown transition metal dichalcogenide (TMD) layers with an emphasis on vertical and lateral TMD heterostructures.

# Control of Elementary Excitations by Acoustic Fields / Kontrolle von elektronischen Anregungen in Halbleiter-Nanostrukturen

Dr. Paulo V. Santos

Dr. Alberto Hernández-Mínguez

This core research area explores dynamic acoustic fields for the control of electronic excitations in semiconductor nanostructures. We use, for that purpose, elastic vibrations propagating in the bulk (bulk acoustic waves, BAW) or along the surface of a solid (surface acoustic waves, SAW). The latter resemble seismic waves created during earthquakes. Both types of waves can be electrically generated using piezoelectric transducers. This standard technique for wave excitation is widely used in signal processing, sensors, and acoustooptical modulation.

The recent years have witnessed a growing interest in the application of acoustic waves for control of electronic effects in semiconductors. Here, one takes advantage of the dynamic and spatially dependent character of the acoustic fields, which are composed of a dynamic strain component and, in piezoelectric semiconductors, of an electric component. Both components induce a time- and spatially dependent modulation of the materials band structure, which produces moving potentials for the confinement and transport of electronic excitations. Interestingly, the dynamic fields produced by high-frequency acoustic waves in the GHz range have wavelengths on the order of one micrometer, thus being comparable to the dimensions of semiconductor components. The acoustic and acoustoelectric effects can, furthermore, be exploited for novel device functionalities. Quite naturally the studies also include the development of piezoelectric materials compatible with semiconductors as well as efficient processes for the electrical excitation of acoustic waves in non- or only weakly piezoelectric materials (such as, e. g. Si and SiC).

In dieser Core Research Area werden dynamische akustische Felder zur Steuerung elektronischer Anregungen in Halbleiter-Nanostrukturen untersucht. Hierfür verwenden wir elastische Schwingungen, die sich als Volumenwellen (Bulk Acoustic Waves, BAW) oder entlang der Oberfläche eines Festkörpers als akustische Oberflächenwellen (Surface Acoustic Waves, SAW) ausbreiten. Letztere ähneln seismischen Wellen, die bei Erdbeben entstehen. Beide Arten von Wellen können zum Beispiel mit piezoelektrischen Wändlern elektrisch erzeugt werden. Diese Standardtechnik für Schwingungsanregung wird häufig in der Signalverarbeitung, bei Sensoren und bei der akustooptischen Modulation verwendet.

In den letzten Jahren ist das Interesse, akustische Wellen zur Kontrolle elektronischer Effekte in Halbleitern einzusetzen, gewachsen. Hierbei wird ausgenutzt, dass sich diese Felder aus einer dynamischen Verzerrungskomponente und bei piezoelektrischen Halbleitern zudem aus einer dynamischen elektrischen Komponente zusammensetzen. Beide Komponenten induzieren eine zeit- und ortsbabhängige Modulation der Bandstruktur des Halbleiters, wodurch sich bewegende Potentiale ergeben, die zum Einsperren und zum Transport elektronischer Anregungen genutzt werden können. Interessanterweise haben die Felder, die durch hochfrequente Schallwellen im GHz-Bereich erzeugt werden, Wellenlängen in der Größenordnung von einem Mikrometer und sind damit mit den Abmessungen von Halbleiterbauelementen vergleichbar. Die akustischen und akustoelektrischen Effekte können darüber hinaus für neuartige Bauelementfunktionalitäten genutzt werden. Selbstverständlich umfassen die

The activities carried out in 2019 include investigations of (i) the acoustic modulation of the emission properties of single defect centers in hexagonal boron nitride (h-BN), (ii) the acoustic transport of carrier and spins in semiconductor quantum wires (QWR), and (iii) the generation of high-frequency BAWs on semiconductor nanostructures and their application for the control of microcavity polaritons (MP). We highlight three contributions from this Core Research.

The first report (by A. Hernández-Mínguez and co-workers) addresses the interaction between SAWs and quantum light emitters in h-BN. We study the coupling of SAWs to luminescence centers contained in two kinds of h-BN samples, namely flakes consisting of multiple h-BN layers and epitaxial films with just a few h-BN layers. In the first samples, we show the broadening of the luminescence lines for selected quantum light emitters under the application of the SAW. This change in the emission line shape is caused by the dynamic strain of the SAW: the oscillating tensile and compressive strain modulates periodically the crystal structure of the luminescent center, thus leading to the oscillation of its optical transition energy around the equilibrium value. In addition, we show that SAWs can also suppress the spectral fluctuation of the quantum light centers in the few-layer h-BN films. We attribute this optical stabilization to the control of the ionization states of nearby charge traps by the piezoelectric field of the SAW. Our results show that SAWs are a powerful tool to modulate and control the electronic states of two-dimensional materials.

In the second contribution (by P. Helgers and co-workers) we address the acoustic transport of spins in planar semiconductor QWRs. These QWRs are fabricated using a special epitaxial overgrowth process on structured GaAs substrates. They act as one-dimensional interconnects for the transport of quantum information in the form of electron spins between remote locations on a chip. The transport process is me-

Studien auch die Entwicklung von halbleiterkompatiblen piezoelektrischen Materialien sowie von effizienten Prozessen zur elektrischen Anregung von Schallwellen in nicht- oder nur schwachen piezoelektrischen Materialien (wie z. B. Si und SiC).

Die im Jahr 2019 durchgeföhrten Aktivitäten umfassen Untersuchungen zu (i) der akustischen Modulation der Emissions-eigenschaften einzelner Defektzentren in BN, (ii) dem akustischen Transport von Ladungsträgern und Spins in Halbleiter-quantendrähten (QWR) und (iii) der Erzeugung von hochfrequenten BAWs auf Halbleiternanostrukturen und deren Anwendung zur Modulation von Mikrokavitätspolarito-nen (MP). Diese kurze Zusammenfassung zeigt drei dieser Aktivitäten.

Der erste Beitrag (von A. Hernández-Mínguez und Mitarbeitern) befasst sich mit der Wechselwirkung zwischen SAWs und Quantenlichtemittern in h-BN. Wir untersuchen die Kopplung von SAWs an Lumineszenzzentren, die in zwei Arten von h-BN-Proben enthalten sind, nämlich Flocken, die aus mehreren h-BN-Schichten bestehen, und epitaktischen Filmen mit nur wenigen h-BN-Schichten. In der ersten Art von Proben zeigen wir, dass die Modulation durch SAWs zu einer Verbreiterung der Lumineszenzlinien führt. Diese Änderung der Emissionslinienform wird durch die dynamischen Verzerrungsfelder der SAW verursacht: Die oszillierende Ausdehnung und Kompression moduliert periodisch die Kristallstruktur des Lumineszenz Zentrums und führt so zu einem Oszillieren seiner optischen Über-gangsenergie um den Gleichgewichtswert. Darüber hinaus zeigen wir, dass SAWs auch die spektrale Fluktuation der Quantenlicht-zentren in h-BN-Filmen mit wenigen Schich-ten unterdrücken kann. Wir führen diese optische Stabilisierung auf die Kontrolle der Ionisationszustände benachbarter Ladungs-fallen durch das piezoelektrische Feld der akustischen Oberflächenwelle zurück. Unsere Ergebnisse zeigen, dass SAWs ein leistungsfähiges Werkzeug zur Modulation und Kontrolle der elektronischen Zustände zweidimensionaler Materialien sind.

diated by the moving piezoelectric potential of a SAW, which captures optically excited, spin polarized carriers and transports them over several micrometer with the velocity of the acoustic wave. We show that the spin vector rotates during the acoustic transport due to precession along the spin-orbit field. Furthermore, the spin transport distances in QWRs is more efficient than in a quantum well, which is attributed to the reduction of Dyakonov-Perel spin relaxation due to the narrow width of the QWR channel. These results demonstrate the feasibility of long-distance charge and spin transport by a SAW for application in quantum interconnects.

The last contribution (by A. Kuznetsov and co-workers) introduces a novel platform for opto-mechanics in the super high frequency (SHF) range based on the interaction between stimulated BAWs and (MPs) in an (In,Al,Ga)As planar microcavity. We developed for that purpose special piezoelectric transducer for the excitation and detection of BAWs on the microcavity surface. The microcavities are designed to confine both BAWs and MPs in their spacer region, thus leading to a strong interaction between the two types of particles. We show that the electrically excited BAWs with a frequency of 7 GHz modulate the MPs spectral lines with amplitudes of several meV. These strong modulation levels demonstrate the potentials of this novel optomechanics platform in the SHF domain.

Im zweiten Bericht (von P. Helgers und Mitarbeitern) befassen wir uns mit dem akustischen Transport von Spins in planaren Halbleiter-QWRs. Diese QWRs werden durch einen speziellen epitaktischen Überwachungsprozesses auf strukturierten GaAs-Substraten hergestellt. Sie fungieren als eindimensionale Transport-Kanäle für den Austausch von Quanteninformationen in Form von Elektronenspins zwischen entfernten Orten auf einem Chip. Der Transportprozess erfolgt durch das sich bewegende piezoelektrische Potential einer SAW, das optisch angeregte Spins einfängt und mit der Schallgeschwindigkeit über mehrere Mikrometer transportiert. Wir zeigen, dass sich der Vektor des Elektronenspins während des akustischen Transports aufgrund der Präzession entlang des Spin-Bahn-Feldes dreht. Darüber hinaus sind die Spin-Transportdistanzen in QWRs effizienter als in einer Quantentopfzelle, was auf die Verringerung der Dyakonov-Perel-Spinrelaxation aufgrund der geringen Breite des QWR-Kanals zurückgeführt wird. Die Ergebnisse demonstrieren die Machbarkeit von Ladungs- und Spintransport über große Entfernung durch eine SAW für die Anwendung in Quantenverbindungen.

Der letzte Beitrag (von A. Kuznetsov und Mitarbeitern) führt eine neuartige Plattform für die Optomechanik im Superhochfrequenzbereich (Super-High-Frequency, SHF) ein, die auf der Wechselwirkung zwischen stimulierten BAWs und (MPs) in einer planaren (In,Al,Ga)As Mikrokavität beruhen. Hierfür haben wir spezielle piezoelektrische Wandler entwickelt, die BAWs auf der Mikrokavitätsoberfläche effizient erzeugen und detektieren. Die Struktur der Mikrokavitäten ist so ausgelegt, dass sie sowohl BAWs als auch MPs in ihrem Spacer-Bereich einsperren, was zu einer starken Wechselwirkung zwischen den beiden Partikeltypen führt. Wir zeigen, dass elektrisch angeregten BAWs mit einer Frequenz von 7 GHz die MP-Spektrallinien mit Amplituden von mehreren meV modulieren. Diese starken Modulationsniveaus zeigen das Potenzial dieser neuen optomechanischen Plattform im SHF-Bereich.

# III-V Nanowires for Optoelectronics / III-V-Nanodrähte und deren Anwendung in der Optoelektronik

Dr. Lutz Geelhaar  
Dr. Oliver Brandt

Semiconductor nanowires are structures with an extremely high aspect ratio and a diameter typically smaller than 100 nm. In bottom-up approaches, feature sizes down to 10 nm and below can be achieved without any lithography. Complementary top-down approaches offer higher level of control, in particular for the fabrication of regular nanowire arrays. The quasi-one-dimensional shape and the nanometric size of nanowires result in unique properties, often independently of the concrete nanowire material. Their characteristics make nanowires an exciting subject for fundamental studies and offer many conceptual advantages for various applications.

The goal of our research is to inspire and demonstrate new functionalities for optoelectronic applications by employing III-V nanowires. To this end, we investigate fundamental nanowire properties that crucially influence such applications to assess nanowire suitability. We grow both group-III-nitride and group-III-arsenide nanowires by molecular beam epitaxy but pursue also top-down approaches. We analyze nanowire microstructure and optical as well as electronic properties, and we employ technology to guide growth, enable electrical measurements, and process demonstrator devices.

Three different *synthesis* methods represent our platform for both fundamental investigations aimed at elucidating formation mechanisms and the fabrication of nanowire samples for dedicated studies of

Halbleiter-Nanodrähte sind Strukturen mit extrem hohem Aspektverhältnis und Durchmessern von typischerweise weniger als 100 nm. In sogenannten ‚bottom-up‘-Ansätzen (englisch für ‚von unten nach oben‘) werden Nanodrähte hergestellt, indem Material durch Wachstum hinzugefügt wird. Auf diese Weise können Strukturgrößen bis hinunter zu 10 nm ohne lithographische Prozesse erzielt werden. Komplementäre ‚top-down‘-Verfahren („von oben nach unten“), bei denen aus einer größeren Probe Material durch Ätzprozesse abgetragen wird, ermöglichen ein größeres Maß an Kontrolle, insbesondere für die Herstellung von regelmäßigen Nanodraht-Arrays. Die quasi eindimensionale Form und die Größe im Bereich von Nanometern resultieren in einzigartigen Eigenschaften von Nanodrähten, oftmals unabhängig von deren konkretem Material. Ihre Besonderheiten machen Nanodrähte zu einem spannenden Objekt für grundlegende Untersuchungen und bieten zahlreiche konzeptionelle Vorteile für unterschiedliche Anwendungen.

Unser Forschungsziel ist es, durch den Einsatz von III-V-Nanodrähten neue Funktionalitäten für optoelektronische Anwendungen zu inspirieren und zu demonstrieren. Dazu untersuchen wir fundamentale Nanodraht-Eigenschaften, die solche Anwendungen entscheidend beeinflussen, und beurteilen die Eignung von Nanodrähten. Wir züchten Gruppe-III-Arsenid und -Nitrid-Nanodrähte mittels Molekularstrahlepitaxie aber verfolgen auch ‚top-down‘-Ansätze. Wir analysieren die Mikrostruktur sowie die opti-

material properties and applications. First, the best-known bottom-up method resulting in uniaxial growth of nanowires utilizes the vapor-liquid-solid mechanism in which the formation of a solid nanowire from the vapor phase is mediated by a tiny liquid metal droplet. We employ this approach (using Ga as the metal) for the synthesis of group-III-arsenide nanowires on Si(111) substrates. Selective area vapor-liquid-solid growth is readily obtained by patterning these substrates by electron beam lithography and reactive ion etching, leading to ordered nanowire arrays.

Second, an alternative bottom-up approach exists for materials that exhibit the tendency to form nanowires under suitable growth conditions spontaneously, i. e., without any external guidance. GaN is one of these materials, and is prone to the spontaneous formation of nanowires on a wide variety of substrates, including amorphous and crystalline insulators, semiconductors, and metals. We are currently focusing on the growth of group-III nitride nanowires on metallic substrates, and in particular on TiN – both as sputtered film and flexible foil – and graphene. In either case, ensembles of vertical GaN nanowires with excellent structural and optical properties can be obtained.

Spontaneously formed GaN nanowires invariably grow along the  $[000\bar{1}]$  direction, i.e., they are N polar. In order to synthesize Ga-polar group-III-nitride nanowires, we utilize as our third synthesis method a top-down process. In particular, we fabricate ordered arrays of nanowires from high-quality group-III-nitride layers and heterostructures by selective area sublimation. This complementary approach allows us to study phenomena depending on, for example, nanowire diameter in a systematic fashion.

In our studies of nanowire *properties*, we pay special attention to phenomena that are a direct consequence of the peculiar wire-like

schen und elektronischen Eigenschaften von Nanodrähten und nutzen Technologie für die Herstellung regelmäßiger Nanodraht-Arrays, um elektrische Messungen zu ermöglichen und um Demonstrator-Baulemente zu prozessieren.

shape and nanometric size and are independent of the material the nanowires consist of. For example, the high surface-to-volume ratio of nanowires has several important consequences. In particular, lattice-mis-matched axial heterostructures relax their strain elastically at the free sidewalls, and the formation of dislocations is avoided. For radial heterostructures, a new type of structure only possible due to the nanowire geometry, the strain is shared between core and shell. In both cases, the strain distribution is very complex. Since many semiconductor properties depend sensitively on strain, the dedicated investigation of strain in nanowires is crucial for an understanding of their optoelectronic properties.

Another consequence of sidewall surfaces are radial electric fields induced by surface states. The strength of these fields depends on the doping density in the nanowire and may be large enough to dissociate excitons. Electric fields and doping crucially affect device design and are thus important topics of investigation.

Furthermore, nanowires are not ideal single crystals but exhibit structural defects. Some of these defects, such as twin boundaries, stacking faults, and inversion domain boundaries, act as two-dimensional radiative defects that may dominate luminescence. Others, such as dislocations created by the coalescence of nanowires in close vicinity, act as nonradiative defects. Nonradiative recombination also occurs at the free surface or interfaces and at point defects. Investigations of the microstructure and internal quantum efficiency are thus essential to elucidate the actual potential of group III-V nanowires for optoelectronic applications.

In general, our research relates to *applications* based on either light emission or light absorption, e. g. optical data transmission or energy harvesting. Since the nanowire geometry facilitates the integration of dissimilar materials, substrates with attrac-

tive properties can be employed that were excluded for planar growth. Furthermore, the spectral region of optoelectronic devices can be widened. Also, radial nanowire heterostructures drastically increase the size of the active region, which is associated with stronger light emission and absorption. In addition, light-matter interaction can be tailored by design of nanowire dimensions and their arrangement in arrays.

Currently, we work towards a laser monolithically integrated on Si. Such a laser is of strategic relevance for the application field Si photonics. Our concept will provide the direct coupling of light between arrays of vertical III-V nanowires and planar Si waveguides. This project (MILAS) is funded by the Federal Ministry of Education and Research, and our partner is Technical University of Berlin.

In the nanowire geometry, the chemical composition can be changed in both the axial and the radial direction, leading to corresponding heterostructures and / or doping profiles. Such design concepts still strongly resemble established planar structures. Beyond those strategies, we investigate more advanced structures with the aim to tailor functionality in entirely new directions. For example, we synthesize nanowire heterostructures that are bent in a pre-defined way and employ the resulting complex strain gradients to influence radiative recombination processes. In addition, in many III-V nanowires both the wurtzite and zincblende crystal structure form. We exploit this polytypism to study crystal phase quantum structures of various dimensionalities with inherently atomically sharp interfaces and free from alloy disorder. In combination with compositional heterostructures, we realize complex topologies like quantum rings. Furthermore, we utilize dielectric confinement to modify radiative recombination in ultrathin nanowires.

In the project InterPhase funded by the Federal Ministry of Education and Research, we

study with different partners in Germany charge and energy transfer processes at hybrid organic/inorganic semiconductor interfaces. In particular, group-III nitride nanowires and nanowire heterostructures are coated with organic molecules to demonstrate and analyze two different effects. On the one hand, we aim to passivate the nanowire surface to favor radiative recombination processes in the inorganic semiconductor. On the other hand, our goal is to exploit Förster resonant energy transfer (FRET) to combine efficient charge carrier transport in inorganic semiconductors with highly efficient light emission in organic semiconductors.

This year, we have continued our efforts to passivate the surface of GaN nanowires with organic molecules within the InterPhase project, focusing now on the aim to modify the band bending at the  $\text{GaN}(1\bar{1}00)$  surface that forms the nanowire sidewall facets. Two phosphonic acids with the same anchor group for covalent bonding to oxides such as  $\text{GaO}_x$ , but with backbones of very different electronegativity, have been selected for this investigation. Employing x-ray photoelectron spectroscopy to probe the density and orientation of the molecules, we have found both acids to self-assemble on oxidized  $\text{GaN}(0001)$  and  $\text{GaN}(1\bar{1}00)$  surfaces into a dense molecular monolayer. The experiments furthermore show that the more electropositive molecule reduces the band bending at the  $\text{GaN}(1\bar{1}00)$  surface to almost zero. GaN nanowires coated with these molecules exhibit a significantly higher (up to a factor of five) luminous efficiency than the as-grown sample. This result confirms that the internal quantum efficiency of GaN nanowires is controlled not by the density of defects, but by exciton dissociation in the radial electric fields associated to surface band bending.

When shells are grown around nanowires by directional deposition techniques like molecular beam epitaxy, material is depos-

ited only on those nanowire facets that are in direct line of sight to the source. Substrate rotation enables sequential impingement on all sidewall facets, but for alloy growth the different constituents arrive at a given facet not at the same time. For  $(\text{In},\text{Ga})\text{N}$  shells around GaN nanowires, we have found that this sequential deposition strongly affects growth. Since the group-III metals and N impinge continuously on the nanowire top facet, growth is favored there over the sidewalls, and cathodoluminescence spectroscopy has revealed substantially higher In contents. By implementing specific shutter and rotation protocols, we have sequentially deposited all three constituents on only one sidewall facet, thus significantly reducing growth on the top facet. We have tailored the emission wavelength by adjusting growth conditions, and ensemble homogeneity has been improved by the use of regular nanowire arrays resulting from top-down fabrication.

The photoluminescence spectra of GaAs nanowires are typically dominated by transitions related to polytypism. Instead, we have found that ordered arrays of GaAs nanowires can exhibit spectra virtually indistinguishable from those of epitaxial GaAs layers. The characteristic near band-edge transitions of GaAs dominate even at the lowest excitation densities, revealing a very low density of stacking defects, which in turn has allowed us to obtain a detailed understanding of the carrier and exciton dynamics in these GaAs nanowires by photoluminescence experiments with an excitation density varying over more than six orders of magnitude. With increasing excitation density, we have first observed a saturation of the carbon-related lines, followed by an abrupt Mott transition from excitonic to electron-hole plasma recombination accompanied by progressive band filling. Modelling the dependence of the emission intensity with excitation density has enabled us to determine the nanowires' internal quantum efficiency, which we have found to approach unity for photogene-

rated carrier densities in the degenerate regime ( $>10^{16} \text{ cm}^{-3}$ ) beyond the Mott transition.

Core-shell nanowires based on the (In,Ga)As/GaAs material system could be the basis for light emitters monolithically integrated on Si. However, for Si photonics applications the emission wavelength has to lie in a range in which Si is transparent. We have overcome the challenges associated with lattice mismatch by introducing a

novel coaxial dot-in-a-well heterostructure. InAs quantum dots are embedded in a radial (In,Ga)As quantum well shell around GaAs nanowires. The formation of quantum dots on the nanowire sidewall facets is facilitated by providing Bi as a surfactant, an approach we pioneered previously. We have fabricated a light-emitting diode based on such nanowires grown on Si that emits electroluminescence at room temperature at  $1.26 \mu\text{m}$ , i.e. in the telecommunication O band.

# Intersubband Emitters: GaAs-based Quantum-Cascade Lasers / Intersubbandemitter: GaAs-basierte Quantenkaskadenlaser

Prof. Dr. Holger T. Grahn

Dr. Lutz Schrottke

The excellent state of semiconductor science and technology allows for the development and application of sophisticated devices such as quantum-cascade lasers (QCL). These devices rely on the comprehensive understanding and the high-quality growth of complex planar heterostructures. For the terahertz spectral region, which typically ranges from 0.1 to 10 THz and bridges the electronics-based microwave region with the optics-based infrared region, GaAs/(Al,Ga)As-based heterostructures are the material of choice. The THz region is of great current interest for spectroscopic applications, since rotational states of many molecules, impurity transitions in semiconductors, and fine-structure transitions in atoms as well as ions can result in THz absorption or emission. The advantages of THz QCLs, covering at present the emission frequency range of about 1 to 5 THz, are their compactness, extremely narrow emission lines, and optical output powers of typically several mW to several tens of mW. Therefore, THz QCLs are already used as local oscillators in heterodyne receivers and are promising sources for high-resolution absorption spectroscopy, for instance for the precise determination of the absolute density of atoms and ions in technologically relevant plasma processes. In particular, QCLs for local oscillators at 4.75 THz are currently unrivaled for heterodyne detection of atomic oxygen, which is important in planetary and interstellar science. Currently, the implementation of stabilized THz QCLs for future space mis-

Der hervorragende Stand der Halbleiterwissenschaft und -technologie erlaubt die Entwicklung und Anwendung von anspruchsvollen Bauelementen wie Quantenkaskadenlasern (QCL). Diese Bauelemente erfordern ein umfassendes Verständnis und das Wachstum komplexer planarer Heterostrukturen von hoher Qualität. Für den Terahertz-Spektralbereich, der typischerweise von 0,1 bis 10 THz reicht und den Bereich der elektronisch erzeugten Mikrowellenstrahlung mit dem der optisch erzeugten Infrarotstrahlung verbindet, sind GaAs/(Al,Ga)As-Halbleiterheterostrukturen das bevorzugte Materialsystem. THz-Strahlung ist derzeit für spektroskopische Untersuchungen von großem Interesse, da Rotationszustände vieler Moleküle, Übergänge in Fremdatomen in Halbleitern sowie Feinstrukturübergänge in Atomen und Ionen zu Absorption oder Emission in diesem Spektralbereich führen können. Die Vorteile von QCLs, deren Frequenzbereich sich derzeit von ca. 1 bis 5 THz erstreckt, bestehen in ihrer Kompaktheit, extrem schmalen Emissionslinien und Ausgangsleistungen von typischerweise einigen mW bis zu einigen 10 mW. Diese Laser werden bereits als Lokaloszillatoren in Heterodyn-Empfängern für astronomische Untersuchungen verwendet und sind vielversprechende Quellen für die hochauflösende THz-Spektroskopie, unter anderem für die genaue Bestimmung der absoluten Dichte von Atomen und Ionen in technologisch relevanten Plasmen. Insbesondere sind zur Zeit QCLs als Lokaloszillatoren bei

sions based on passive cooling is of great interest.

In contrast to conventional interband semiconductor lasers, QCLs are so-called intersubband emitters, since the lasing transition takes place within the conduction band rather than across the energy gap. Therefore, they are unipolar lasers, i. e., only one type of carrier, typically electrons, is injected into the laser structure. In order to obtain population inversion between subbands of the conduction band, a rather complex semiconductor heterostructure with typically 6 to 20 layers with thicknesses in the range of a few to about 20 nanometers has to be realized, which is repeated about 100 times forming a semiconductor superlattice with a complex unit cell. The total thickness of the complete structure typically amounts to about 10 µm. The realization of such a structure requires both, a design strategy based on appropriate modeling and a highly accurate growth technique such as molecular beam epitaxy with a very good stability of the growth parameters over up to 20 hours. This growth expertise is one of the core competences of our institute. After growth, the wafers are processed using wet chemical or dry etching to form edge-emitting Fabry-Pérot ridge lasers. For single-mode operation, distributed-feedback lasers using lateral gratings of different order, two-section cavity lasers, or very short Fabry-Pérot cavities are realized. Typical dimensions of the laser ridges are widths of 15 to 200 µm and lengths of 0.5 to 7.5 mm.

Our activities in the field of THz QCLs cover the design, the growth, the fabrication, and the determination of the operating parameters of these lasers. Since 2014, QCLs developed in our institute have been used as local oscillators in the *German REceiver for Astronomy at Terahertz frequencies (GREAT)* on board the *Stratospheric Observatory For Infrared Astronomy (SOFIA)* for the detection of the fine-structure transition of interstellar neutral atomic oxygen

4,75 THz für den Nachweis von atomarem Sauerstoff, der in der Planeten- und Weltraumforschung wichtig ist, konkurrenzlos. Gegenwärtig ist die Realisierung stabilisierter, für passive Kühlung geeigneter THz-QCLs für zukünftige Raumfahrtmissionen von großem Interesse.

Im Gegensatz zu konventionellen Interband-Halbleiterlasern sind QCLs Intersubbandemitter, da der Laserübergang innerhalb des Leitungsbands und nicht über die Energielücke erfolgt. Deshalb sind QCLs unipolare Halbleiterlaser, das heißt nur eine Ladungsträgerart, typischerweise Elektronen, wird in die Laserstruktur injiziert. Um Besetzungsinversion zwischen den Subbändern des Leitungsbandes zu erreichen, wird eine komplexe Heterostruktur mit etwa 100 Perioden, die typischerweise innerhalb einer Periode 6 bis 20 Schichten mit Dicken zwischen etwa 1 und 20 nm enthält und insgesamt etwa 10 µm dick ist, realisiert. Die Entwicklung von THz-QCLs erfordert sowohl das Design auf der Grundlage geeigneter Modellierung der Laser als auch die Herstellung komplexer Heterostrukturen. Dafür wird eine sehr präzise Wachstumsmethode wie die Molekularstrahl-Epitaxie mit einer guten Stabilität der Wachstumsparameter über bis zu 20 Stunden benötigt. Das Wachstum mittels Molekularstrahl-Epitaxie ist eine der Kernkompetenzen unseres Instituts. Die Laser werden anschließend mittels nass-chemischer Verfahren oder Trockenätzten als kantenemittierende Fabry-Pérot-Laserstreifen hergestellt. Für den Einzelmodenbetrieb werden Resonatoren mit verteilter Rückkopplung unter Verwendung von lateralen Gittern verschiedener Ordnungen, Zweisektionslaser oder sehr kurze Fabry-Pérot-Resonatoren verwendet. Typische Abmessungen der Laserstreifen sind Breiten von 15 bis 200 µm und Längen von 0,5 bis 7,5 mm.

Unsere Aktivitäten auf dem Gebiet der THz-QCLs beinhalten das Design, das Wachstum, die Herstellung und die Bestimmung der Betriebsparameter dieser Laser.

(OI) at 4.7448 THz. Currently, a QCL with improved operating parameters is employed in an advanced astronomical THz receiver based on multichannel detection (upGREAT). The key challenges for applications continue to be the increase of the practical operating temperature, i.e., the temperature at which the lasers emit powers of at least 1 mW, beyond 75 K and of the wall plug efficiency to reduce the necessary cooling power so that miniature mechanical cryocoolers can be employed.

QCLs for the THz spectral region are usually based on  $\text{GaAs}/\text{Al}_x\text{Ga}_{1-x}\text{As}$  heterostructures with  $0.1 \leq x \leq 0.25$ . Since 2016, we have been able to realize  $\text{GaAs}/\text{AlAs}$  QCLs operating at 4.75 THz, which exhibit an about three times higher wall plug efficiency than  $\text{GaAs}/\text{Al}_{0.25}\text{Ga}_{0.75}\text{As}$  QCLs with an almost identical design. Substituting AlAs for the  $\text{Al}_{0.25}\text{Ga}_{0.75}\text{As}$  barriers leads to a larger energy separation between the subbands so that the probability for leakage currents through parasitic states and the reabsorption of the laser radiation can be reduced. Based on this alternative materials system, we have realized QCLs with improved wall plug efficiencies emitting at 4.75 THz with operating parameters adequate for spaceborne applications. In the framework of a project funded by the European Space Agency, we are trying to increase the practical operating temperature so that in the future these QCLs may be appropriate for passive cooling, i.e., no additional energy source is necessary for cooling the QCL. Furthermore, we have successfully enlarged the frequency range of THz QCLs based on  $\text{GaAs}/\text{AlAs}$  heterostructures so that frequencies between 3.3 and 5.6 THz are now available.

In particular between 3.3 and 5.0 THz, several frequencies are of interest. In atmospheric science, the rotational transition of the hydroxyl radical (OH) at 3.55 THz and the fine-structure line of OI at 4.75 THz are important. Both can be measured with QCL-based heterodyne receivers.

Seit 2014 werden von uns entwickelte QCLs im *German REceiver for Astronomy at Terahertz frequencies* (GREAT) während der Beobachtungsflüge des *Stratospheric Observatory For Infrared Astronomy* (SOFIA) für den Nachweis eines Feinstrukturübergangs in interstellarem neutralem atomarem Sauerstoff (OI) bei 4,7448 THz verwendet. Gegenwärtig wird ein QCL mit verbesserten Betriebsparametern in einem weiterentwickelten astronomischen THz-Empfänger auf der Grundlage von Mehrkanal-Detektion (upGREAT) eingesetzt. Die Kernherausforderungen für Anwendungen bestehen nach wie vor in der Erhöhung der praktischen Betriebstemperatur, d.h. der Temperatur, bei der die Laser eine Ausgangsleistung von mindestens 1 mW aufweisen, über 75 K hinaus und in der Verbesserung des Gesamtwirkungsgrades, um die notwendige Kühlleistung zu reduzieren, so dass miniaturisierte mechanische Kühler verwendet werden können.

THz-QCLs beruhen üblicherweise auf  $\text{GaAs}/\text{Al}_x\text{Ga}_{1-x}\text{As}$ -Heterostrukturen mit  $0.1 \leq x \leq 0.25$ . Seit 2016 können wir  $\text{GaAs}/\text{AlAs}$ -Laser für 4,75 THz mit einem mehr als dreifachen Gesamtwirkungsgrad im Vergleich zu  $\text{GaAs}/\text{Al}_{0.25}\text{Ga}_{0.75}\text{As}$ -Lasern herstellen. Der Ersatz der  $\text{Al}_{0.25}\text{Ga}_{0.75}\text{As}$ -durch AlAs-Barriären führt zu einem größeren Energieabstand der Subbänder, so dass die Wahrscheinlichkeit von Leckströmen durch parasitäre Zustände reduziert wird. Auf Grundlage dieses alternativen Materialsystems haben wir verbesserte 4,75-THz-Laser, die für weltraumgestützte Beobachtungsmissionen geeignet sein können, realisiert. Im Rahmen eines durch die Europäische Raumfahrtbehörde geförderten Projektes versuchen wir die praktische Betriebstemperatur soweit zu erhöhen, dass die QCLs für passive Kühlung geeignet sind, das heißt ohne zusätzliche Energiequelle für die Kühlung auskommen. Weiterhin haben wir erfolgreich den Frequenzbereich von THz-GaAs/AlAs-QCLs erweitert, so dass nun Frequenzen zwischen 3,3 und 5,6 THz verfügbar sind.

For fundamental research and industrial applications, high-resolution absorption spectroscopy based on fine-structure transitions in Al, N<sup>+</sup>, and O at 3.36, 3.92, and 4.75 THz, respectively, is expected to allow for the quantitative determination of the atom and ion densities in plasma processes. Furthermore, QCLs emitting in the atmospheric windows around 3.43, 4.32, and 4.92 THz are of interest for applications if the THz radiation has to be transmitted through air over a distance of up to 10 m. Starting from a laser structure operating at 4.75 THz, we developed GaAs/AlAs QCLs with emission frequencies between 3.3 and 5.0 THz by a gradual scaling of the layer structure toward lower and higher frequencies. The corresponding frequencies of the gain maxima are achieved by an adjustment of the quantum well thicknesses and a fine tuning of the thicknesses of some particular barriers. For 3.50 and 4.75 THz, the optimization of the lasers has already started so that the wall plug efficiencies for these lasers are larger than  $1.8 \times 10^{-3}$  and  $1.1 \times 10^{-3}$ , respectively. Typical output powers of 1 mW correspond to electrical driving powers of less than 1 W so that the operation in a miniature mechanical cryocooler becomes feasible.

In collaboration with the Leibniz-Institut für Plasmaforschung und Technologie (INP Greifswald), we are developing a spectrometer based on our THz QCLs for the detection of different species of atoms and ions in plasmas, which are crucial for the plasma-assisted deposition of Si-based films and AlN layers. The density of Si, Al, N<sup>+</sup>, and O can be directly determined using their fine-structure transitions at 2.31, 3.36, 3.92, and 4.75 THz, respectively, in a transmission setup. For that purpose, single-mode THz QCLs emitting precisely at these frequencies are required. In order to also cover broadened absorption lines at elevated pressures, a tuning range of at least 5 GHz is desirable for each frequency. Recently, we have provided QCLs emitting at 3.36, 3.92, and 4.75 THz to the INP Greifswald. In order

Insbesondere zwischen 3,3 und 5,0 THz sind mehrere Frequenzen von Interesse. In der Atmosphärenforschung sind der Rotationsübergang des Hydroxyl-Radikals (OH) bei 3,55 THz und die Feinstrukturlinie von OI bei 4,75 THz von Bedeutung. Beide Übergänge können mittels QCL-basierten Heterodyn-Empfängern detektiert werden. Sowohl für die Grundlagenforschung als auch für industrielle Anwendungen ist hochauflösende Absorptionsspektroskopie der Feinstrukturübergänge in Al, N<sup>+</sup> und O bei 3,36, 3,92 und 4,75 THz ein vielversprechender Ansatz zur quantitativen Analyse der Atom- bzw. Ionendichten in Plasmaprozessen. Weiterhin sind QCLs, die in den atmosphärischen Fenstern um 3,43, 4,32 und 4,92 THz emittieren, für Anwendungen interessant, in denen die Strahlung über eine Entfernung von bis zu 10 m übertragen werden muss. Ausgehend von einer Laserstruktur für 4,75 THz haben wir GaAs/AlAs-QCLs mit Emissionsfrequenzen zwischen 3,3 und 5,0 THz durch eine graduelle Skalierung der Schichtstruktur zu niedrigeren und höheren Frequenzen hin entwickelt. Die jeweiligen Maxima der optischen Verstärkungsspektren wurden durch eine Anpassung der Quantentopfdicken und eine Feinabstimmung einiger Barrierendicken erreicht. Für 3,50 bzw. 4,75 THz wurden bereits optimierte Laser mit einem Gesamtwirkungsgrad von mehr als  $1,8 \times 10^{-3}$  bzw.  $1,1 \times 10^{-3}$  realisiert. Typischen Ausgangsleistungen von 1 mW stehen elektrische Pumpleistungen von weniger als 1 W gegenüber, so dass der Betrieb in miniaturisierten mechanischen Kühlern möglich ist.

Aufbauend auf unseren THz-QCLs entwickeln wir in Zusammenarbeit mit dem Leibniz-Institut für Plasmaforschung und Technologie (INP Greifswald) ein Spektrometer für die Detektion verschiedener Atom- und Ionenarten in Plasmen, die für die Plasmagestützte Abscheidung von Si-basierten Filmen und AlN-Schichten sehr wichtig sind. Die Dichten von Si, Al, N<sup>+</sup> und O können direkt unter Verwendung ihrer Feinstrukturübergänge bei 2,31, 3,36, 3,92 und 4,75 THz

to test the spectrometer, we prepared also a QCL emitting at 4.767 THz for the detection of NH<sub>3</sub>. By employing absorption lines of NH<sub>3</sub> at about 4.767 THz and of H<sub>2</sub>O at about 4.764 THz, a precise frequency calibration can be established.

The QCLs emitting at 4.75 THz are continuously improved in order to increase their practical operating temperature and to reduce the requirements for the cooling of the lasers, in particular for future applications in spaceborne instruments. A QCL with laser ridge dimensions of 0.08 × 0.87 mm<sup>2</sup> allows for a maximum value of the practical operating temperature of 72 K. This type of laser can readily be operated in a miniature mechanical cryocooler with a cooling power of about 1 W. An increase of the optical output power can be achieved if the reflectivity on the back side of the laser is enhanced by an additional external back-facet mirror. For a laser from the same wafer with ridge dimensions of 0.08 × 0.58 mm<sup>2</sup> and an additional back-facet mirror, the optical output power is enhanced by up to 83 %. In cooperation with the Institut of Optische Sensorsysteme (IOS) of the Deutsches Zentrum für Luft und Raumfahrt (DLR) in Berlin, output powers of up to 8 mW and a practical operating temperature above 76 K have been demonstrated for this frequency, if the laser is operated in a miniature mechanical cryocooler with an appropriate thermal management and optimized optical components. This QCL emits a single mode, which can be tuned across the frequency of atomic oxygen from -2.7 to +9.4 GHz.

Since THz QCLs can be conveniently operated in liquid-coolant-free mechanical coolers, new paths have been opened toward various applications. Based on an approach for tuning the lasers by near-infrared optical excitation developed at our institute, the group of Prof. Dr. Heinz-Wilhelm Hübers (IOS, DLR, Berlin) has demonstrated a technique to simultaneously stabilize the frequency and output power of a THz

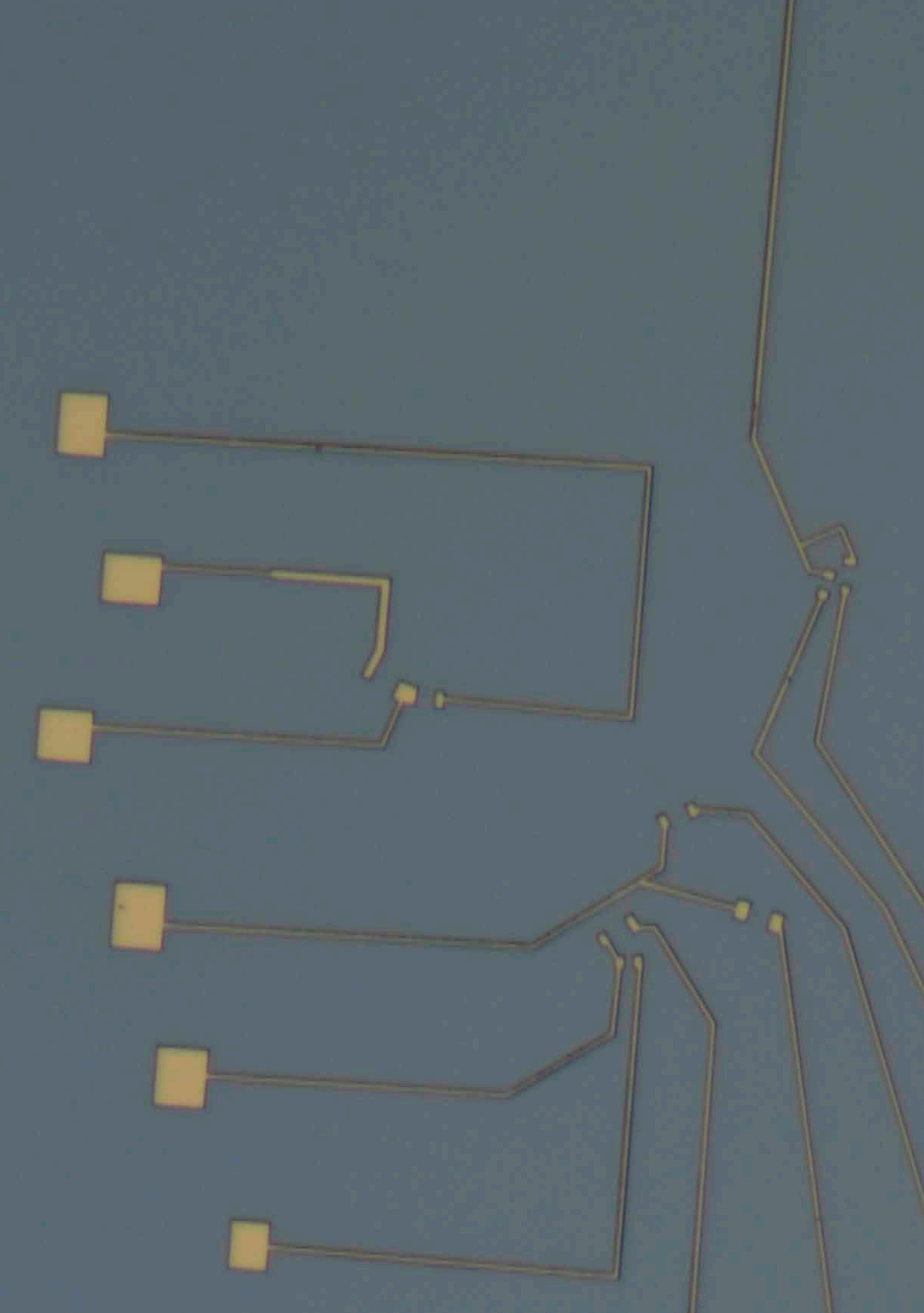
in einem Transmissionsaufbau bestimmt werden. Hierfür sind THz-QCLs, die im Einzelmodenbetrieb genau bei diesen Frequenzen emittieren, notwendig. Um auch verbreiterte Absorptionslinien bei höheren Drücken abzudecken, ist für jede Frequenz ein Abstimmungsbereich von wenigstens 5 GHz wünschenswert. Kürzlich haben wir dem INP Greifswald QCLs für 3,36, 3,92 und 4,75 THz zur Verfügung gestellt. Für einen Test des Spektrometers haben wir auch einen Laser für die Detektion einer Absorptionslinie von NH<sub>3</sub> bei 4,767 THz bereitgestellt. Durch die Nutzung dieser NH<sub>3</sub>-Absorptionslinie und einer Line von H<sub>2</sub>O bei etwa 4,764 THz konnte eine genaue Frequenz-Kalibrierung des Spektrometers erreicht werden.

Die QCLs, die bei 4,75 THz emittieren, werden fortlaufend verbessert, um ihre praktische Betriebstemperatur zu erhöhen und die Erfordernisse für ihre Kühlung, insbesondere für den zukünftigen Einsatz in Weltraum-gestützten Instrumenten, zu reduzieren. Ein QCL mit den Abmessungen des Laserstreifens von 0,08 × 0,87 mm<sup>2</sup> erlaubt eine praktische Betriebstemperatur von 72 K. Dieser Lasertyp kann leicht in einem miniaturisierten mechanischen Kühler mit einer Kühlleistung von etwa 1 W betrieben werden. Die optische Ausgangsleistung kann durch ein verstärktes Reflexionsvermögen auf der Rückseite des Lasers durch einen zusätzlichen externen Spiegel erhöht werden. Für einen Laser vom selben Wafer mit Streifenabmessungen von 0,08 × 0,58 mm<sup>2</sup> und einem zusätzlichen Spiegel an der Rückfacette wurde die optische Ausgangsleistung um bis zu 83 % erhöht. In Zusammenarbeit mit dem Institut für Optische Sensorsysteme (IOS) des Deutschen Zentrums für Luft- und Raumfahrt (DLR) in Berlin wurden für diese Frequenz Ausgangsleistungen von bis zu 8 mW und eine praktische Betriebstemperatur oberhalb von 76 K realisiert, wenn der Laser in einem miniaturisierten mechanischen Kühler mit geeignetem Wärmemanagement und optimierten optischen Komponenten betrieben wird. Dieser QCL emit-

QCL. It does not require an external THz optical modulator. By locking the frequency to a molecular absorption line, a long-term (one-hour) linewidth of 260 kHz (full width at half maximum) and a root-mean-square power stability below 0.03 % have been achieved. Finally, the high level of design and growth of THz QCLs in our institute is demonstrated by several requests for scientific and commercial applications of our QCLs in various systems.

tiert eine Einzelmode, die über die Frequenz des atomaren Sauerstoffs von -2,7 bis +9,4 GHz verschoben werden kann.

Da die THz-QCLs problemlos in mechanischen Kühlern ohne kryogene Flüssigkeiten betrieben werden können, eröffnen sich neue Anwendungsmöglichkeiten. Basierend auf THz-QCLs und einer Methode für die Frequenzabstimmung auf der Grundlage der Beleuchtung mit nahinfraroter Strahlung, die in unserem Institut entwickelt wurde, hat die Gruppe von Prof. Dr. Heinz-Wilhelm Hübers (IOS, DLR, Berlin) ein Verfahren zur gleichzeitigen Stabilisierung der Frequenz und der Ausgangsleistung eines THz-QCLs demonstriert. Sie erfordert keinen externen optischen Modulator. Durch die Kopplung der Laserfrequenz an eine molekulare Absorptionslinie wurde eine Linienbreite über einen Zeitraum von einer Stunde von 260 kHz (Halbwertsbreite) und eine Leistungsstabilität (Effektivwert) von unter 0,03 % erreicht. Schließlich zeigt sich das hohe Niveau des Designs und des Wachstums von THz-QCLs in unserem Institut durch mehrere Anfragen für wissenschaftliche und kommerzielle Anwendungen unserer Laser in verschiedenen Systemen.



# Brief Reports

## Kurzberichte

Growth of (In,Ga)N on partially relaxed (0001)(In,Ga)N buffer using pulsed InN/GaN molecular beam epitaxy .....	60
Nonmetallic ferromagnetism in metastable FeGe <sub>2</sub> thin films.....	63
The p-type transparent semiconducting oxide SnO: From source to film .....	66
MBE growth of semiconducting oxides on graphene and SiC for gas sensing applications .....	69
Electron tomography and spectroscopy of three-dimensional InGaN/GaN nanostructures .....	72
Tomographic reconstruction of dislocations based on annular bright-field imaging mode .....	75
In-situ transmission electron microscopy of solid phase epitaxy of Ge on Fe <sub>3</sub> Si.....	78
Magnetic characteristics of epitaxial NiO films studied by Raman spectroscopy: Influence of disorder and biaxial strain.....	81
Metastable FeGe <sub>2</sub> thin films as interlayers in vertical spin valve structures: Room temperature anisotropic magnetoresistance .....	84
Quantum point contacts meet open resonators .....	87
Coaxial GaAs/(In,Ga)As dot-in-a-well nanowire heterostructures for electrically driven infrared light generation on Si in the telecommunication O band .....	90
Photoluminescence spectroscopy of GaAs nanowires with a low degree of polytypism ..	93
Circumferential and one-sided (In,Ga)N Shells on GaN Nanowires: From self-assembled to ordered arrays.....	96
External control of the band bending at the GaN(1̄100) surface using phosphanate self-assembled monolayers.....	99
Charge and spin transport in sidewall quantum wires on GaAs(001) substrates .....	102
Polariton-based optomechanics at super high frequencies.....	105
Extending the frequency range of GaAs/AlAs terahertz quantum-cascade lasers from 4.7 to 3.3 THz .....	108
High performance 4.75 THz quantum-cascade laser with an additional back-facet mirror .....	111

# Growth of $(\text{In}, \text{Ga})\text{N}$ on partially relaxed $(0001)(\text{In}, \text{Ga})\text{N}$ buffer using pulsed $\text{InN}/\text{GaN}$ molecular beam epitaxy

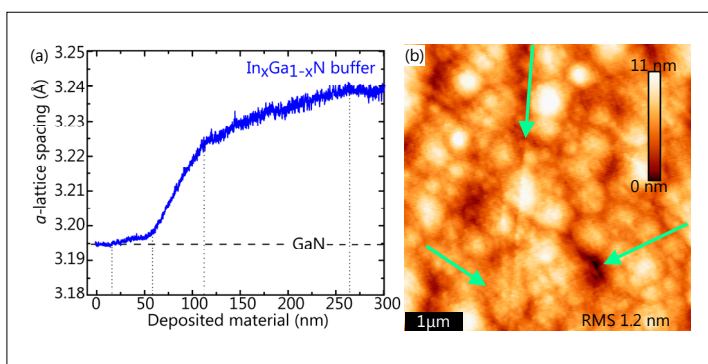
C. Chèze, T. Ernst, M. Ramsteiner, R. Calarco

Efficient light emitters used for solid-state lighting, display technologies, and diode lasers are presently based on layers of the  $(\text{In}, \text{Ga})\text{N}$  ternary alloy, which retains a direct bandgap covering a wide spectral range from ultraviolet (GaN) through visible to infrared (InN). However, the large lattice mismatch between InN and GaN (11%) as well as their incompatible optimum growth temperature have limited the structural quality of  $(\text{In}, \text{Ga})\text{N}$  layers on GaN substrates, particularly for high In content as required for emission towards the red spectral range. Consequently, relatively low efficiencies can be achieved for devices based on such layers. To overcome this issue, binary  $\text{InN}/\text{GaN}$  short-period superlattices (SPSLs) were proposed as a suitable design [A. Yoshikawa *et al.* Appl. Phys. Lett. 90, 073101 (2007)]. However, the fabrication of pure binary  $\text{InN}/\text{GaN}$  SPSLs by alternating pulses of InN and GaN have in-

stead yielded  $(\text{In}, \text{Ga})\text{N}/\text{GaN}$  SPSLs with a maximum In content of about 30% in a single  $(\text{In}, \text{Ga})\text{N}$  monolayer (ML) that consists of intra-plane ordered patches of  $(\text{In}, \text{Ga})\text{N}$  [C. Chèze *et al.* Appl. Phys. Lett. 110, 072104 (2017); L. Lymerakis *et al.*, Phys. Rev. Materials 2, 011601(R) (2018)]. This finding has been interpreted as a strain-related effect that promotes the stability of a  $(2\sqrt{3} \times 2\sqrt{3})R30^\circ$  surface reconstruction of In atoms. To overcome this limitation in In content, a possible strategy is to choose a substrate that offers a smaller lattice mismatch with InN than the one of GaN [A. I. Duff *et al.* Phys. Rev. B 89, 085307 (2014)].

Here, we investigate the influence of strain engineering on the formation of  $(\text{In}, \text{Ga})\text{N}/\text{GaN}$  SPSLs on a partially relaxed  $(\text{In}, \text{Ga})\text{N}$  buffer. We have grown a sample with 100 periods nominally consisting of 1 ML InN and 2 MLs GaN on a partially relaxed  $\text{In}_{0.19}\text{Ga}_{0.81}\text{N}(0001)$  buffer with 300 nm thickness by plasma-assisted molecular beam epitaxy. In order to get a starting surface as smooth as possible, the buffer was grown at 610 °C with a growth rate of 0.6 ML/s under metal excess, while the pulsed InN-GaN layers were deposited at 450 °C with a growth rate of 0.2 ML/s under nominal N excess. Utilizing a low temperature for the SPSL deposition, we aimed at limiting the decomposition of InN and the diffusion and desorption of In. Moreover, the reduction of the growth rate was more suitable for the precise in-situ monitoring of the lattice parameter evolution along the whole deposition process by reflection high-energy electron diffraction (RHEED) in the  $(10\bar{1}0)$  azimuth. We have further investigated ex situ the morpholog-

**Fig. 1.** (a) Evolution of the in-plane lattice parameter measured by RHEED during the growth of the thick relaxed  $(\text{In}, \text{Ga})\text{N}$  buffer on a  $(0001)$  GaN template. (b) AFM image of a relaxed buffer with 200 nm thickness grown under identical conditions. The green arrows underline the network of misfit dislocations aligned along  $(10\bar{1}0)$ .



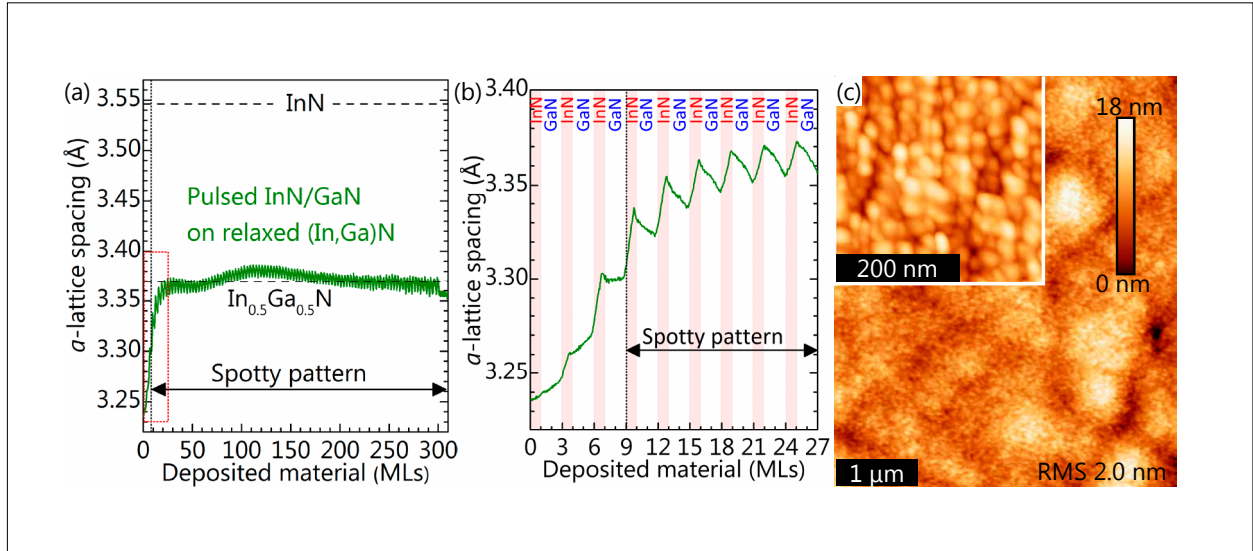


**Fig. 2.** (a) Evolution of the in-plane lattice parameter measured by RHEED during the pulsed growth of 100 periods of 1 ML InN / 2 MLs GaN on a relaxed (In,Ga)N buffer. The dash black lines indicate the unstrained lattice constants of InN and  $\text{In}_{0.5}\text{Ga}_{0.5}\text{N}$ . (b) Close view of the first nine periods marked by the red box in (a), where the flux pulses are marked by the shaded area. The black dotted line highlights the transition from streaky to spotty RHEED patterns. (c) AFM images of the as grown sample revealing islands at the surface (inset).

ical, structural and vibrational properties of this sample by atomic force microscopy (AFM), X-ray diffractometry (XRD) and Raman spectroscopy.

During the growth of the (In,Ga)N buffer, different relaxation stages were observed in RHEED, that can possibly be associated to different strain states along the (In,Ga)N buffer [Fig.1(a)]. AFM of an (In,Ga)N layer grown under identical conditions but with a thickness of 200 nm [Fig.1(b)] concurrently revealed the formation of trigonal patterns of misfit dislocations aligned along  $\langle 10\bar{1}0 \rangle$  [Srinivasan *et al.*, Appl. Phys. Lett. 83, 5187 (2003)]. During the pulsed InN-GaN deposition, RHEED indicated that the streaky pattern of the (In,Ga)N buffer turned spotty from the ninth period corresponding with a two dimensional to three dimensional (2D – 3D) growth transition, i.e. growth occurred following the Stransky-Krastanov mode. Plastic relaxation set in immediately during the very first deposited InN ML and the in-plane lattice parameter mainly increased

along the first sixth periods before reaching an average steady state value [Fig.2(a) and (b)]. The evolution of the in-plane lattice parameter exhibited undamped sawtooth oscillations with a period equal to the one of the flux pulses superimposed on the global progression. Though this effect may be attributed to the periodic change of the In content along the growth direction, it more likely results from the elastic distortion at the free edges of islands. The latter were revealed after growth by AFM [Fig.2(c)].

The characterization by the ex-situ methods concurrently indicated that the supplied In is fully incorporated. However, XRD  $\omega$ - $2\theta$  scans around the  $0002_{\text{GaN}}$  reflection did not evidence any peak characteristic for a periodic structure. Thus, no superlattices formed but a thick (In,Ga)N layer instead with a high degree of strain relaxation and an averaged In content of about 38% [Fig.3(a)]. Raman spectroscopy also showed only phonon modes correspond-

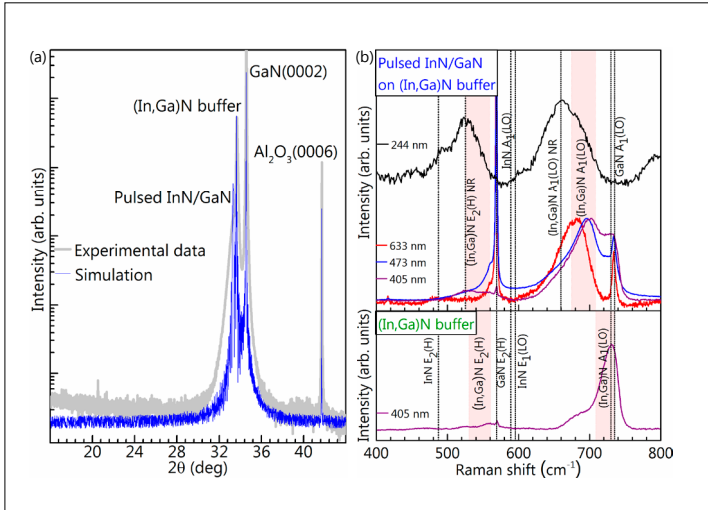


**Fig. 3.** (a)  $\omega$ - $2\theta$  scan of the pulsed (InN/GaN) SL on relaxed (In,Ga)N around the  $0002_{\text{GaN}}$  reflection, revealing the presence of only three peaks related to the buffer, an additional (In,Ga)N layer, and the GaN template. (b) Raman spectra of the relaxed (In,Ga)N buffer (bottom) with laser excitation of 405 nm and of the pulsed (InN/GaN) SL on relaxed (In,Ga)N (top) with resonant excitation of 405, 473 and 633 nm and with non-resonant (NR) excitation of 244 nm (optical probing depth smaller than the total SL thickness). No phonon modes corresponding to InN are detected.

ing to (In,Ga)N with a broad distribution in In content which was higher toward the sample surface, as revealed by the comparison of optical excitations in resonance and far above the range of (In,Ga)N bandgaps [Fig.3(b)].

To summarize and conclude, we have monitored the growth of 100 pulses of 1 ML InN/ 2 MLs GaN on a partially relaxed (0001) (In,Ga)N buffer by RHEED. Similar to growth on GaN, relaxation set in during the very first InN ML. After the deposition of 9 MLs, a 2D – 3D growth occurred and no superlattice was formed, as assessed ex situ by XRD and Raman spectroscopy. Therefore, other designs enabling the mitigation of the strain limitation on InN incorporation and relaxation effects are necessary.

Funding of this work by the European Union's Horizon 2020 research and innovation program (Marie Skłodowska-Curie Actions) under Grant Agreement SPRInG No. 642574 is gratefully acknowledged.

# Nonmetallic ferromagnetism in metastable FeGe<sub>2</sub> thin films

S. Gaucher, B. Jenichen, J. Herfort

Magnetic semiconductors have promising technological applications in the field of spintronics. While conventional semiconductors are useful for devices in which charge currents are involved, adding magnetism could provide a way to control conduction via electronic spin currents, hence supporting an extra degree of freedom for information processing. Magnetism is usually induced by doping traditional semiconductors with transition metals, yielding compounds referred to as dilute magnetic semiconductors. This approach is often seen as the most promising, since those materials can be made similar to widespread semiconductors already being used in the industry (e.g. GaMnAs, doped ZnO and TiO<sub>2</sub>). Most ferromagnetic semiconductors, however, have a Curie temperature below room temperature, which prevents their utilization for everyday microelectronics. A search for better candidates remains an ongoing challenge.

We report the observation of nonmetallic ferromagnetism in recently obtained FeGe<sub>2</sub> thin films. The material was first produced by annealing during the solid-phase epitaxy of amorphous Ge thin films over Fe<sub>3</sub>Si surfaces, in the context of an investigation to create lattice-matched metal/semiconductor heterojunctions [S. Gaucher *et al.*, *Appl. Phys. Lett.* **110**, 102103 (2017)]. TEM studies revealed a layered structure with space group *P4mm*, where monolayer Fe planes sit between tetragonal Ge bilayers. The material is metastable and does not exist in a bulk form, its creation rather being interpreted as an ordering phenomenon induced by minimization of the elastic energy of the epitaxial film [B. Jenichen *et al.*, *Phys. Rev. Materials* **2**, 051402 (2018)]. In order to characterize this new material, eliminating the underlying Fe<sub>3</sub>Si film is essential, oth-

erwise transport and magnetometry measurements would be dominated by metallic features. We claim that it was possible to do so for a 8 nm film, by first growing a few monolayers of crystalline Fe<sub>3</sub>Si, and then thicker amorphous Ge in a ratio such as to obtain the right stoichiometry for FeGe<sub>2</sub>. We note that the more straightforward use of pure Fe instead of Fe<sub>3</sub>Si is not successful in this case, as the reactivity of Fe with the underlying GaAs substrate is much stronger. Assuming a complete absorption of the Fe<sub>3</sub>Si implies that 17 % of Si atoms in fact sit on Ge sites, as per the following chemical reaction equation:



For convenience and to improve text readability, we still refer to the obtained compound as FeGe<sub>2</sub>. Converting the molar volume to film thickness, the ratio of Fe<sub>3</sub>Si to Ge required to achieve a complete incorporation is 1:3. FeGe<sub>2</sub> is also assumed to be lattice-matched with the GaAs(001) substrate.

As shown in Fig. 1 a), it was possible to realize FeGe<sub>2</sub> films with nominal thickness ranging from 8 to 20 nm, quoted as (2+6), (3+9) and (5+15) nm to keep track of the initial Fe<sub>3</sub>Si and Ge films. On all but one X-ray diffraction (XRD) curves, three broad characteristic peaks can be attributed to FeGe<sub>2</sub>, with intensity proportional to the thickness of the films. Those peaks are absent on the bottom red curve (corresponding to 1.5 nm Fe<sub>3</sub>Si plus 4.5 nm Ge), indicating what seems to be a lower limit in the thickness required to form FeGe<sub>2</sub> using the annealing technique. Traces of remaining "unused" Fe<sub>3</sub>Si are hardly detectable among the diffraction signals, either due to the films being too thin or completely absorbed and

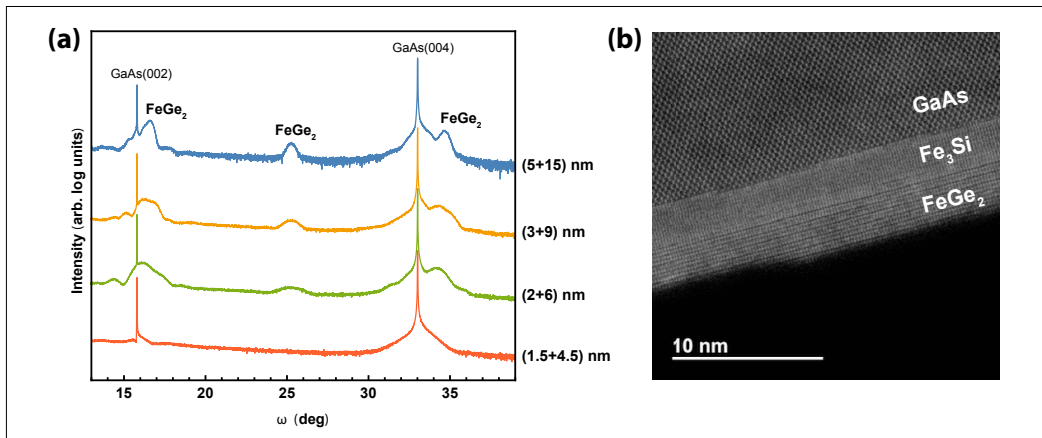


**Fig. 1.** (a) Wide angle XRD curves showing samples with different FeGe<sub>2</sub> thicknesses on GaAs(001) substrates. The films show distinctive broad FeGe<sub>2</sub> peaks. FeGe<sub>2</sub> did not form when the film had a combined thickness of 6 nm. b) TEM of the (3+9) nm sample showing a 2 nm residue of Fe<sub>3</sub>Si.

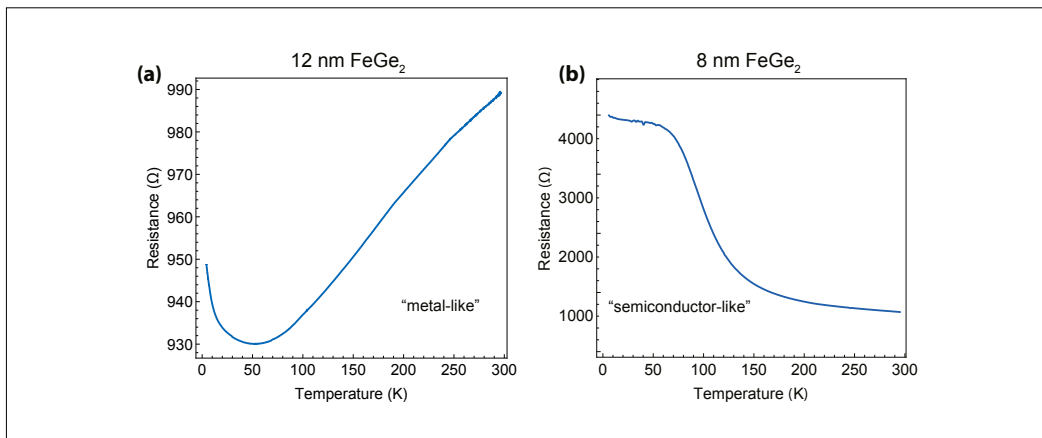


**Fig. 2.** (a) Resistance as a function of temperature in a 12 nm thin film of FeGe<sub>2</sub>. The slope indicates a metallic behaviour, which is in fact caused by the leftover Fe<sub>3</sub>Si still present after annealing. (b) Resistance as a function of temperature in an 8 nm thin film of FeGe<sub>2</sub>. The slope indicates a non-metallic behaviour. We can reasonably assert that the behaviour is a characteristic of FeGe<sub>2</sub> alone. The Hall bars for both samples have the same dimensions.

mixed with Ge during annealing. In Fig. 1 b), on the other hand, transmission electron microscopy (TEM) reveals that there is 2 nm of Fe<sub>3</sub>Si remaining after annealing the (3+9) nm sample. We assume that the attempts to produce thicker FeGe<sub>2</sub> films (more than 8 nm) will usually leave some Fe<sub>3</sub>Si, since the diffusion of atoms cannot happen over a certain number of monolayers. It might still be possible to fine-tune the

annealing procedure such as to minimize its contribution in case of thicker layer stacks.

The remaining Fe<sub>3</sub>Si of the (3+9) nm sample can also be detected through transport measurements. Fig. 2 displays the temperature dependence of the resistance for FeGe<sub>2</sub> samples having different thicknesses. In Fig. 2(a), the 12 nm film shows a decrease in resistance with temperature, which is

characteristic of metals. The conduction is therefore dominated by the residual  $\text{Fe}_3\text{Si}$  film seen in the TEM micrograph. However, in Fig. 2 b), the 8 nm  $\text{FeGe}_2$  film shows a drastically different behaviour, with the resistance increasing by over 400 % as the temperature is lowered. This nonmetallic behaviour cannot originate from conduction through any remaining  $\text{Fe}_3\text{Si}$ , and we therefore conclude that only  $\text{FeGe}_2$  is being probed in this measurement. The presence of two separate conduction regimes was also reported in independent studies of similar  $\alpha\text{-FeSi}_2$  [G. Cao *et al.*, Phys. Rev. Lett. **114**, 147202 (2015)], which further supports our result.

Lastly, the magnetic properties of the 8 nm  $\text{FeGe}_2$  film were probed by low-temperature anomalous Hall effect (AHE) measurements. The AHE requires a combination of magnetic polarization and spin-orbit coupling to produce a finite Hall voltage without the presence of an out of plane magnetic field. Fig. 3 shows the hysteresis curve obtained by sweeping the in-plane field, hence changing the magnetic polarization orientation, and measuring the Hall voltage  $V_{xy}$ . The strong anomalous Hall signal suggest the presence of ferromagnetism (as opposed to paramagnetism). In short,  $\text{FeGe}_2$  provides an interesting framework to study the interplay between chemical bonding and magnetism in metastable layered materials, and could open new ways for applications involving ferromagnetic semiconductors.

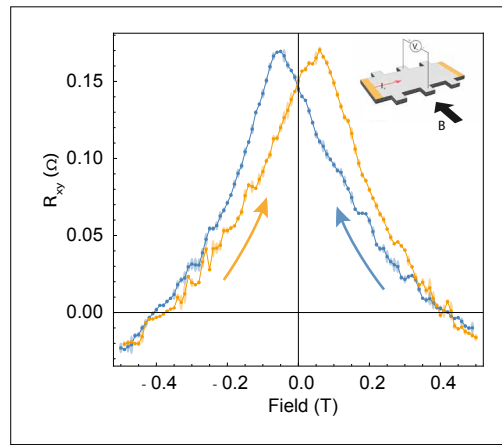


**Fig. 3.** Hall resistance hysteresis characteristic to the anomalous Hall effect in the 8 nm  $\text{FeGe}_2$  film, with in-plane external magnetic field applied perpendicular to the direction of the current ( $10\mu\text{A}$ ). The measurement was done at 4 K.

# The *p*-type transparent semiconducting oxide SnO: From source to film

M. Budde, G. Hoffmann, P. Mazzolini, J. Feldl, M. Ramsteiner, O. Bierwagen

Metal oxides (MO) such as  $\text{In}_2\text{O}_3$ ,  $\text{Ga}_2\text{O}_3$ , and  $\text{SnO}_2$  are well-known *n*-type transparent semiconducting oxides (TSOs). The possibility to combine a wide band gap with a tunable electrical conductivity at reasonable electron mobilities ( $\mu \approx 100 \text{ cm}^2/\text{Vs}$ ), makes MOs interesting for many applications such as gas sensors, solar cells, touch screens, transparent diodes or thin film transistors as well as UV detectors and power electronics [K. H. L. Zhang *et al.*, *J. Phys. Condens. Mat.* **28**, 383002 (2016)].

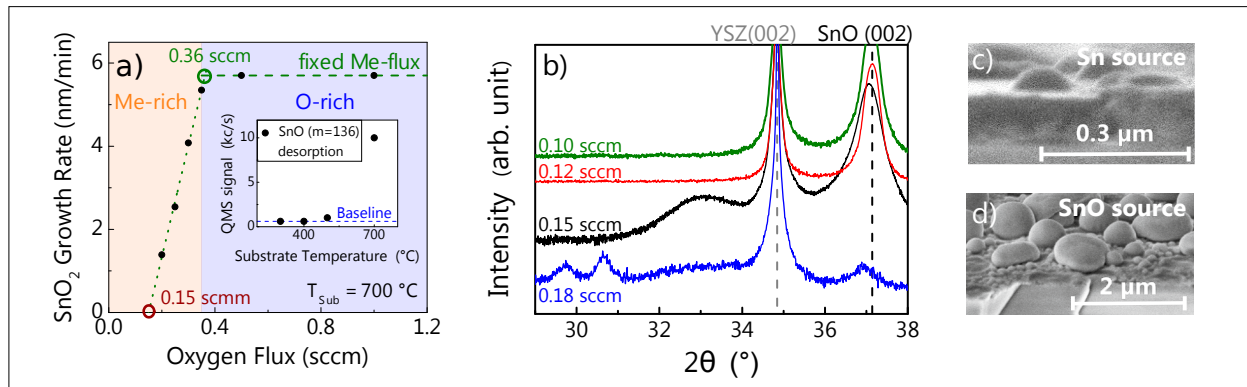
Plasma-assisted molecular beam epitaxy (PAMBE) is a powerful tool for the growth of MO thin films in the single crystalline form which is required for basic investigations and high-end applications. However, when using bare metal sources in combination with the oxygen plasma for the PAMBE of MOs new challenges arise. In fact, MOs possessing volatile sub-oxides share complex growth kinetics. For example, the deposition of  $\text{SnO}_2$  is ruled by a two-step process. The first step is the formation of its suboxide  $\text{SnO}$  on the growth surface ( $\text{Sn} + \text{O} \rightarrow \text{SnO}$ ), while its further oxidation

to  $\text{SnO}_2$  is the second one ( $\text{SnO} + \text{O} \rightarrow \text{SnO}_2$ ) which competes with the desorption of the  $\text{SnO}$  [P. Vogt *et al.*, *Phys. Rev. Mat.* **2**, 120401 (2018)].

In its crystalline solid state, the suboxide  $\text{SnO}$  is a *p*-type semiconductor with hole mobilities around  $3-5 \text{ cm}^2/\text{Vs}$ . This is a quite high mobility for *p*-type TSOs whose valence band structure often results in strongly localized holes and mobilities well below  $1 \text{ cm}^2/\text{Vs}$  [K.H.L. Zhang *et al.*, *J. Phys. Condens. Mat.* **28**, 383002 (2016)]. *P*-type TSOs are indispensable for oxide *p-n* junction devices in combination with the *n*-type TSOs mentioned above. However, creating a stable single-phase  $\text{SnO}$  thin film is challenging since  $\text{SnO}$  is meta-stable and can be easily over-oxidized into *n*-type  $\text{SnO}_2$  or reduced into metallic Sn.

The two step process for the conventional PAMBE growth of  $\text{SnO}_2$  described above should allow the growth of the intermediate  $\text{SnO}$  by reducing the oxygen flux to choke the second reaction step. Therefore, the growth

**Fig. 1.** (a)  $\text{SnO}_2$  growth rate variation with different oxygen fluxes for the growth by the Sn cell. Inset:  $\text{SnO}$  desorption measured by QMS (line-of-sight). (b) XRD measurements performed on samples deposited at different oxygen fluxes. (c) SEM image of a  $\text{SnO}$  sample grown from a Sn metal source (0.1 sccm oxygen plasma). (d) SEM image of a  $\text{SnO}$  sample grown from a  $\text{SnO}$  source using the  $\text{SnO}_2 + \text{Sn}$  charge (without oxygen plasma).



rate (GR) of  $\text{SnO}_2$  was measured in-situ by laser reflectometry for different oxygen fluxes at constant Sn flux ( $T_{\text{Sn}} = 1175 \text{ }^\circ\text{C}$ ) and a sufficiently high substrate temperature ( $T_{\text{Sub}} = 700 \text{ }^\circ\text{C}$ ) for  $\text{SnO}$  desorption. In the oxygen rich regime all  $\text{SnO}$  can be fully oxidized to  $\text{SnO}_2$  [constant  $\text{SnO}_2$  GR, blue shaded region in Fig. 1(a)], but in the metal rich regime, the volatile  $\text{SnO}$  desorbs without further oxidation [decreasing  $\text{SnO}_2$  GR, orange shaded region in Fig. 1(a)]. Thus, using the Sn source, solely  $\text{SnO}$  should be formed for a  $\text{SnO}_2$  GR of zero, which is at an extrapolated oxygen flux of 0.15 sccm (and 300 W plasma power in our case). Nonetheless, in order to enable the growth of  $\text{SnO}$  on a substrate its desorption must be prevented by reducing the growth temperature. The desorbing  $\text{SnO}$  flux [monitored by quadrupole mass spectrometer (QMS) in line-of-sight on substrate area] as function of substrate temperature shown in the inset of Fig. 1(a) indicates negligible  $\text{SnO}$  desorption at  $T \leq 400 \text{ }^\circ\text{C}$ , allowing the identification of a suitable temperature window for  $\text{SnO}$  growth experiments.

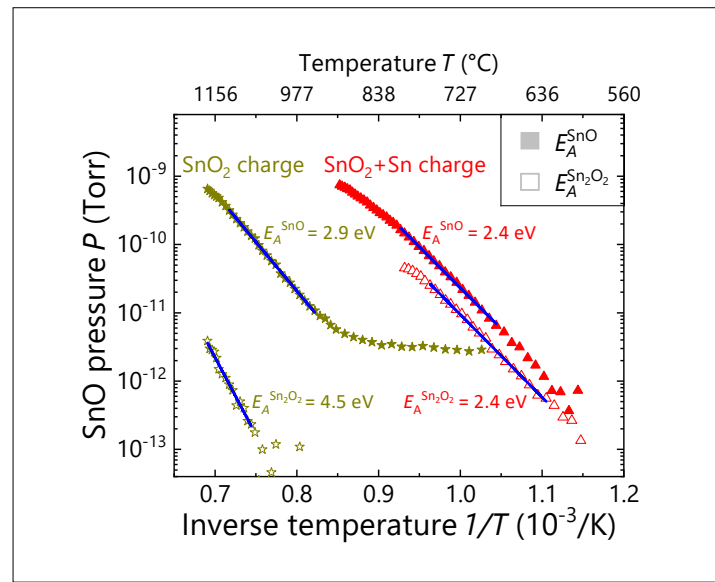
For optimization of  $\text{SnO}$  growth the oxygen flux was varred between 0.10 and 0.18 sccm ( $T_{\text{Sub}} = 400 \text{ }^\circ\text{C}$ ). In Fig. 1(b) X-ray diffraction (XRD) measurements indicate the growth of  $\text{SnO}(001)$  for oxygen fluxes of 0.10 and 0.12 sccm, whereas additional peaks occurred for higher fluxes. However, Raman measurements show the intermediate phase  $\text{Sn}_3\text{O}_4$  even in the sample grown at 0.12 sccm (not shown), identifying Raman as a useful tool for phase investigations [B. Eifert et al., Phys. Rev. Mat. **1**, 014602 (2017)]. Nevertheless, we can report phase pure, single crystalline  $\text{SnO}(001)\parallel\text{YSZ}(001)$  for an oxygen flux of 0.10 sccm [green curve in Fig. 1(b)], independently confirmed by Raman and XRD. The SEM cross-sectional image (0.10 sccm sample) reported in Fig. 1(c) shows the presence of a continuous layer.

Regarding the electrical properties, Hall measurements performed on the same sample (0.1 sccm) show a mobility of  $2.6 \text{ cm}^2/\text{Vs}$  at a hole concentration ( $p$ ) of

$9.7 \times 10^{18} \text{ cm}^{-3}$ . Interestingly, the mobility could be increased to  $3.5 \text{ cm}^2/\text{Vs}$  – with a slight decrease of  $p = 7.3 \times 10^{18} \text{ cm}^{-3}$  – by post growth rapid thermal annealing at  $300 \text{ }^\circ\text{C}$  for 10 min in  $\text{N}_2$  maintaining the  $\text{SnO}$  phase. In addition, *p*-type conductivity was confirmed by Seebeck measurements ( $S \approx +500 \mu\text{V/K}$ ). Concerning the air and time stability of the as-grown films, air stored samples measured after six weeks showed no changes in their properties within the measurement uncertainty.

Nonetheless, it could be possible to simplify the  $\text{SnO}$  growth directly providing the monoxide from the effusion cell. This idea has already become state of the art for the growth of the complex oxide  $\text{BaSnO}_3$  using a  $\text{SnO}_2$  source replacing the standard Sn-metal cell [S. Raghavan et al., APL Mater., **4**, 016106 (2016)]. However, the decomposition of the  $\text{SnO}_2$  source material to  $\text{SnO}$  ( $\text{SnO}_2 \rightarrow \text{SnO} + \text{O}$ ) requires high cell-temperatures ( $T > 1000 \text{ }^\circ\text{C}$ ) for adequate growth rates. In addition, the additional oxygen produced in the reaction could reduce

**Fig. 2.** Arrhenius diagram of  $\text{SnO}$  (solid icons) and  $\text{Sn}_2\text{O}_2$  (empty icons) partial pressures from  $\text{SnO}_2$  and  $\text{SnO}_2 + \text{Sn}$  charges. From the linear fits (blue solid lines) the activation energies were determined.



the lifetime of inner MBE components. As an alternative approach, the use of  $\text{SnO}_2 + \text{Sn}$  mixture as charge could overcome the additional oxygen production according to the reaction  $\text{SnO}_2 + \text{Sn} \rightarrow 2\text{SnO}$  [P. Vogt et al., Appl. Phys. Lett. **106**, 081910 (2015)]. This could be a promising candidate for both increased SnO fluxes (i.e. higher growth rates for lower cell temperatures) and longer lifetimes of inner MBE components. Thus, we evaluated the charges  $\text{SnO}_2$  and  $\text{SnO}_2 + \text{Sn}$  in an effusion cell measuring the resulting direct suboxide fluxes as function of cell temperature using a QMS mounted line-of-sight (focused on effusion cell).

For the  $\text{SnO}_2$  and  $\text{SnO}_2 + \text{Sn}$  mixture we found SnO activation energies ( $E_A^{\text{SnO}}$ ) of 2.9 eV and 2.4 eV, respectively (Fig. 2). The lower activation energy of the  $\text{SnO}_2 + \text{Sn}$  charge compared to the  $\text{SnO}_2$  charge is a clear sign of increased SnO suboxide flux at lower cell temperatures for the former charge. However, the activation energies of the higher oligomer  $\text{Sn}_2\text{O}_2$  ( $E_A^{\text{Sn}_2\text{O}_2}$ ) of 4.5 eV and 2.4 eV for the  $\text{SnO}_2$  and  $\text{SnO}_2 + \text{Sn}$  charges, respectively, indicate an abundance of  $\text{Sn}_2\text{O}_2$  when using the  $\text{SnO}_2 + \text{Sn}$  charge that might affect the growth.

Thus we tested the use of a  $\text{SnO}_2 + \text{Sn}$  charge as a direct SnO source as a possible way to achieve stoichiometric *p*-type SnO films without the employment of an oxygen plasma. For this deposition we used the same substrate temperature previously employed for the SnO growth starting from Sn cell and oxygen plasma source. Nonetheless, the growth from a  $\text{SnO}_2 + \text{Sn}$  charge just showed the deposition of Sn-metal independently confirmed by XRD and Raman measurements. Moreover, as it is possible to see from the cross-sectional SEM image reported in Fig. 1(d) the deposited layer is not continuous. Consequently, it was not possible to perform Hall measurements on this sample. These results suggest a decomposition of the SnO or  $\text{Sn}_2\text{O}_2$  in molecular form on the growth surface in marked contrast to the stability of SnO as crystal-

line, solid-state film at the same (growth) temperature. To clarify the role of the  $\text{Sn}_2\text{O}_2$  species in the source flux we will investigate the growth of SnO from the almost  $\text{Sn}_2\text{O}_2$ -free source that uses the decomposition of pure  $\text{SnO}_2$ .

# MBE growth of semiconducting oxides on graphene and SiC for gas sensing applications

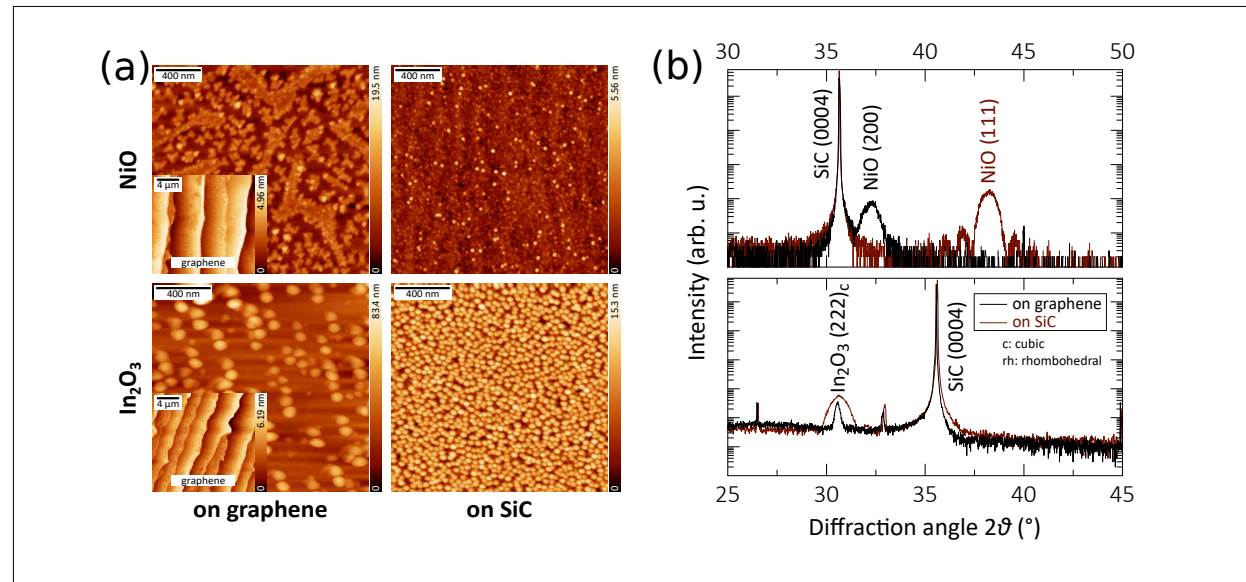
A. Papadogianni, M. Budde, S. Saadat Niavol<sup>1</sup>, J. M. J. Lopes, M. Hanke, F. Schipani<sup>2</sup>, N. Barsan<sup>2</sup>, and O. Bierwagen

Semiconducting oxides, such as the *p*-type NiO and *n*-type  $\text{In}_2\text{O}_3$  are traditionally known for their gas-sensing application, based on the measured response of the oxides' resistance to the composition of the surrounding atmosphere at elevated temperatures. Recently, nanoparticulate graphene functionalized by such oxides, using reduced graphene oxide and solution-based processes, has moved into the focus of gas-sensing research for improved sensitivity and selectivity. [S. G. Chatterjee *et al.*, *Sens. Actuators B* **221**, 1170 (2015)] We have recently demonstrated the possibility to utilize NiO and  $\text{In}_2\text{O}_3$  in the form of epitaxial layers grown by molecular beam epitaxy (MBE) to study the fundamentals of

oxide-based gas sensing [M. Budde *et al.*, *J. Appl. Phys.* **123**, 195301 (2018); J. Rombach *et al.*, *Sens. Actuators B* **236**, 909 (2016)] as well as the preparation of single crystalline graphene layers on SiC(0001) substrates. [M.H. Oliveira *et al.*, *Appl. Phys. Lett.* **99**, 111901 (2011)]

Here, we are joining these two research directions for the epitaxial combination of NiO and  $\text{In}_2\text{O}_3$  with single-crystalline graphene to provide simple, layered, oxide-graphene model systems for fundamental studies of gas sensing based on oxide-functionalized graphene. Towards their realization, we present an initial MBE growth study of nominally 10 nm-thick, cu-

**Fig. 1.** (a) Atomic force microscopy (AFM) images of the NiO (top row) and  $\text{In}_2\text{O}_3$  (bottom row) layers on graphene (left column) and SiC (right column). For reference, the insets show AFM images of the pristine graphene layers before oxide growth. (b) X-ray diffraction (XRD) symmetric on-axis  $2\theta - \omega$  scans of the oxide layers on graphene and SiC. The corresponding reflexes are labeled.



<sup>1</sup> Department of Solid State Physics, University of Mazandaran, Babolsar, Iran

<sup>2</sup> Institute of Physical Chemistry, University of Tübingen, Germany

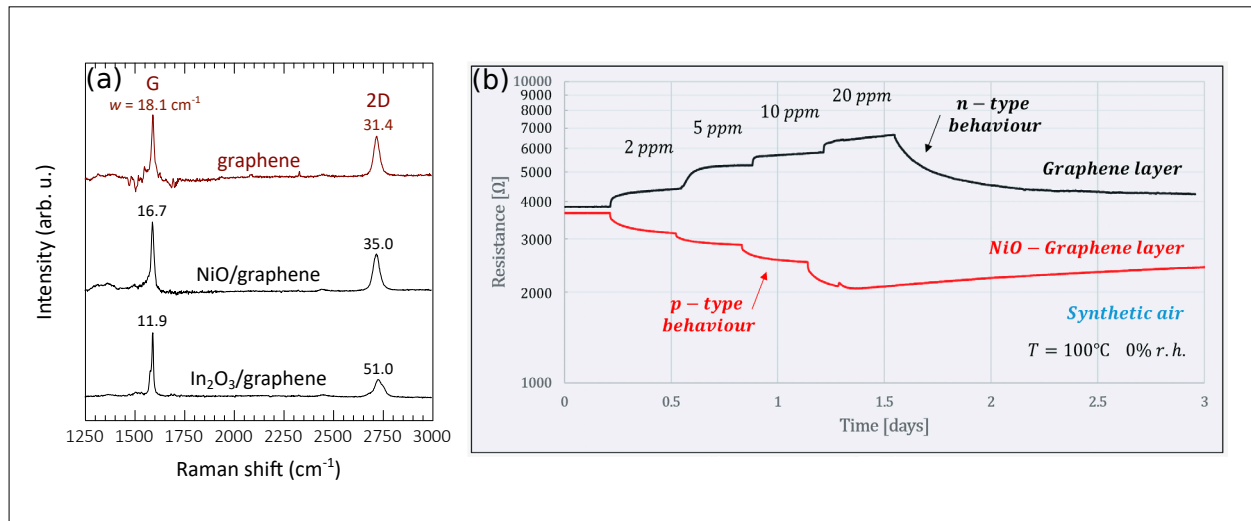


**Fig. 2.** (a) Raman spectra of the graphene layers after the oxide growth on top. For reference a representative spectrum of a pristine graphene layer before oxide growth is given. (b) Comparison of the resistance response of NiO-covered graphene to that of pristine graphene at  $100^\circ\text{C}$  in dry synthetic air (80% N<sub>2</sub>/20% O<sub>2</sub>) to traces of NO<sub>2</sub> (given in ppm).

bic NiO and In<sub>2</sub>O<sub>3</sub> layers on graphene. The morphology of the films and their epitaxial relation to the graphene will be discussed and compared to the results of growth on co-loaded SiC(0001) substrates without a graphene layer, allowing us to compare oxide MBE in vastly different substrate-to-film/adatom bonding scenarios.

The NiO and In<sub>2</sub>O<sub>3</sub> layers were grown at substrate temperatures of  $100^\circ\text{C}$  and  $500^\circ\text{C}$  at nominal growth rates of  $0.05 \text{ \AA/s}$  and  $1.5 \text{ \AA/s}$  using molecular oxygen and plasma-activated oxygen, respectively. Oxygen plasma is known to etch graphene [T. Schumann *et al.*, Phys. Rev. B **85**, 235402 (2012)] but required for the growth of In<sub>2</sub>O<sub>3</sub>. To minimize the plasma damage we started growth by deposition of  $\sim 1.5 \text{ nm}$  of metallic In before exposing the growth front to the plasma for the remaining layer growth and turning off the plasma directly after the deposition.

Fig. 1(a) shows the morphology of our oxide films on graphene in comparison to those on bare SiC, as well as that of the pristine graphene layer for reference. After

overgrowth the smooth surface of SiC or graphene is covered by an oxide layer consisting of islands. The islands on graphene are significantly taller and their density is significantly lower compared to those on SiC, indicating larger surface ad-atom diffusivity on graphene than on SiC. Comparison of the NiO morphology to that of the pristine graphene additionally suggests a clustering of NiO islands on features that correspond to patches of either monolayer or bilayer graphene, highlighting a markedly different layer nucleation and bonding of ad-atoms on those types of graphene. The x-ray diffraction scans shown in Fig. 1(b) indicate the out-of-plane crystalline orientation of the oxide films on graphene and SiC. The growth of three-fold rotationally symmetric cubic (111)-oriented In<sub>2</sub>O<sub>3</sub> and NiO layers is expected to be energetically favorable on the six-fold rotationally symmetric graphene - as observed in our growth on the six-fold rotationally symmetric SiC(0001) surface. In contrast, NiO grows in the (100) orientation on graphene, similarly to MBE-grown cubic EuO and SrO as reported in [A. G. Swartz *et al.*, ACS Nano **6**, 10063 (2012); A. S. Ahmed *et al.*, J. Crystal Growth

447, 5 (2016)]. For NiO, EuO, and SrO this orientation (for  $\text{In}_2\text{O}_3$  the (111)-orientation) has the lowest surface free energy.

Thus, the larger diffusivity and the surface-energy-minimization driven layer orientation on graphene, both, confirm significantly weaker bonds of ad-atoms and oxide film to graphene than to SiC.

Fig. 2(a) shows the Raman spectra taken before and after the oxide growth. The presence of the G and 2D peaks confirm the preservation of the underlying graphene layers after oxide growth. Thus,

the pre-deposition of In and the short growth time prevented plasma-etching of the graphene during  $\text{In}_2\text{O}_3$  growth. The wider 2D peak for this sample, however, indicates intercalation of oxygen from the plasma between graphene and its SiC substrate.

The initial gas-response measurements shown in Fig. 2(b) demonstrate NiO (which itself is rather insulating) to increase the relative resistance change of graphene upon exposure to traces of  $\text{NO}_2$  as well as an inversion of the conductivity type from *n*-type to *p*-type.

# Electron tomography and spectroscopy of three-dimensional InGaN/GaN nanostructures

L. Nicolai, Ž. Gačević<sup>1</sup>, E. Calleja<sup>1</sup>, A. Trampert

The ongoing process of miniaturization of optoelectronic devices has given rise to the development of complex, three-dimensional (3D) nanostructures. The complicated geometry of 3D nanostructures issues a huge challenge for standard transmission electron microscopy (TEM): A single TEM micrograph only provides a two-dimensional (2D) projection of a volume. Hence, the interpretation of standard TEM micrographs of 3D objects can be very difficult. This applies in particular to micrographs of a sample containing only a small fraction of one material embedded in another, especially if the contrast between both materials is low. This report shows that electron tomography in combination with energy dispersive x-ray (EDX) spectroscopy is a powerful tool to fully characterize such complex 3D nanostructures.

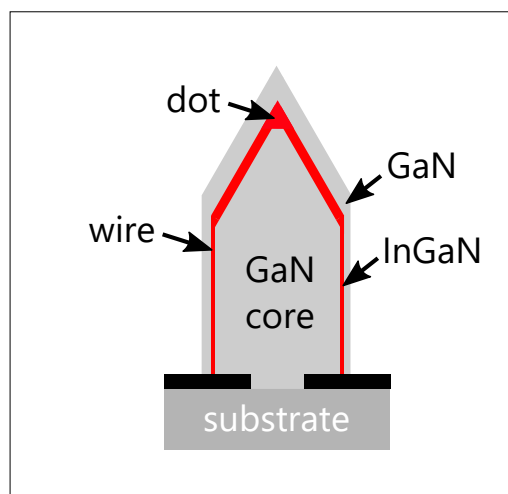
An (In,Ga)N/GaN "dot-in-wire" (DIW) structure is used as case study. Hexagonal, pencil-shaped GaN nanowires (NW) were first grown on top of a GaN template using selective area growth by molecular beam epitaxy. Subsequently, this structure was overgrown by (In,Ga)N/GaN shells fabricating the DIW structure on the multifaceted tip of the GaN core. A schematic of the NW structure is shown in Fig. 1.

A sophisticated preparation technique is necessary to obtain needle-shaped tomography specimens containing only one single NW. The NWs were embedded by carbon to protect them during the preparation process. A dual-beam focused ion-beam (FIB) microscope system was used to isolate an individual NW and to transfer it to a tomography holder allowing a full 180° rotation in-

side the TEM. The high-angle annular dark-field (HAADF) mode was used to record a tomography tilt series. This particular mode was chosen due to the predominantly chemical contrast which is a prerequisite for electron tomography. Within this work, two different methods are applied for the visualization of the reconstruction: The inner structure is visualized by 2D slices with a finite thickness which are extracted from the 3D reconstructed volume and the NW morphology is visualized by isosurfaces (surfaces of equal voxel [3D pixel] intensities) of the GaN-to-C interface. Posterior measured selective area diffraction patterns are used to correlate the orientation of the reconstruction with the crystal axes of the NW.

The morphology of the investigated NW is shown in Fig. 2. The figure reveals the outer crystal shape and surface faceting, re-

**Fig. 1.** Schematic of the core-shell DIW structure.



<sup>1</sup> ISOM-ETSIT, Universidad Politécnica de Madrid, Spain

spectively. The NW consists of a hexagonal base with regular non-polar  $\{1\bar{1}00\}$  *m*-plane surface facets. The NW top reflects a pyramidal shape consisting of  $\{1\bar{1}01\}$  *s*-plane facets and  $\{1\bar{1}02\}$  *r*-plane facets as well as a small triangular shaped  $\{2\bar{2}01\}$ -type surface facet (labeled by a green arrow). Above the  $\{2\bar{2}01\}$  facet an irregular "hat" is formed at the very top. This irregular shape is associated with the presence of stacking faults and the change of the crystal lattice from hexagonal to cubic.

The inner structure of the NW is visualized by cross-sectional and plan-view slices extracted from the reconstructed volume. The slices are presented in Fig. 3(a). The reconstructed voxels of  $(\text{In},\text{Ga})\text{N}$  have slightly higher intensities compared to those of GaN. Consequently, referring to the color code of Fig. 3(a), GaN is presented in green whereas indium containing layers appear reddish for clarification. The  $(\text{In},\text{Ga})\text{N}$  shell replicates the morphology of the GaN core. The tip of the inner shell is expanded forming the DIW configuration with increased indium content and the shape of an inverse truncated pyramid with hexagonal base composed of *c*-plane facets as upper and lower boundaries. Additionally, the figure gives an overview of the various  $(\text{In},\text{Ga})\text{N}$  layer thicknesses and the indium distribution. The indium atoms are not homogeneously distributed along the shell structure, because the indium incorporation rate depends on the facet orientation with the highest value in *c*-plane layers. In addition, it seems that in some areas of the shell, the concentration is higher close to the interfaces. The reconstruction reveals a higher roughness for the lower interface of the DIW than for the upper. The origin of this roughness can be linked to the nucleation mechanism of  $(\text{In},\text{Ga})\text{N}$  on the multi-faceted apex of the GaN NW core. The much higher indium content on *c*-plane results in the growth of strained 3D nuclei. These nuclei generate stress on its surrounding that will deform the interface and finally lead to the measured roughness. The  $(\text{In},\text{Ga})\text{N}$

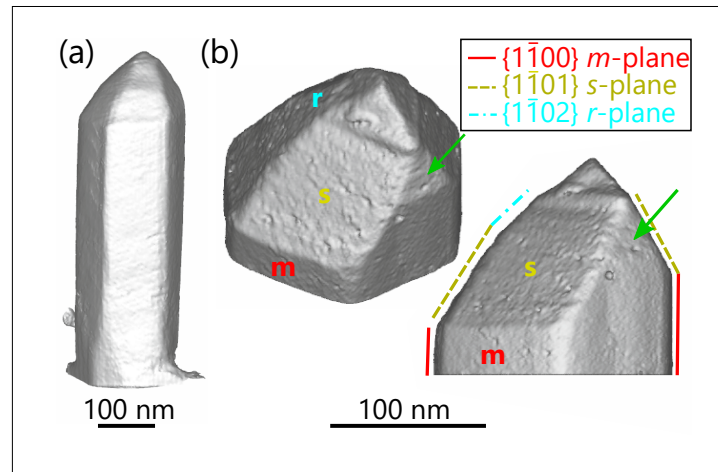


**Fig. 2.** (a) Isosurface representation of a single NW and (b) the NW apex with a perspective view and a view along the low index  $[11\bar{2}0]$  direction. The green arrow indicates a facet of  $\{2\bar{2}01\}$ -type.

shell is not always parallel to the *m*-, *r*-, or *s*-plane faceted GaN sidewall. In the lower part of the NW, the  $(\text{In},\text{Ga})\text{N}$  shell reproduces one-to-one the shape of the GaN core with *m*-plane facets just like the GaN outer shell. On the other hand, at the pyramidal tip of the NW, the inner  $(\text{In},\text{Ga})\text{N}$  shell deviates from the hexagonal shape of the GaN outer shell. For example, the plan-view slice at height B in Fig. 3 shows that the GaN outer facet and the  $(\text{In},\text{Ga})\text{N}$  shell have facets which are  $30^\circ$  rotated to the expected orientation based on symmetry reasons.

Although the reconstruction is based on HAADF micrographs, the voxel intensity is not only influenced by changes of the sample chemistry. It is known that defects can lead to HAADF contrast variations and various reconstruction artifacts can directly influence the reconstructed voxel intensities. Therefore, an additional EDX analysis is performed on the identical sample, cf. Fig. 3(b). An  $\text{In}_{\text{La}}$ -map of the NW apex was recorded and spectra are extracted at three different regions of NW apex (DIW [I],  $(\text{In},\text{Ga})\text{N}$  shell [II] and GaN shell [III]). The EDX results confirm the prior conclusions regarding the faceted DIW, the indium distribution and interface roughnesses. Addi-

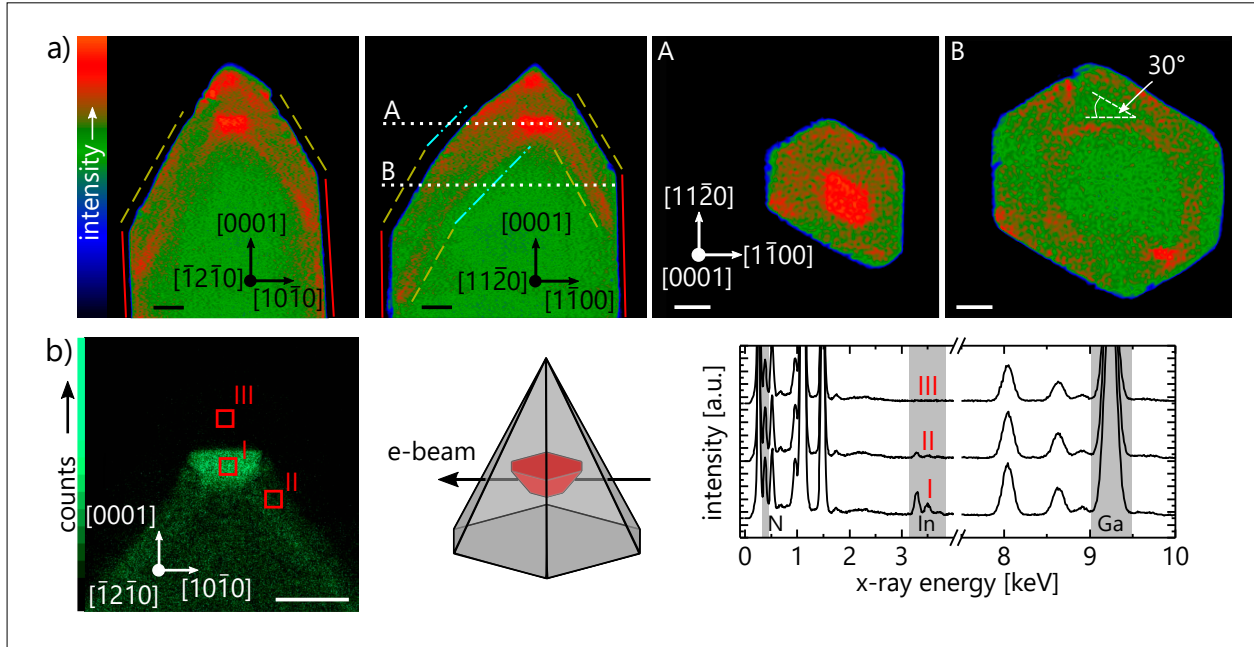


**Fig. 3.** (a) Tomographic cross-sectional slices along two low index crystal directions and plan-view slices at the heights labeled A and B. Facets are marked by colored lines referring to the color code of Fig. 2. Slice thickness is 7 nm for the cross-sectional and 3.6 nm for the plan-view slices. (b) In<sub>Lα</sub> EDX map of NW apex. Schematic of the EDX experiment geometry showing that the electron beam passes partially through GaN shell and DIW configuration. Spectra taken at the position of the DIW configuration (I), the (In,Ga)N shell (II) and the GaN tip (III). Length of scale bars corresponds to 25 nm.

tionally, the In<sub>Lα</sub>-map allows to identify contrasts not arising from an increased indium composition: The higher voxel intensities above the DIW are most probably caused by the presence of stacking faults. A schematic of the x-ray experiment shows the complexity of the EDX signal generation: The electron beam passes through various layers of (In,Ga)N and GaN with varying thicknesses. As a consequence, a quantitative EDX analysis of the DIW indium concentration requires the knowledge of the (In,Ga)N/GaN volume ratios. This ratio can be easily accessed by determining the dimensions of the DIW and the GaN shell using the reconstruction. First, the "projected indium composition" was calculated by

evaluating the change of the Ga<sub>Kα</sub>/N<sub>Kα</sub>-ratio from the DIW region (I) to the pure GaN shell region (III) assuming an exact stoichiometric composition. Then, the DIW indium composition was calculated by multiplying the prior value with a correction factor obtained from the volume ratios. Consequently, the indium content of the DIW is estimated to be (32 ± 7) %. This method allows a full 3D quantitative EDX analysis of such nanostructures. Both, EDX map and reconstruction indicate indium fluctuations. Therefore, future investigations point at the alloy stability and potential alloy fluctuations on the nm-scale and their spatial distribution because they strongly affect the emission characteristics.

# Tomographic reconstruction of dislocations based on annular bright-field imaging mode

H. Drube, A. Trampert

In recent years, electron tomography has become a powerful tool in materials science to study the three-dimensional (3D) microstructure. Typically, the high-angle annular dark-field imaging mode in scanning transmission electron microscopy (STEM) is used for tomography because of the high chemical contrast between different materials which eventually is applied to study buried interfaces. The 3D investigation of dislocations in regards to spatial distribution and crystallographic orientation is still challenging because of the strong orientation dependency of diffraction contrast, typically observed in conventional transmission electron microscopy (TEM) under two beam condition.

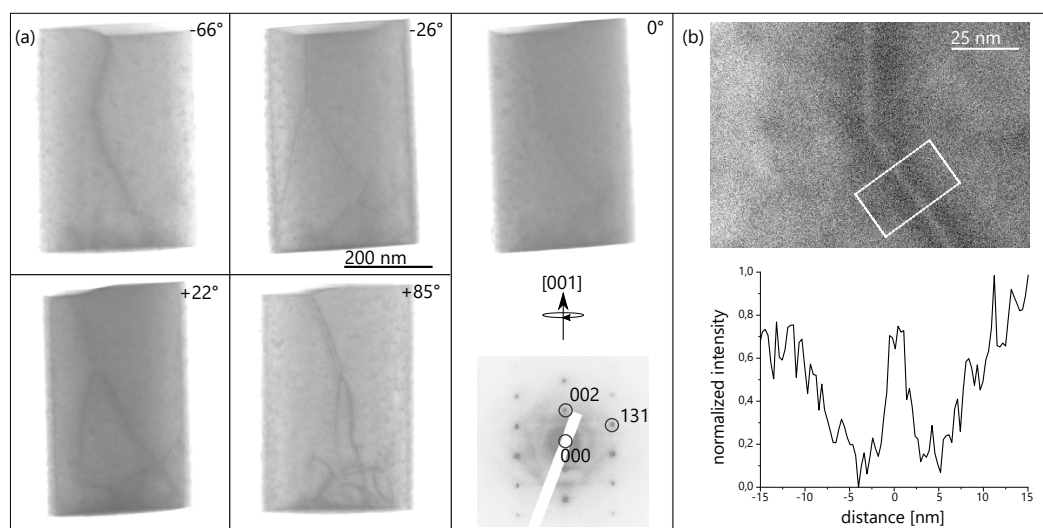
Here, we have tested the applicability of annular bright-field (ABF) STEM imaging mode for electron tomography of 3D dislocation structures. The sample under investigation is a 500 nm-thick GaSb film grown on Si(001) substrate. Due to the large mis-

match in the lattice constant and thermal expansion coefficient, these epilayers are characterized by a large number of misfit and threading dislocations.

A focused ion-beam setup is used to prepare a cylindrical shaped tomography needle of about 380 nm in diameter with the needle axis approximately in the [001] film growth direction. ABF images in STEM are generated by locating the annular detector within the direct-beam disc. A tilt series is then recorded from  $-90^\circ$  to  $+90^\circ$  with  $2^\circ$  steps. The ABF STEM imaging mode combines Bragg diffraction with diffuse scattering information resulting in a number of benefits compared to conventional TEM. For example, dislocation imaging can be performed in thicker samples and the bend contour and thickness fringe contrast are almost completely suppressed.

Figure 1(a) represents an exemplary selection of ABF micrographs of the tilt series

**Fig. 1.** (a) ABF tilt series with contrast enhancement by histogram thresholding. SAD image shows that the  $0^\circ$  position of the specimen is in [130] zone axis. (b) Upper image shows typical dislocation contrast in ABF, lower image is a line plot of the marked area of the dislocation.



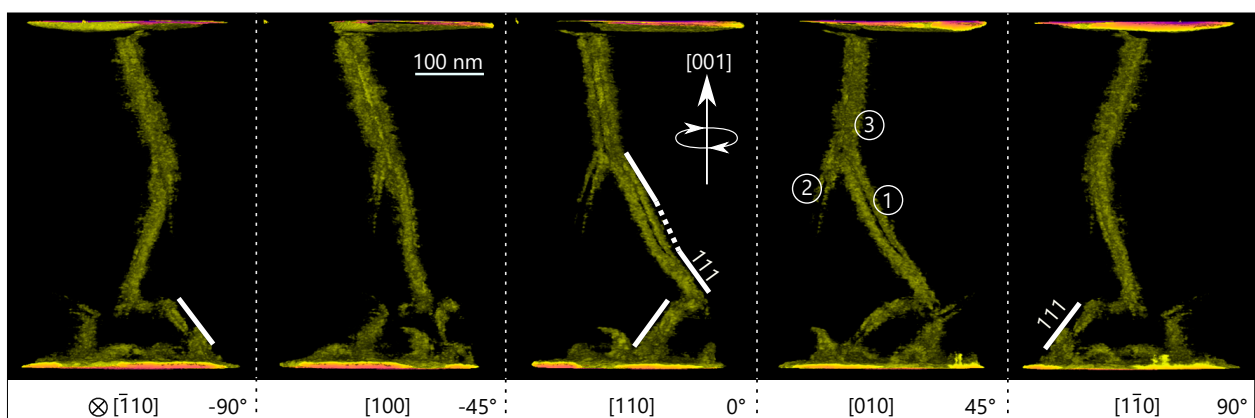
after contrast enhancement. The threading dislocation structure in the GaSb film is visible over a wide tilt range as essential condition for the successful tomographic reconstruction. In addition, selected area diffraction (SAD) patterns are taken for defining the exact crystallographic directions, the [130] zone axis is arbitrarily selected as 0° position. Figure 1(b) shows an enlarged part with a contrast detail of the dislocation line and the corresponding intensity area profile across the dislocations line. The contrast is composed of a bright sharp line surrounded by two parallel dark bands forming an W-type contrast. The bright line corresponds to the dislocation core, while the dark bands correlate to the atomic displacement induced by the elastic strain field.

The selected ABF contrast features shown in Fig. 1 are used for the tomographic reconstruction via simultaneous iterative reconstruction technique (SIRT). Figure 2 illustrates the result of the reconstruction showing the dislocation arrangement along low index axes. The tomogram is aligned along the [001] direction with the film surface on top and the substrate at the bottom side. Near the interface to the Si substrate, a high density of threading dislocations is detectable that is strongly reduced within the first 100 nm of the GaSb

film due to dislocation interactions and annihilation processes. Some dislocation lines end at the side surface of the needle. The projections along the  $\langle 110 \rangle$  directions allow the end-on view on the four  $\{111\}$  slip planes. As expected, most of the threading dislocations propagate along these slip planes. Moreover, cross slip is also observed between two parallel  $\{111\}$  slip planes. In the middle of the tomogram, two dislocation segments 1 and 2 merge and the resulting dislocation segment 3 runs roughly parallel to the growth direction towards the film surface. This dislocation line is not located in a  $\{111\}$  slip plane. Therefore, its propagation must be the result of a non-conservative motion during growth. Dislocation segment 2 is not reconstructed completely because the voxel intensities of the reconstruction are in another intensity level area than the illustrated dislocations. The reason might be its position close to the needle surface reducing the diffuse scattering contrast.

The ABF STEM tomography method provides additional information about the dislocations besides their spatial distribution. Figure 3(a) shows a slice through the tomogram perpendicular to [001] near the interface to the substrate as an example for the possibility to determine dislocation densities at particular positions of the GaSb film. The spatial distribution of five

**Fig. 2.** 180° rotation of the tomogram around [001] growth direction starting from  $[\bar{1}10]$  to  $[1\bar{1}0]$  in 45° steps. Dislocations lying on  $\langle 110 \rangle$  planes as well as cross slip of dislocation segment 1 is indicated.



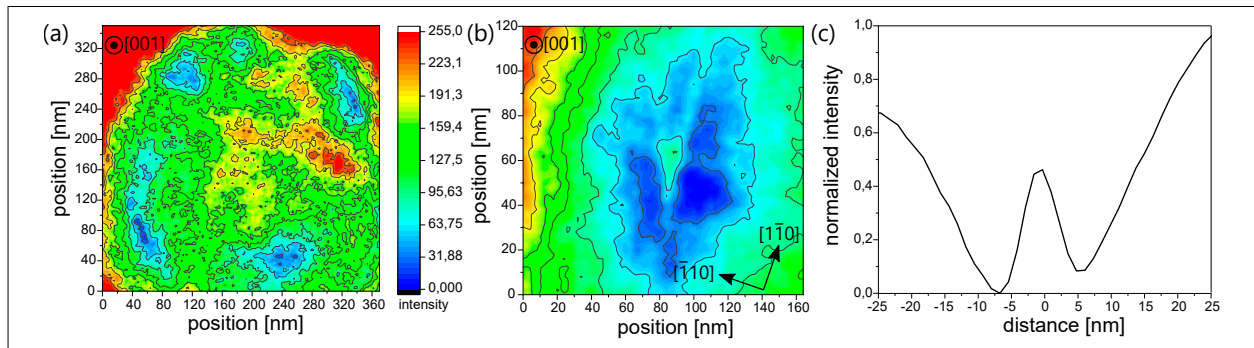


**Fig. 3.** Slices through the tomogram near the interface to the substrate (a), and across the dislocation line with its core in the center (b), (c) line profile of dislocation segment 3.

dislocation distortion fields (blue) is detectable with this technique. Thus, the dislocation density of the specimen is here in the range of  $10^{11} \text{ cm}^2$ , a value that is typically found in these material systems close to the interface. Figure 3(b) displays a 10 nm-thick slice of the tomogram through dislocation segment 3. The voxel intensities are linked to the dark lines and thus the strain field next to the bright dislocation core in Fig. 1(b). The 2D map shows a symmetry distortion in the  $[1\bar{1}0]$  direction. This is a result of the tilt of the dislocation with respect to the  $[001]$  growth direction and the thickness of the slice. The dislocation core as well as the surrounding bulk area show the same intensity profile as observed in the original micrographs. Although the exact contrast mechanism for ABF is still not fully understood, we still can reconstruct the 3D shape of the displacement field. This opens new possibilities for the characterization of the dislocation type (edge/screw) because of the relationship between the strain field symmetry and the location of the Burgers vector.

vector with respect to the line direction. The line profile taken from a central slice of the reconstruction in Fig. 3(c) exhibits the same W-shape for the dislocation contrast as the original micrographs, which is an indication for a successful reconstruction of the dislocation with this technique. We also conclude, that a minimal spatial separation of 20 nm to 30 nm between different dislocations is needed for this technique. Close to dislocation nodes, this limit will be exceeded and artifact formation needs to be taken into consideration.

Here we report the combination of the less widely used ABF STEM mode with tomographic reconstruction. This gives new insights into the spatial orientation of dislocations and their characterization through the corresponding strain field.

Parts of this work have been funded by the European Union and the State of Berlin via the EFRE project 2016011843.

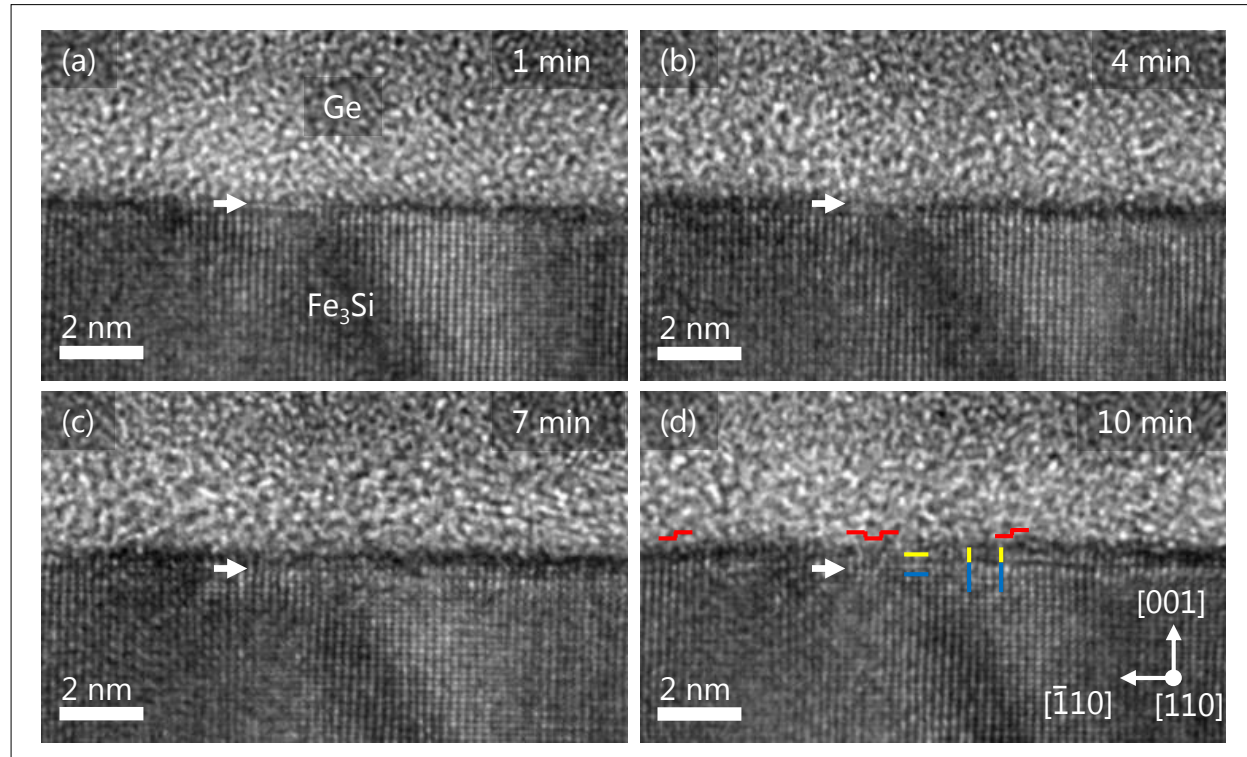
# In-situ transmission electron microscopy of solid phase epitaxy of Ge on $\text{Fe}_3\text{Si}$

M. Terker, B. Jenichen, J. Herford, A. Trampert

The direct epitaxial growth of layer stacks consisting of very dissimilar materials like semiconducting Ge on semimetallic  $\text{Fe}_3\text{Si}$  has been demonstrated to be quite challenging due to the very different growth temperatures used for the various materials. One approach to circumvent this fundamental problem is the application of the so-called solid-phase epitaxy (SPE) which offers great flexibility with regards to the combined materials as well as the interface topology. There, the material is first deposited in an amorphous state and subsequently annealed in the growth chamber to receive the crystalline, epitaxially aligned film. However, the details of the SPE process are difficult to observe because of the amorphous material covering the surface. Therefore, it is advantageous to investigate this process in-situ, in real space and with cross-sectional geometry.

In-situ transmission electron microscopy (TEM) is a technique that is rapidly gaining in popularity due to the development of novel sample holders. These allow for the

**Fig. 1.** Snapshots of the video recording for in-situ annealing at 240 °C taken at (a) 1 min, (b) 4 min, (c) 7 min, (d) 10 min after reaching the target temperature. The white arrow marks the location of the Ge/ $\text{Fe}_3\text{Si}$  interface. The growing crystalline film shows epitaxial alignment in both [1̄10] and [001] direction, as indicated with blue and yellow lines. Further the growth front of the crystalline film shows some monoatomic steps, indicated here with red lines.



controlled application of stimuli like high temperatures or electrical voltages while simultaneously observing the specimen with high-resolution (HR) TEM. In this work in-situ heating is applied to directly observe with high spatial resolution the amorphous/crystalline (a/c) phase transition of Ge on  $\text{Fe}_3\text{Si}$  and the effect of the interface on the nucleation process.

Molecular beam epitaxy was used to grow first a 38 nm crystalline  $\text{Fe}_3\text{Si}$  film on  $\text{GaAs}(001)$  substrate followed by the deposition of a nominal 5 nm thick amorphous Ge layer. For the in-situ TEM studies, cross-sectional specimens were prepared conventionally by mechanical grinding and  $\text{Ar}^+$ -ion milling and then transferred to a micro-electro-mechanical systems-chip using a focused ion beam device.

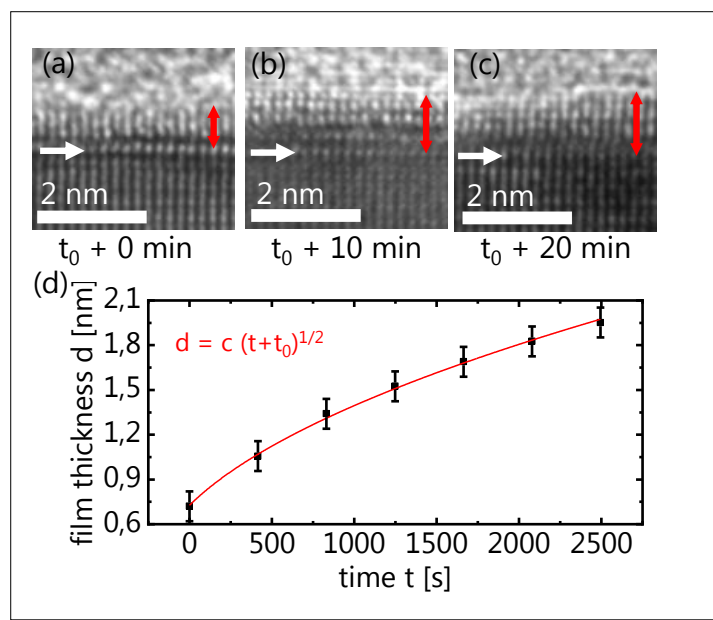
Annealing experiments were performed at different temperatures to study the nucleation and growth stage as well as the ordering phenomenon during a/c-phase transition. For the observation of the nucleation the a-Ge layer was heated to 240 °C and kept there for 10 min simultaneously recording the dynamics of structural changes. Figure 1 presents a set of HRTEM micrographs of the interface region at different times. In all images, the c-Ge layer appears atomically smooth with a large number of mono-atomic steps at the growth front indicating the two-dimensional growth mode. Some of these steps are marked in Fig. 1(d) with red lines. The growing film is epitaxially aligned with the cube-on-cube-relationship (001) Ge || (001)  $\text{Fe}_3\text{Si}$  and [110] Ge || [110]  $\text{Fe}_3\text{Si}$ .

Figure 2 summarizes the results of the crystallization kinetics. At this point, the sample was annealed to 300 °C and kept at this temperature for about 10 min before starting the video recording. The initial state is therefore described by an already crystallized film of about 0.7 nm thickness [Fig. 2(a)]. In Fig. 2(d) the time dependency of the growth of the film thickness  $d$  is

plotted describing a square root behavior which indicates that the process of SPE is diffusion controlled.

When the annealing was continued at 350 °C, a change in the structure of the crystallized film is observed as presented in Fig. 3. In Fig. 3(a), the film still shows the same structure as in the previous growth while in Fig. 3(b) after 40 min of annealing the crystalline film has not only increased in thickness but also shows a periodic modulation in the phase-contrast image. Figure 3(c) and (d) show line scans across the film after Fourier filtering out only the spots in [001]-direction. There, it can be seen that the 0.29 nm periodicity corresponding to the (002)-lattice spacing of Ge has given way to a modulation twice as wide. This reduction in symmetry could indicate indiffusion of Fe resulting in a crystal lattice rearrangement towards the P4mm structure of  $\text{FeGe}_2$  observed in

**Fig. 2.** Snapshots of the video recording for in-situ annealing at 300 °C taken (a) directly after reaching the target temperature, (b) after 10 min and (c) after 20 min. The white arrow indicates the location of the initial a-Ge/ $\text{Fe}_3\text{Si}$  interface and the red double arrows show the thickness of the crystalline layer. (d) Graph showing the square root shaped growth at the location of the red double arrow.



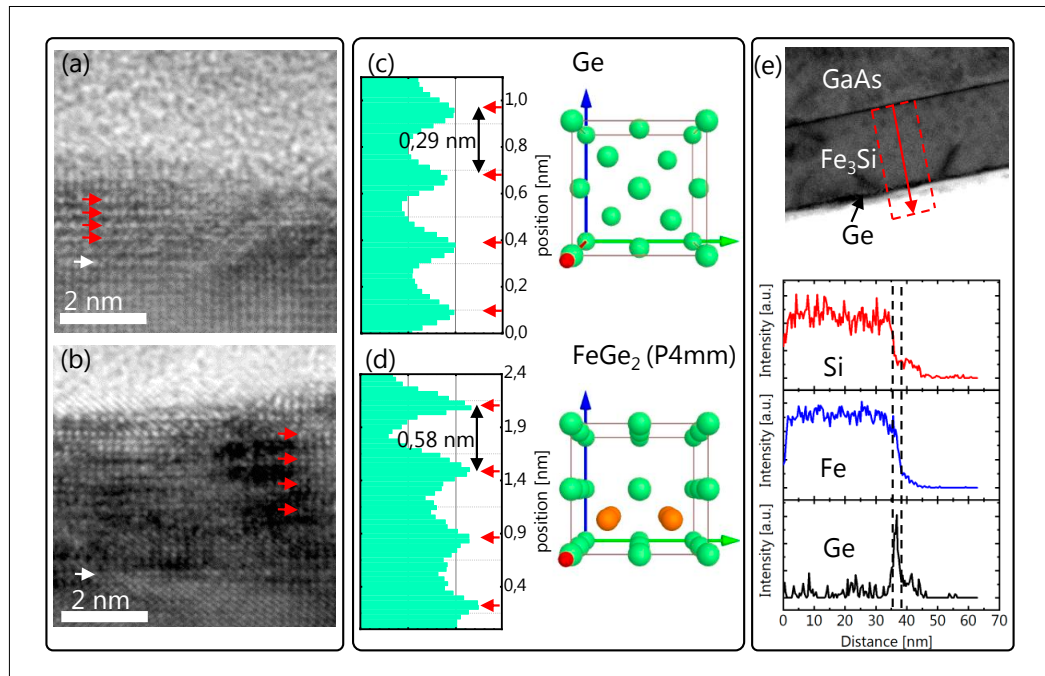


**Fig. 3.** Snapshots of the video recording for in-situ annealing at 350 °C taken a) directly after reaching the target temperature and b) after 40 min. (c) shows line scans across the film after Fourier filtering out only the spots in [001]-direction. The red arrows in (a) and (c) indicate the (002) periodicity, while in (b) and (d) they correspond to a modulation with twice the width. The unit cells of Ge and FeGe<sub>2</sub> are depicted next to the line scans, respectively. (e) shows an EDX-line of the region indicated in (e) scan after cooling down the sample to RT again.

a previous work [Jenichen *et al.* Phys. Rev. Materials **2**, 051402(R) (2018)]. This structure has a periodicity in (001)-direction of 0.5517 nm. The HRTEM image in Fig. 3(b) is characterized by large lattice distortion, indicating that the phase transition is still not complete. To confirm the interdiffusion of Fe into the Ge layer, EDX line scans were performed across the hetero-structure after cooling down the sample from 350 °C to room temperature. The profiles for Si, Fe and Ge are plotted in Fig. 3(e). The two vertical dashed lines indicate the location of

the Ge-rich film. The Si signal directly drops at the interface between the Fe<sub>3</sub>Si and the crystallized film, while the Fe signal continues into the Ga-rich area.

Further in-situ experiments on this material system could explore the crystallization on longer time scales and different temperatures with thicker initial a-Ge films. In particular, this could help to clarify the temporal evolution of interdiffusion and correlate it with the structural rearrangement of the film.

# Magnetic characteristics of epitaxial NiO films studied by Raman spectroscopy: Influence of disorder and biaxial strain

J. Feldl, M. Budde, O. Bierwagen, M. Ramsteiner

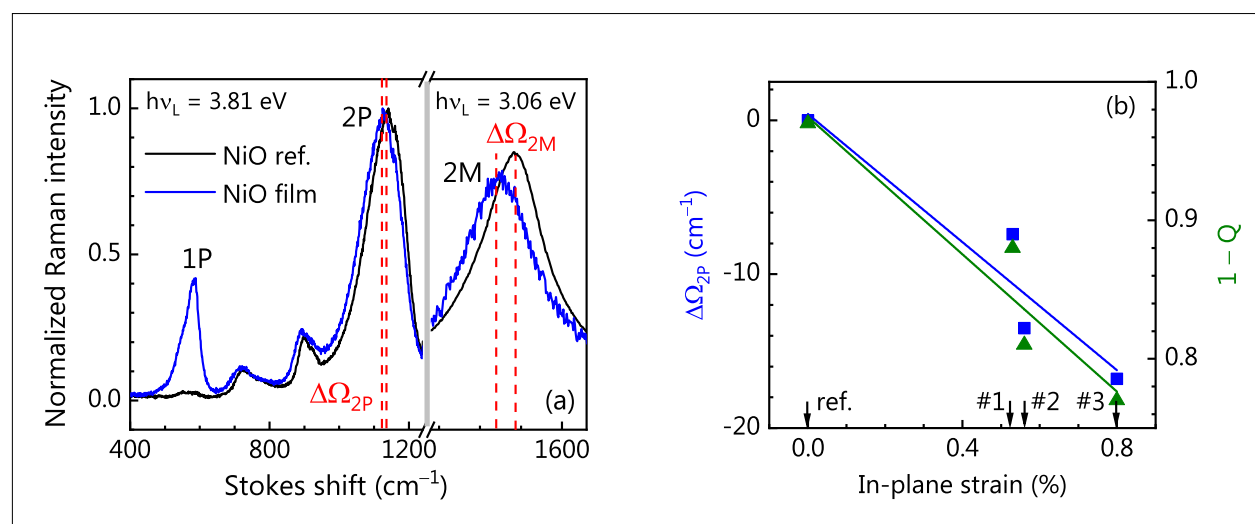
NiO is one of the rare transparent oxides (bandgap around 3.7 eV), which can be utilized as a *p*-type semiconductor. Furthermore, as one of the most common antiferromagnetic oxides (Néel temperature of  $T_N = 523$  K), NiO is of interest for both fundamental studies and spintronic applications. NiO has a rock salt structure with ferromagnetic alignment of the magnetic moments in each {111} plane and antiferromagnetic coupling between neighboring {111} planes. However, in NiO thin films (NTF) synthesized by various methods, the antiferromagnetic coupling is commonly modified and often deteriorated by disorder and strain.

Here, we utilize Raman spectroscopy to study the magnetic characteristics of NTFs on MgO(100) substrates. The investigat-

ed samples are grown by plasma-assisted molecular beam epitaxy at substrate temperatures covering a large range: sample #1 at 700 °C, sample #2 at 200 °C, and sample #3 at 20 °C. As a consequence, the biaxial strain in the NTFs determined by x-ray diffraction reciprocal space mapping is found to increase with decreasing substrate temperature. Details about the growth and structural characterization have already been published [M. Budde et al., J. Appl. Phys. **123**, 195301 (2018)].

The structural properties of the NTFs are investigated using Raman scattering by optical phonons. Figure 1(a) displays room temperature Raman spectra of sample #3 and a reference bulk NiO sample (with nearly perfect structural quality). For the lower frequency range (up to 1220 cm<sup>-1</sup>),

**Fig. 1.** (a) Room temperature Raman spectra of sample #3 and a reference bulk NiO sample excited at 3.81 eV (lower frequency range) and 3.06 eV (frequency range above 1220 cm<sup>-1</sup>). (b) Frequency shift of the 2P Raman peak  $\Delta\Omega_{2P}$  as well as the deviation from the perfect crystal structure  $1 - Q$  for bulk NiO (ref.) and all three NTFs (samples #1, #2, #3) as a function of the in-plane strain.

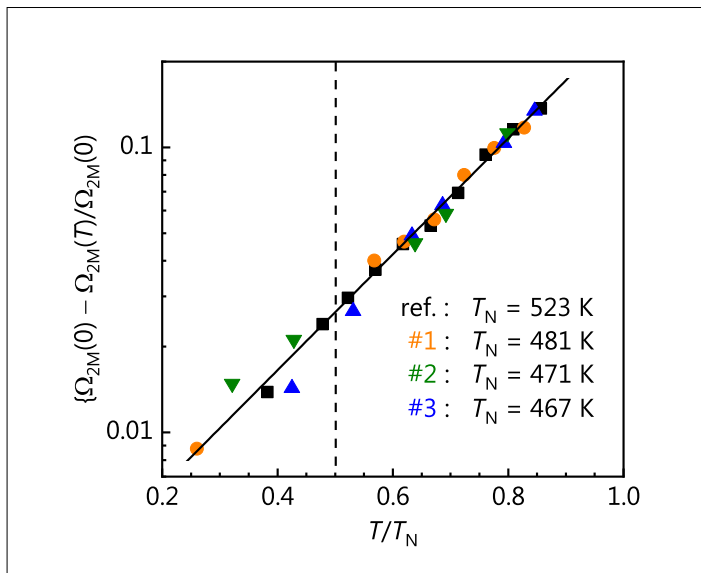


optical excitation at 3.81 eV close to the NiO bandgap is used. This condition enables a high sensitivity for optical-phonon scattering due to resonance-enhanced Raman scattering. Since first-order Raman scattering by optical phonons is forbidden for the rock salt structure, the spectrum of bulk NiO exhibits only peaks due to second-order phonon scattering at 730, 900, and 1130 cm<sup>-1</sup> (2P). In contrast, the NTF reveals also first-order Raman scattering at 580 cm<sup>-1</sup> (1P). As a further deviation from the spectrum of bulk NiO, the 2P peak of the NTF is shifted to lower frequencies. This redshift  $\Delta\Omega_{2P}$  is attributed to biaxial strain in the NTF. Indeed,  $\Delta\Omega_{2P}$  exhibits a monotonic dependence on the experimentally determined tensile in-plane strain (x-ray diffraction reciprocal space mapping) as shown in Fig. 1(b). The quality index  $Q = I_{1P}/I_{2P}$  is an inverse figure of merit for the crystal quality [M. Budde et al., J. Appl. Phys. **123**, 195301 (2018)], where  $I_{1P}$  and  $I_{2P}$  denote the intensi-

ty of the 1P and 2P Raman peak, respectively. Note that  $Q = 0$  corresponds to NiO with perfect rock salt ordering. We can then use the observation of the first-order Raman peak in the NTF to define the deviation from the perfect crystal structure as  $1-Q$ , which exhibits nearly the same dependence on the in-plane strain as shown in Fig. 1(b).

Temperature-dependent second-order Raman scattering by magnons is utilized to study the magnetic properties of the NTFs. For this purpose, non-resonant optical excitation at 3.06 eV is used in order to suppress the relative contribution of second-order phonon scattering. The corresponding room temperature Raman spectra shown in Fig. 1(a) clearly show the presence of the two-magnon peak (2M) at about 1450 cm<sup>-1</sup> both, for the bulk NiO sample and sample #3. Note that, for nanosized NiO prepared for example by a plasma synthesis, no 2M peaks could be resolved in the Raman spectra at room temperature [N. Mironova-Ulmane et al., J. Phys. Conf. Ser. **93**, 012039 (2007)] and, therefore, no signature of antiferromagnetism could be observed. However, the intensity of the 2M peak of the present NTF is reduced, and its position is shifted by  $\Delta\Omega_{2M}$  to lower frequencies. Both findings are explained by a reduction in the antiferromagnetic coupling via superexchange interaction. Another important characteristic of an antiferromagnet is  $T_N$ . In order to introduce our method to determine  $T_N$  for NTFs, we show in Fig. 2 the relative shift of the 2M peak  $[\Omega_{2M}(0) - \Omega_{2M}(T)] / \Omega_{2M}(0)$  for bulk NiO and the three NTFs as a function of the reduced temperature  $T / T_N$ . In the range  $0.5 \leq T / T_N \leq 1.0$ , all data points follow the function  $A \exp(cT/T_N)$  with constant values for  $A$  and  $c$ . This common relationship has been demonstrated previously for different antiferromagnets [R. E. Dietz et al., Phys. Rev. B **4**, 2302 (1971)]. Within our approach, we first determine the parameters  $A$  and  $c$  by fitting the data of the reference bulk sample, keeping the well-known value of  $T_N = 523$  K fixed. The obtained values  $A$  and  $c$  are then used for the fits of the

**Fig. 2.** Relative frequency shift of the 2M peak  $[\Omega_{2M}(0) - \Omega_{2M}(T)] / \Omega_{2M}(0)$  for bulk NiO (ref.) and the NTFs (samples #1, #2, #3) as a function of the reduced temperature  $T / T_N$ . The values of  $T_N$  for the three NTFs have been determined as described in the text. The solid line represents the function  $A \exp(cT/T_N)$  with  $A = 2.54 \times 10^{-3}$  and  $c = 4.68$ .



data from the three NTFs with  $T_N$  as the only free parameter. The obtained values of  $T_N$  for the three NTFs are included in Fig. 2. With our approach, we are able to establish a very reliable method for the determination of the Néel temperature in NTFs by Raman spectroscopy.

In order to correlate the structural and magnetic properties of the NTFs, we show in Fig. 3(a) the shift of the low-temperature 2M peak frequency  $\Delta\Omega_{2M}^0$  as well as the shift of the Néel temperature  $\Delta T_N$  as a function of the in-plane strain. The nearly linear relationship found for both quantities reveals the dependence of the magnetic characteristics on the structural properties of the NTFs. Since both,  $\Omega_{2M}^0$  and  $T_N$ , are proportional to the antiferromagnetic exchange constant  $J$ , a monotonic relationship with lattice strain, i. e. atomic distances, is expected. However, comparing our results with those obtained for bulk NiO by measurements under hydrostatic pressure [M. J. Massey et al., Phys. Rev. B **42**, 8776 (1990)], our data shown in Fig. 3(a) are difficult to explain by biaxial strain alone. In particular, the shift of  $T_N$  is much larger than expected. For NiO with perfect rock salt ordering, a constant ratio  $\hbar\Omega_{2M}^0 / k_B T_N$  is maintained also under hydrostatic pressure. As shown in Fig. 3(b), the ratio  $\hbar\Omega_{2M}^0 / k_B T_N$  of the NTFs strongly deviates from the expected value. Since also the quality factor exhibits a linear relationship with the in-plane strain [cf. Fig. 1(a)], we conclude that also lattice disorder contributes to the decrease in the

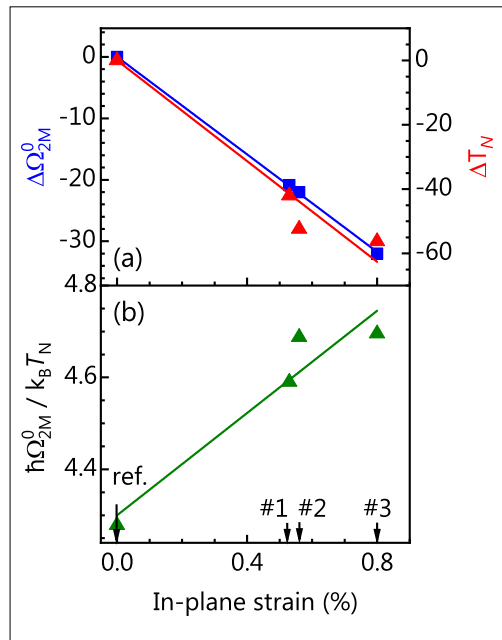


**Fig. 3.** (a) Shift of the low-temperature 2M peak frequency  $\Delta\Omega_{2M}^0$  as well as shift of the Néel temperature  $\Delta T_N$  for bulk NiO (ref.) deviation from the perfect crystal structure and all three NTFs (samples #1, #2, #3) as a function of the in-plane strain. (b) Ratio  $\hbar\Omega_{2M}^0 / k_B T_N$  for bulk NiO (ref.) and all three NTFs (samples #1, #2, #3) as a function of the in-plane strain.

antiferromagnetic exchange constant  $J$ . The tetragonal distortion induced by the biaxial strain might be a further contribution. Finally, our results demonstrate the impact of both biaxial strain and lattice disorder (and/or lattice distortion) on the magnetic characteristics of epitaxial NiO thin films.

# Metastable $\text{FeGe}_2$ thin films as interlayers in vertical spin valve structures: Room temperature anisotropic magnetoresistance

D. Czubak, S. Gaucher, J. Herfort, H. T. Grahn, M. Ramsteiner

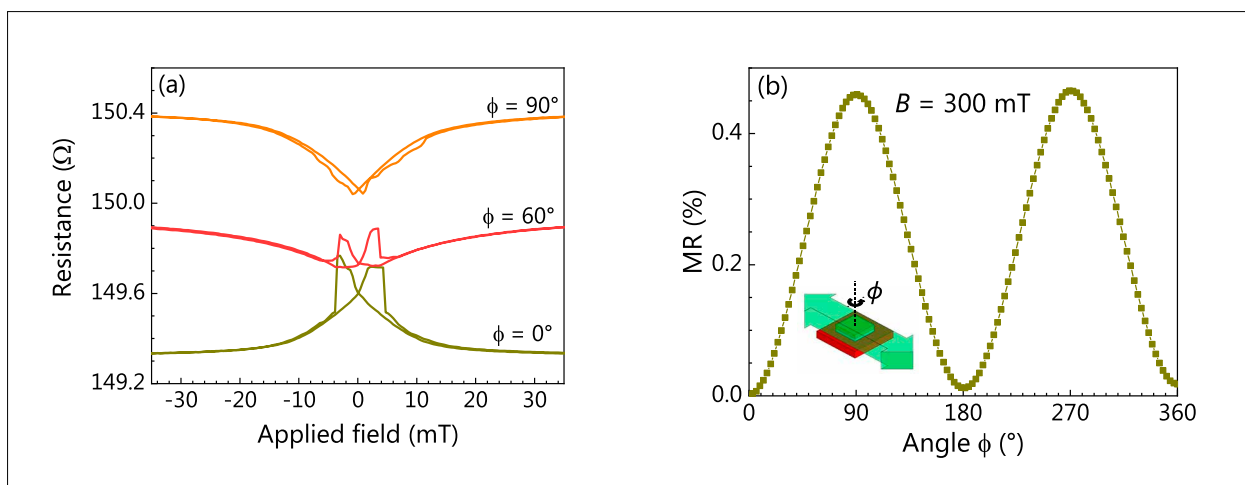
The synthesis of the metastable material  $\text{FeGe}_2$  with a layered tetragonal structure (space group  $P4mm$ ) by solid-phase epitaxy enables the exploration of its so far unknown physical properties at ambient conditions. For the more studied counterpart  $\alpha\text{-FeSi}_2$ , a wide tunability of the electronic and magnetic properties has been predicted with nonmetallic transport and ferromagnetism being observed in strain-stabilized thin films [G. Cao *et al.*, Phys. Rev. Lett. **114**, 147202 (2015)]. With a similar tunability of the physical properties,  $\text{FeGe}_2$  films might be utilized both as ferromagnetic electrodes and tunnel barriers for spintronic applications.

Here, we study the potential and the characteristics of  $\text{FeGe}_2$  films as interlayers between ferromagnetic electrodes in vertical

spin valves. The  $\text{Fe}_3\text{Si}$  and  $\text{Co}_2\text{FeSi}$  films grown by molecular beam epitaxy on semi-insulating  $\text{GaAs}(001)$  substrates are used as the bottom (FM1) and top (FM2) ferromagnetic electrodes. For the fabrication of the spin valve devices, photolithography and reactive wet etching are used to define quadratic pillars with a surface area of  $1 \mu\text{m}^2$ . For the magnetoresistance measurements, the device resistance is measured with a fixed current of 1 mA.

Figure 1(a) displays the resistance of a vertical spin valve with  $\text{Fe}_3\text{Si}$  (FM1) and  $\text{Co}_2\text{FeSi}$  (FM2) electrodes as a function of an external magnetic field  $B$  swept in different directions. Thereby,  $\Phi = 0^\circ$  and  $90^\circ$  correspond to orthogonal  $\langle 110 \rangle$  directions in the surface of the  $\text{GaAs}(001)$  substrate. In all cases, extrema in the resistance are

**Fig. 1.** (a) Room-temperature resistance of a vertical spin valve with  $\text{Fe}_3\text{Si}$  (FM1) and  $\text{Co}_2\text{FeSi}$  (FM2) electrodes as a function of an external magnetic field  $B$  swept in different directions ( $\Phi = 0^\circ$  and  $90^\circ$  correspond to orthogonal  $\langle 110 \rangle$  directions). (b) Magnetoresistance  $\text{MR}(\Phi) = [R(0^\circ) - R(\Phi)]/R(0^\circ)$  measured for  $B = 300$  mT as a function of the angle  $\Phi$ .



observed, which are characteristics for spin valve operations. The magnetoresistance at  $\Phi = 0^\circ$  exhibits the commonly detected maxima as a signature of the switching from parallel to antiparallel magnetization of the electrodes FM1 and FM2. In contrast, resistance minima are observed for  $\Phi = 90^\circ$ . This behavior resembles the one reported for vertical spin transport through Fe/GaAs/Au structures, which has been explained by a tunneling anisotropic magnetoresistance (TAMR) induced by an interference of Bychkov-Rashba spin-orbit coupling (SOC) at the Fe/GaAs interface and the Dresselhaus (SOC) in GaAs [Y. Moser et al., Phys. Rev. Lett. **99**, 056601 (2007)]. In order to verify a possible contribution of TAMR to the magnetoresistance in our spin valve structures, we measured the angular dependence of the magnetoresistance at a magnetic-field strength  $B$ , where the magnetizations of the electrodes FM1 and FM2 are forced to follow the direction of the magnetic field. The resulting magnetoresistance shown in Fig.1(b) clearly reveals an uniaxial asymmetry in agreement with the TAMR effect reported for Fe/GaAs/Au system. Since the angular dependence shown in Fig.1(b) differs from that of the anisotropic magnetoresistane in the bottom Fe<sub>3</sub>Si electrode, we attribute the angle-dependent spin transport phenomena in our vertical spin valve structures to a TAMR effect induced by the FeGe<sub>2</sub> interlayer. Since TAMR-based devices can be operated with a single magnetic lead, FM1/FeGe<sub>2</sub> structures are promising candidates for enabling new spintronic functionalities.

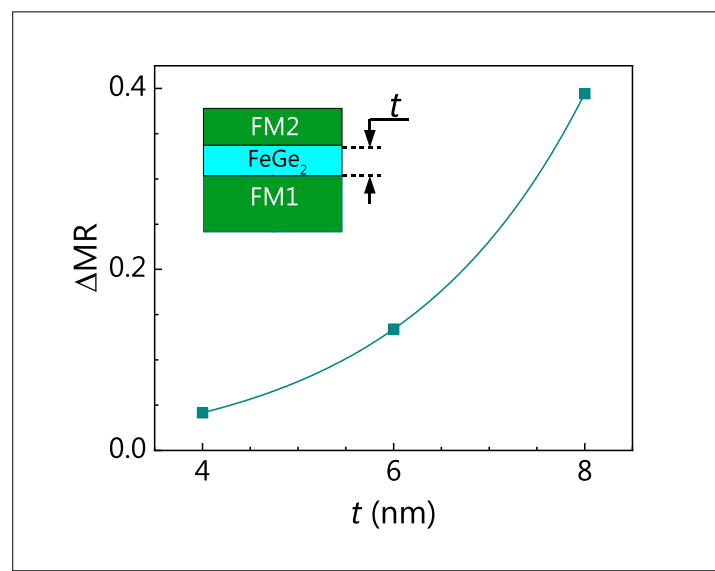
The assumed tunneling process included in this assignment implies a nonmetallic characteristic of the thin FeGe<sub>2</sub> film. Tunneling as the transport mechanism through the FeGe<sub>2</sub> film is also confirmed by spin valve measurements using different FeGe<sub>2</sub> interlayer thicknesses. As shown in Fig.2, the spin valve signal  $\Delta MR$  does not decrease with increasing FeGe<sub>2</sub> film thickness so that spin relaxation processes in the interlayer can be excluded. Furthermore, the increase

of  $\Delta MR$  even indicates a spin filtering behavior during the tunneling process through the FeGe<sub>2</sub> film.

In contrast to the behavior in conventional devices, the spin valve signals in our FM1/FeGe<sub>2</sub>/FM2 structures decrease when lowering the temperature, as illustrated in Fig.3(a) for  $\Phi = 0^\circ$ . At 20 K, the magnitude of the magnetoresistance peak is reduced by a factor of 5 as compared to room temperature. It is tempting to assume that the decrease in the spin valve signals is related to the fact that FeGe<sub>2</sub> films become ferromagnetic at temperatures below 200 K. In order to verify this relationship, we display in Fig.3(b) the temperature dependence of the spin valve signals  $\Delta MR$  for  $\Phi = 0$  and  $90^\circ$ . Indeed, these signals closely follow the remanent magnetization of a FeGe<sub>2</sub> film determined experimentally.

Consequently, we explain the suppression of the spin valve signals in our structures FM1/FeGe<sub>2</sub>/FM2 by the paramagnetic-to-ferromagnetic phase transition occurring around 200 K. This result demonstrates that magnetoresistance measurements

**Fig. 2.** Spin valve signal  $\Delta MR$  for  $\Phi = 0^\circ$  as a function of the FeGe<sub>2</sub> film thickness  $t$ .



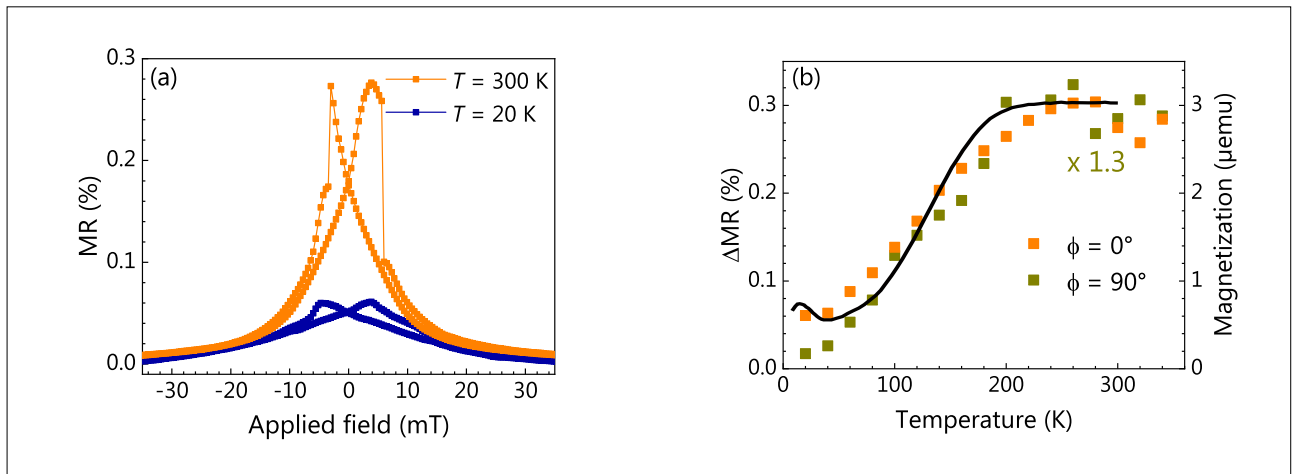


**Fig. 3.** (a) Magnetoresistance of a vertical spin valve with  $\text{Fe}_3\text{Si}$  (FM1) and  $\text{Co}_2\text{FeSi}$  (FM2) electrodes as a function of an external magnetic field ( $\Phi = 0^\circ$ ) measured at 300 and 20 K. (b) Temperature dependence of the spin valve signal  $\Delta\text{MR}$  for  $\Phi = 0^\circ$  and  $90^\circ$  together with the magnetization of a  $\text{FeGe}_2$  film determined by superconducting-quantum-interference device magnetometry.

can be utilized to extract the magnetization behavior of  $\text{FeGe}_2$  films incorporated in a magnetic trilayer structure, which is otherwise difficult to accomplish. The influences of ferromagnetism in semiconducting or insulating interlayers on the characteristics of vertical spin valves can be explained by cal-

culations based on the nearly-free-electron approximation [Y. Li *et al.*, Phys. Rev. B **57**, 1079 (1998)]. Finally, it is important to note that experimental evidence for room temperature in-plane TAMR has not been reported so far for other semiconducting or insulating interlayers.

# Quantum point contacts meet open resonators

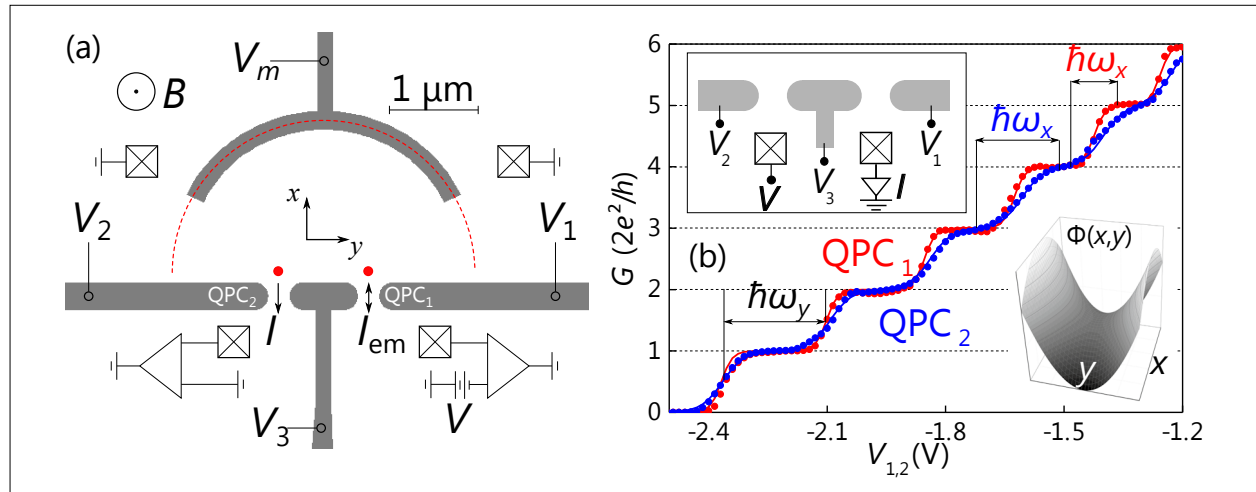
J. Freudenfeld, V. Umansky<sup>1</sup>, S. Ludwig

Quantum point contacts (QPC) are fundamental building blocks of envisioned integrated quantum circuits. We study the coupled system of two QPCs and an elliptic mirror shaping an open cavity in the ballistic and coherent regime. In such a system, the quantum mechanical phase represents an additional degree of freedom that can be used to encode information, as required for quantum information applications.

The nanostructure is defined electrostatically within a two-dimensional electron system (2DES) residing 110 nm below the surface of a high-mobility GaAs/(Al,Ga)As heterostructure by applying negative voltages to the metallic gates depicted in Fig. 1(a). Ballistic transport conditions are met, as the cavity dimensions are much smaller than the measured elastic mean free path,  $l_m = 52 \mu\text{m}$ . To characterize the

QPCs, we apply a gate voltage  $V_3 = -1.5 \text{ V}$  depleting the 2DES below the gate and measure the pinch-off curves for  $\text{QPC}_{1,2}$  separately,  $G(V_{1,2}) = I(V_{1,2})/V$  [plotted in Fig. 1(b) after subtraction of the lead resistance]. Both QPCs feature conductance steps at  $G = N2e^2/h$  with  $e$  denoting the elementary charge,  $h$  the Planck constant, and  $N = 1,2,3,\dots$ , reflecting the one-dimensional conductance quantization. Fitting the curves using the transmission formula of a saddle point potential including a finite anharmonicity allows us to gain information about the QPC potentials: the plateau spacings of both QPCs indicate an almost identical lateral confinement in the  $y$ -direction (step size  $\hbar\Omega_y$ ). The confinement potentials are almost perfectly harmonic (parabolic) with an anharmonicity of less than 4%. Consequently, the electronic eigenfunctions of the QPCs can be approxi-

**Fig. 1.** (a) Sketch of the sample: gray areas indicate metallic nanostructures on the sample surface. Negative voltages  $V_{1,2,3,m}$  are used to electrostatically define  $\text{QPC}_{1,2}$  and the elliptic mirror in the 2DES 110 nm below the surface. The red dashed line emphasizes the elliptic shape of the mirror with its two focal points close to the QPCs (red dots). Crossed squares indicate ohmic contacts. (b) Colored dots: measured quantized conductance for  $\text{QPC}_{1,2}$ ,  $G(V_{1,2}) = I(V_{1,2})/V$  with  $V_3 = -1.5 \text{ V}$  and  $V = -0.1 \text{ mV}$  (see top left inset). Lines are fits assuming a parabolic saddle potential (illustrated in the bottom right inset) including a slight anharmonicity.



<sup>1</sup> Department of Condensed Matter Physics, Weizmann Institute of Science, Rehovot 7610001, Israel

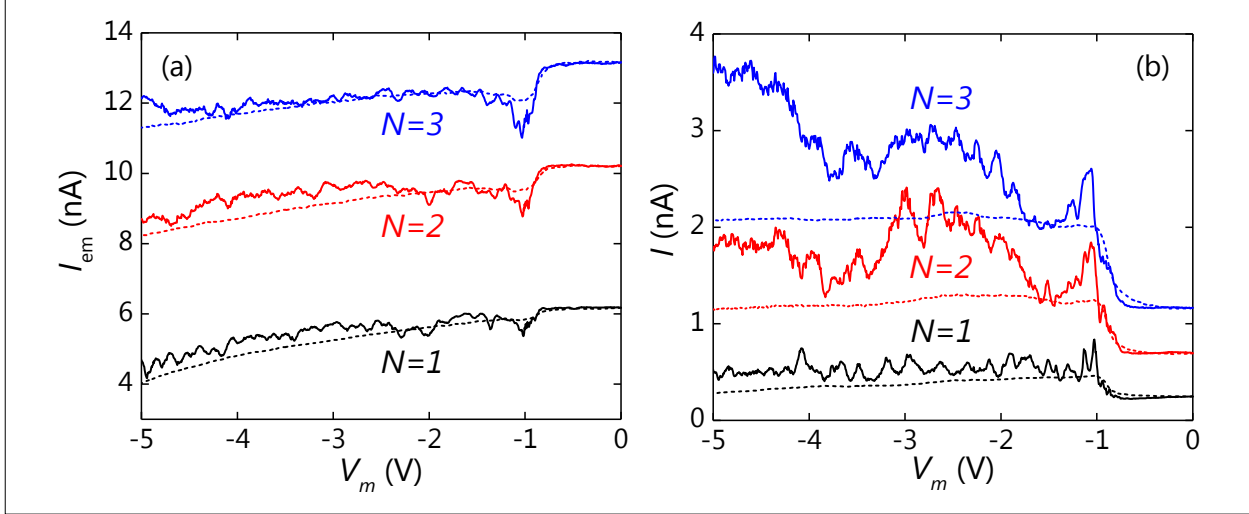


**Fig. 2.** (a)  $I_{em}(V_m)$  through the emitter QPC<sub>1</sub> and (b)  $I(V_m)$  through the detector QPC<sub>2</sub> with both QPCs tuned to  $G_1 = G_2 = N2e^2/h$  and  $N = 1, 2$ , and  $3$ . Solid lines are data for a temperature of 280 mK, dashed lines are for 10 K.

mated by the well known Hermite functions giving rise to Gaussian electron beams. Slightly wider transitions between adjacent plateaus ( $\hbar\Omega_x$ ) indicate a steeper potential barrier in the current ( $x$ -) direction for QPC<sub>2</sub> compared to QPC<sub>1</sub>.

To study the interplay of the QPCs coupled via an elliptic mirror, we define a cavity by applying a gate voltage  $V_m$  depleting the 2DES below the mirror gate, cf. Fig. 1(a). The two focal points of the elliptic mirror are located close to the QPCs (red dots). We apply a source-drain voltage  $V = -0.1$  mV at the emitter contact, causing a current  $I_{em}(V_m)$  such that electrons flow through the emitter QPC<sub>1</sub> into the cavity. Inside the cavity, electrons can scatter from the elliptic mirror and the QPC gates, before they either traverse the detector QPC<sub>2</sub> contributing to  $I(V_m)$ , backscatter into the emitter QPC<sub>1</sub>, or leave the cavity to the grounded side contacts. In Figs. 2(a) and 2(b), we plot  $I_{em}(V_m)$  and  $I(V_m)$ , respectively, where both QPCs are set to the same conductance  $G_1 = G_2 = N2e^2/h$  with  $N = 1, 2$ , or  $3$  at 280 mK (solid lines) and 10 K (dashed lines). For moderate voltages ( $-0.9 \leq V_m \leq -0.1$  V), the mirror gate is transparent for electrons, while for  $V_m \leq -1$  V the 2DES below the gate

is depleted and an open cavity including the two QPCs is formed. For more negative values of  $V_m$ , the depleted area below the mirror gate increases, giving rise to a smaller cavity size with a larger resistance such that  $I_{em}(V_m)$  decreases, cf. data for 10 K in Fig. 2(a). The detector current  $I(V_m)$  increases sharply at the formation of the cavity, indicating an enhanced coupling by ballistic electrons between the two QPCs. As the temperature is lowered to 280 mK, additional reproducible fine structures occur in both signals, which are caused by coherent resonator modes. We interpret an additional increase of  $I(V_m)$  for  $N > 1$  and  $V_m < -1.5$  V as coherent focusing, indicating an enhanced coupling between the QPCs for specific cavity modes.

Finally, we study the dependence of the cavity modes on a magnetic field applied perpendicular to the plane of the 2DES. In Fig. 3(a), we present  $I_{em}(V_m, B)$  for  $N = 2$ . The pattern is symmetric around  $B = 0$ , confirming the Onsager relations. Beyond the depletion point  $V_m \leq -1$  V, where  $I_{em}(V_m, B)$  decreases, it establishes a pronounced minimum around  $B = 0$  [red line in red line in Figs. 3(a) and 2(a)] which can be explained in terms of cavity-induced weak localiza-

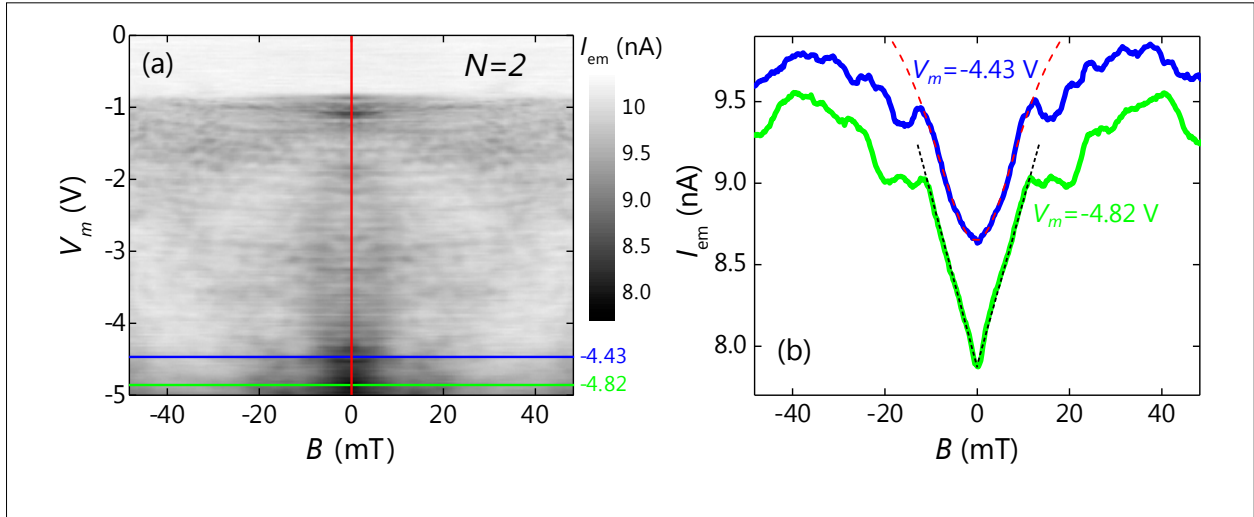


**Fig. 3.** (a)  $I_{\text{em}}$  for  $N = 2$  at 280 mK as a function of the perpendicular magnetic field  $B$  and  $V_m$ . The red line along  $I_{\text{em}}(B = 0, V_m)$  corresponds to the red line in Fig. 2(a). (b) Line cuts of  $I_{\text{em}}(B)$  as indicated in (a) for  $V_m = -4.43$  V (blue line) and  $V_m = -4.82$  V (green line). The red dashed line is a Lorentzian fit to the weak localization feature indicating chaotic cavity modes (see text). The black dashed lines are a guide to the eye highlighting the linear weak localization feature indicating non-chaotic cavity modes.

tion. The characteristic  $I_{\text{em}}(B)$  dependence reflects the nature of scattering inside the cavity. It allows to distinguish between a chaotic and a deterministic scattering dynamics inside the cavity. In particular, it has been shown that the weak localization feature exhibits a Lorentzian shape for chaotic cavities, whereas deterministic cavities give rise to a triangular lineshape [A. M. Chang *et al.*, Phys. Rev. Lett. **73**, 2111 (1994)]. As demonstrated in Fig. 3, our tunable structure permits to switch between chaotic and deterministic behavior: for  $V_m = -4.43$  V [blue line in Fig. 3(a)], we find a Lorentzian  $I_{\text{em}}(B)$  profile indicating chaotic behavior [blue line in Fig. 3(b)] with red dashed Lorentzian fit curve]. However, as we further decrease the cavity size, the weak localization feature at  $V_m = -4.82$  V [green line in Fig. 3(a)] clearly shows a V shape, pointing

to a deterministic cavity regime [green line in Fig. 3(b) with black dashed line as guide for the eyes]. The transition from chaotic to deterministic behavior is expected when the focal points of the ellipse are pushed behind the QPCs (outside the cavity). By decreasing  $V_m$ , we increase the depletion area beneath the mirror gate and thereby move the effective mirror position and its focal points towards the QPCs and beyond [cf. Fig. 1(a)].

In summary, we have presented two QPCs coupled via an elliptic cavity. Both the emitter and the detector QPC currents indicate coherent ballistic modes inside the cavity. The magnetic-field dependence additionally reveals a transition from chaotic to deterministic cavity behavior depending on the effective mirror position.

# Coaxial GaAs/(In,Ga)As dot-in-a-well nanowire heterostructures for electrically driven infrared light generation on Si in the telecommunication O band

J. Herranz, P. Corfdir, E. Luna, U. Jahn, R. B. Lewis, L. Schrottke, J. Lähnemann, A. Tahraoui, A. Trampert, O. Brandt, and L. Geelhaar

GaAs-based core-shell nanowires (NW) monolithically integrated on Si constitute a promising class of nanostructures that could enable light emitters for fast inter- and intrachip optical connections. Here we introduce and demonstrate a novel coaxial GaAs/(In,Ga)As dot-in-a-well (DWELL) NW heterostructure to reach spontaneous emission in the transparent region of Si, which is crucial for such applications. Our approach combines the NW geometry for integration on Si substrates with the DWELL heterostructure that enables to shift the emission to longer wavelengths, demonstrating a new functionality by integrating quantum dots (QD) into NWs.

The samples studied in this work were grown by molecular beam epitaxy (MBE) on Si(111) substrates. The coaxial DWELL heterostructure was formed around GaAs NWs with a diameter of about 100 nm and consists of an InAs QDs shell embedded in a 9 nm-thick  $In_{0.15}Ga_{0.85}As$  quantum well (QW) shell. To promote QD formation, a Bi flux was supplied during the deposition of InAs [R. B. Lewis *et al.* *Nano Lett.* **17**, 4255–4260 (2017)].

The presence of QDs in the heterostructure is evidenced by a structural analysis based on scanning transmission electron microscopy (STEM). Figure 1(a) shows a micrograph acquired using the scanning high-angle annular dark field (HAADF) mode. Electron scattering is determined by the atomic number Z. The NW exhibits a clear hexagonal cross-section defined by {110} side facets and the coaxial active region is clearly visible in the HAADF micrograph. An

enlarged, false-color micrograph of the facet marked by the dashed box in Fig. 1(a) is presented in Fig. 1(b) to illustrate the presence of QDs in the DWELL heterostructure. The yellow areas indicate higher HAADF intensity, corresponding to a locally enhanced In composition within the projected volume, which can be attributed to the QDs.

In addition, we investigate the spontaneous emission of the DWELL NWs by photoluminescence (PL) spectroscopy from 10 to

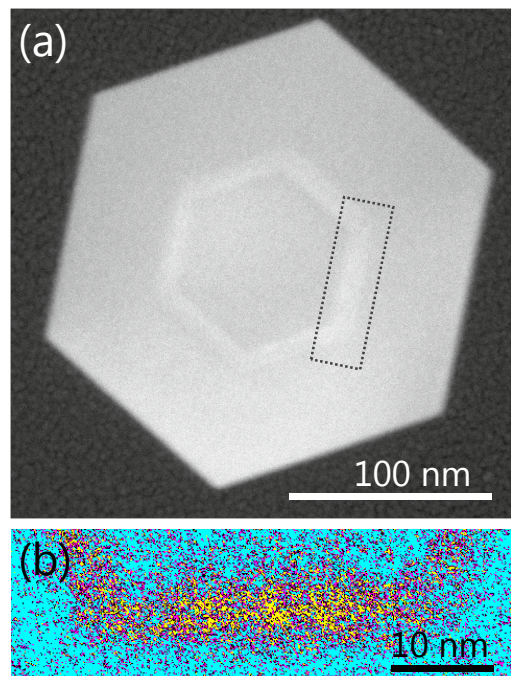


**Fig. 1.** (a) Plan-view HAADF STEM micrograph of a DWELL NW. (b) Enlarged, false color, baseline corrected HAADF STEM micrograph of the facet indicated by the grey box in (a).

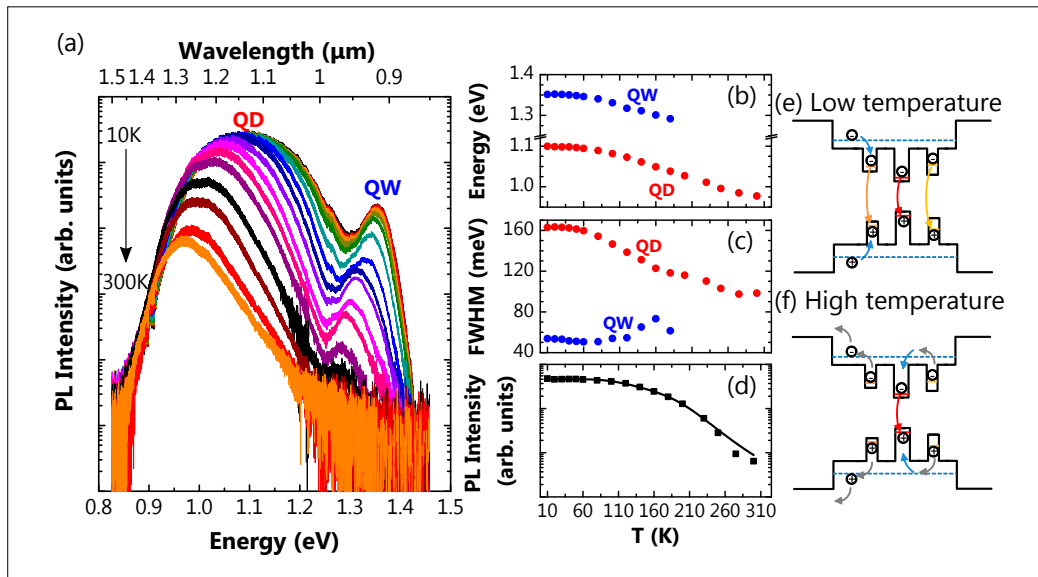


**Fig. 2.** (a) PL spectra of a DWELL NW ensemble measured from 10 to 300 K. (b) Peak emission energy, (c) FWHM and (d) integrated intensity ( $I_{PL}$ ) of the DWELL NWs as a function of temperature. The black solid curve in (d) is a fit of the experimental data to the phenomenological model described in the text. (e, f) Schematics of the main recombination processes at low (e) and high (f) temperature. These schematic band diagrams include the QW energy level (blue line) and three different energy levels for QDs representing variations of size and/or In content.

300 K, as presented in Figure 2. We observe two different emission bands: a high energy component (1.35 eV at 10 K) originating from QW transitions and a low energy component (1.10 eV at 10 K) attributed to QD transitions. The attribution to QD emission is supported by cathodoluminescence (CL) spectroscopy that shows sharp, spatially localized spectral features, as well as by low temperature PL spectra of few (2-3) NWs which exhibit spectral lines with widths below 1 meV.

The evolution with temperature of the peak emission energy, full width at half maximum (FWHM) for the QW and QD bands as well as the integrated PL intensity ( $I_{PL}$ ) integrated over the full spectral range are summarized in Figs. 2(b), 2(c) and 2(d), respectively. With increasing temperature, the low energy QD component shows a strong redshift to 0.97 eV at 300 K. Simultaneously, the FWHM is reduced from 162 meV at

10 K to 104 meV at 300 K. In contrast, the FWHM of the high energy QW component increases from 53 meV at 10 K to 71 meV at 160 K. The  $I_{PL}$  decreases with increasing temperature by about two orders of magnitude. We analyze this variation with a simple phenomenological model considering two non-radiative channels for charge carriers. A fit of the experimental data results in the activation energies for the non-radiative channels  $E_1 = (44 \pm 5)$  meV and  $E_2 = (188 \pm 37)$  meV. The activation energy  $E_2$  is comparable to the energy difference between the QW and QD bands and, therefore, points to the thermal escape of carriers from the QDs to the QW. This finding along with the narrowing and the strong redshift of the emission, as well as the fact that the thermal quenching is moderate compared to the four orders of magnitude intensity reduction observed for standard (In,Ga)As/GaAs shell QW NWs suggest a thermal redistribution of charge carriers

in the QDs of the DWELL heterostructure, which is well established for planar DWELL heterostructures.

The carrier redistribution processes are schematically presented in Figs. 2(e) and 2(f). At low temperature, the charge carriers populate both QD and QW levels and recombine mostly radiatively, thus contributing to the broad PL spectrum. With increasing thermal energy, charge carriers can escape shallow energy levels of smaller QDs and undergo non-radiative recombination, as observed by the quenching of the PL intensity above 160 K, or are recaptured in larger QDs with deeper energy levels, which manifests itself in the narrowing and redshift of the emission. The deeper confinement in larger QDs provides protection from non-radiative recombination centers and explains the enhanced room temperature emission as well as the longer emission wavelength. At room temperature, the emission is dominated by the QD component and the peak emission wavelength of these DWELL NWs is 1.27  $\mu\text{m}$ , thus reaching the telecommunication O band (1.26–1.36  $\mu\text{m}$ ).

In order to demonstrate the feasibility of the presented DWELL NWs as electrically driven light emitters on a Si platform, we fabricated light emitting diodes (LED) from self-assembled ensembles of DWELL NWs with a radial *p-i-n* junction. The electroluminescence (EL) spectrum of a DWELL NW LED measured at room temperature

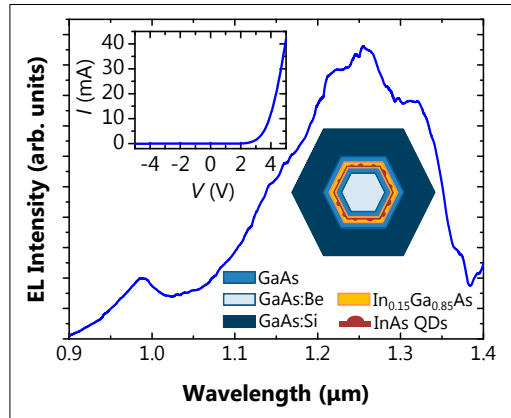


**Fig. 3.** Room-temperature EL spectrum of 300  $\mu\text{m}$  diameter DWELL NW LED driven at 19 mA. The current-voltage ( $I$ - $V$ ) characteristic of the DWELL NW LED and a cross-sectional schematic of the DWELL NWs with radial *p-i-n* junction are included as insets.

at an injected current of 19 mA is presented in Fig. 3. The emission band peaks at 1.26  $\mu\text{m}$ , consistent with the previously presented characterization of undoped structures. This result demonstrates the room temperature operation of electrically driven light emitters in the telecommunication O band (1.26–1.36  $\mu\text{m}$ ) monolithically integrated on Si and, furthermore, represents an extension of the EL wavelength by more than 100 nm for devices made from GaAs-based NWs or related structures. Therefore, our work opens up new perspectives for Si photonics integration and data communication applications.

# Photoluminescence spectroscopy of GaAs nanowires with a low degree of polytypism

M. Oliva, M. Góra, J. Herranz, M. Ramsteiner, R. B. Lewis, L. Geelhaar, O. Brandt

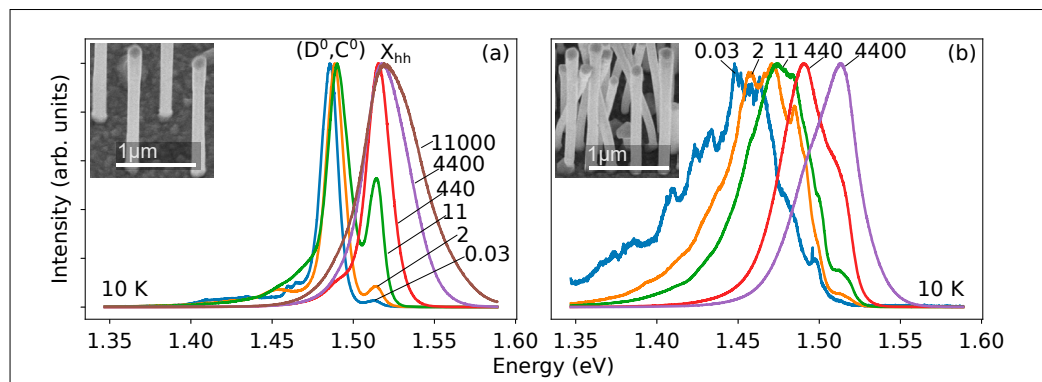
GaAs nanowires (NW) offer several conceptual advantages compared to their planar counterparts, such as the possibility to synthesize them directly on Si substrates, enabling the integration of III-V optoelectronics on the Si platform. However, the vapor-liquid-solid growth of GaAs NWs frequently results in the coexistence of the wurzite and zincblende polytypes of GaAs within the same NW. This phenomenon, known as polytypism, constitutes one of the major obstacles for the use of GaAs NWs in applications, because it has a detrimental impact on both carrier transport and recombination. For example, the vast majority of the reported photoluminescence (PL) spectra of GaAs NWs are dominated by numerous sub-bandgap transitions induced by stacking defects, impeding a detailed understanding of the carrier and exciton dynamics in these GaAs NWs.

In this work, we show that GaAs NWs with a very low degree of polytypism can be reproducibly obtained in ordered arrays of NWs

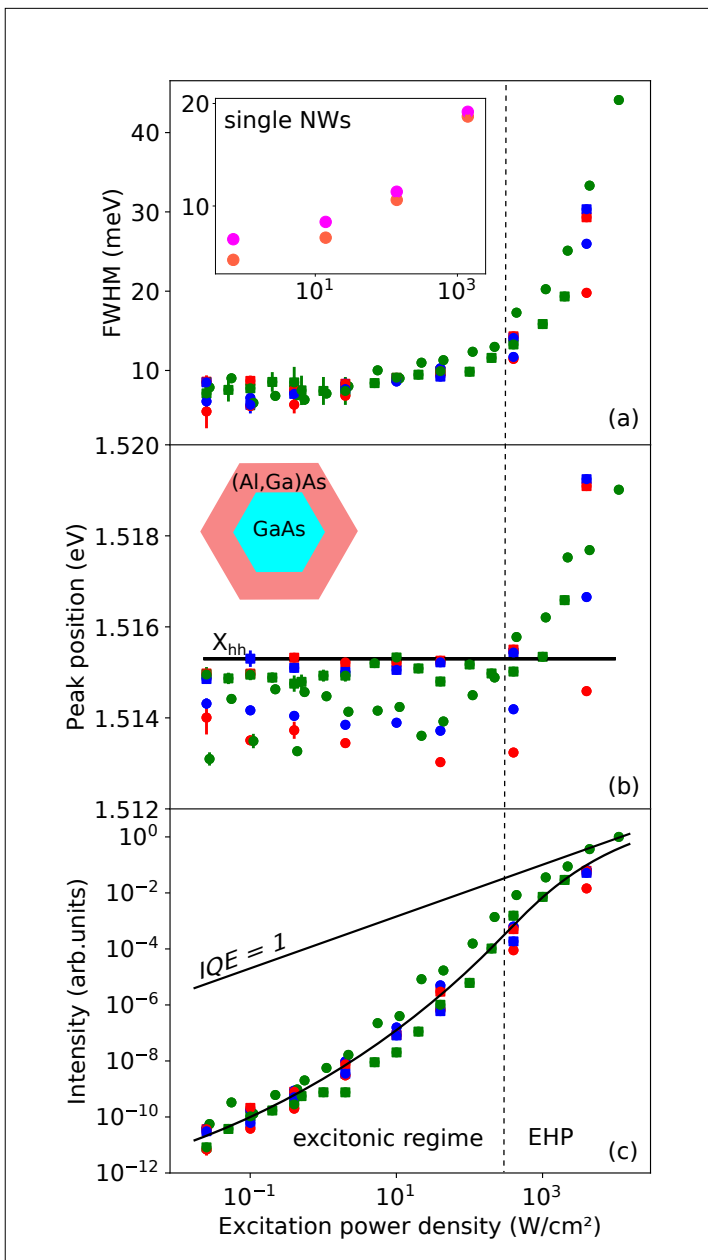
with a certain minimum separation (in our case 0.7  $\mu\text{m}$ ). The samples were fabricated by molecular beam epitaxy on Si(111) substrates covered by a patterned thermal oxide. Ordered arrays of GaAs NWs were selectively grown within  $100 \times 100 \mu\text{m}^2$  microfields, where holes of different sizes and distances (pitch) were previously patterned in the oxide layer by electron beam lithography. Sample A was realized by first growing 4  $\mu\text{m}$  long and 100 nm thick GaAs NWs utilizing the self-assisted vapor-liquid-solid mechanism and an As/Ga flux ratio of 3.9. The GaAs NWs were then passivated with 30 nm thick  $\text{Al}_{0.33}\text{Ga}_{0.67}\text{As}$  shells. Sample B was grown under the same conditions as sample A, but with a shell consisting of 30 nm thick  $\text{Al}_{0.10}\text{Ga}_{0.90}\text{As}$ . The NWs are unintentionally *p*-type doped with C.

Figure 1 depicts low-temperature  $\mu$ -PL spectra excited by a He-Ne laser (632.8 nm) focused to a spot of 3  $\mu\text{m}$  onto two different microfields of sample A with different excitation densities. The selected micro-

**Fig. 1.** Normalized low-temperature (10 K)  $\mu$ -PL spectra of regular arrays of GaAs NWs with (a) 700 and (b) 200 nm pitch on sample A recorded with different excitation densities. The insets show bird's eye view secondary electron micrographs of the respective NW arrays. Each spectrum is labeled with the corresponding excitation density in  $\text{W}/\text{cm}^2$ .



**Fig. 2.** (a) FWHM, (b) spectral position, and (c) integrated intensity of the free  $X_{hh}$  transition of GaAs NWs with a low degree of polytypism versus the excitation density. Circles (squares) correspond to measurements on sample A (B). Green, blue and red data points correspond to ensemble measurements on microfields with a pitch of 700 nm and hole sizes of, respectively, 90, 70, and 50 nm. The solid line at 1.5153 eV in (b) indicates the energy of the  $X_{hh}$  in bulk GaAs. The upper solid line in (c) indicates the case of an IQE of unity, and the lower one is a guide to the eye. The inset in (a) shows the FWHM of the  $X_{hh}$  line for two different single NWs. The inset in (b) depicts a schematic topview of the present core-shell GaAs/(Al,Ga)As NW heterostructure. The vertical dashed line at around 300 W/cm<sup>2</sup> indicates the Mott transition.



fields have the same hole size of 90 nm, but different pitches of 700 and 200 nm [Figs. 1(a) and 1(b), respectively]. The spectra in Fig. 1(a) only exhibit two near-band-edge transitions, also characteristic for epitaxial GaAs layers, namely, the free exciton ( $X_{hh}$ ) and the donor-acceptor-pair transition [(D<sup>0</sup>,C<sup>0</sup>)] related to the presence of C. The dominance of these two lines even at the lowest excitation densities is a strong indication for a high phase purity of the NWs. With increasing excitation density, we observe first a saturation of the (D<sup>0</sup>,C<sup>0</sup>) transition, and then a pronounced band filling and the associated Mott transition from excitonic to electron-hole-plasma (EHP) recombination. In contrast, the continuous shift of the broad band in Fig. 1(b) as well as the pronounced structure at low excitation density are typical features of GaAs NWs affected by a high degree of polytypism. This band of transitions arises from random stacking sequences in the NWs and the resulting localized states with an almost continuous energy variation. Note that even for the highest excitation density, the peak energy of this band does not correspond to that of the  $X_{hh}$ .

Systematic  $\mu$ -PL measurements on both samples A and B demonstrate that spectra similar to those in Fig. 1(a) are obtained for a pitch equal or larger than 700 nm, while all PL spectra from fields with a pitch equal or smaller than 400 nm are dominated by polytypism similar to the spectra in Fig. 1(b). These very different degrees of polytypism occur reproducibly for microfields in immediate vicinity, and are thus caused by the different pitch of the fields. In fact, it is known that the preferred polytype depends on pitch via the shadowing of the Ga flux, with zincblende being favored for larger pitch, and we attribute the higher phase purity observed here to the same effect.

Figures 2(a)–2(c) depict the full width at half maximum (FWHM), the spectral position, and the integrated intensity of the

$X_{hh}$  line, respectively, as a function of excitation density. These quantities were determined by line-shape fits of spectra measured on various microfields on samples A (circles) and B (squares).

Regardless of sample, hole size and pitch, the data are seen to follow the same trends, except for the spectral position of the  $X_{hh}$  line shown in Fig. 2(b). For excitation densities lower than  $300 \text{ W/cm}^2$ , the  $X_{hh}$  line from sample A (B) is redshifted with respect to the  $X_{hh}$  energy in unstrained GaAs (indicated by the horizontal line) by, on average,  $(1.2 \pm 0.3) [(0.3 \pm 0.1)] \text{ meV}$ . These values coincide with the redshift expected from the tensile strain exerted on the GaAs core by the respective  $(\text{Al},\text{Ga})\text{As}$  shell. At the lowest excitation densities, the FWHM of the  $X_{hh}$  line amounts to values of 5–8 meV [see Fig. 2(a)], remarkably narrow compared to the values commonly observed for GaAs NWs, but still rather broad compared to the  $X_{hh}$  line in planar GaAs for which we observe an FWHM of 2 meV. Measurements on single NWs [inset of Fig. 2(a)] yield similar values as measured for the NW arrays, demonstrating that the line broadening is not an ensemble effect.

For excitation densities exceeding  $300 \text{ W/cm}^2$ , the  $X_{hh}$  line is observed to abruptly broaden and blueshift due to the Mott transition from the excitonic regime to an EHP accompanied by a pronounced band filling. The moderate excitation density at which

we observe this transition, which occurs at an exciton density on the order of  $10^{16} \text{ cm}^{-3}$ , implies comparatively long exciton lifetimes in the ns range.

The integrated intensity of the  $X_{hh}$  transition as a function of excitation density exhibits a linear dependence at the lowest and highest densities, joined by a superlinear increase at intermediate ones [Fig. 2(c)]. This superlinear behavior is caused here by two distinct processes: first, by the saturation of the  $(\text{D}^0,\text{C}^0)$  transition for excitation densities between 1 and  $10 \text{ W/cm}^2$  (the intensity integrated over the entire spectrum depends indeed linearly on excitation density up to  $10 \text{ W/cm}^2$ ), and second, by the increasingly bimolecular character of the radiative process between 20 and  $200 \text{ W/cm}^2$ , which thus gains dominance over a competing nonradiative Shockley-Read-Hall (SRH) recombination channel. Eventually, the radiative process takes over, and the intensity approaches the one expected for an internal quantum efficiency (IQE) of unity in the EHP regime. At low excitation densities, the IQE of these GaAs NWs amounts to roughly 1% when integrating over both near-band edge transitions. No difference is observed regarding the IQE of samples A and B despite their different Al contents in the NW shells. This fact suggests that the nonradiative process is not related to interface recombination, but to bulk point defects acting as SRH centers.

# Circumferential and one-sided (In,Ga)N Shells on GaN Nanowires: From self-assembled to ordered arrays

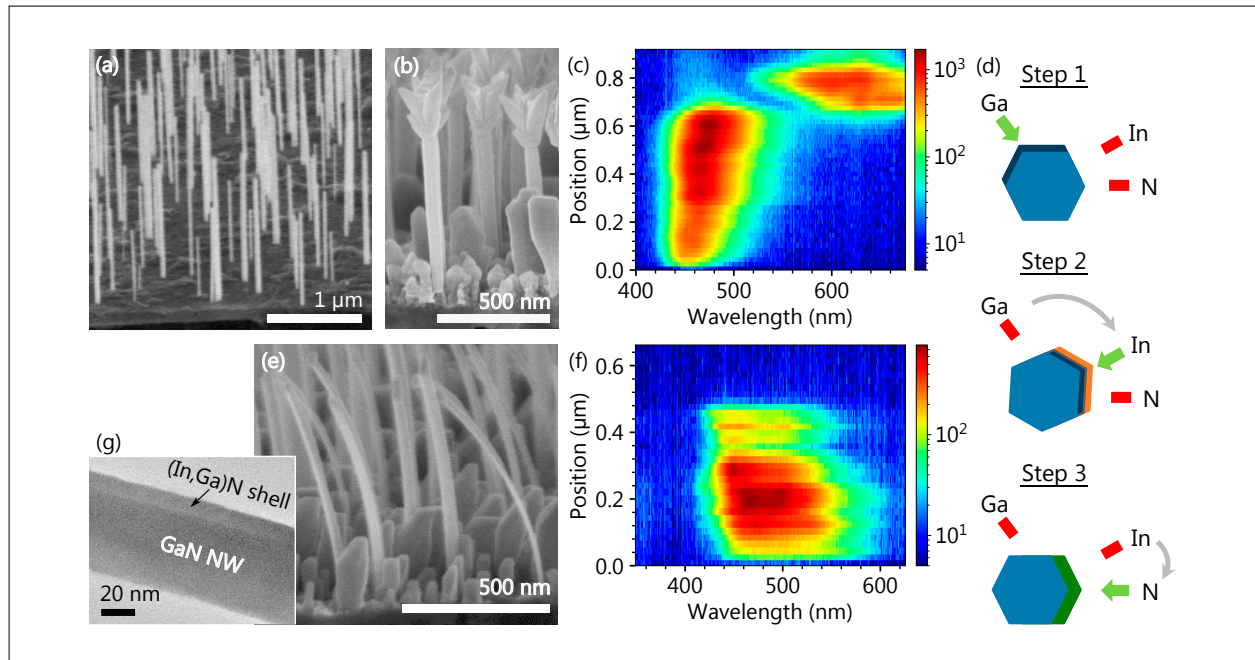
J. Lähnemann, D. van Treeck, G. Gao, A. Tahraoui, O. Brandt, S. Fernández-Garrido, L. Geelhaar

Core-shell nanowire (NW) heterostructures offer a route to increase the active region per substrate area, as the junction area scales with the NW length. This conceptual advantage is exploited in efforts towards light-emitting diodes for micro-pixelated displays based on GaN NWs with (In,Ga)N shells. Another advantage for the III-nitrides is that in shells on non-polar sidewall facets the quantum-confined Stark effect is absent. To date, almost all experimental realizations of such structures were achieved by metal-organic vapor phase epitaxy,

which inevitably results in the simultaneous growth of circumferential shells covering all NW sidewalls. In contrast, in molecular beam epitaxy (MBE), precursor species are delivered as directional fluxes that impinge only on one side of the NWs at a time. In this study, we investigate in detail the consequences of this flux directionality for the growth of (In,Ga)N shells around GaN NWs.

The first important aspect for shell growth by MBE is that, if the NW density is too high, shadowing of the molecular beams

**Fig. 1.** Scanning electron microscopy (SEM) images of (a) a self-assembled GaN NW template grown on a TiN substrate and (b) a similar NW ensemble overgrown with a circumferential (In,Ga)N shell using continuous substrate rotation. (c) CL spectral line scan acquired at a sample temperature of 20 K for a single, dispersed NW from the ensemble in (b) with the intensity color-coded on a logarithmic scale. (d) Sketch of the sequential directional deposition procedure. (e) SEM image of a NW ensemble on TiN with a one-sided shell. (f) Corresponding spectral line scan for a single, dispersed NW. (g) Bright-field TEM image showing the presence of a one-sided shell on the NW.



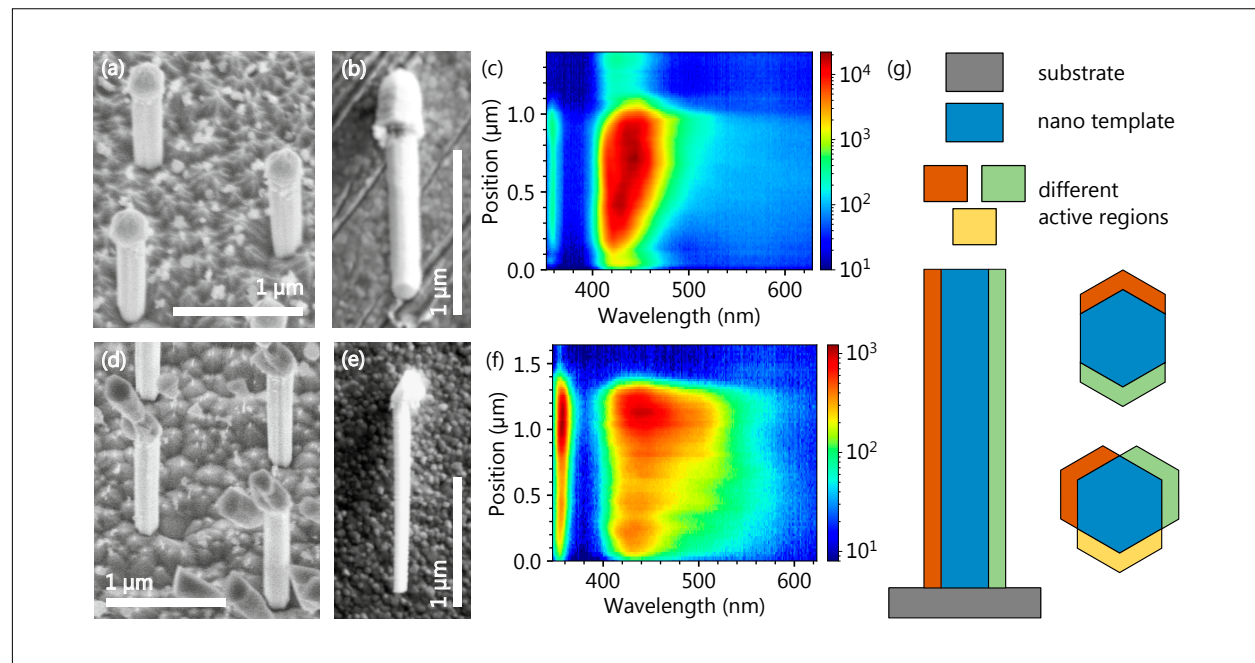
impedes the deposition of a homogeneous shell. Thus, to obtain the GaN NW template needed for shell growth, we make use of our previous study demonstrating the formation of self-assembled NW ensembles with sufficiently low density on TiN [D. van Treeck *et al.*, *Nano Res.* **11**, 565 (2018)], as illustrated in Fig. 1(a). For the growth of compounds such as (In,Ga)N by MBE, the constituents are typically provided as separate beams that reach the substrate from different azimuthal angles, and homogeneity is ensured by rotation of the substrate. In the NW geometry, these fluxes impinge on different side facets. Adding substrate rotation, the sidewalls are exposed to pulsed fluxes.

The resulting NW morphology is depicted in Fig. 1(b). Successful shell growth can be inferred from the increase in the NW diameter. Using cathodoluminescence hyperspectral line scans along the axis of single, dispersed NWs from such samples, as ex-

emplified in Fig. 1(c), an emission band centered around 470 nm and only a slight gradient in emission wavelength are observed. This emission demonstrates the presence of a rather homogeneous (In,Ga)N shell. Comparative measurements for different NWs (from the same sample) show a lower emission wavelength and thus reduced In content for thicker NWs. Nevertheless, the wire-to-wire fluctuations in the core-shell heterostructures are much lower than those observed for axial (In,Ga)N heterostructures [J. Lähnemann *et al.*, *Nanotechnology* **25**, 394010 (2014)].

As visible in Fig. 1(b), the core-shell NWs develop significantly enlarged, crown-like top segments, which are unfavorable for device processing. The longer CL emission wavelength shows that the In incorporation is increased in these crowns. Their formation can be understood from the deposition geometry and the adatom diffusion. During

**Fig. 2.** (a) SEM image of NWs with a continuous (In,Ga)N shell grown on a NW template obtained by selective area sublimation. (b) Single, dispersed NW from this ensemble. (c) CL spectral line scan obtained along the axis of this NW. (d) NW ensemble with a one-sided (In,Ga)N shell grown on a sublimated template. (e) Single, dispersed NW and (f) corresponding CL line scan for the latter sample. (g) Sketch of the proposed geometry of a NW with different active regions integrated on the side facets.



substrate rotation, the anion and cation beams are provided as subsequent pulses to the side facets, but continuously to the NW top facet. From a comprehensive analysis of binary GaN shell growth combined with modeling, we have learned that the lateral diffusion of metal adatoms between different side facets is inhibited, and only diffusion along the NW axis is relevant. Since N is always available at the NW top, metal adatoms are preferentially incorporated there, which in turn facilitates their diffusion to this region.

These insights lead us to the innovative approach for the shell growth sketched in Fig. 1(d): we rotate the substrate relative to the deposition sources step-by-step and pulse the shutters accordingly so that the constituents of the ternary alloy impinge on the same facet. This sequential directional deposition enables the growth of (In,Ga)N only on one side of the GaN NWs, which, for sufficiently high In content, manifests itself in the strain-induced bending of the NWs seen in Fig. 1(e). We find that a sub-monolayer deposition of the metals during each iteration as well as the specific deposition sequence of In, Ga, and then N are crucial for In incorporation on the side facets. The morphology of these NWs reveals a significantly reduced growth on the top facet due to the fact that only one flux at a time impinges on the NW. By systematically varying the substrate temperature and the In/Ga flux ratio, we obtain homogeneous one-sided (In,Ga)N shells with an emission wavelength tunable between 380 and 500 nm, the latter being exemplified by a CL line scan in Fig. 1(f). The efficient carrier transfer from the core to the (In,Ga)N shell for these NWs with diameters below 100 nm is evidenced by the absence of a pronounced band-edge emission from GaN. The presence of an about 10-nm-thick, one-sided

(In,Ga)N shell is independently confirmed in Fig. 1(g) by bright-field transmission electron microscopy (TEM).

We extend our investigation to arrays of ordered NWs obtained by in-situ selective area sublimation of GaN templates [S. Fernández-Garrido *et al.*, *Nanoscale Adv.* **1**, 1893 (2019)], which offer thicker (200–500 nm diameter) NW cores with a reduced diameter distribution and controlled pitch for the subsequent (In,Ga)N growth. To this end, a pattern of AlN dots defined by electron beam lithography serves as mask for the thermal decomposition of a GaN template layer.

First, we again deposit circumferential shells as depicted in Figs. 2(a)–2(c). Due to the increased NW diameter ( $\approx 250$  nm for the shown NWs), a weak emission from the GaN core is detected. As before, the shell emission is homogeneous with only a slight wavelength gradient along the NW axis. For the ordered arrays, we find an improved wire-to-wire reproducibility of the shell emission.

Second, we also deposit one-sided shells on a sublimated NW template with the resulting morphology and emission shown in Figs. 2(d)–2(f). Due to the only partial coverage with (In,Ga)N, the GaN core emission is enhanced. In comparison with the circumferential shells, the emission band is broadened towards longer wavelengths.

As a perspective, directional deposition opens up new prospects for device design. As sketched in Fig. 2(g), active regions with different functionalities may be combined on different side facets of one and the same NW, which, for example, could lead to RGB light emitting diodes based on a single NW for ultra-high resolution displays.

# External control of the band bending at the GaN(1̄100) surface using phosphanate self-assembled monolayers

T. Auzelle, F. Ullrich<sup>1,2</sup>, S. Hietzschold<sup>1,3</sup>, C. Sinito, S. Brackmann<sup>1,3</sup>, W. Kowalsky<sup>1,3,4</sup>, E. Mankel<sup>1,2</sup>, R. Lovrincic<sup>1,3</sup>, O. Brandt, and S. Fernández-Garrido

Inorganic semiconductors typically exhibit a surface band bending ( $\Phi$ ) resulting from a charge transfer between bulk and surface electronic states. The related space charge region and electric field affect both carrier transport and recombination in the vicinity of the surface. These effects are of vital importance for semiconductor nanowires featuring a large surface-to-volume ratio. In particular, GaN nanowires, which are of interest for applications in optoelectronics and photovoltaics, would greatly benefit from the possibility to influence or even tune the surface band bending. Here, we aim to modify the band bending in GaN by coating both GaN(0001) and GaN(1̄100) surfaces with organic molecules of different electronegativity that covalently bond to the GaN surfaces.

We focus on the upward surface band bending observed in unintentionally doped GaN as shown schematically in Fig.1(a). The band bending affects not only the conduction and valence band minima (CBM and VBM, respectively), but also the core levels. For organic coating, we select two phosphonic acids referred to as PFOPA and OPA as schematically depicted in Fig.1(b).

The acid function acts as an anchor group and allows covalent bonding to oxides such as  $\text{GaO}_x$ . The fluorine decorating the PFO-

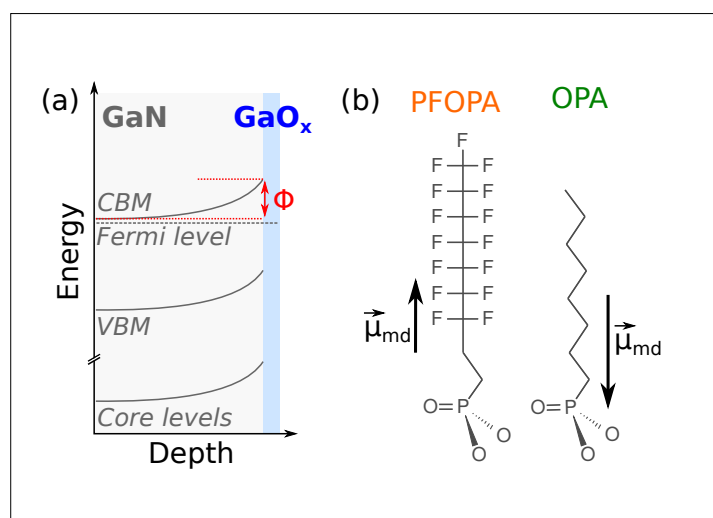


**Fig.1.** (a) Sketch of the GaN band bending in the vicinity of its oxidized surface (right). The amplitude of the surface band bending ( $\Phi$ ) is highlighted. (b) Schematic representation of PFOPA (1H,1H,H,2H-perfluoroctanephosphonic acid) and OPA (n-octylphosphonic acid).

PA backbone provides an increased electronegativity to this molecule compared to OPA, and additionally results in molecular dipoles ( $\vec{\mu}_{\text{md}}$ ) pointing in opposite directions for these two molecules.

Freestanding GaN layers with either (0001) or (1̄100) orientation and self-assembled GaN nanowires on Si and TiN substrates are

<sup>1</sup> InnovationLab Heidelberg, Deutschland

<sup>2</sup> Institut für Materialwissenschaft, Technische Universität Darmstadt, Deutschland

<sup>3</sup> Institut für Hochfrequenztechnik, Technische Universität Braunschweig, Deutschland

<sup>4</sup> Kirchhoff-Institut für Physik, Universität Heidelberg, Deutschland

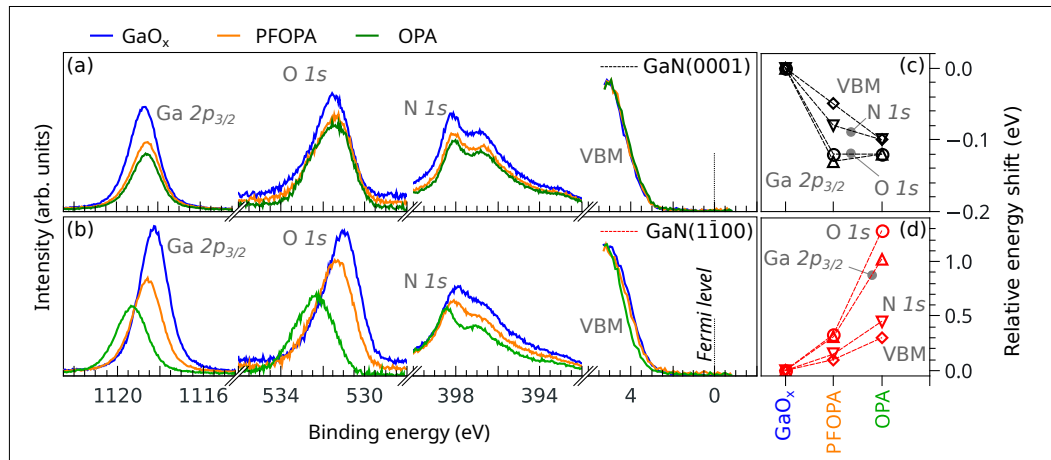


**Fig. 2.** (a)–(b) Binding energies of the Ga 2p<sub>3/2</sub>, O1s and N1s core levels and of the valence band maximum (VBM) measured by XPS for bare oxidized GaN surfaces and after the grafting of PFOPA or OPA. The VBM onset is normalized in intensity. (c)–(d) Shift of the core levels and VBM relative to the bare GaO<sub>x</sub> surface. (a)–(c) refers to GaN(0001) and (b)–(d) to GaN(1̄100).

coated with organic molecules as follows. We first oxidize the GaN surface in a reproducible manner by HCl etching followed by an O<sub>2</sub> plasma exposure. Next, the phosphonic acids are physisorbed by immersing the GaN samples in an ethanol solution with 2mmol/L of PFOPA or OPA. Chemisorption is subsequently fostered by annealing the samples in air at 140 °C. Finally, the samples are thoroughly washed with ethanol to remove any adsorbates loosely attached to the surface. The presence of P atoms on the GaN surfaces is confirmed by x-ray photo-electron spectroscopy (XPS), which is also used to examine the work function of the coated free-standing layers. Compared to the bare GaO<sub>x</sub> surface, PFOPA (OPA) grafting is found to increase (decrease) the work function by  $\approx 0.5\text{ eV}$ , indicating that the molecules induce a macroscopic surface dipole. In particular, the polarity of this surface dipole matches the direction of the molecular dipole exhibited by PFOPA and OPA. Hence, these results suggest that PFOPA and OPA self-assemble on oxidized GaN(0001) and GaN(1̄100) surfaces into a dense monolayer, providing a well-defined organic/inorganic interface.

To quantitatively determine the impact of PFOPA and OPA adsorption on the GaN surface band bending, we record XPS spectra of the pristine and functionalized GaN layers as shown in Figs.2(a)–2(b).

No remarkable changes are observed for the GaN(0001) orientation upon the deposition of the phosphonic acids. In contrast, both OPA and PFOPA induce large energy shifts of the core levels and the VBM for the GaN(1̄100) orientation. As shown in Figs.2(c)–2(d), the energy shifts observed are actually different for each core level and the VBM, reflecting a modification of both the surface band bending and the GaO<sub>x</sub> oxidation state. If we assume that the surface GaO<sub>x</sub> does not contain an appreciable amount of N, and is thus unaffected by its oxidation state, we can directly obtain the relative modification of the surface band bending from the N1s core level shifts.  $\Delta\Phi$  values of 0.20 and  $0.45 \pm 0.05\text{ eV}$  for the PFOPA and OPA coatings, respectively, shows that these phosphonic acids act as surface donors: by filling GaO<sub>x</sub> surface states, they push up the Fermi level energy, thus reducing the GaN surface band bending. The larger band bending reduction

obtained for OPA is in agreement with the fact that it is the more electropositive molecule.

The insensitivity of the oxidized GaN(0001) surface to grafting with PFOPA and OPA may stem from a larger density of surface states compared to the (1100) plane, thus pinning the Fermi level. Alternatively, a different energy alignment between the  $\text{GaO}_x$  surface states and the highest occupied molecular orbital of the phosphonic acids may prevent the latter to act as surface donors. In any case, our results suggest that the GaN(0001) surface of planar GaN-based devices is difficult to passivate, while GaN nanowires with their (1100) sidewalls may profit from a coating with OPA.

The radial electric field in GaN nanowires due to surface band bending is strong enough to field-ionize excitons even for a doping level of  $10^{16}\text{cm}^{-3}$ . Indeed, this is the mechanism that limits the internal quantum efficiency (IQE) of self-assembled GaN nanowires. The reduction of the surface band bending provided by OPA deposition gives reason to the hope of an enhanced IQE in the structures grafted with OPA. Figure 3 shows the photoluminescence (PL) intensity of GaN nanowire ensembles after oxidation and after a subsequent coating by PFOPA and OPA. While coating with PFOPA has little effect or even results in a slight decrease of the PL intensity, we systematically observe a significant increase of the PL intensity upon OPA coating.

By tailoring the electronegativity of phosphonic acids attached to the oxidized GaN(1100) surface, we gain control in the amplitude of the surface band bending with a detectable impact on the GaN IQE. This result may open perspectives for sensing applications. In particular, GaN nanowire-based biosensors could offer improved biocompatibility with equal sensitivity compared to state-of-the-art Si nanowire-based devices.

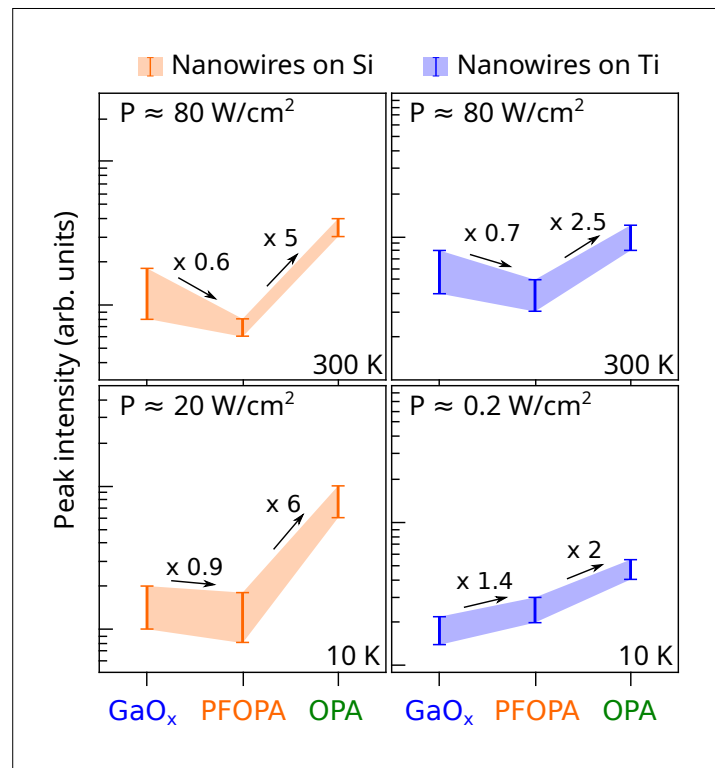


**Fig. 3.** Peak photoluminescence intensity of oxidized GaN nanowire ensembles measured before and after PFOPA/OPA grafting, both at 300 and 10 K. The error bars highlighted by the colored areas depict the dispersion at the scale of the sample.

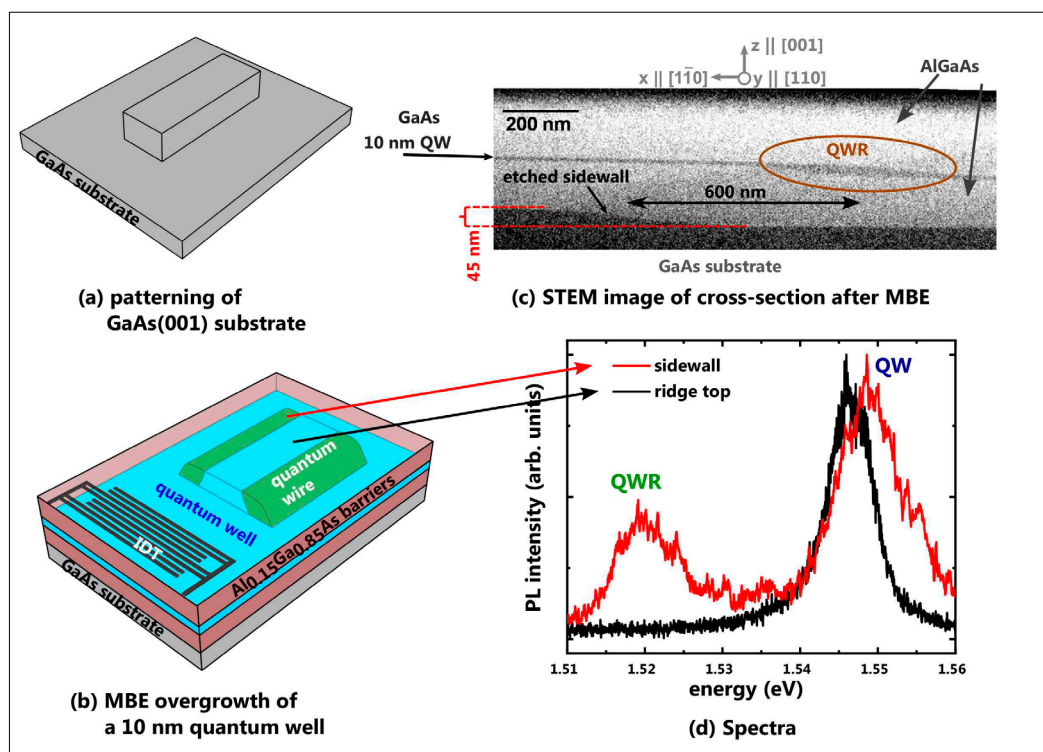
# Charge and spin transport in sidewall quantum wires on GaAs(001) substrates

P. L. J. Helgers, H. Sanada<sup>1</sup>, Y. Kunihashi<sup>1</sup>, K. Biermann, P. V. Santos

Planar quantum wires (QWR) are one-dimensional (1D) interconnects for information exchange between distant locations on a chip. Such information can be either encoded as charge bits, photonic qubits or spin qubits. Photonic information can be processed via the conversion of photons to electron-hole pairs, which can be stored and propelled along the QWR by the

piezoelectric potential of a surface acoustic wave (SAW). After transport, the carriers can recombine, thus reconverting the information to photons. In this process, the photon polarization can be encoded in the electron spin, which can also be transported by SAWs. The moving type-II piezoelectric potential of a SAW spatially separates electrons and holes, thus increasing the

**Fig. 1.** (a) Prepatterned ridges (etching depth 45 nm) on GaAs(001) substrates by photolithography and wet chemical etching. (b) Sample structure after the MBE overgrowth of a 10 nm thick QW sandwiched between two Al<sub>0.15</sub>Ga<sub>0.85</sub>As barriers, showing the formation of QWRs at the ridge sidewalls oriented along the [110] surface direction. (c) Scanning transmission electron micrograph of the ridge cross-section showing the QWR (highlighted by a brown circle). (d) Comparison of photoluminescence spectra recorded at the ridge top and sidewall.



<sup>1</sup> NTT Basic Research Laboratories, Atsugi, Japan

carrier recombination lifetime and simultaneously suppressing spin relaxation due to the exchange interaction between electrons and holes. A further advantage of 1D transport channels is the suppression of Dyakonov-Perel spin relaxation [Kiselev *et al.* Phys. Rev. B **61**, 13115 (2000)]. Thus, the combination of narrow QWR channels with acoustic transport by a SAW provides a promising approach for the long-distance spin transport.

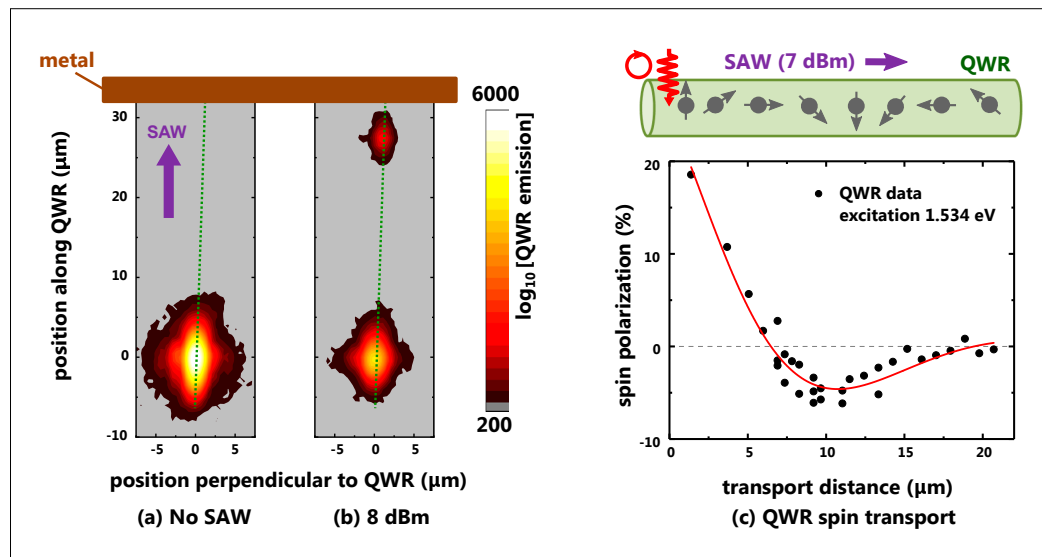
Previous studies on acoustic transport have been restricted to QWRs on GaAs(113)A [Alsina *et al.* Phys. Stat. Sol. (c) **5**, 2907 (2008)]. In this contribution, we demonstrate the acoustic transport of both charge and spins along quasi-planar QWRs fabricated by molecular beam epitaxy (MBE) on GaAs(001) substrates prepatterned with shallow ridges [Helgers *et al.* Phys. Rev. Applied **11**, 064017 (2019)]. The formation of sidewall QWRs using a similar procedure was reported by Lee *et al.* [IEEE Trans. on Nano. **6**, 70 (2007)]. These studies, however, only addressed the QWR structural

properties and no attention was given to the optical and transport properties.

In the fabrication process, the shallow ridges are defined by photolithography and wet chemical etching (cf. Fig. 1(a)). The substrate is then overgrown by MBE with a 10 nm GaAs quantum well (QW, depicted in blue in Fig. 1(b)), sandwiched between two  $\text{Al}_{0.15}\text{Ga}_{0.85}\text{As}$  barriers (red). The anisotropic epitaxial overgrowth leads to the formation of a QWR (green) via a local increase in thickness of the QW on both sidewalls of ridges oriented along the [110] direction. The QWR is highlighted by a brown circle in the cross-sectional scanning transmission electron micrograph of the final sample displayed in Fig. 1(c). From this image, we extract values for the thickness and width of the QWRs of  $25 \pm 5$  nm and  $200 \pm 5$  nm, respectively.

QWRs with high carrier mobility require straight ridges with small line edge roughness (LER), defined as the standard deviation of the edge shape. LER was measured

**Fig. 2.** Spatially resolved PL along the QWR (dashed line) recorded in the (a) absence and (b) presence of a SAW excited by 8 dBm. A metal stripe at 30  $\mu\text{m}$  screens the SAW piezoelectric field and induces carrier recombination. (c) Spin polarization of PL measured along the QWR axis.



to be in the range from 4 nm to 9 nm. The latter was found to be similar to the roughness of the photoresist edges, thus indicating that it mainly originates from the photolithography process. Since the LER is much smaller than the QWR width, it is expected to play only a minor role in the transport properties.

A comparison of photoluminescence (PL) spectra recorded on the top and sidewall of the ridge (cf. Fig. 1(d)) confirms that the QWRs only form at both ridge sidewalls and reveals a 27 meV red-shift of the QWR emission relative to the QW emission, which should protect QWR carriers against escaping to the QW during transport.

The optically detected transport studies were carried out using SAWs with a wavelength  $\lambda_{\text{SAW}} = 4 \mu\text{m}$ , generated by interdigital transducers (IDT) deposited on the sample surface. Figures 2(a) and 2(b) compare spatially resolved PL maps recorded by exciting carriers within a small spot (diameter of approx. 2  $\mu\text{m}$ ), focused on the QWR as indicated by a green dashed line, in the absence and presence of a SAW, respectively. In the former case, we observe carrier diffusion with a Gaussian profile with full-width-at-half-maximum of approx. 4  $\mu\text{m}$  around the excitation spot. When a SAW with a power of 8 dBm is applied (Fig. 2(b)), the intensity of the QWR emission at the excitation spot decreases. This is attributed to the separation of electrons and holes and their transport away from the excitation spot by the SAW piezoelectric potential [Rocke *et al.* Phys. Rev. Letters **78**, 4099 (1997)]. Additionally, we observe remote emission from the excited QWR at a position of 30  $\mu\text{m}$ , where a metal stripe screens the SAW potential and induces recombination of transported carriers. The acoustic transport distance over tens of  $\mu\text{m}$  is much longer than the diffusion length without SAW.

In the absence of acoustic excitation, the measured spin lifetimes  $\tau_s$  in the QWR (approx. 2–3 ns) exceeds those in the surrounding QW ( $\tau_s \approx 0.6 \text{ ns}$ ). The latter is mainly attributed to suppression of Dyakonov-Perel spin relaxation. The acoustic transport of spins was studied by exciting spin polarized carriers using a circularly polarized laser and detecting the polarization of the PL emitted along the QWR. The dependence of the spin polarization on the transport distance is shown in Fig. 2(c). The oscillation of the polarization arises from the precession of the spin states around the effective magnetic field associated with the spin-orbit interaction [Hernández-Mínguez *et al.* Phys. Stat. Sol. b **251**, 1736 (2014)]. A fit to an exponentially decaying cosine function (red line in Fig. 2(d)) yields a precession length of  $26 \pm 1 \mu\text{m}$ . The latter is consistent with the calculated spin precession length in the QWR of  $30 \pm 7 \mu\text{m}$ . Furthermore, this precession length is much larger than the one of  $7 \pm 1 \mu\text{m}$  predicted for the QW. The extracted spin lifetimes during acoustic transport along the QWR (of approx. 2.4 ns) is also larger than in the QW (approx. 1.7 ns).

In conclusion, we have investigated the structural, optical and transport properties of planar sidewall QWRs fabricated on GaAs(001) substrates. We show the feasibility of long-distance charge and spin transport by a surface acoustic wave. The spin transport was found to be more efficient in the QWR than in a surrounding QW, thus making them promising candidates for quantum interconnects for the exchange of spin information between distant locations on a chip. [This project has received funding from the European Union's Horizon 2020 research and innovation program under grant agreement No 642688.]

# Polariton-based optomechanics at super high frequencies

A. S. Kuznetsov, D. H. O. Machado, A. C. Poveda, K. Biermann, P. V. Santos

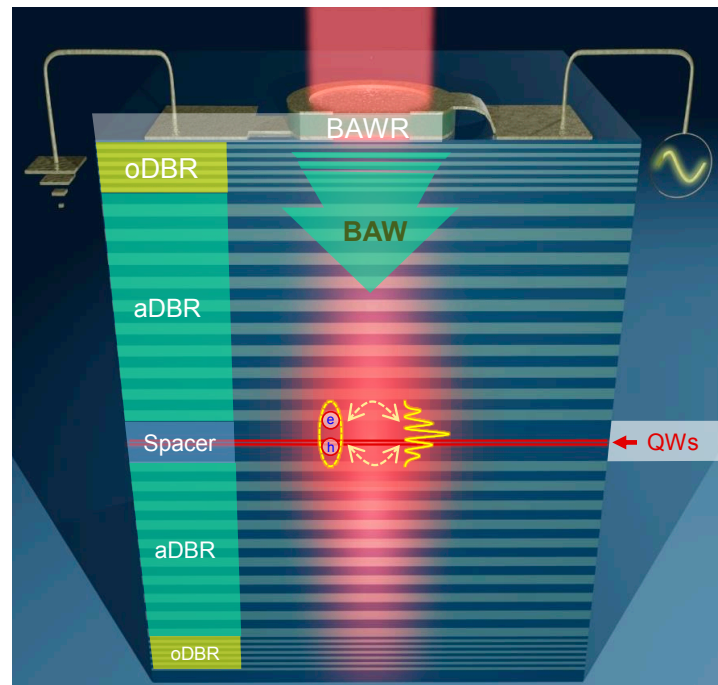
Optomechanics — the coupling between photons and mechanical vibrations at the nanoscale — offers multiple advanced applications such as, precision force-sensing, acoustically-induced topology and coherent control of elementary solid-state excitations, including macroscopic quantum phases. The coherent coupling between light and sound leads to the appearance of acoustically induced side-bands in the optical spectrum, which enables optical cooling to the ground-state and phonon lasing. Equally important is the field of cavity quantum electrodynamics and its specific regime of the strong-coupling between photons and excitons. Such coupling gives rise to exciton-polariton (EP) quasiparticles, which inherit low photon-like effective mass and strong exciton-like nonlinearities. EPs can be considered as solid-state analogues to ultra-cold atoms, showing similar nonlinear phenomena such as, for instance, Bose-Einstein condensation (BEC), bistability and quantum correlations in the 10-300 K temperature range.

Due to the low effective mass resulting in  $\mu\text{m}$ -large de Broglie wavelength, EPs can be confined in 1D and 2D potentials. Recently, we have demonstrated lattices of coupled confined EPs that support polariton-BEC phases [A. S. Kuznetsov *et al.*, Phys. Rev. B **97**, 195309 (2018)], which can be controlled using strain fields of piezoelectrically generated MHz surface acoustic waves [A. S. Kuznetsov *et al.*, submitted (2019)].

Here we demonstrate an optomechanical platform for the coherent coupling between EP and monochromatic super high frequency (SHF) acoustic phonons generated by piezoelectric transducers. The platform is based on planar microcavity (MC) designed to simultaneously confine EPs and SHF ion-

itudinal acoustic waves. The piezoelectric transducers are used to generate and probe the sound waves as they propagate through the microcavity. This propagation leads to a mixing of the acoustic spectrum of the MC and the acoustic spectrum of the resonator formed by the substrate. Thus, acoustic quality factor Q values of up to 5000 are obtained. The high acoustic Q leads to a large acousto-optic interaction with EP in the same MC. Specifically, we show the coherent modulation of the EP energies with amplitudes up to 8 meV by 7 GHz strain fields, which far exceeds the EP Rabi coupling and can be further increased by in-

**Fig. 1.** Cross-section of the MC sample. oDBR and aDBR stand for the optical and acoustic distributed Bragg reflectors, respectively. A bulk acoustic wave (BAW) is generated by a bulk acoustic wave resonator (BAWR) driven with RF voltage. The quantum wells (QW) are placed at the antinodes of both acoustic and optical fields, which allows QW-excitons to couple to both photons and phonons.



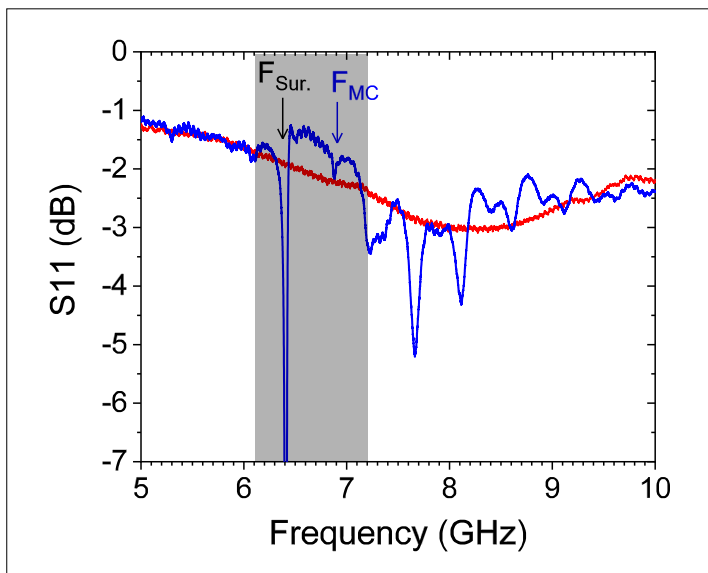
creasing the radio-frequency (RF) power applied to the transducers.

The hybrid optomechanical (Al,Ga)As MC designed to confine near-IR EPs and 7 GHz phonons, illustrated in Fig. 1, was fabricated by molecular beam epitaxy. Two 15 nm thick InGaAs quantum wells (QW) were positioned at the overlap of the antinodes of optical and acoustic fields. The coherent GHz waves were electrically generated using a bulk acoustic wave resonator (BAWR), fabricated on the surface of the upper mirror [D. H. O. Machado *et al.*, Arxiv 1907.09787, (2019)]. The active region of a typical BAWR consists of a 260 nm-thick piezoelectric ZnO film with the c-axis oriented perpendicular to the MC surface. The thickness of the film corresponds to the half of the acoustic wavelength and thus defines the central frequency. This active region is sandwiched between two 50 nm-thick metal contacts.

Special features of our BAWR design are the apertures in the bottom and top contacts for optical access.

The BAWR converts the applied RF voltage into an acoustic wave over a broad range of RF frequencies around 8 GHz (cf. red curve in Fig. 2). Due to the broad spectral response of the BAWR we can excite specific acoustic modes, simply, by fixing the frequency of the RF generator. The BAWR can also detect the acoustic waves as they propagate through the MC. In particular, we can measure the acoustic stopband and identify acoustic modes of the MC in electrical characterization, cf. blue curve in Fig. 2. Further analysis show that the mode at  $F_{MC} = 6.9 \pm 0.06$  GHz is the mode of the MC. Excitation of the BAWR around that frequency thus results in a generation of the bulk acoustic wave (BAW) confined in the MC spacer.

**Fig. 2.** Electrical response at 300 K of BAWRs on a GaAs substrate (red curve) and on the MC for Fig. 1 (blue curve). Both devices have nominally identical ZnO thickness of 260 nm. The gray shaded area designates the acoustic stopband spectral range for the BAWR on the MC. The two modes within the stopband correspond to the MC acoustic mode with  $F_{MC} = 6.9$  GHz and the surface mode  $F_{Sur.} = 6.4$  GHz. The latter is due to an acoustic cavity formed by the air-BAWR-upper aDBR, cf. Fig. 1.



In photoluminescence (PL) measurements at 10K, a 631 nm pulsed laser diode was focused on the center of a BAWR aperture, see Figure 3(a). The MHz-pulsed electrical output of the laser controller was used to trigger the RF generator. The PL signal was imaged onto the slit of a single pass spectrometer, producing PL spectra spatially resolved across the BAWR aperture. In order to rule out the heating effects due to the RF excitation, we first measured PL with acoustic ( $F_{RF} = 6.931$  GHz) and laser pulses out-of-phase. The corresponding PL image shows no spatial and spectral modification within the dimensions of the BAWR aperture, see Figure 3(b).

When the laser pulses coincide with the RF pulses, the in-phase condition, we observe large change in the detected PL signal. The most pronounced change is the energy-broadening of the spectrum whose magnitude increases towards the center of the aperture, cf. Figure 3(c). This indicates that the BAWR ring-geometry concentrates the acoustic field. Comparison of the out-of-phase and in-phase spectra at the

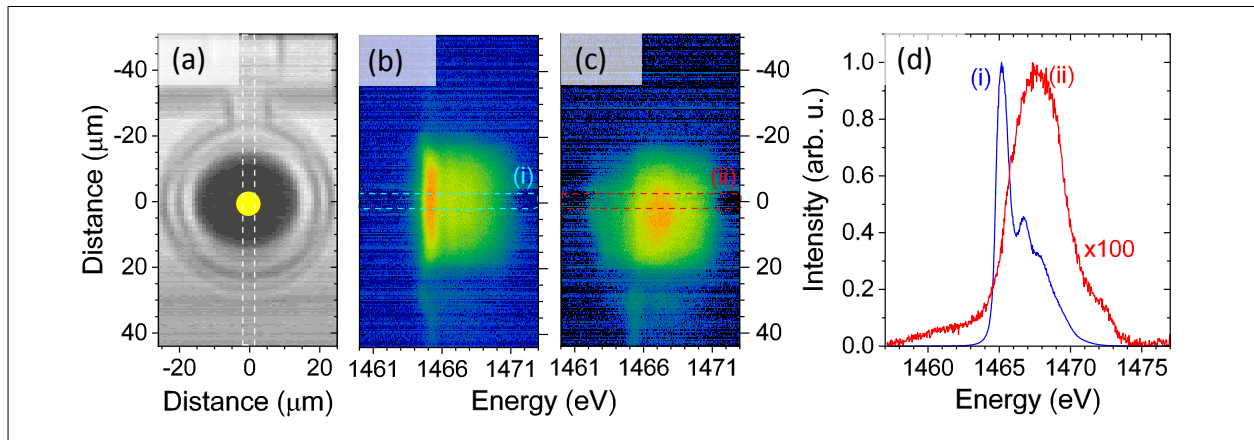


**Fig. 3.** (a) Optical micrograph of the BAWR showing the laser spot focused at the center of its optical aperture. (b)-(c) Photoluminescence (PL) maps recorded along the region defined by the vertical dashed lines in (a) in the absence and presence of a  $F_{RF} = 6.931$  GHz acoustic wave, respectively. (d) Comparison of PL spectra along the horizontal dashed regions in (b) and (c).

aperture center shows that the broadening (which is the result of the time-integration over billions of acoustic cycles) takes place at both flanks of the unmodulated spectrum, see Figure 3(d). A detailed analysis of the spectroscopic data leads us to conclude that the main coupling mechanism is the deformation potential. At larger acoustic powers, we observe strong quenching of the total PL. We propose two mechanisms: (i) dissociations of excitons by in-plane electrical fields; (ii) periodic switching between weak and strong coupling as the BAW-induced energy modulation by far exceeds the Rabi-splitting energy ( $\Omega_{Rabi} = 2$  meV).

In conclusion, our work demonstrates a novel platform for SHF EP optomechanics based on electrically stimulated vibrations.

The energy modulation amplitude can be conveniently tuned over a very large range. These results open a way to reach the non-adiabatic regime with acoustic sidebands. In fact, the vibration energy of approximately 30 μeV is comparable or larger than the typical polariton-BEC linewidth. Excitation of 20 GHz vibrations can be achieved using the same BAWR technology. Advanced sample design allows not only for the piezoelectric generation of coherent acoustic waves but also for the detection acoustic waves generated in the cavity. Future studies will address the detection of mechanical self-oscillations and phonon lasing.

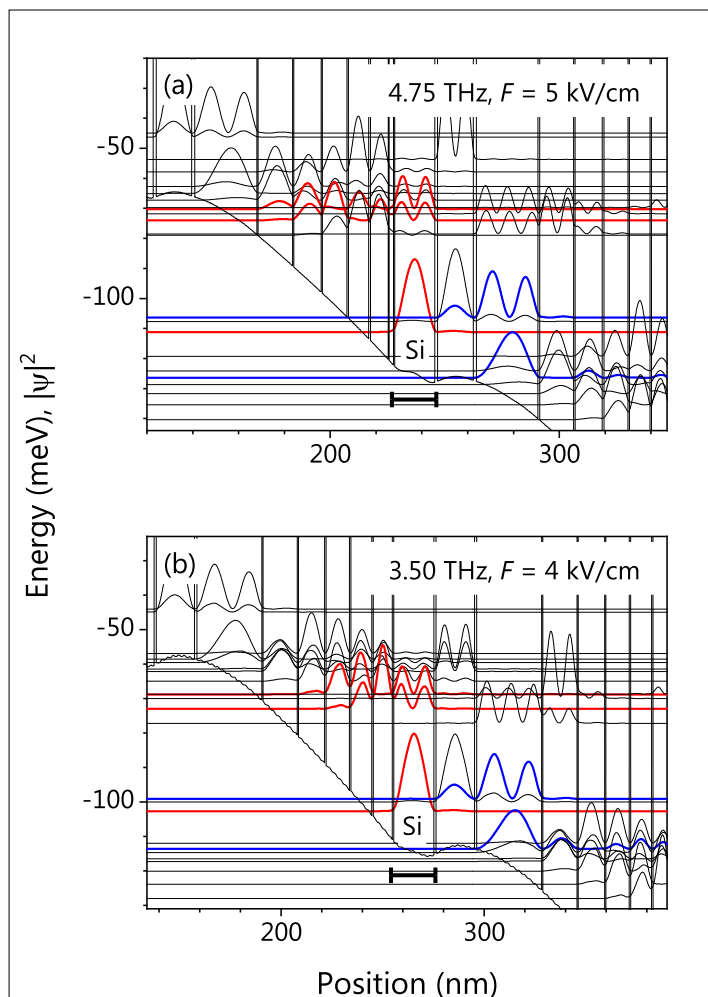
We acknowledge the financial support from the DFG (grant 359162958).

# Extending the frequency range of GaAs/AlAs terahertz quantum-cascade lasers from 4.7 to 3.3 THz

L. Schrottke, X. Lü, B. Röben, K. Biermann, H. T. Grahn

The invention of quantum-cascade lasers (QCL) about 25 years ago opened the path to a variety of spectroscopic approaches in the mid- to far-infrared spectral region. In particular, QCLs for the terahertz (THz)

**Fig. 1.** Conduction band profiles, subband structures, and positions of the Si doping of QCLs for (a) 4.75 and (b) 3.50 THz. The blue lines depict the laser states, while the red lines indicate the initial and final states for the main transitions, which are resonant to the energy of the longitudinal optical phonon.



spectral region allow for high-resolution spectroscopy of molecules, atoms, and ions utilizing rotational or fine-structure transitions. In atmospheric science, the rotational transition of OH at 3.55 THz and the fine-structure line of atomic oxygen (OI) at 4.75 THz are of particular interest. Both can be measured with QCL-based heterodyne receivers. For fundamental research and industrial applications, high-resolution absorption spectroscopy based on fine-structure transitions in Al, N<sup>+</sup>, and O at 3.36, 3.92, and 4.75 THz, respectively, is expected to allow for the quantitative determination of the atom and ion densities in plasma processes. Furthermore, QCLs emitting in the atmospheric windows around 3.43, 4.32, and 4.92 THz are of interest for applications if the THz radiation has to be transmitted through air over a distance of about 10 m.

We recently demonstrated that a 4.75-THz-QCL based on GaAs/AlAs heterostructures exhibits a significantly larger wall plug efficiency, a higher slope efficiency, a lower threshold current density, and a larger intrinsic tuning range than similar lasers relying on Al<sub>0.25</sub>Ga<sub>0.75</sub>As barriers [L. Schrottke *et al.*, Appl. Phys. Lett. **108**, 102102 (2016)]. Therefore, we developed THz QCLs based on GaAs/AlAs heterostructures with emission frequencies between 3.4 and 5.0 THz starting from a laser structure operating at 4.75 THz followed by a gradual scaling of the layer structure toward lower or higher frequencies. The corresponding frequencies of the gain maxima are achieved by an adjustment of the quantum well thicknesses and a corresponding fine-tuning of the thicknesses of some particular barriers. Figures 1(a) and 1(b) depict the calculated subband structures using the nominal lay-

er thicknesses of the designs for 4.75 and 3.50 THz, respectively, as examples, which demonstrate that the scaling maintains the essential subband structure.

The lasers were grown by molecular beam epitaxy, which is particularly challenging for the very thin AlAs barriers with 2–4 monolayer thicknesses. Our approach consists in nominal growth rates of 0.11 and 0.13 nm/s for AlAs and GaAs, respectively, leading to a minimum Al shutter opening time of 5 s for the thinnest barrier and an overall growth time of about 22 h for the whole cascade structure. The average growth rates amount to 0.13 nm/s, while fluctuations in the growth rates are below 1% due to the use of a closed-loop rate control system based on optical reflection measurements for the in-situ growth control. During growth, the substrate was rotated at a speed of about 12 rpm. The exact value is adjusted so that it corresponds to an integer number of rotations per period of the cascade structure.

Figure 2 exhibits a compilation of operating parameters of 21 GaAs/AlAs QCLs based on the hybrid active-region design. For 3.50 and 4.75 THz, three different wafers were used, while for 3.92 THz the lasers were fabricated from two different wafers. For all other frequencies, only one wafer was used to fabricate the lasers. The output power of Fabry-Pérot lasers based on single-plasmon waveguides is shown for continuous-wave (cw) operation as a function of the emission frequency. The typical ridge dimensions of these lasers are about  $0.12 \times 1.0 \text{ mm}^2$ , and their threshold current densities vary between 100 and  $300 \text{ A/cm}^2$ . Since the achieved frequencies are rather equally distributed between 3.4 and 5.0 THz, we expect that lasers emitting at any frequency in this range can be developed by a straightforward interpolation of designs for adjacent frequencies shown in Fig. 2. For 3.50 and 4.75 THz, the optimization of the lasers has already started, which can be seen by the comparatively larger

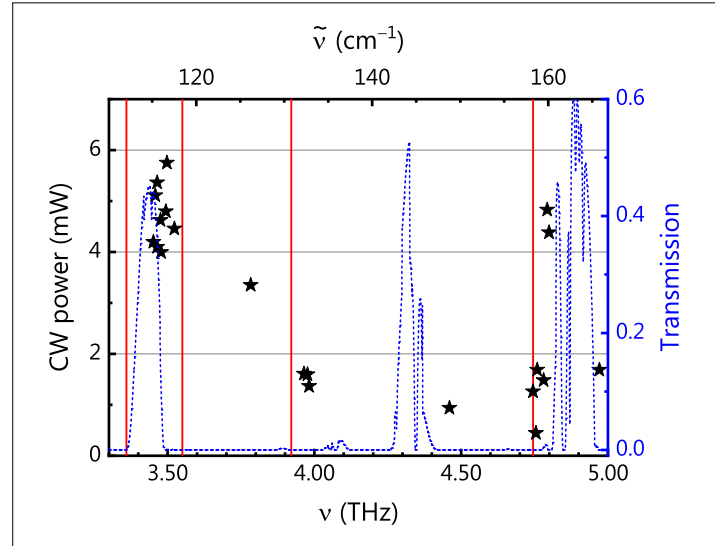


**Fig. 2.** Maximum output power for cw operation as a function of the center emission frequency for 21 GaAs/AlAs QCLs (asterisks) based on the hybrid active-region design measured at a heat sink temperature of 30 K. The vertical lines indicate the frequencies of 3.36, 3.92, and 4.75 THz for fine-structure transitions of Al, N<sup>+</sup>, and O atoms/ions, respectively, and 3.55 THz for OH detection. The dashed line depicts a simulated transmission spectrum of air based on the HITRAN database for ambient conditions for an optical path length of 10 meters, exhibiting maxima at 3.43, 4.32, and 4.92 THz.

powers for these frequencies. The wall plug efficiencies for lasers at 3.50 and 4.75 THz reach values larger than 1.8 and  $1.1 \times 10^{-3}$ , respectively, i.e., for typical output powers of 1 mW, electrical powers of less than 1 W are required so that the operation in a miniature cryocooler becomes feasible.

Figure 3 shows the light output-current density-voltage (*L-J-V*) characteristics as well as the lasing spectra of a 3.50-THz-QCL with emission frequencies between 3.40 and 3.50 THz observed for various operating conditions. The threshold current density is as low as  $240 \text{ A/cm}^2$ , although the confinement factor in the employed single-plasmon waveguide is rather low (about 0.5). The tuning range for individual lasing modes amounts to about 5 GHz, which is sufficient for high-resolution spectroscopy of low-pressure molecular absorption

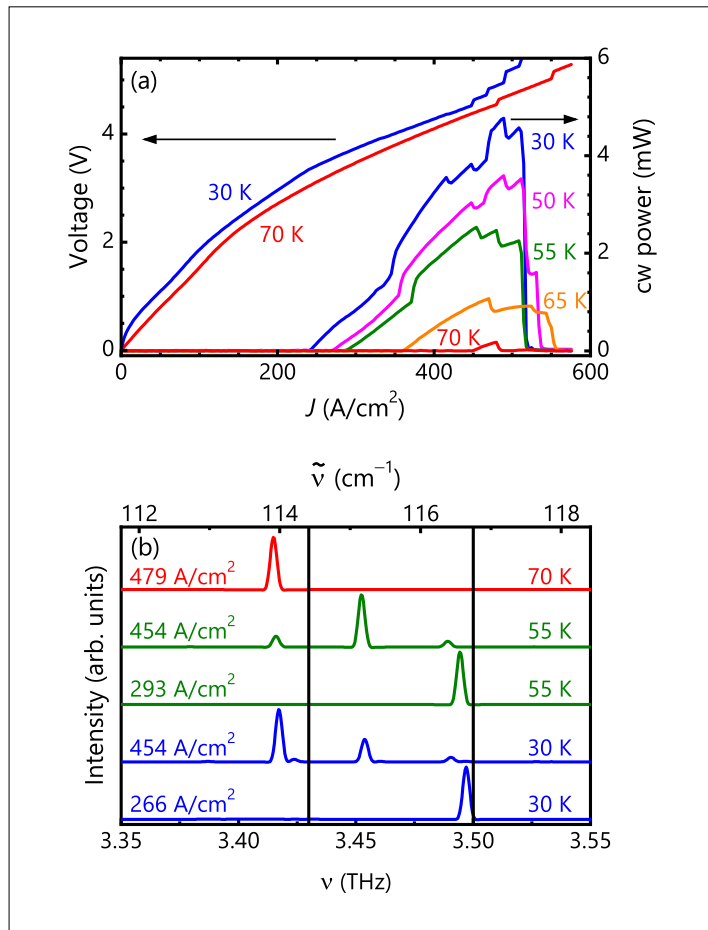


**Fig. 3.** (a)  $L$ - $J$ - $V$  characteristics for several operating temperatures and (b) lasing spectra for several operating temperatures and current densities of the 3.50-THz-QCL with laser ridge dimensions of  $0.12 \times 0.94\text{mm}^2$  under cw operation. The vertical solid lines indicate the target frequencies of 3.43 and 3.50 THz.

lines, for example of methanol. Applying first-order distributed-feedback gratings or two-section cavities, this wafer can be used for the fabrication of single-mode lasers operating around 3.50 THz. The best laser emits currently a power of more than 1 mW at operating temperatures of up to 65 K, which can be improved by varying the length of the ridge laser. By optimizing the balance between the electric-field dependent gain spectra and the non-linear transport properties, i.e., the onset of negative differential conductance, we expect to further improve the operating parameters such as the output power. Similarly, the target frequency of 3.36 THz for the respective fine-structure transition of Al atoms can be reached by a minor adjustment of the active region.

The high gain of the active regions and the rather low electrical input power compensate for the rather low confinement factor of the employed single-plasmon waveguides. Fabry-Pérot resonators with these waveguides allow for a straightforward fine-tuning of the laser modes so that these lasers are suitable for several practical applications in the field of high-resolution terahertz spectroscopy.

# High performance 4.75 THz quantum-cascade laser with an additional back-facet mirror

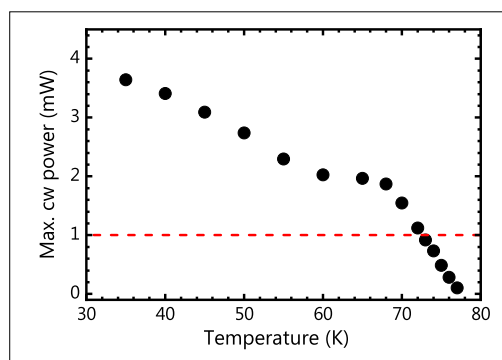
X. Lü, B. Röben, L. Schrottke, K. Biermann, T. Hagelschuer<sup>1</sup>, M. Wienold<sup>1</sup>, H.-W. Hübers<sup>1</sup>, H. T. Grahn

Terahertz (THz) quantum-cascade lasers (QCL) are promising radiation sources for spectroscopic applications such as absorption and heterodyne spectroscopy. Since 2014, a THz QCL developed at our institute has been employed as the local oscillator on board of SOFIA (Stratospheric Observatory For Infrared Astronomy) for the detection of interstellar atomic oxygen. Due to high emission powers and narrow line widths of THz QCLs in continuous-wave (cw) operation, they are excellent radiation sources for high-resolution spectroscopy. For such applications, an intrinsic tuning range of 5 to 10 GHz is required to analyze the line shape of an absorption line. A similar tuning behavior allows for the detection of a possible Doppler shift of radiation received from interstellar objects detected by heterodyne techniques. However, in order to use these sources in actual applications, several specifications for the operating parameters have to be fulfilled. First of all, the wall plug efficiency has to be sufficiently high for operation in a compact mechanical cooler in order to avoid the usage of liquid coolants. We recently demonstrated that THz QCLs based on GaAs/AlAs heterostructures exhibit significantly larger wall plug efficiencies than similar lasers relying on GaAs/Al<sub>0.25</sub>Ga<sub>0.75</sub>As heterostructures [L. Schrottke et al., Appl. Phys. Lett. **108**, 102102 (2016)]. Second, QCLs are the source of choice for many applications if a cw output power of at least 1 mW is necessary. Third, this output power has to be correlated to a maximum operating temperature in order to be useful for spectroscopic applications. Hence, we define a practical operating temperature  $T_{po}$  as

the temperature at which the QCL exhibits an optical output power of at least 1 mW emitted in a fundamental Gaussian mode. In order to further increase the values for  $T_{po}$ , we use QCLs based on Fabry-Pérot resonators with single-plasmon waveguides, for which the reflectivity of the back facet is enhanced by an additional mirror.

We have developed GaAs/AlAs QCLs for 4.75 THz, which is particularly important for the detection of a fine-structure transition of atomic oxygen. The QCL structure consists of 88 periods with 8 quantum wells in each period. The QCL exhibits threshold current densities below 200 A/cm<sup>2</sup>. For cw operation of standard Fabry-Pérot lasers with ridge lengths of up to 1 mm, the typical output powers are several mW. In order to improve the values for  $T_{po}$ , we have fabricated Fabry-Pérot lasers with ridge

**Fig. 1.** Maximum cw output power of a 4.75-THz GaAs/AlAs QCL with ridge dimensions of 0.08 × 0.87 mm<sup>2</sup> operated in a Stirling cooler as a function of heat sink temperature. The dashed line indicates the output power of 1 mW.



<sup>1</sup> Deutsches Zentrum für Luft- und Raumfahrt Institut für Optische Sensorsysteme, Berlin, Deutschland

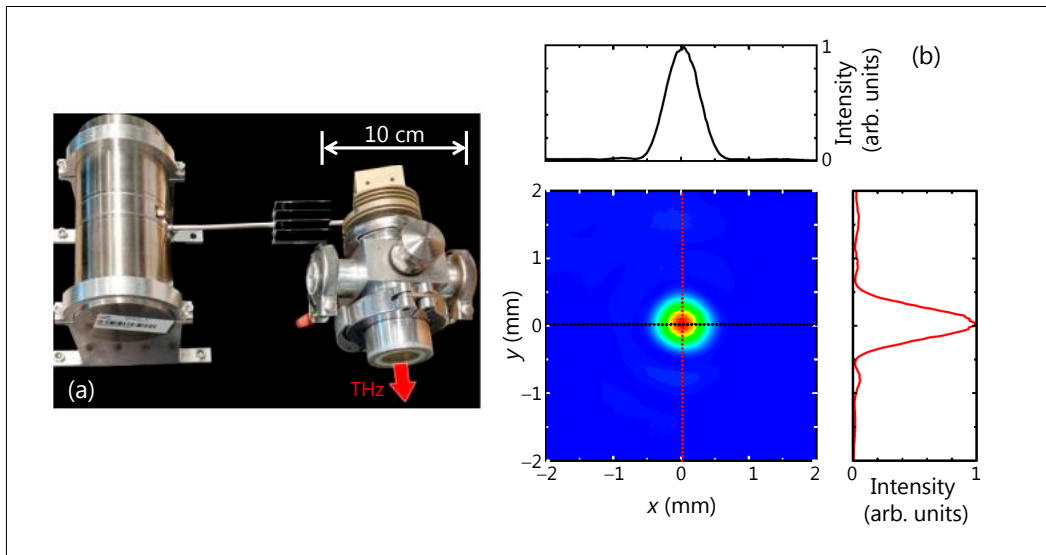


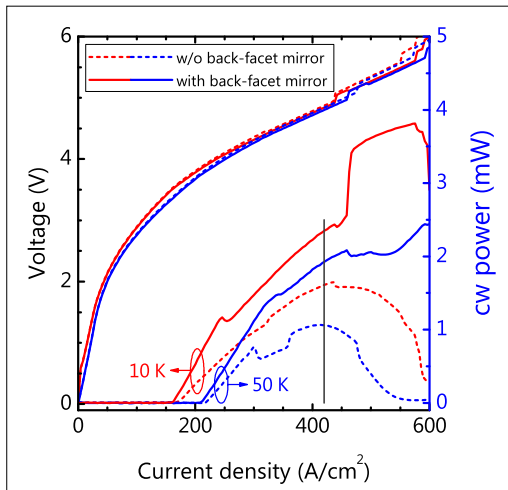
**Fig. 2.** (a) Photograph of a miniature Stirling cryocooler consisting of a cold finger mounted in a vacuum housing and a cylindrical compressor unit. (b) Beam profile of the 4.75-THz GaAs/AlAs QCL with ridge dimensions  $0.08 \times 0.90 \text{ mm}^2$  operated in a miniature Stirling cryocooler.

lengths significantly smaller than 1 mm and ridge widths of 80  $\mu\text{m}$ . Figure 1 shows the maximum cw output power of a QCL with laser ridge dimensions of  $0.08 \times 0.87 \text{ mm}^2$  from this wafer as a function of heat sink

temperature operated in a Stirling cooler. A maximum output power of about 4 mW is obtained, and the maximum value of  $T_{po}$  reaches 72 K.

This type of laser can readily be operated in a miniature cryocooler, as shown in Fig. 2(a), with a cooling power of about 1 W. Figure 2(b) shows the beam profile of another 4.75-THz QCL with ridge dimensions of  $0.08 \times 0.90 \text{ mm}^2$  from the same wafer obtained by using a poly-4-methylpentene-1 (TPX) lens operated in the miniature cryocooler. The beam profile is almost Gaussian shaped with a second reduced intensity maximum due to diffraction at the TPX lens.

**Fig. 3.** Experimental output power-current density-voltage characteristics for cw operation of a 4.75-THz GaAs/AlAs QCL with ridge dimensions of  $0.08 \times 0.58 \text{ mm}^2$  without (dashed lines) and with (solid lines) an additional back-facet mirror at heat sink temperatures of 10 and 50 K.



An increase of the optical output power can be achieved if the reflectivity of the back facet is enhanced using an additional back-facet mirror. This mirror consists of a piece of GaAs coated with 100 nm Au and 50 nm  $\text{SiO}_x$  and was mounted close to the back facet using epoxy. Figure 3 shows the output power-current density-voltage characteristics for another laser from the same wafer with ridge dimensions of  $0.08 \times 0.58 \text{ mm}^2$  with and without (w/o) an

additional back-facet mirror operated in a helium-flow cryostat at 10 and 50 K. Below  $420 \text{ A/cm}^2$  [vertical line in Fig. 3], the optical output power is enhanced by up to 48 and 83 % at 10 and 50 K, respectively, for the QCL with the additional back-facet mirror. This mirror also results in a lower threshold current density and a larger slope efficiency.

Under optimized operating conditions, i.e., the QCL is operated in a miniature cryocooler with an appropriate thermal management and improved properties of the

optical components, this THz QCL can reach output powers of up to 8 mW and a value for  $T_{po}$  above 76 K [T. Hagelschuer *et al.*, IEEE Trans. Terahertz Sci. Technol. **9**, 606 (2019)]. This QCL emits a single mode around the rest frequency of atomic oxygen, which can be tuned from -2.7 to +9.4 GHz. The realization of THz QCLs operating in a miniature cryocooler, which can supply sufficient output power and large intrinsic tuning range, also opens a pathway for the application of THz QCLs as local oscillators in satellite-based instruments for astronomy and atmospheric science.

# Quantum-cascade lasers for terahertz spectroscopy of atoms and ions in plasmas

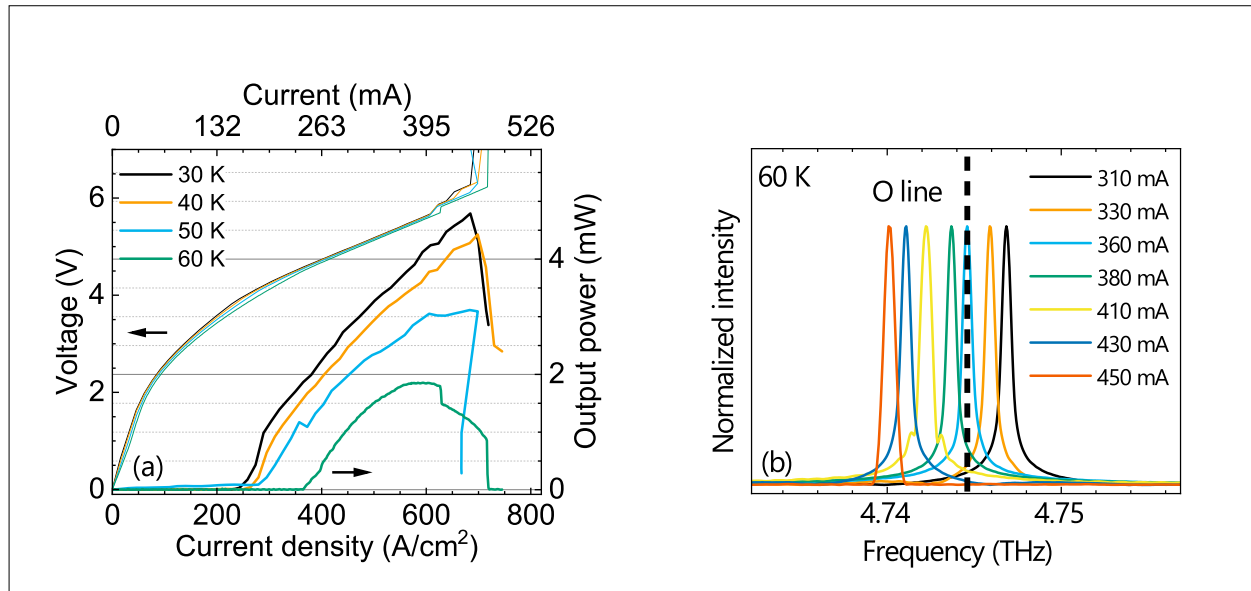
B. Röben, X. Lü, L. Schrottke, K. Biermann, M. Hannemann<sup>1</sup>, J. H. van Helden<sup>1</sup>, J. Röpcke<sup>1</sup>, H. T. Grahn

High-resolution spectroscopy greatly benefits from the application of continuous-wave lasers due to their very narrow linewidths. However, for the far-infrared or terahertz (THz) spectral range, only a few laser sources, which are sufficiently compact, exist. Recently, THz quantum-cascade lasers (QCL), which are unipolar semiconductor heterostructure lasers, have attracted substantial interest for spectroscopic applications due to their many features, which are favorable for high-resolution spectroscopy. In particular, THz QCLs in continuous-wave operation achieve output powers above 1 mW and linewidths in

the MHz (free-running) to kHz (stabilized) range. Additionally, the emission frequencies can be continuously adjusted through bandstructure engineering over the rather large frequency range between 1.2 and 5.4 THz. However, the maximum operating temperature of THz QCLs in continuous-wave operation amounts to only 130 K, hampering practical applications. Fortunately, this drawback can be substantially mitigated by using compact and portable Stirling cryocoolers.

In collaboration with the INP Greifswald, we are developing a spectrometer for the

**Fig. 1.** (a) Output power-current density-voltage characteristics of a GaAs/AlAs QCL emitting at about 4.75 THz for different cold finger temperatures. The QCL stripe has a size of  $120 \times 548 \mu\text{m}^2$ . (b) Emission spectra of the same QCL as in (a) at different injection currents taken at a cold finger temperature of 60 K. The dashed line marks the position of the absorption line of atomic oxygen. The tuning range, i.e., the frequency difference between the modes at the current values of 310 and 450 mA, amounts to 6.7 GHz.



<sup>1</sup> Leibniz-Institut für Plasmaforschung und Technologie Greifswald, Deutschland

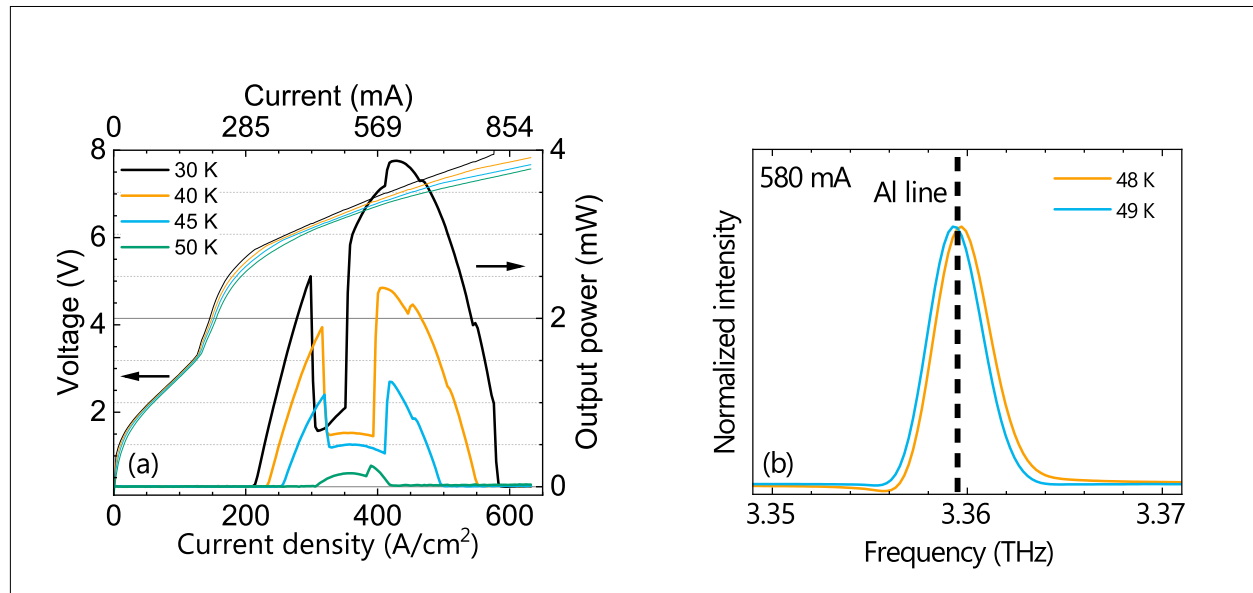
detection of different atoms and ions in plasmas, which are crucial for the (plasma-assisted) deposition of Si-based films and AlN layers, based on our THz QCLs. In order to control the deposition of these films, the quantitative determination of the density of the relevant atoms/ions is required. In contrast to the usually employed indirect detection techniques using for example ultraviolet radiation, the density of Si, Al, N<sup>+</sup>, and O can be directly determined using their fine-structure transitions at 2.31, 3.36, 3.92, and 4.75 THz, respectively, in a transmission setup. For that purpose, single-mode THz QCLs emitting precisely at these frequencies are required. In order to also cover the broadened absorption lines at elevated pressures of the plasma, a tuning range of at least 5 GHz is desirable for each frequency. For low pressures, the width of the absorption line is expected to be 100 MHz or lower.

Figure 1(a) shows the voltage and output power as a function of the current density

of a GaAs/AlAs QCL emitting at about 4.75 THz. Although the length of the QCL amounts to only 548 μm, we obtain almost 5 mW of output power at 30 K and almost 2 mW at 60 K. Figure 1(b) displays the emission spectra at a cold finger temperature of 60 K at different injection currents. The emission frequency can be continuously tuned over the absorption line of O indicated by the dashed line. The total tuning range at this temperature of 60 K amounts to 6.7 GHz, exceeding the minimum tuning range of 5 GHz desired for this application.

In order to allow for the timely development of the plasma spectroscopy setup, we also investigated already available QCLs for their suitability. Figure 2(a) shows the voltage and output power as a function of the current density of a QCL based on (Al,Ga)As barriers, which emits at about 3.36 THz. The dip in the power curves at about 350 A/cm<sup>2</sup> is due to a mode jump to a frequency, at which the absorption by atmospheric water vapor is quite large. Compared to the 4.75-

**Fig. 2.** (a) Output power-current density-voltage characteristics of a GaAs/(Al,Ga)As QCL emitting at about 3.36 THz for different cold finger temperatures. The QCL stripe has a size of 120 × 1186 μm<sup>2</sup>. (b) Emission spectra of the same QCL as in (a) at two different cold finger temperatures operated at an injection current of 580 mA. The dashed line marks the position of the absorption line of Al. The frequency difference between the two modes amounts to about 0.5 GHz.



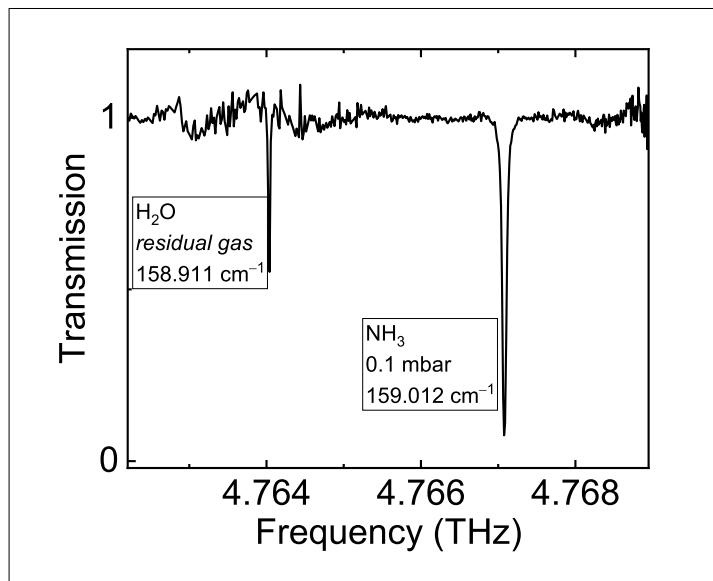


**Fig. 3.** Absorption spectrum of NH<sub>3</sub> at 4.767 THz using a 15-cm-long absorption cell.

THz QCL with AlAs barriers, the maximum output power of the 3.36-THz QCL with (Al,Ga)As barriers is somewhat smaller at 30 K and substantially more reduced toward higher temperatures, while the QCL is about twice as long. The smaller output power is essentially due to the higher thermal dissipation and to the lower wall plug efficiency, which is typical for active regions based on (Al,Ga)As barriers in comparison to AlAs barriers.

Figure 2(b) shows the emission spectra of the THz QCL emitting at about 3.36 THz. At a fixed current of 580 mA and upon increasing the temperature from 48 to 49 K, the emission mode sweeps over the absorption line of Al. More generally, the current-de-

pendent tuning behavior is characterized by mode jumps toward higher frequencies. This also limits the tuning range around the target frequency. Therefore, we continue to develop QCLs based on active regions with AlAs barriers not only for Al and O, but also for Si and N<sup>+</sup>, since this type of active region has been shown to outperform those with (Al,Ga)As barriers in terms of wall plug efficiency and tuning range.

In order to test the spectrometer, we prepared a QCL emitting at 4.767 THz for the detection of NH<sub>3</sub>. This QCL has been fabricated from the same wafer as the 4.745-THz QCL shown in Fig. 1. The absorption spectrum is displayed in Fig. 3, exhibiting an absorption line of NH<sub>3</sub> at about 4.767 THz and of H<sub>2</sub>O at about 4.764 THz. By employing these absorption lines, a precise frequency calibration can be established.

In conclusion, we have realized two QCLs with emission frequencies of 3.36 and 4.75 THz for the spectroscopy of Al and O atoms, respectively, in plasmas aiming at the direct determination of their densities. Together with additional QCLs currently under development, which are targeting at the fine-structure transitions of Si and N<sup>+</sup>, THz plasma spectroscopy using quantum-cascade lasers is expected to result in a better understanding of the processes in plasmas relevant for the deposition of thin films and consequently in their improvement.

We acknowledge the financial support of the Leibniz-Gemeinschaft under grant K54/2017.







# Departments Abteilungen

Department of Epitaxy  
[Abteilung für Epitaxie](#) ..... 120

Department of Semiconductor Spectroscopy  
[Abteilung für Halbleiterspektroskopie](#) ..... 125

Department of Microstructure  
[Abteilung für Mikrostruktur](#) ..... 133

Department of Technology and Transfer  
[Abteilung für Technologie und Transfer](#) ..... 140

# Department of Epitaxy

## Abteilung für Epitaxie

Head of Department: Dr. Lutz Geelhaar, geelhaar@pdi-berlin.de



The overall competence of this research department is the growth of crystalline thin films and nanostructures with extremely well-defined properties by epitaxy. Epitaxy is a process in which one crystal, the adsorbate, is grown on another crystal, the substrate, in such a way that there is a unique relation between the orientations of the two crystal lattices. Typically, the adsorbate is at most a few micrometers thick. Compared to the growth of bulk crystals, epitaxy offers several advantages: First, epitaxy allows the synthesis of materials that are only metastable and cannot be grown as bulk crystals at all. Thus, materials can be grown with specific and tailored properties that could not be obtained in any other way. Second, during epitaxy the composition of the growing crystal can be changed very abruptly—on the atomic scale—so that heterostructures consisting of different materials can be fabricated. In such heterostructures quantum phenomena can be observed, and by tailoring the heterostructures quantum phenomena can be manipulated and new functionalities can be achieved. Therefore, epitaxy is a means to realize nanostructured materials as well as artificial low-dimensional semiconductor systems and to tune their mechanical, optical, electronic, and magnetic properties.

The research activities in the epitaxy department are directed at two complementary tasks. On the one hand, our experimental contribution to the overall research of the institute is the fabrication of custom-designed nanostructured samples. On the other hand, the underlying growth mechanisms themselves are investigated, both for their own scientific sake and in order to optimize properties that are investigated in the core research areas. Our comprehensive expertise is based on the long tradition for

Die Kernkompetenz dieser Abteilung ist die Züchtung kristalliner Schichten und Nanostrukturen mit äußerst präzise definierten Eigenschaften mittels Epitaxie. Mit Epitaxie bezeichnet man den Prozess, in dem ein Kristall – das Adsorbat – auf einem anderen Kristall – dem Substrat – mit einer eindeutigen Beziehung zwischen den Kristallorientierungen gezüchtet wird. Dabei ist das Adsorbat typischerweise nicht dicker als einige Mikrometer. Epitaxie weist einige Vorteile im Vergleich zu der Züchtung von Volumenkristallen auf. So lassen sich mittels Epitaxie auch Materialien herstellen, die nur metastabil und als Volumenkristall gar nicht zu züchten sind. Auf diese Weise können besondere Materialien mit spezifischen, maßgeschneiderten Eigenschaften hergestellt werden. Der zweite wichtige Vorteil der Epitaxie liegt in der Möglichkeit, während des epitaktischen Wachstums die Zusammensetzung des Kristalls sehr abrupt – auf atomarer Skala – zu ändern, so dass sogenannte Heterostrukturen erzeugt werden können, die aus unterschiedlichen Materialien bestehen. In solchen Heterostrukturen können Quantenphänomene beobachtet und durch definiertes Einstellen der Strukturparameter manipuliert werden. Dies ermöglicht die Realisierung und Untersuchung neuer Funktionalitäten, die für Anwendungen interessant sein können. Epitaxie ist somit ein Werkzeug, mit dem nanostrukturierte Materialien wie auch künstliche niedrigdimensionale Halbleiterstrukturen mit einstellbaren mechanischen, optischen, elektronischen und magnetischen Eigenschaften hergestellt werden können.

Die Forschungsaktivitäten in der Epitaxie-Abteilung konzentrieren sich auf zwei komplementäre Linien. Auf der einen Seite werden für ein breites Spektrum an weiterführenden Forschungsaktivitäten am Insti-

the fabrication of two-dimensional heterostructures comprising III-V semiconductors, but in addition we work on more and more other materials. Furthermore, research on the vertical growth of III-V nanowires has become a major activity of this research department.

The technique for crystal growth that we employ at PDI is molecular beam epitaxy (MBE). In MBE, growth takes place under extremely pure conditions in ultra-high vacuum. Crystal growth is fed by beams of neutral atoms or molecules that are typically obtained by evaporating source material in effusion cells. Due to the low pressure, these atoms or molecules do not scatter or interact with each other before they reach the substrate. In order to modify the kinetics of crystal growth, the substrate temperature is adjusted. In general, MBE offers a very high level of control over the growth conditions, and growth can be monitored *in situ* by several characterization techniques.

Arguably the most mature class of compound semiconductors is formed by the group-III arsenides GaAs, AlAs, InAs, and their alloys. Very complex heterostructures can be realized in this material system with impressive precision and reproducibility. Such samples are fabricated for investigation in the core research areas *Intersubband Emitters: GaAs-based Quantum-Cascade Lasers and Control of Elementary Excitations by Acoustic Fields*.

The performance and functionality of future semiconductor devices will be enhanced by making use of three-dimensional nanostructures. Our efforts in this direction concentrate on the creation of such structures directly by growth, i.e. in a bottom-up approach with the help of self-organization mechanisms. In particular, we grow both group-III arsenides and nitrides not only as planar layers but also in the form of nanowires. Nanowires are structures with an extremely high aspect ratio and a diameter of the order of 100 nm. Their formation, prop-

tut maßgeschneiderte nanostrukturierte Proben hergestellt. Auf der anderen Seite werden die Wachstumsmechanismen selbst untersucht – aus wissenschaftlichem Interesse an den zugrundeliegenden Prozessen und um die Materialeigenschaften, die in den Forschungsschwerpunkten untersucht werden, zu optimieren. Unsere umfassende Expertise basiert auf einer langen Tradition der Herstellung zweidimensionaler Heterostrukturen, die aus III-V-Halbleitern bestehen. Mittlerweile arbeiten wir aber auch intensiv an weiteren Materialsystemen. Zudem hat sich das senkrechte Wachstum von III-V-Nanodrähten zu einer Kernaktivität der Abteilung entwickelt.

Am PDI setzen wir als Methode für Kristallzüchtung die Molekularstrahlepitaxie (MBE für englisch molecular beam epitaxy) ein. Bei diesem Verfahren findet das Wachstum unter äußerst reinen Bedingungen im Ultrahochvakuum statt. Das Kristallwachstum wird durch Atom- oder Molekülstrahlen versorgt, die typischerweise durch das Verdampfen von Quellmaterial in Effusionszellen erzeugt werden. Aufgrund des niedrigen Drucks in der Wachstumskammer streuen die Atome beziehungsweise Moleküle nicht und erfahren auch keine Wechselwirkung untereinander, bis sie auf das Substrat treffen. Um die Kinetik des Kristallwachstums zu modifizieren, wird die Substrattemperatur geregelt. Generell bietet MBE ein sehr hohes Maß an Kontrolle über Wachstumsbedingungen, und das Wachstum kann *in situ* mittels mehrerer Charakterisierungs-techniken überwacht werden.

Die wohl am weitesten entwickelte Klasse von Verbindungshalbleitern wird von den Gruppe-III-Arseniden GaAs, AlAs, InAs und deren Legierungen gebildet. In diesem Materialsystem lassen sich sehr komplexe Heterostrukturen mit beeindruckender Präzision und Reproduzierbarkeit herstellen. Solche Proben werden für weitere Untersuchungen in den Forschungsschwerpunkten *Intersubband-Emitter: GaAs-basierte Quan-*

erties, and applications are the subject of the core research area *III-V Nanowires for Optoelectronics*.

Research activities with the focus on the synthesis of materials are carried out in the core research area *Nanofabrication*. At present, the epitaxy of group-III arsenides, group-III nitrides, ferromagnetic Heusler alloys like  $\text{Co}_2\text{FeSi}$  in hybrid structures with group-III arsenide heterostructures and  $\text{MgO}$ , transparent semiconducting oxides ( $\text{Ga}_2\text{O}_3$ ,  $\text{In}_2\text{O}_3$ ,  $\text{NiO}$ , and  $\text{SnO}$ ), phase-change alloys in the material system Ge-Sb-Te, graphene (the two-dimensional allotrope of carbon), and hexagonal BN is investigated. This research takes place in close collaboration with the core research area *Nanoanalytics* in which the emphasis of the research is on materials properties.

In practice, the key features of MBE described before can only be achieved by combining a considerable number of different technical components, and hence MBE systems are fairly complex. The core component of such systems is a chamber made from stainless steel in which ultra-high vacuum is maintained and the actual crystal growth takes place. In order to preserve ultra-purity and avoid cross-contamination, each material system requires its own, dedicated MBE chamber. For the two main material systems of PDI, group-III arsenides and group-III nitrides, we can pursue the multitude of research projects only by operating more than one MBE chamber each. In total, there are at present eleven MBE systems in use. For the fabrication of hybrid structures comprising different materials, growth on the same sample has to take place subsequently in more than one MBE chamber. In order to avoid contamination of the interface between two materials, such samples have to be transported from one MBE chamber to the other under ultra-high vacuum conditions. Thus, some of our MBE chambers are connected as cluster systems. As an alternative, mobile ultra-high vacuum shuttle chambers are

*tenkaskadenlaser und Kontrolle von Elementaranregungen durch akustische Felder hergestellt.*

Die Leistung und Funktionalität zukünftiger Halbleiter-Bauelemente wird durch die Verwendung von dreidimensionalen Nanostrukturen verbessert werden. Unsere Bemühungen in diesem Zusammenhang konzentrieren sich auf die Ausbildung solcher Strukturen direkt während des Wachstums, das heißt durch Ausnutzung von Selbstorganisationsphänomenen. Insbesondere züchten wir sowohl Gruppe-III-Arsenide als auch -Nitride nicht mehr nur als planare Schichten, sondern auch als Nanodrähte. Nanodrähte sind Strukturen, die ein äußerst hohes Aspektverhältnis und einen Durchmesser in der Größenordnung von 100 nm aufweisen. Die Bildung, die Eigenschaften und die Anwendungen von Nanodrähten sind Untersuchungsgegenstand des Forschungsschwerpunkts *III-V-Nanodrähte für Optoelektronik*.

Die Synthese von Materialien steht hingegen im Fokus des Forschungsschwerpunkts *Nanofabrikation*. Gegenwärtig werden hier die Epitaxie von Gruppe-III-Arseniden und -Nitriden, ferromagnetischen Heusler-Legierungen wie  $\text{Co}_2\text{FeSi}$  in Hybridstrukturen mit Gruppe-III-Arsenid-Heterostrukturen und  $\text{MgO}$ , transparenten halbleitenden Oxiden ( $\text{Ga}_2\text{O}_3$ ,  $\text{In}_2\text{O}_3$ ,  $\text{NiO}$  und  $\text{SnO}$ ), Phasenwechsel-Materialien des Systems Ge-Sb-Te, Graphen (das zweidimensionale Allotrop von Kohlenstoff) und hexagonalem BN untersucht. Diese Forschung wird in enger Zusammenarbeit mit dem Forschungsschwerpunkt *Nanoanalytik* durchgeführt.

In der Praxis lassen sich die beschriebenen Schlüsselmerkmale von MBE nur erreichen, wenn eine beträchtliche Anzahl unterschiedlicher technischer Komponenten kombiniert wird. Daher sind MBE-Anlagen recht komplex. Die Kernkomponente eines solchen Systems ist eine Kammer, die aus Edelstahl gefertigt wird. Hier findet das

also employed to transfer samples between MBE systems.

As a distinctive experimental feature, PDI owns three special MBE chambers that allow the in-situ, real-time analysis of growth processes by x-ray diffraction. To this end, these chambers can be connected to our own beamline at the synchrotron BESSY II (Helmholtz-Zentrum Berlin für Materialien und Energie). The successful operation of such a setup critically depends on the continuous stationary operation of the MBE system at the synchrotron, since a high quality of the epitaxial layers and interfaces is imperative for a reliable quantitative analysis. Consequently, at least one of these special MBE chambers is always located at the synchrotron. Currently, a system equipped for the study of semiconducting oxides is installed there.

This year, we have updated one of our MBE systems for group-III nitrides by replacing the entire sample transfer system and the substrate manipulator. The former modification necessitated also an exchange of the corresponding vacuum chambers. The update aims at improving the reliability of that system. Furthermore, as a strategic extension of our materials characterization possibilities, we have purchased an x-ray and ultraviolet photoelectron spectroscopy system. This system will be beneficial for research at PDI in multiple ways. We can analyze chemical bonding states close to the surface, which is particularly relevant for van der Waals materials and heterostructures. Also, the composition of novel complex alloys like ternary oxides can be determined, and in combination with a sputter source depth profiles can be extracted. Likewise, interfacial reactions in extreme heterostructures, e.g. involving metals and semiconductors, can be analyzed. In addition, we can study the work function of novel materials, and investigate band bending and band offsets. We are excited about these new opportunities for our research and look forward to such studies.

eigentliche Kristallwachstum statt. Um die extreme Reinheit zu erhalten und wechselseitige Verunreinigungen zu vermeiden, braucht jedes Materialsystem seine eigene, dedizierte Wachstumskammer. Für die zwei zentralen Materialsysteme des PDI, Gruppe-III-Arsenide und -Nitride, lässt sich die Vielfalt der Forschungsprojekte nur durchführen, wenn jeweils mehr als eine Kammer zur Verfügung steht. Insgesamt sind am Institut zurzeit elf MBE-Anlagen in Betrieb. Wenn hybride Strukturen aus unterschiedlichen Materialien hergestellt werden sollen, muss das Wachstum an derselben Probe nach einander in mehr als einer MBE-Kammer stattfinden. Um eine Verunreinigung der Grenzfläche zwischen zwei Materialien zu vermeiden, müssen diese Proben zwischen MBE-Kammern unter Ultrahochvakuumbedingungen transportiert werden. Deshalb sind einige unserer MBE-Anlagen als Cluster-Systeme konzipiert. Alternativ verwenden wir kleine mobile Ultrahochvakuumkammern, um den Probentransfer zwischen MBE-Kammern zu gewährleisten.

Als experimentelle Besonderheit stehen dem PDI drei spezielle MBE-Anlagen zur Verfügung, die In-situ-Studien der Wachstumsprozesse mittels Röntgenbeugung in Echtzeit ermöglichen. Hierfür können die Kammern mit unserem eigenen Strahlrohr am Synchrotron BESSY II (Helmholtz-Zentrum Berlin für Materialien und Energie) verbunden werden. Der erfolgreiche Betrieb eines derartigen Aufbaus hängt wesentlich vom kontinuierlichen, stationären Einsatz der MBE-Anlage am Synchrotron ab. Infolgedessen befindet sich mindestens eine dieser speziellen MBE-Anlagen stets am Synchrotron. Zurzeit wird dort eine MBE-Anlage betrieben, die für die Analyse halbleitender Oxide eingerichtet ist.

In diesem Jahr rüsteten wir eines unserer MBE-Systeme für Gruppe-III-Nitride auf indem wir das gesamte Probentransfersystem und den Substratmanipulator ersetzen. Die erstere Modifikation machte auch

einen Austausch der entsprechenden Vakuumkammern erforderlich. Diese Aufrüstung zielt darauf ab, die Zuverlässigkeit dieses Systems zu verbessern. Darüber hinaus schafften wir als strategische Erweiterung unserer Möglichkeiten zur Materialcharakterisierung ein System für Röntgen- und Ultraviolettspektralphotoelektronenspektroskopie an. Dieses System wird für die Forschung am PDI in mehrfacher Hinsicht von Nutzen sein. Wir können chemische Bindungszustände nahe der Oberfläche analysieren, was insbesondere für van der Waals-Materialien und -Heterostrukturen relevant ist. Außerdem können die Zusammensetzung neuartiger komplexer Legierungen wie ternärer Oxide bestimmt und in Kombination mit einer Sputterquelle Tiefenprofile extrahiert werden. Ebenso können Grenzflächenreaktionen in extremen Heterostrukturen, zum Beispiel aus Metallen und Halbleitern, analysiert werden. Zudem können wir die Austrittsarbeit neuartiger Materialien untersuchen und Bandverbiegungen und Bandkantensprünge untersuchen. Wir sind begeistert über diese neuen Möglichkeiten für unsere Forschung und freuen uns auf solche Studien.

# Department of Semiconductor Spectroscopy

## Abteilung für Halbleiterspektroskopie

Head of Department: Prof. Dr. Holger T. Grahn, htgrahn@pdi-berlin.de

The overall competence of this research department lies in the physics and applications of semiconductor hetero- and nanostructures, in particular with regard to their electronic and optical properties. The research topics include the investigation of elementary excitations in solids controlled by surface acoustic waves, the optical properties of III-V nanowires and heterostructures, terahertz quantum-cascade lasers, spin generation and transport in ferromagnet-semiconductor hybrid structures, quantum transport in semiconductor-based nanoscale systems, and topological insulators. Dedicated spectroscopic and magneto-transport techniques are used to determine the electronic, optical, and transport characteristics of these semiconductor hetero- and nanostructures.

- Elementary excitations controlled by acoustic fields are investigated in solids by optical spectroscopy. Photons, electrons, and spins can be manipulated at gigahertz frequencies using surface acoustic waves opening new perspectives for applications in optoelectronic devices.
- The optical properties of III-V nanowires and heterostructures are investigated by spatially and time-resolved photoluminescence spectroscopy as well as by cathodoluminescence spectroscopy in a scanning electron microscope. Of particular importance is the correlation between structural defects and optical properties in III-V nanowires.
- Quantum-cascade lasers for the terahertz spectral region are designed, their optical as well as transport properties are simulated, complete lasers are realized, and their lasing properties are investigated. These lasers are compact sources, can be operated in single mode, exhibit

Die übergreifende Kompetenz dieser Forschungsabteilung liegt in der Physik und den Anwendungen von Hetero- und Nanostrukturen aus Halbleitern, insbesondere bezüglich ihrer elektronischen und optischen Eigenschaften. Die Forschungsthemen umfassen die Untersuchung von Elementaranregungen in Festkörpern kontrolliert durch akustische Oberflächenwellen, optischen Eigenschaften von III-V-Nanodrähten und -Heterostrukturen, Terahertz-Quantenkaskadenlasern, Spinerzeugung und -transport in Ferromagnet-Halbleiter-Hybridstrukturen, Quantentransport in nanoskaligen Halbleiter-Systemen und topologischen Isolatoren. Dedizierte spektroskopische und Magnetotransport-Methoden werden zur Bestimmung der elektronischen, optischen und Transport-Charakteristika von diesen Hetero- und Nanostrukturen aus Halbleitern verwendet.

- Elementaranregungen kontrolliert durch akustische Felder werden in Festkörpern mittels optischer Spektroskopie untersucht. Photonen, Elektronen und Spins können bei Gigahertz-Frequenzen mittels akustischer Oberflächenwellen manipuliert werden, was neue Perspektiven für Anwendungen in optoelektronischen Bauelementen eröffnet.
- Die optischen Eigenschaften von III-V-Nanodrähten und -Heterostrukturen werden mit räumlich und zeitlich aufgelöster Photolumineszenz-Spektroskopie sowie Kathodolumineszenz-Spektroskopie in einem Rasterelektronenmikroskop untersucht. Von besonderer Bedeutung ist die Korrelation von strukturellen Defekten mit den optischen Eigenschaften von III-V-Nanodrähten.
- Quantenkaskadenlaser werden für den Terahertz-Spektralbereich entwickelt,



typical optical output powers between several mW and several tens of mW, and function at temperatures, which do not require cooling with liquid helium.

- The generation and the transport of spins in ferromagnet-semiconductor hybrid structures are studied by analyzing their magneto-optical and magneto-transport properties. In order to achieve spin control, all-electrical spin injection and detection are investigated using lateral and vertical spin valve devices.
- The electronic and spin properties of semiconductor-based nanoscale systems such as nanowires and quantum dots defined laterally in heterostructures are studied by quantum-transport experiments aiming at the development of new strategies for information processing.
- The electronic transport properties of topological insulators, in which charges are only transported on the surface and not in the bulk, are investigated by examining the weak antilocalization effect due to spin orbit coupling and the electron-electron interaction.

The facilities for optical spectroscopy include Raman spectroscopy to study the vibrational modes in semiconductor films, heterostructures, and nanowires as well as in topological insulators and graphene. Continuous-wave photoluminescence and photoluminescence excitation spectroscopy from the ultraviolet (244 nm) to the near-infrared spectral region ( $1.7 \mu\text{m}$ ) are used to investigate III-V films, heterostructures, and nanowires. The spectroscopic techniques for the near-infrared to ultraviolet spectral regions such as Raman and photoluminescence spectroscopy can also be used with a spatial resolution down to about  $0.5 \mu\text{m}$  and in magnetic fields up to 8 T. With cathodoluminescence spectroscopy and imaging in a scanning electron microscope, the spatial resolution can be enhanced into the range of ten nanometers. In addition, element identification is achieved by energy- and wavelength-dis-

deren optische und Transport-Eigenschaften werden berechnet, vollständige Laser werden realisiert und deren Laser-eigenschaften werden untersucht. Diese Quantenkaskadenlaser sind kompakte Quellen, erlauben Einzelmodenbetrieb, besitzen typische optische Ausgangsleistungen zwischen einigen mW und einigen zehn mW, und funktionieren bei Temperaturen, die keine Kühlung mit flüssigem Helium erfordern.

- Die Erzeugung und der Transport von Spins werden in Ferromagnet-Halbleiter-Hybridstrukturen untersucht, indem ihre magneto-optischen und Magnetotransport-Eigenschaften analysiert werden. Um Kontrolle über Spins in einem Halbleiter zu erhalten, wird die rein elektrische Injektion und Detektion von Spins mit lateralen und vertikalen Spinventil-Bau-elementen untersucht.
- Die elektronischen und Spin-Eigenschaften von nanoskaligen Halbleiter-Systmen wie beispielsweise Nanodrähte und Quantenpunkte, die lateral in Heterostrukturen definiert sind, werden mittels Quantentransportexperimenten für die Entwicklung neuer Strategien in der Informationsverarbeitung untersucht.
- Die elektronischen Transporteigenschaften von topologischen Isolatoren, in denen Ladungsträger nur an der Oberfläche und nicht im Volumen transportiert werden, werden durch Analyse der schwachen Antilokalisierung infolge der Spin-Bahn-Kopplung und der Elektron-Elektron-Wechselwirkung untersucht.

Im Bereich der spektroskopischen Messmethoden steht uns die Ramanspektroskopie für Untersuchungen der Schwingungsmoden in Halbleiterschichten, Heterostrukturen, Nanodrähten, topologischen Isolatoren und Graphen zur Verfügung. Darüber hinaus werden III-V-Schichten, -Heterostrukturen und -Nanodrähte mittels Photolumineszenz- und Photolumineszenzanregungs-Spektroskopie vom ultravioletten (244 nm) bis zum nah-infraroten ( $1,7 \mu\text{m}$ )

persive x-ray spectroscopy, and the crystallographic orientation as well as the strain state can be determined using electron backscatter diffraction. Time-resolved photoluminescence spectroscopy on a pico- to microsecond time scale from the ultraviolet (240 nm) to the near-infrared spectral region (1.3  $\mu\text{m}$ ) and pump-and-probe spectroscopy with a subpicosecond time resolution are employed to investigate the carrier and polarization dynamics in III-V films, heterostructures, and nanowires. Fourier-transform spectroscopy is used in the far-infrared or terahertz spectral region to record the lasing parameters of quantum-cascade lasers and in the mid-infrared region to study vibrational modes. The magneto-transport experiments on ferromagnet-semiconductor hybrid devices, semiconductor-based nanoscale systems, and topological insulators can be performed in magnetic fields up to 16 T and at temperatures down to 20 mK.

In 2019, a solid-state platform for dynamic polariton control has been introduced, which is based on the combination of intra-cavity potential traps, defined by a spatial modulation of the microcavity thickness, with dynamic control via nonlinear polariton-polariton interactions as well as time and spatially dependent strain fields. First, important functionalities of the platform have been demonstrated such as dynamic control of the energy and internal degrees of freedom as well as the energy matching of neighboring traps. Then, the coherent modulation and symmetry control of a lattice of coupled traps by strain fields have been established, which enables the creation of dynamic states within the band gap of the lattice. As an important characteristic, the acoustic modulation was found to maintain the coherence of macroscopic polariton states and does not depend on the polariton density. These functionalities of the strongly nonlinear, tunable, and spatially compact polariton platform can be well described by a theoretical framework and represent important steps towards

Spektralbereich untersucht. Die spektroskopischen Methoden für den nah-infraroten bis ultravioletten Spektralbereich wie die Raman- und Photolumineszenz-Spektroskopie können auch mit einer räumlichen Auflösung von bis zu 0,5  $\mu\text{m}$  und in Magnetfeldern von bis zu 8 T eingesetzt werden. Mit der Kathodolumineszenz-Spektroskopie in Kombination mit den Abbildungsmöglichkeiten eines Rasterelektronenmikroskops kann die Ortsauflösung bis in den Bereich von zehn Nanometern verbessert werden. Hinzu kommt die Möglichkeit, chemische Elemente durch energie- und wellenlängendiffusive Röntgenspektroskopie zu identifizieren. Mittels der Elektronenrückstreuung erhalten wir Informationen über die kristallographische Orientierung sowie Verspannungen im Material. Zeitaufgelöste Photolumineszenz-Spektroskopie auf einer Zeitskala von Piko- bis Mikrosekunden vom ultravioletten (240 nm) bis zum nah-infraroten (1,3  $\mu\text{m}$ ) Spektralbereich sowie Anrege-Abtast-Spektroskopie mit einer Zeitauflösung unterhalb einer Pikosekunde werden eingesetzt, um die Ladungsträger- und Polarisationsdynamik in III-V-Schichten, -Heterostrukturen und -Nanodrähten zu untersuchen. Mittels Fouriertransform-Spektroskopie werden im ferninfraroten Spektralbereich die Emissionseigenschaften von Terahertz-Quantenkaskadenlasern und im mittleren infraroten Spektralbereich Schwingungsmoden untersucht. Die Magnetotransport-Experimente an Ferromagnet-Halbleiter-Hybrid-Bauelementen, nanoskaligen Halbleiter-Systemen und topologischen Isolatoren können in Magnetfeldern bis zu 16 T und Temperaturen bis herunter zu 20 mK durchgeführt werden.

Im Jahr 2019 wurde eine Festkörper-Plattform für die dynamische Polaritonenkontrolle eingeführt, die auf einer Verknüpfung von Potenzialfallen innerhalb des Resonators, die durch eine räumliche Modulation der Dicke des Mikroresonators definiert sind, mit der dynamischen Kontrolle mittels nichtlinearer Polariton-Polariton-Wechselwirkung sowie zeit- und räumlich abhängi-

tunable polaritonic devices based on lattices of interacting polariton traps.

The piezoelectric generation and propagation of longitudinal bulk acoustic waves with frequencies up to 20 GHz in GaAs crystals have been investigated using bulk acoustic-wave resonators based on piezoelectric thin ZnO films, where the electro-acoustic conversion efficiency depends sensitively on the sputtering conditions of the ZnO films. The investigations have been extended to frequency and temperature ranges, which have so far not been experimentally accessed. The acoustic absorption of GaAs in the temperature range from 80 to 300 K is dominated by scattering with thermal phonons. In contrast, at lower temperatures, the acoustic absorption saturates at a frequency-dependent value. Devices with a high quality factor fabricated on top of acoustic Bragg reflectors are also demonstrated. These results prove the feasibility of high-quality acoustic resonators embedding GaAs-based nanostructures, thus opening the way for the modulation and control of their properties by electrically excited superhigh-frequency longitudinal bulk acoustic waves.

Several of the key issues of planar (Al,Ga)N-based deep-ultraviolet light-emitting diodes could potentially be overcome by utilizing nanowire heterostructures, exhibiting high structural perfection and improved light extraction. The spontaneous emission of GaN/(Al,Ga)N nanowire ensembles grown on Si(111) by plasma-assisted molecular beam epitaxy has been studied. The nanowires contain single GaN quantum disks embedded in long (Al,Ga)N nanowire segments essential for efficient light extraction. These quantum disks have been found to exhibit intense light emission at unexpectedly high energies, namely, significantly above the GaN bandgap, almost independent of the disk thickness. An in-depth investigation has revealed a spontaneously formed Al gradient both, along and across the nanowire, resulting in a complex

ger Verspannungsfelder beruht. Als erstes wurden wichtige Funktionalitäten dieser Plattform wie die dynamische Kontrolle der Energie und der internen Freiheitsgrade sowie der Energieabgleich benachbarter Fallen aufgezeigt. Als nächstes wurde die kohärente Modulation und Symmetriekontrolle eines Gitters von gekoppelten Fallen durch Verspannungsfelder nachgewiesen, was die Erzeugung dynamischer Zustände innerhalb der Bandlücke des Gitters ermöglicht. Eine wichtige Eigenschaft ist, dass die akustische Modulation die Kohärenz makroskopischer Polariton-zustände erhält und nicht von der Polariton-dichte abhängt. Diese Funktionalitäten der stark nichtlinearen, durchstimmmbaren und räumlich komprimierten Polariton-Plattform können durch ein theoretisches Modell beschrieben werden und stellen einen wichtigen Schritt in Richtung durchstimmbarer polaritonischer Bauelemente dar, die auf Gittern von wechselwirkenden Polariton-fallen basieren.

Die piezoelektrische Erzeugung und Ausbreitung von longitudinalen akustischen Wellen mit Frequenzen bis zu 20 GHz in GaAs-Kristallen wurde mittels Resonatoren für akustische Wellen im Volumen basierend auf piezoelektrischen, dünnen ZnO-Schichten untersucht, bei denen die elektroakustische Umwandlungseffizienz empfindlich von den Sputterbedingungen der ZnO-Schichten abhängt. Die Untersuchungen wurden auf Frequenz- und Temperaturbereiche erweitert, die bisher nicht experimentell zugänglich waren. Die akustische Absorption von GaAs im Bereich von 80 bis 300 K wird durch Streuung an thermischen Phononen dominiert. Dagegen sättigt die akustische Absorption bei tieferen Temperaturen auf einen frequenzabhängigen Wert. Bauelemente mit einem hohen Gütefaktor wurden auf akustischen Bragg-Reflektoren hergestellt. Diese Resultate zeigen die Realisierbarkeit von akustischen Resonatoren hoher Güte, die GaAs-Nanostrukturen einbetten, so dass der Weg für die Modulation und Kontrolle ihrer Eigen-

core/shell structure with an Al-deficient core and an Al-rich shell with continuously varying Al content along the entire length of the (Al,Ga)N segment. This compositional change along the nanowire growth axis induces a polarization doping of the shell that results in a degenerate electron gas in the disk, thus screening the built-in electric fields. The high carrier density not only results in the unexpectedly high transition energies, but also in radiative lifetimes depending only weakly on temperature, leading to a comparatively high internal quantum efficiency of the GaN quantum disks up to room temperature.

While the properties of wurtzite GaAs have been extensively studied during the past decade, little is known about the influence of the crystal polytype on ternary (In,Ga)As quantum well structures. This question has been addressed with a unique combination of correlated, spatially resolved measurement techniques on core/shell nanowires that contain extended segments of both the zincblende and wurtzite polytypes. Cathodoluminescence hyperspectral imaging reveals a blue-shift of the quantum well emission energy in the wurtzite polytype segment. Nanoprobe x-ray diffraction and atom probe tomography have enabled  $k \cdot p$  calculations for the specific sample geometry to reveal two comparable contributions to this shift. First, there is a 30% drop in In mole fraction going from the zincblende to the wurtzite segment. Second, the quantum well is under compressive strain, which has a much stronger impact on the hole ground state in the wurtzite than in the zincblende segment. The results highlight the role of the crystal structure in tuning the emission of (In,Ga)As quantum wells and pave the way to exploit the possibilities of band gap engineering in core/shell nanowire heterostructures.

Terahertz quantum-cascade lasers (THz QCLs) are currently unparalleled for high-resolution spectroscopy of very sharp absorption lines in the range between 2 and

schaften durch elektrisch angeregte longitudinale akustische Wellen im Volumen bei superhohen Frequenzen bereitet ist.

Einige der Schlüsselfragen von planaren (Al,Ga)N-basierten Leuchtdioden für den tiefen Ultraviolettbereich könnten möglicherweise durch die Verwendung von Nanodraht-Heterostrukturen, die eine hohe strukturelle Perfektion und eine verbesserte Lichtauskopplung aufweisen, gelöst werden. Die spontane Emission von GaN/(Al,Ga)N-Nanodrahtensembles, die mittels Plasma-unterstützter Molekularstrahl-epitaxie auf Si(111) gewachsen wurden, ist untersucht worden. Die Nanodrähte enthalten einzelne GaN-Quantenscheiben eingebettet in langen (Al,Ga)N-Nanodrahtsegmente, die für die effiziente Lichtauskopplung essentiell sind. Diese Quantenscheiben zeigen intensive Lichtemission bei unerwartet hohen Energien, und zwar deutlich oberhalb der GaN-Bandlücke, nahezu unabhängig von der Scheibendicke. Eine gründliche Untersuchung hat einen spontan gebildeten Al-Gradienten sowohl entlang des Nanodrahts als auch senkrecht dazu aufgezeigt, so dass eine komplexe Kern/Schalen-Struktur mit einem Al-armen Kern und einer Al-reichen Schale mit kontinuierlich sich änderndem Al-Gehalt über die gesamte Länge des (Al,Ga)N-Segments entsteht. Die Zusammensetzungsänderung entlang der Nanodraht-Wachstumsrichtung induziert eine Polarisationsdotierung der Schale, die ein entartetes Elektronengas in der Scheibe zur Folge hat, so dass die eingebauten elektrischen Felder abgeschirmt werden. Die hohe Ladungsträgerdichte resultiert nicht nur in den unerwartet hohen Übergangsenergien, sondern auch in strahlenden Lebensdauern, die nur schwach von der Temperatur abhängen. Dies führt zu einer vergleichsweise hohen internen Quantenausbeute der GaN-Quantenscheiben bis hin zu Raumtemperatur.

Während die Eigenschaften von Wurtzit-GaAs im letzten Jahrzehnt eingehend

5.4 THz. Since the frequency range accessible by a single QCL is determined by its typically very limited tuning range, a particular QCL has to be fabricated for each specific application. The frequencies of the modes in THz QCLs with a Fabry-Pérot resonator have been quantitatively analyzed as a function of its length taking into account waveguide dispersion. Based on these results, a process based on mechanical polishing of the front facet has been developed to adjust the emission frequency with a precision of 1 GHz. The demonstrated process makes it possible to reliably fabricate THz QCLs for the spectroscopy of very sharp absorption lines.

For application-defined emission frequencies between 3.4 and 5.0 THz, GaAs/AlAs heterostructures have been developed to realize THz QCLs. Due to their rather large intrinsic tuning range, these THz QCLs can be used as local oscillators in airborne or satellite-based astronomical instruments or as radiation sources for high-resolution absorption spectroscopy, which is expected to allow for a quantitative determination of the density of atoms and ions in plasma processes. The GaAs/AlAs THz QCLs can be operated in mechanical cryocoolers and even in miniature cryocoolers due to the comparatively high wall-plug efficiency of around 0.2%. These lasers exhibit output powers of more than 1 mW at operating temperatures up to about 70 K, which is sufficient for most of the abovementioned applications.

The influence of free carriers on the Raman scattering in *n*-type  $\text{In}_2\text{O}_3$  has been investigated. For high-quality cubic single crystals, electronic single-particle excitations have been identified as a relatively broad Raman feature in the frequency range below  $300 \text{ cm}^{-1}$ . Furthermore, discrete phonon lines in the same frequency range exhibit asymmetric lineshapes characteristic for Fano resonances. The two observed spectral features contain the potential to be utilized for the quantitative determination

untersucht worden sind, ist über den Einfluss des Kristallpolytypen auf ternäre (In,Ga)As-Quantenschichtstrukturen bisher wenig bekannt. Dieser Frage ist mit einer einzigartigen Verbindung von korrelierten, räumlich aufgelösten Messmethoden angewandt auf Kern/Schale-Nanodrähte, die ausgedehnte Segmente von sowohl Zinkblende- als auch Wurtzit-Polytypen enthalten, nachgegangen worden. Hyperspektrale Bildgebung mit der Kathodolumineszenz-Spektroskopie lassen eine Blauverschiebung der Emissionsenergie der Quantenschicht in dem Wurtzit-Polytyp-Segment erkennen. Nanosonden-Röntgenbeugung und Atomsonden-Tomographie haben dazu geführt, dass die Ergebnisse von  $k \cdot p$ -Berechnungen für die spezifische Probengeometrie auf zwei vergleichbare Beiträge zu dieser Verschiebung hinweisen. Als erstes ist ein 30-prozentiger Rückgang des In-Gehalts vom Zinkblende- zum Wurtzit-Segment zu beobachten. Zweitens ist die Quantenschicht unter Druckspannung, was einen deutlich stärkeren Effekt auf den Lochgrundzustand im Wurtzit- als im Zinkblende-Segment hat. Die Resultate heben die Rolle der Kristallstruktur bei der Abstimmung der Emission der (In,Ga)As-Quantenschichten hervor und sind ein Wegbereiter für die Nutzung der Möglichkeiten von Bandlückenengineering in Kern/Schalen-Nanodraht-Heterostrukturen.

Terahertz-Quantenkaskadenlaser (THz-QCL) sind derzeit ohnegleichen für hochauflösende Spektroskopie von sehr scharfen Absorptionslinien im Bereich von 2 bis 5,4 THz auf Grund der sehr schmalen Linienbreiten. Da der Frequenzbereich, der durch einen einzigen QCL abgedeckt wird, durch einen sehr begrenzten Abstimmbereich bestimmt wird, muss für jede spezifische Anwendung ein spezieller QCL hergestellt werden. Die Frequenzen der Moden eines THz-QCLs mit einem Fabry-Pérot-Resonator sind als Funktion seiner Länge unter Berücksichtigung der Wellenleiterdispersion quantitativ analysiert worden. Auf der Grundlage dieser Resultate ist basie-

of the free carrier concentration in *n*-type  $\text{In}_2\text{O}_3$  using Raman spectroscopy as a contactless experimental technique.

Electrically induced resistive switching resulting from ionic transport and electrochemical redox reactions is promising for future generations of non-volatile memory devices and artificial neural computing. In this context, the key ingredient for the highly efficient neural computing is a memristor, which is a special type of a resistive two-terminal element whose electrical properties depend not only on the state of the element, but also on the history how the state has been achieved. Memristor characteristics have been demonstrated in a bilayer junction of Al and a Bi-Cu-S alloy utilizing electrically reversible generation of an insulating interface. The high resistance due to the interface layer drops abruptly by orders of magnitude when the barrier is annihilated electrochemically under a bias. The barrier is made to be robust by applying a reverse bias, giving rise to a controllable memory effect on the switching phenomenon. The switching mechanism based on the manipulation of a barrier, which is complementary to conventional bridging conductive filaments, will open the way for new functionalities as device elements.

rend auf dem mechanischen Abschleifen der vorderen Facette ein Verfahren entwickelt worden, die Emissionsfrequenz mit einer Genauigkeit von 1 GHz einzustellen. Dieses aufgezeigte Verfahren ermöglicht es, THz-QCLs für die Spektroskopie von sehr scharfen Emissionslinien zuverlässig herzustellen.

Für anwendungsbestimmte Emissionsfrequenzen zwischen 3,4 und 5,0 THz wurden GaAs/AlAs-Heterostrukturen entwickelt, um Terahertz-Quantenkaskadenlaser (THz-QCL) zu realisieren. Auf Grund ihres großen intrinsischen Abstimmungsbereichs können diese THz-QCLs als Lokaloszillatoren in Flugzeug- oder Satellit-basierten astronomischen Messinstrumenten oder als Strahlungsquellen für hochauflösende Absorptionsspektroskopie, die eine quantitative Bestimmung der Dichte von Atomen und Ionen in Plasmaprozessen ermöglichen könnte, eingesetzt werden. Die GaAs/AlAs-THz-QCLs können auf Grund ihrer vergleichsweise hohen Gesamtwirkungsgrade von ungefähr 0,2% in mechanischen Kryokühlern und sogar in Miniatur-Kryokühlern betrieben werden. Diese Laser besitzen Ausgangsleistungen von mehr als 1 mW für Betriebstemperaturen bis zu 70 K, was für die meisten der obengenannten Anwendungen ausreichend ist.

Der Einfluss von freien Ladungsträgern auf die Raman-Streuung in *n*-artigen  $\text{In}_2\text{O}_3$  wurde untersucht. Für kubische Einkristalle hoher Qualität wurden elektronische Einteilchenanregungen als ein relativ breites Raman-Merkmal im Frequenzbereich unterhalb von  $300 \text{ cm}^{-1}$  identifiziert. Weiterhin zeigen diskrete Phononlinien in dem gleichen Frequenzbereich asymmetrische Linienformen, die charakteristisch für Fano-Resonanzen sind. Die beiden beobachteten spektralen Merkmale bieten die Möglichkeit, diese für die quantitative Bestimmung der Konzentration freier Ladungsträger in *n*-artigen  $\text{In}_2\text{O}_3$  mittels der Raman-Spektroskopie als eine kontaktlose experimentelle Methode zu nutzen.

Elektrisch induziertes Widerstandsschalten auf Grund von ionischem Transport und elektrochemischen Redoxreaktionen ist vielversprechend für zukünftige Entwicklungsstufen von nichtflüchtigen Speicherbauelementen und künstliches Neuro-Computing. In diesem Zusammenhang ist der zentrale Bestandteil für das hocheffiziente Neuro-Computing ein Memristor, der ein spezieller Typ eines widerstandsartigen zweipoligen Elementes ist, dessen elektrische Eigenschaften nicht nur vom Zustand des Elements abhängen, sondern auch von dem Verlauf, wie dieser Zustand erreicht wurde. Die Charakteristik eines Memristors wurde für einen Zweischichtenübergang aus Al und einer Bi-Cu-S-Legierung gezeigt, in dem eine isolierende Grenzschicht elektrisch reversibel erzeugt wurde. Der hohe Widerstand auf Grund der Grenzschicht fällt schlagartig um mehrere Größenordnungen, wenn die Barriere elektrochemisch unter einer Vorspannung zum Verschwinden gebracht wird. Die Barriere wird durch eine Sperrvorspannung stabil, was zu einem kontrollierbaren Memory-Effekt bei dem Schaltphänomen führt. Der Schaltmechanismus basierend auf der Manipulation einer Barriere, der komplementär zur konventionellen Überbrückung von leitenden Filamenten ist, ermöglicht neue Funktionalitäten für Bauelemente.

# Department of Microstructure

## Abteilung für Mikrostruktur

Head of Department: Dr. Achim Trampert, trampert@pdi-berlin.de

The major research goal of the department Microstructure is to understand material properties on the basis of detailed knowledge of their microstructure (structure-property-relation). Here the term "microstructure" in the broadest sense includes all kinds of defects, i.e. all deviations from the regular structure, and their geometry and physical configuration—regardless of length scales. The probe volume detecting these features must therefore range from the microscopic scale to the single atom level. Consequently, advanced X-ray and electron diffraction techniques, transmission electron microscopy imaging and spectroscopy as well as scanning tunneling microscopy and spectroscopy are applied with high spatial resolution and high sensitivity to analyze quantitatively the structural, chemical and electronic properties of the wide range of material systems grown at PDI or by external collaborators. Examples are low-dimensional semiconductor heterostructures, 2D layered materials, ferromagnet-semiconductor hybrid systems, and metastable materials and novel material combinations. Experimental studies are focused on hetero-phase interfaces and phase stabilities, epitaxial strain and strain relaxation processes, and the formation of extended and complex defects. The results are compared with computer simulations and supported by theoretical modeling. Finite element calculations can virtually cover any non-trivial geometry and chemical composition profile of low-dimensional structures and may thereby provide a highly realistic view of elastic strain and piezoelectric polarization fields within heteroepitaxial systems.

Transmission electron microscopy (TEM) is one of the key tools for direct imaging of the local atomic structure of materials.

Das Ziel der Abteilung Mikrostruktur liegt darin, Materialeigenschaften auf der Basis einer detaillierten Kenntnis ihrer Mikrostruktur zu verstehen (Struktur-Eigenschaftsbeziehung). Hierbei werden als „Mikrostruktur“ alle Arten von Defekten in Kristallen, also alle Abweichungen von der regelmäßigen Struktur, deren Geometrie und physikalischen Konfiguration unabhängig von der Längenskala verstanden. Das Volumen, innerhalb dessen die Struktur detektiert wird, muss infolgedessen den gesamten Bereich von mikroskopischer Dimension über die Nanometerskala bis zur Ebene einzelner Atome abdecken. Dementsprechend werden Röntgen- und Elektronenbeugungstechniken, abbildende und analytische Transmissionselektronenmikroskopie sowie Rastertunnelmikroskopie jeweils mit hoher räumlicher Auflösung und Empfindlichkeit eingesetzt, um die strukturellen, elektronischen und chemischen Eigenschaften einer großen Vielfalt von Materialsystemen, die am PDI oder von externen Kooperationspartnern hergestellt werden, quantitativ zu untersuchen. Beispiele für untersuchte Materialien sind niedrigdimensionale Halbleiterheterostrukturen, 2D Materialien, Ferromagnet-Halbleiter Hybridstrukturen sowie metastabile Materialien und neuartige Materialkombinationen. Experimentelle Ergebnisse zu Phasengrenzflächen und zur Phasenstabilität, zu Relaxationsmechanismen der Gitterfehlanpassung und zur Entstehung ausgedehnter und komplexer Defekte, sowie zu künstlichen Nanostrukturen werden mit Computersimulationen verglichen und die Interpretationen durch theoretische Modelle untermauert. Aufgrund ihrer universellen Möglichkeiten bei der Simulation sehr realitätsnaher Modelle mit nicht-trivialer Geometrie und chemischer Komposition kommt der Methode der Finiten Elemente hierbei eine



Important supplements are the high-angle annular dark-field and (annular) bright-field detectors in a scanning (S)TEM, which are used for chemical sensitive contrast imaging with atomic resolution. Electron energy-loss spectroscopy and energy dispersive x-ray spectroscopy complete the analytical performance of our microscope tools in the field of chemical bonding and composition, and allow two-dimensional (2D) mappings.

As one of our strengths high-resolution and analytical (S)TEM is used to quantitatively determine the structural roughness of semiconductor heterostructure interfaces and their chemical intermixing. In particular, we are able to analyze the composition profiles of planar interfaces up to the atomic level. Moreover, there is an attempt to correlate the interface property with the physical functionality of the heterostructure. Examples are here the investigations of ultra-thin (Al,Ga)As/GaAs interface profiles in quantum cascade lasers or of Ga(Sb,Bi)/GaSb quantum wells in infrared laser diodes. Another example refers to the interface study of monolithically integrated III-V layers on Si. On the other hand, the atomic configurations—atom position and type—at coherent interfaces between dissimilar materials or in nanosized clusters are analyzed on the basis of (S)TEM in combination with image contrast simulations. Further examples comprise the interface character in three-dimensional core/shell or axial heterojunction nanowires and epitaxial interfaces in van der Waals heterostructures such as graphene on BN or on SiC substrates.

In parallel to our scientific research on specific materials issues, we continually refine and develop our experimental methods per se. For some years now, we have been using electron tomography, a technique that allows us to reconstruct complex structures and nanoscale materials in three dimensions. Essential condition for this purpose is on the one hand a suitable imaging method fulfilling the tomographic

Schlüsselrolle zu. Als numerisches Pendant zu rein analytischen Ansätzen liefert diese quantitativ, räumlich aufgelöst Deformations- und Spannungstensoren in realen Objekten, sowie für heteroepitaktische Systeme mit fehlender Inversionssymmetrie ein dreidimensionales Bild der piezoelektrischen Polarisation.

Die Transmissionselektronenmikroskopie (TEM) ist eines der zentralen Werkzeuge, um die lokale atomare Struktur von Materialien abzubilden. Wesentliche Erweiterungen im Raster-(S)TEM-Betrieb sind der ringförmige Weitwinkel-Dunkelfeld- sowie der Hellfeld-Detektor, die eine chemisch sensible Abbildung mit atomarer Auflösung ermöglichen. Dazu vervollständigen die Elektronenenergieverlustspektroskopie und die energiedispersive Röntgenspektroskopie die analytische Leistungsfähigkeit unserer Mikroskope im Bereich der Messung chemischer Bindungen und Zusammensetzungen, und ermöglichen zweidimensionale (2D) Kartierungen.

Eine unserer besonderen Stärken liegt im Einsatz von hochauflösender und analytischer TEM, um die strukturelle Grenzflächenrauhigkeit und Durchmischung von Halbleiterübergängen zu bestimmen. Insbesondere das chemische Zusammensetzungsprofil über planare Grenzflächen kann bis auf die atomare Ebene quantitativ ermittelt und modelliert werden. Darüber hinaus wird versucht, die strukturelle Grenzflächeneigenschaft direkt mit der physikalischen Funktionalität der Heterostruktur zu korrelieren. Als Beispiele dienen die Untersuchungen der Profile von ultradünnen (Al,Ga)As/GaAs Grenzflächen in Quantenkaskadenlasern oder von Ga(Sb,Bi)/GaSb Quantentöpfen in Infrarotlaserdioden. Ein weiteres aktuelles Beispiel ist die Grenzflächenuntersuchung von monolithisch integrierten III-V Schichten auf Si. Andererseits wird die atomare Konfiguration – das heißt, die Art und Position der Atome – an kohärenten Grenzflächen zwischen stark unterschied-

projection requirement, and, on the other hand, a tomography sample preparation using focused ion beam technique. In 2019, tomography investigations on the three-dimensional (3D) morphology of (In,Ga)N/GaN nanowires with a pencil-like apex were carried out to unambiguously identify the "dot-in-a-wire" configuration including indium composition fluctuations inside the dot. Furthermore, we have developed an innovative tomographic method to visualize the 3D character of buried interfaces and to analyze their structural and chemical roughness quantitatively. The final goal is to study not only the structure and morphology but also its related physical and chemical properties.

The tomography activities are part of our newly established "Application Laboratory Electron Tomography". The Application Laboratory is financially supported by the European Regional Development Fund (ERDF) and by the Senate of Berlin. The reconstruction of our specially designed laboratory was completed in 2019 with the successful commissioning of our grant-funded new cutting-edge aberration corrected (Cs-STEM) microscope. This new Cs-STEM greatly improves the performance of the tomography method. Objective of the Application Laboratory is the methodical development and extensions to promote materials research, to collaborate with external partners and to utilize the tomography method to industrial applications.

A further methodical development affects our in-situ electron microscopy of dynamic processes. Heating experiments in the microscope serve to analyze defect formation and propagation, structural phase transitions and solid-state reactions with high spatial resolution. The direct observation of atoms in real-time and their correlated motion open the opportunity for basic understanding of material properties and functionalities. Currently, the amorphous-crystalline phase transitions during solid state epitaxy of Ge on Fe<sub>3</sub>Si has been

lichen Materialien oder in nanoskopischen Clustern mit Hilfe von (Raster-) TEM in Kombination mit Bild-Kontrastsimulationen analysiert. Weitere Beispiele umfassen die Natur von Grenzflächen in Nanosäulen mit lateraler oder axialer Heterostruktur, oder in van-der-Waals-gebundenen Schichtsystemen wie Graphen auf BN oder SiC Substraten.

Parallel zu unserer Forschung zu spezifischen Materialeigenschaften, bei der ein breites Spektrum mikroskopischer Techniken als Werkzeug verwendet wird, verbessern und entwickeln wir kontinuierlich die experimentellen Methoden selbst. So haben wir die Technik der Elektronentomographie eingeführt – eine Technik, mit der man dreidimensionale (3D) Rekonstruktionen komplexer nanoskaliger Strukturen und Materialien erhalten kann. Eine wesentliche Voraussetzung dazu ist die Herstellung spezieller Tomographieproben unter Nutzung fokussierter Ionenstrahlen. In 2019 wurden Untersuchungen zur 3D Morphologie von (In,Ga)N/GaN Nanosäulen mit stiftähnlicher Spitze weitergeführt, um die „Dot-in-a-wire“ Konfiguration sowie die Indium Fluktuationen innerhalb des Dots eindeutig zu bestimmen. Darüber hinaus haben wir eine innovative Tomographiemethode entwickelt, um den 3D Charakter von vergrabenen Grenzflächen darzustellen und ihre Rauigkeit im Detail zu analysieren. Ziel ist hierbei, nicht nur die Struktur und Morphologie, sondern auch die physikalischen und chemischen Eigenschaften zu studieren und miteinander in Bezug zu setzen.

Die Tomographiearbeiten sind Bestandteil des neu gegründeten „Applikationslabor Elektronentomographie“. Das Applikationslabor wird vom Berliner Senat sowie aus Mitteln des Europäischen Fonds für regionale Entwicklungen (EFRE) gefördert. Der Aufbau eines speziell entwickelten Labors ist in 2019 mit der Inbetriebnahme des aus Fördermittel neu angeschafften und topmodernen aberrationskorrigierten Rastertransmissionselektronenmikroskops

observed with atomic resolution. It could be shown that the crystallization occurs layer by layer and the growth kinetics follows a square root time dependency indicating a diffusion-driven growth process.

The physical properties of ultimately small structures at solid-vacuum interfaces are explored by low-temperature scanning tunneling microscopy (LTSTM) carried out in ultrahigh vacuum and at liquid-helium temperature. Our microscopes feature a highly stable "Besocke-Beetle" type scanner design allowing us (i) to manipulate single atoms and molecules adsorbed on a surface, and (ii) to probe the local density of electronic states as well as elementary excitations of individual nanostructures by scanning tunneling spectroscopy. In this way, the correlation between structure and properties of semiconductor-based nanostructures can be analyzed at the atomic scale. Starting at a base temperature of 5 K, the sample temperature can be varied in-situ up to ~100 K, enabling to study, e. g., surface diffusion at the single-atom level, as well as the competition between thermally excited and current-induced dynamics of engineered nanostructures and molecular switches linked to the semiconductor surface. One of our microscopes offers the capability to detect current-induced light emitted from the tunnel junction to combine optical spectroscopy with the spatial resolution of STM.

X-ray diffraction as a non-destructive probe can penetrate fairly thick layers and therefore allows to study beside surfaces, buried interfaces and structures inside the volume of the crystal. As a diffraction technique, it combines sub-Ångstrom resolution with a large interaction volume that provides statistically reliable structural properties. Results are analyzed quantitatively on the basis of modeling and simulation of diffraction data and complemented by electron microscopy measurements. In this way, we were recently able to discover a novel superlattice-like structure of ultra-thin epi-

(Cs-STEM) abgeschlossen worden. Das Cs-STEM verbessert die Leistungsfähigkeit der Elektronentomographie in erheblichem Maße. Aufgabe dieses Applikationslabors ist es, die Methode und ihre Weiterentwicklungen in der Materialforschung und Materialentwicklung voranzutreiben, mit externen Partnern zu kooperieren und die Elektronentomographie für industrielle Anwendungen nutzbar zu machen.

Eine weitere methodische Entwicklung betrifft unsere in-situ Elektronenmikroskopie dynamischer Prozesse. Temperaturabhängige Experimente im Mikroskop nutzen wir dazu, Defektbildung und -propagation, strukturelle Phasenübergänge und Festkörperreaktionen an Grenzflächen mit hoher räumlicher Auflösung zu studieren. Durch die direkte Beobachtung von Atomen und deren korrelierte Bewegung in Echtzeit eröffnet sich die Möglichkeit, ein grundlegendes Verständnis von Materialverhalten und -eigenschaften zu gewinnen. Gegenwärtig untersuchen wir den amorph-kristallinen Phasenübergang während der Festphasenepitaxie von Ge auf Fe<sub>3</sub>Si. Es konnte gezeigt werden, dass die Kristallisation Lage für Lage stattfindet und die Wachstumskinetik einem zeit-abhängigen Quadratwurzelgesetz folgt, das auf diffusionsgetriebenes Wachstum hindeutet.

Die physikalischen Eigenschaften von kleinsten Strukturen an der Grenzfläche zwischen Festkörper und Vakuum werden mit Tieftemperatur-Rastertunnelmikroskopie untersucht. Diese Experimente finden im Ultrahochvakuum und bei Temperaturen von flüssigem Helium statt. Unsere Mikroskope sind mit einem äußerst stabilen „Besocke-Beetle“-Scanner Typ ausgestattet, der es uns ermöglicht, einzelne Atome und Moleküle, die auf einer Oberfläche adsorbiert sind, abzubilden und zu manipulieren. Ortsaufgelöste Tunnelspektroskopie-Experimente erlauben uns, die lokale elektronische Zustandsdichte auszumessen und Elementaranregungen zu untersuchen, die

taxial FeGe<sub>2</sub> layers, which has been formed during solid phase epitaxy of Ge on Fe<sub>3</sub>Si/GaAs(100) substrate. Moreover, in the x-ray laboratory of our institute the basic parameters of many grown structures are quickly obtained in order to give immediate feedback for further growth experiments.

PDI's PHARAO end station at Berlin Synchrotron BESSYII (Helmholtz-Zentrum Berlin, HZB) facilitates in-situ x-ray diffraction during molecular beam epitaxy (MBE) in order to study growth dynamics of epitaxial layers. A direct, surface sensitive access to crystal symmetry, elastic strain and surface reconstruction in a realistic growth environment, and, in real-time, improves our understanding of fundamental growth-related phenomena as interface formation, strain relaxation and reconstruction dynamics. In 2019 a state-of-the-art 2D hybrid detector (EIGER 500k) has been fully implemented into the PHARAO infrastructure enabling a highly parallelized and thus even faster data acquisition. This in general opens new perspectives towards reciprocal space mappings on a time scale of seconds. Our recent work focuses on epitaxial growth modes in group-III oxides, in particular we study the interface formation at thin layers and in vertical stacks of dissimilar materials. This activity relies on active contributions of the Departments Microstructure and Epitaxy. It requires a continuous stationary operation of an MBE system at BESSYII, since quality of the epitaxial layers is imperative for a reliable quantitative analysis.

Addressing questions, which require very specific source characteristics as brilliance or spot size, we are regularly applying for and performing complementary x-ray diffraction measurements at dedicated third-generation synchrotron sources like PETRAIII (Hamburg), the Diamond Light Source (UK) and the ESRF (France). Of particular interests are newly approaching techniques like diffraction with highly focused x-rays to study individual low-dimensional structures. Thereby, we overcome the

durch inelastische Streuung der Tunnel elektronen selbst induziert werden.

Die Kombination, einerseits Halbleiter-Nanostrukturen aus einzelnen Atomen aufbauen zu können, und andererseits ihre Eigenschaften lokal zu charakterisieren, ermöglicht es uns, Korrelationen zwischen Struktur und Eigenschaften auf atomarer Skala zu studieren. Der hier experimentell erreichbare Temperaturbereich zwischen 5 K und 100 K lässt uns zum Beispiel Oberflächendiffusionsprozesse mit atomarer Auflösung studieren, und ermöglicht es, die Wechselwirkung zwischen thermisch angeregter und strominduzierter Dynamik von künstlichen Nanostrukturen und molekularen Schaltern auf Halbleiteroberflächen zu untersuchen. Eines unserer Mikroskope bietet die Möglichkeit, strominduziertes Licht, das im Tunnelkontakt erzeugt wird, zu detektieren, um so optische Spektroskopie mit ortsaufgelöster Rastertunnelmikroskopie zu verbinden.

Das PHARAO Experiment des Institutes am Berliner Synchrotron BESSYII (Helmholtz-Zentrum Berlin, HZB) ermöglicht die in-situ Röntgenbeugung während der Molekularstrahlepitaxie (MBE), um die Wachstumsdynamik von Epitaxie-Schichten zu untersuchen. Ein direkter, oberflächensensitiver Zugang zu Kristallsymmetrie, elastische Dehnung und Oberflächenrekonstruktion in einer realistischen Wachstumsumgebung und in Echtzeit verbessert unser Verständnis grundlegender wachstumsbezogener Phänomene wie Grenzflächenbildung, Spannungsrelaxation und Rekonstruktionsdynamik. Im Jahr 2019 wurde ein hochmoderner 2D Hybriddetektor (EIGER 500k) in die PHARAO Infrastruktur implementiert, der eine hochgradig parallelisierte und damit noch schnellere Datenerfassung ermöglicht. Dies eröffnet neue Perspektiven für reziproke Raumkarten auf der Zeitskala von Sekunden. Unsere jüngsten Arbeiten konzentrieren sich auf epitaktische Wachstumsmodi in Gruppe-III-Oxiden, insbesondere untersuchen wir die

ensemble average inherent to x-ray techniques applying millimeter-sized x-ray foci. On the other hand, investigations of ultra-thin 2D van der Waals layers, especially if consisting of weak scatterers, as B, N, and C-atoms, require extremely brilliant sources and have been performed at the external sources as well.

Grenzflächenbildung an dünnen Schichten und in vertikalen Stapeln unterschiedlicher Materialien. Diese Arbeit stützt sich auf aktive Mitwirkung der Abteilungen Mikrostruktur und Epitaxie. Sie erfordert einen kontinuierlichen stationären Betrieb eines MBE-Systems bei BESSYII, da die Qualität der Epitaxieschichten für die zuverlässige quantitative Analyse unerlässlich ist.

Zur Adressierung von Fragestellungen, die den Einsatz höchstbrillianter Quellen erfordert, beantragen und nutzen wir regelmäßig den Zugang zu Synchrotronquellen der 3. Generation wie beispielsweise PETRAIII in Hamburg, Diamond Light Source (UK) und ESRF in Grenoble. Von besonderem Interesse sind neu angewandte Techniken wie die Beugung mit hochfokussierter Röntgenstrahlung zur Untersuchung einzelner niedrigdimensionaler Strukturen. Dabei überwinden wir die Mittelwertbildung, die den Röntgentechniken mit millimetergroßen Röntgenstrahlen innewohnt. Untersuchung von ultradünnen, 2D van der Waals Schichten, die zudem oft aus leichten und daher weniger stark streuenden Elementen wie B, N und C bestehen, sind extrem brillante Quellen erforderlich, so dass die entsprechende Experimente dazu ebenfalls an externen Quellen durchgeführt werden.

ACCELAR<sup>TM</sup>

JEM-ARM200F  
Atomic Resolution analytical Microscope



# Department of Technology and Transfer

## Abteilung für Technologie und Transfer

Head of Department: Dr. Carsten Hucho, [hucho@pdi-berlin.de](mailto:hucho@pdi-berlin.de)



The Department of Technology and Transfer combines all science-supporting activities of the institute. These include semiconductor technology with its scientific head Dr. Abbes Tahraoui, the building services and workshop headed by Jörg Pfeiffer, as well as personnel support in the hands of Human Resources Manager Andreas Hartung, the purchasing and finance section of Kerstin Arnhold, and the processing of third-party funds by Anja Holldack. Intellectual Property, its screening and securing is in the hands of Mercedes Reischel, Kai Hablizel answers all questions concerning EU research funding and coordinates the GraFOx Science Campus. The scientific special library is currently undergoing a modernization push by librarian Anne Timm. The head of department is the administrative director of the institute and coordinates the administrative necessities of the research operation with the aim of keeping non-scientific work away from researchers as far as possible. As scientific-administrative coordinator, he advises the Director on strategic research planning and develops the Institute's knowledge transfer activities.

### Utilities Management

PDI is tenant in a building administered by Humboldt-Universität (HU). While the central services are provided by HU, the special infrastructural needs of a materials science institute are coordinated within this department. This comprises the supply with technical gases (especially liquid Helium for temperature-dependent experiments and liquid Nitrogen as a coolant for MBE-systems), electricity, the data- and communication-infrastructure, the operation of clean-rooms and chemistry labs and air-conditioning as well as cooling systems of the research laboratories.

In der Abteilung Technologie und Transfer sind alle wissenschaftsunterstützenden Aktivitäten des Instituts vereint. Zu diesen zählt die Halbleitertechnologie mit ihrem wissenschaftlichen Leiter Dr. Abbes Tahraoui, die von Jörg Pfeiffer geleitete Haustechnik und feinmechanische Werkstatt, ebenso wie die Personalbetreuung in den Händen des Human Resources Managers Andreas Hartung, der Bereich Einkauf und Finanzen von Kerstin Arnhold und die Drittmittelsachbearbeitung durch Anja Holldack. Intellectual Property, dessen Sichtung und Sicherung liegt in den Händen von Mercedes Reischel, Kai Hablizel unterstützt bei allen Fragen im Bereich der EU Forschungsförderung und koordiniert den GraFOx Wissenschaftscampus. Die wissenschaftliche Spezialbibliothek erfährt momentan einen Modernisierungsschub durch die Bibliothekarin Anne Timm. Der Abteilungsleiter ist Verwaltungsleiter des Instituts und koordiniert die administrativen Notwendigkeiten des Forschungsbetriebes mit dem Ziel, wissenschaftsfremde Arbeiten möglichst weitgehend von Forschenden fernzuhalten. Er berät als wissenschaftlich-administrativer Koordinator den Direktor bei der strategischen Forschungsplanung und entwickelt die Wissenstransferaktivitäten des Instituts.

### Haustechnik

Das PDI ist Nutzer eines Gebäudes, das von der Humboldt-Universität verwaltet wird. Während zentrale Dienste (Strom, Heizung, Wasser) durch die HU sichergestellt werden, werden die spezielleren Infrastrukturbedürfnisse eines materialwissenschaftlichen Instituts innerhalb der Abteilung Technologie und Transfer koordiniert. Dies umfasst neben der Versorgung mit Spezialgasen (wie Helium für temperaturabhängige Experimente und flüssigem

### Semiconductor Technology

Most materials that are grown in the epitaxy department need further processing for subsequent scientific investigations. Our technologists provide structuring on sub-micrometer scales and processes like metallization and contacting, cutting of wafers, prepatterning, cleaning and electrical characterization of processed structures. The semiconductor technology group operates clean rooms with facilities for the whole process of photolithography (mask-design, mask-writing, exposing and developing) which is employed to prepare the samples for subsequent selective metallization or overgrowth (with, e.g., piezoelectric material), wet and dry etching, sputtering and thermal evaporation. The rather limited resolution of photolithography is offset by its high flexibility and extended by electron-beam lithography. Photolithography can be used for rapid prototyping as well as for small series.

The wet chemical etching and the dry etching capabilities are optimized for the materials prepared within the epitaxy department and are constantly developed further.

### Administration

The administration of PDI relies on the backbone of the central administration of Forschungsverbund Berlin e.V. (FVB). All legally binding processes like salaries, work-contracts, purchase-orders, the administration of travel-reimbursement, etc. are administered at FVB. At the institute a small number of specially trained administrative staff provide an interface between research and administration, supervised by the scientific administrative coordinator. All necessary paperwork related to the job is taken care of and new staff is supported in a way that makes the unavoidable bureaucracy when arriving from a different country bearable. Purchasing and finances and the administration of third-party-funded projects is supported in a way that shields scientists from the intricacies of accounting as much as possible.

Stickstoff für MBE-Systeme), Strom, die Daten- und Kommunikations-Infrastruktur, den Betrieb der Reinräume und Chemielabore und Klima und Gerätekühlung für die Labore.

### Halbleiter-Technologie

Die meisten Materialien, die in der Abteilung Epitaxie gewachsen werden, benötigen eine weitere Prozessierung für anschließende wissenschaftliche Untersuchungen – zum Beispiel Vereinzen von Wafern, Strukturierungen, Metallisierung und das Überwachsen mit Schichten außerhalb der MBE, elektrische und strukturelle Charakterisierungen, etc. Unsere Technologie ermöglicht laterale Strukturierungen auf der sub-Mikrometer-Skala mittels konventioneller optischer Lithographie und Elektronenstrahlolithographie und stellt Verfahren für die Metallisierung, Kontaktierung, das Vereinzen, Reinigen und einfache elektrische Charakterisierungen zur Verfügung. Die Halbleiter Technologie verfügt über einen Reinraum mit einer Prozessstrecke für Foto- und Elektronenstrahlolithographie (vom Maskenentwurf und -schreiben über Belichtung und Entwicklung bis zum Ätzen und Beschichten). Hierbei stehen nasschemische Ätzverfahren und Trockenätzverfahren sowie Sputteranlagen und Anlagen für das thermische Verdampfen von Metallen zur Verfügung.

Die Ätzverfahren werden auf die Materialien angepasst, die in der Abteilung Epitaxie hergestellt werden und werden ständig weiterentwickelt.

### Verwaltung

Die Verwaltung des PDI baut auf die zentrale Verwaltung des Forschungsverbund Berlin e.V. (FVB) auf, dem gemeinsamen Träger von acht Instituten. Alle rechtlich bindenden Prozesse wie die Zahlbarmachung von Gehältern, Arbeitsverträge, Beschaffungsaufträge, die Abrechnung von Dienstreisen etc. werden zentral im FVB durchgeführt. Am Institut werden alle Personalvorgänge vorbereitet und die Mit-

This interfacing-approach is set up to free scientist from administrative burden as much as possible while at the same time translating their needs for the professional administration at FVB and reconciling the sometimes complex administrative needs with the reality of rapidly developing research activities, involving strategic changes, unforeseeable developments, and international staff with varying bureaucratic necessities but also the need for practical, personal support.

### **Knowledge Transfer**

The simplistic approach to ask for proof of practicability or usability of research results—especially from institutes doing 'hard' science—is recently being substituted by a deeper understanding of the necessities of transferring knowledge into society. Rather than proving short-term applicability of our research results, our understanding of transfer ranges from informing the public about nanotechnology and materials science at large (involving public relations, developing concepts for science-communication and -visualization), providing expertise to industry, education and politics, to tracing, securing and making available intellectual property—be it in the frame of open source arrangements, licensing or marketing of patents.

The engagement of our technology transfer manager has in recent years lead to a considerable professionalization of the transfer activities. Besides the development of transfer-concepts and the definition of internal processes, the idea of technology transfer of PDI is being discussed within Leibniz-Gemeinschaft and in an increasing network of technology transfer professionals. The Head of the Technology and Transfer department is speaker of the workgroup Knowledge transfer of Leibniz-Gemeinschaft and member of the group initiated by the president defining the guidelines for knowledge-transfer.

arbeiterinnen und Mitarbeiter sowie Gäste werden bei allen Fragen zu Verträgen und Aufenthalt persönlich unterstützt. Diese Schnittstellenaktivitäten werden am Institut organisiert, um die Übersetzung zwischen wissenschaftlichen und Wissenschafts-unterstützenden Aktivitäten zu optimieren.

### **Wissenstransfer**

Wissenschaft zum Wohl der Gesellschaft zu betreiben, ist ein Kernpunkt des Selbstverständnisses der Einrichtungen der Leibniz-Gemeinschaft. Dies bedeutet, dass Leibniz-Einrichtungen die Verwendbarkeit ihrer Forschungsergebnisse fördern. Das PDI, dessen Forschung auf fundamentale Fragen der Materialwissenschaften zielt, die künftige Anwendungen beeinflussen, inspirieren oder gar erst ermöglichen, sieht eine wichtige Aufgabe darin, dieses Wissen zum gesellschaftlichen Nutzen zur Verfügung zu stellen.

In der Abteilung Technologie und Transfer werden Kompetenzen und Ressourcen für den Technologietransfer (im Technologietransferbüro durch die Transferbeauftragte) ebenso bereitgestellt wie für den Transfer des Wissens in die Gesellschaft. In der Leibniz-Gemeinschaft wird Transfer disziplinübergreifend verstanden. Die Disziplinspezifika werden schließlich bei der Umsetzung durch die maßgeschneiderten Transferwerkzeuge sichtbar. Das PDI stellt seit November 2014 mit dem Leiter der Abteilung Technologie und Transfer den Sprecher des Arbeitskreises Wissenstransfer der Leibniz-Gemeinschaft – der als Mitglied der Präsidiumsgruppe auch das Leibniz Leitbild für Wissenstransfer mitformulierte





# Facts & Figures

## Zahlen und Fakten

Publications .....	146
Ph.D. Theses.....	153
Master Theses .....	153
Students Working on their Master Thesis .....	153
Students Working on their Bachelor Thesis.....	135
Conferences and workshops organized by the Institute.....	154
Seminar of Visitors .....	154
Budget Summary .....	157
Summary of External Funding .....	158
Visiting Scientists .....	160
Staff.....	163
Non-Scientific Staff .....	165

# Facts & Figures / Zahlen und Fakten

## Publications

Alam, T., M. Wienold, X. Lü, K. Biermann, L. Schrottke, H. T. Grahn, and H.-W. Hübers,  
Wideband, high-resolution terahertz spectroscopy by light-induced frequency tuning of  
quantum-cascade lasers,  
*Opt. Express* **27**, 5420–5432 (2019). DOI: 10.1364/OE.27.005420

Alam, T., M. Wienold, X. Lü , K. Biermann, L. Schrottke, H. T. Grahn, and H.-W. Hübers,  
Frequency and power stabilization of a terahertz quantum-cascade laser using near-infrared  
optical excitation,  
*Opt. Express* **27**, 36846–36854 (2019). DOI: 10.1364/OE.27.036846

Anikeeva, M., M. Albrecht, F. Mahler, J. W. Tomm, L. Lymerakis, C. Chèze, R. Calarco,  
J. Neugebauer, and T. Schulz,  
Role of hole confinement in the recombination properties of InGaN quantum structures.  
*Sci. Rep.* **9**, 9047, 10 pages (2019). DOI: 10.1038/s41598-019-45218-8

Auzelle, T., G. Calabrese, and S. Fernández-Garrido,  
Tuning the orientation of the top-facets of GaN nanowires in molecular beam epitaxy by thermal  
decomposition,  
*Phys. Rev. Mater.* **3**, 013402, 11 pages (2019). DOI: 10.1103/PhysRevMaterials.3.013402

Auzelle, T., F. Ullrich, S. Hietzschold, S. Brackmann, S. Hillebrandt, W. Kowalsky, E. Mankel,  
R. Lovrincic, and S. Fernández-Garrido,  
Electronic properties of air-exposed GaN(1100) and (0001) surfaces after several device processing  
compatible cleaning steps,  
*Appl. Surf. Sci.* **495**, 143514, 6 pages (2019). DOI: 10.1016/j.apsusc.2019.07.256

Bastiman, F., H. Küpers, C. Somaschini, V. G. Dubrovskii, and L. Geelhaar,  
Analysis of incubation time preceding the Ga-assisted nucleation and growth of GaAs nanowires on  
Si(111), *Phys. Rev. Mater.* **3**, 073401, 8 pages (2019). DOI: 10.1103/PhysRevMaterials.3.073401

Bilobran, A. L. O., A. García-Cristóbal, P. V. Santos, A. Cantarero, and M. M. de Lima, Jr.,  
Thermally tunable surface acoustic wave cavities,  
*IEEE Trans. Ultrason. Ferroelectr. Freq. Control* **67**, 850–854 (2020), published online 11 November 2019.  
DOI: 10.1109/TUFFC.2019.29529821

Bin Anooz, S., A. Popp, R. Grüneberg, C. Wouters, R. Schewski, M. Schmidbauer, M. Albrecht, A. Fiedler,  
M. Ramsteiner, D. Klimm, K. Irmscher, Z. Galazka, and G. Wagner,  
Indium incorporation in homoepitaxial  $\beta$ -Ga<sub>2</sub>O<sub>3</sub> thin films grown by metal organic vapor phase epitaxy,  
*J. Appl. Phys.* **125**, 195702, 10 pages (2019). DOI: 10.1063/1.5090213

Boniardi, M., J. E. Boschker, J. Momand, B. J. Kooi, A. Redaelli, and R. Calarco,  
Evidence for thermal-based transition in superlattice phase change memory,  
*Phys. Status Solidi RRL* **13**, 1800634, 6 pages (2019). DOI: 10.1002/pssr.201800634

Buß, J. H., S. Fernández-Garrido, O. Brandt, D. Hägele, and J. Rudolph,  
Electron spin dynamics in mesoscopic GaN nanowires,  
*Appl. Phys. Lett.* **114**, 092406, 5 pages (2019). DOI: 10.1063/1.5080508

Calabrese, G., G. Gao, D. van Treeck, P. Corfdir, C. Sinito, T. Auzelle, A. Trampert, L. Geelhaar, O. Brandt,  
and S. Fernández-Garrido,  
Interfacial reactions during the molecular beam epitaxy of GaN nanowires on Ti/Al<sub>2</sub>O<sub>3</sub>,  
*Nanotechnol.* **30**, 114001, 9 pages (2019). DOI: 10.1088/1361-6528/aaf9c5

Chagas, T., M. Pelc, P. H. R. Gonçalves, I. Antoniazzi, J. W. González, A. Ayuela, J. M. J. Lopes, M. H. Oliveira, Jr., R. Magalhães-Paniago, and A. Malachias, Self-assembled triangular graphene nanostructures: Evidence of dual electronic response, *Carbon* **142**, 580–591 (2019). DOI: 10.1016/j.carbon.2018.10.059

Chen, J. X., L. Qiu, Z. L. Li, G. H. Gao, W. H. Zhong, P. X. Zhang, Y. J. Gong, and L. B. Deng, Chitin-derived porous carbon loaded with Co, N and S with enhanced performance towards electrocatalytic oxygen reduction, oxygen evolution, and hydrogen evolution reactions, *Electrochim. Acta* **304**, 350–359 (2020). DOI: 10.1109/TUFFC.2019.2952982

Corfdir, P., O. Marquardt, R. B. Lewis, C. Sinito, M. Ramsteiner, A. Trampert, U. Jahn, L. Geelhaar, O. Brandt, and V. M. Fomin, Excitonic Aharonov-Bohm oscillations in core-shell nanowires, *Adv. Mater.* **31**, 1805645, 6 pages (2019). DOI: 10.1002/adma.201805645

Crespo Poveda, A., D. D. Bühler, A. Cantarero Sáez, P. V. Santos, and M. M. de Lima, Jr., Semiconductor optical waveguide devices modulated by surface acoustic waves, *J. Phys. D: Appl. Phys.* **52**, 253001, 23 pages (2019). DOI: 10.1088/1361-6463/ab1464

Delorme, O., L. Cerutti, R. Kudrawiec, E. Luna, J. Kopaczek, M. Gladysiewicz, A. Trampert, E. Tournié, and J.-B. Rodriguez, GaSbBi alloys and heterostructures: Fabrication and properties, in *Bismuth-Containing Alloys and Nanostructures*, edited by S. Wang and P. Lu, Springer Series in Materials Science **285** (Springer Nature Singapore, 2019), pp. 125–161. DOI: 10.1007/978-981-13-8078-5\_6

Delorme, O., L. Cerutti, E. Luna, A. Trampert, E. Tournié, and J.-B. Rodriguez, Molecular-beam epitaxy of GaInSbBi alloys, *J. Appl. Phys.* **126**, 155304, 9 pages (2019). DOI: 10.1063/1.5096226

Delsing, P., A. N. Cleland, M. J. A. Schuetz, J. Knörzer, G. Giedke, J. I. Cirac, K. Srinivasan, M. Wu, K. C. Balram, C. Bäuerle, T. Meunier, C. J. B. Ford, P. V. Santos, E. Cerdá-Méndez, H. Wang, H. J. Krenner, E. D. S. Nysten, M. Weiβ, G. R. Nash, L. Thevenard, C. Gourdon, P. Rovillain, M. Marangolo, J.-Y. Duquesne, G. Fischerauer, W. Ruile, A. Reiner, B. Paschke, D. Denysenko, D. Volkmer, A. Wixforth, H. Bruus, M. Wiklund, J. Reboud, J. M. Cooper, Y. Q. Fu, M. S. Brugger, F. Rehfeldt, and C. Westerhausen, The 2019 surface acoustic waves roadmap, *J. Phys. D: Appl. Phys.* **52**, 353001, 40 pages (2019). DOI: 10.1088/1361-6463/ab1b04

Di Biagio, F., S. Cecchi, F. Arciprete, and R. Calarco, Crystallization study of Ge-rich  $(\text{GeTe})_m(\text{Sb}_2\text{Te}_3)_n$  using two-step annealing process, *Phys. Status Solidi RRL* **13**, 1800632, 4 pages (2019). DOI: 10.1002/pssr.201800632

Fandan, R., J. Pedrós, A. Hernández-Mínguez, F. Iikawa, P. V. Santos, A. Boscá, and F. Calle, Dynamic local strain in graphene generated by surface acoustic waves, *Nano Lett.* **20**, 402–409 (2020), published online 2 December, 2019. DOI: 10.1021/acs.nanolett.9b04085

Fernández-Garrido, S., T. Auzelle, J. Lähnemann, K. Wimmer, A. Tahraoui, and O. Brandt, Top-down fabrication of ordered arrays of GaN nanowires by selective area sublimation, *Nanoscale Adv.* **1**, 1893–1900 (2019). DOI: 10.1039/c8na00369f

Fernando-Saavedra, A., S. Albert, A. Bengoechea-Encabo, D. Lopez-Romero, M. Niehle, S. Metzner, G. Schmidt, F. Bertram, M. A. Sánchez-García, A. Trampert, J. Christen, and E. Calleja, Ordered arrays of defect-free GaN nanocolumns with very narrow excitonic emission line width, *J. Cryst. Growth* **525**, 125189, 5 pages (2019). DOI: 10.1016/j.jcrysgr.2019.125189

Foerster, M., N. Statuto, B. Casals, A. Hernández-Mínguez, S. Finizio, A. Mandziak, L. Aballe, J. M. Hernández Ferràs, and F. Macià, Quantification of propagating and standing surface acoustic waves by stroboscopic X-ray photoemission electron microscopy, *J. Synchrotron Rad.* **26**, 184–193 (2019). DOI: 10.1107/S1600577518015370

## Facts & Figures – Publications

García-Tecedor, M., J. Bartolomé, D. Maestre, A. Trampert, and A. Cremades,  
 $\text{Li}_2\text{SnO}_3$  branched nano- and microstructures with intense and broadband white-light emission,  
*Nano Res.* **12**, 441–448 (2019). DOI: 10.1007/s12274-018-2236-0

Golz, C., Z. Galazka, J. Lähnemann, V. Hortelano, F. Hatami, W. T. Masselink, and O. Bierwagen,  
Electrical conductivity tensor of  $\beta\text{-Ga}_2\text{O}_3$  analyzed by van der Pauw measurements: Inherent  
anisotropy, off-diagonal element, and the impact of grain boundaries,  
*Phys. Rev. Mater.* **3**, 124604, 13 pages (2019). DOI: 10.1103/PhysRevMaterials.3.124604

Hagelschuer, T., H. Richter, M. Wienold, X. Lü, B. Röben, L. Schrottke, K. Biermann, H. T. Grahn,  
and H.-W. Hübers,  
A compact 4.75-THz source based on a quantum-cascade laser with a back-facet mirror,  
*IEEE Trans. Terahertz Sci. Technol.* **9**, 606–612 (2019). DOI: 10.1109/TTHZ.2019.2935337

Hartmann, J., I. Manglano Clavero, L. Nicolai, C. Margenfeld, H. Spende, J. Ledig, H. Zhou, F. Steib,  
A. Jaros, A. Avramescu, M. Strassburg, A. Trampert, H.-H. Wehmann, H.-J. Lugauer, T. Voss, and A. Waag,  
3D GaN fins as a versatile platform for  $\alpha$ -plane-based devices,  
*Phys. Status Solidi B* **256**, 1800477, 9 pages (2019). DOI: 10.1002/pssb.201800477

Helgers, P. L. J., H. Sanada, Y. Kunihashi, A. Rubino, C. J. B. Ford, K. Biermann, and P. V. Santos,  
Sidewall quantum wires on GaAs (001) substrates,  
*Phys. Rev. Appl.* **11**, 064017, 13 pages (2019). DOI: 10.1103/PhysRevApplied.11.064017

Herranz, J., P. Corfdir, E. Luna, U. Jahn, R. B. Lewis, L. Schrottke, J. Lähnemann, A. Tahraoui,  
A. Trampert, O. Brandt, and L. Geelhaar,  
Coaxial GaAs/(In,Ga)As dot-in-a-well nanowire heterostructures for electrically driven infrared light  
generation on Si in the telecommunication O band,  
*ACS Appl. Nano Mater.* **3**, 165–174 (2020), published online Dec. 16<sup>th</sup>, 2019. DOI: 10.1021/acsanm.9b01866

Hoffmann, G., J. Herfort, and M. Ramsteiner,  
Spin generation in completely MBE-grown  $\text{Co}_2\text{FeSi}/\text{MgO}/\text{GaAs}$  lateral spin valves,  
*Phys. Rev. Mater.* **3**, 074402, 7 pages (2019). DOI: 10.1103/PhysRevMaterials.3.074402

Hoffmann, G., B. Jenichen, and J. Herfort,  
Epitaxial growth of  $\text{Co}_2\text{FeSi}/\text{MgO}/\text{GaAs}(001)$  heterostructures using molecular beam epitaxy,  
*J. Cryst. Growth* **512**, 194–197 (2019). DOI: 10.1016/j.jcrysgro.2019.02.029

Hortelano, V., H. Weidlich, W. T. Masselink, and Y. Takagaki,  
Magnetic-field-induced transport asymmetry in two-terminal circular ballistic bends,  
*J. Appl. Phys.* **125**, 145301, 10 pages (2019). DOI: 10.1063/1.5064689

Hubert, C., Y. Baruchi, Y. Mazuz-Harpaz, K. Cohen, K. Biermann, M. Lemeshko, K. West, L. Pfeiffer,  
R. Rapaport, and P. V. Santos,  
Attractive dipolar coupling between stacked exciton fluids,  
*Phys. Rev. X* **9**, 021026, 12 pages (2019). DOI: 10.1103/PhysRevX.9.021026

Ilikawa, F., A. Hernández-Mínguez, I. Aharonovich, S. Nakhaie, Y.-T. Liou, J. M. J. Lopes, and P. V. Santos,  
Acoustically modulated optical emission of hexagonal boron nitride layers,  
*Appl. Phys. Lett.* **114**, 171104, 5 pages (2019). DOI: 10.1063/1.5093299

Jenichen, B., Z. Cheng, M. Hanke, J. Herfort, and A. Trampert,  
Lattice matched Volmer-Weber growth of  $\text{Fe}_3\text{Si}$  on GaAs(001) — The influence of the growth rate,  
*Semicond. Sci. Technol.* **34**, 124002, 5 pages (2019). DOI: 10.1088/1361-6641/ab4c79

Jovic, V., S. Moser, A. Papadogianni, R. J. Koch, A. Rossi, C. Jozwiak, A. Bostwick, E. Rotenberg,  
J. V. Kennedy, O. Bierwagen, and K. E. Smith,  
The itinerant 2D electron gas of the indium oxide (111) surface: Implications for carbon- and  
energy-conversion applications,  
*Small* **16**, 1903321, 7 pages (2019). DOI: 10.1002/smll.201903321

Kaganer, V. M., J. Lähnemann, C. Pfüller, K. K. Sabelfeld, A. E. Kireeva, and O. Brandt,  
 Determination of the carrier diffusion length in GaN from cathodoluminescence maps around threading  
 dislocations: Fallacies and opportunities,  
*Phys. Rev. Appl.* **12**, 054038, 13 pages (2019). DOI: 10.1103/PhysRevApplied.12.054038

Kroh, T., J. Wolters, A. Ahlrichs, A. W. Schell, A. Thoma, S. Reitzentstein, J. S. Wildmann, E. Zallo,  
 R. Trotta, A. Rastelli, O. G. Schmidt, and O. Benson,  
 Slow and fast single photons from a quantum dot interacting with the excited state hyperfine  
 structure of the Cesium D<sub>1</sub>-line,  
*Sci. Rep.* **9**, 13728, 11 pages (2019). DOI: 10.1038/s41598-019-50062-x

Kudrawiec, R., J. Kopaczek, O. Delorme, M. P. Polak, M. Gladysiewicz, E. Luna, L. Cerutti, E. Tournié,  
 and J. B. Rodriguez,  
 Type I GaSb<sub>1-x</sub> Bi<sub>x</sub>/GaSb quantum wells dedicated for mid infrared laser applications:  
 Photoreflectance studies of bandgap alignment,  
*J. Appl. Phys.* **125**, 205706, 12 pages (2019). DOI: 10.1063/1.5094159

Küpers, H., P. Corfdir, R. B. Lewis, T. Flissikowski, A. Tahraoui, H. T. Grahn, O. Brandt, and L. Geelhaar,  
 Impact of outer shell structure and localization effects on charge carrier dynamics in GaAs/(In,Ga)As  
 nanowire core-shell quantum wells,  
*Phys. Status Solidi RRL* **13**, 1800527, 5 pages (2019). DOI: 10.1002/pssr.201800527

Küpers, H., R. B. Lewis, and L. Geelhaar,  
 Predictive model for the temporal evolution of the shape of GaAs nanowires,  
*J. Cryst. Growth* **531**, 125320, 4 pages (2020), published online Oct. 30<sup>th</sup>, 2019.  
 DOI: 10.1016/j.jcrysGro.2019.125320

Kuznetsov, A. S., K. Biermann, and P. V. Santos,  
 Dynamic acousto-optical control of confined polariton condensates: From single traps to coupled lattices,  
*Phys. Rev. Res.* **1**, 023030, 14 pages (2019). DOI: 10.1103/PhysRevResearch.1.023030

Lähnemann, J., M. O. Hill, J. Herranz, O. Marquardt, G. Gao, A. Al Hassan, A. Davtyan, S. O. Hruszkewycz,  
 M. V. Holt, C. Huang, I. Calvo-Almazán, U. Jahn, U. Pietsch, L. J. Lauhon, and L. Geelhaar,  
 Correlated nanoscale analysis of the emission from wurtzite versus zincblende (In,Ga)As/GaAs  
 nanowire core-shell quantum wells,  
*Nano Lett.* **19**, 4448–4457 (2019). DOI: 10.1021/acs.nanolett.9b01241

Lazić, S., A. Espinha, S. Pinilla Yanguas, C. Gibaja, F. Zamora, P. Ares, M. Chhowalla, W. S. Paz,  
 J. J. Palacios Burgos, A. Hernández-Mínguez, P. V. Santos, and H. P. van der Meulen,  
 Dynamically tuned non-classical light emission from atomic defects in hexagonal boron nitride,  
*Commun. Phys.* **2**, 113, 8 pages (2019). DOI: 10.1038/s42005-019-0217-6

Lewis, R. B., A. Trampert, E. Luna, J. Herranz, C. Pfüller, and L. Geelhaar,  
 Bismuth-surfactant-induced growth and structure of InAs/GaAs(110) quantum dots,  
*Semicond. Sci. Technol.* **34**, 105016, 7 pages (2019). DOI: 10.1088/1361-6641/ab3c23

Lopes, J. M. J.,  
 MBE growth of graphene,  
 in *Molecular Beam Epitaxy: Materials and Applications for Electronics and Optoelectronics*,  
 edited by H. Asahi and Y. Horikoshi (Wiley, 2019), pp. 395–409. DOI: 10.1002/9781119354987.ch24

Ludwig, S.,  
 Noise put to use,  
*Nat. Phys.* **15**, 310–311 (2019). DOI: 10.1038/s41567-019-0442-7

Luna, E., M. Wu, T. Aoki, M. R. McCartney, J. Puustinen, J. Hilska, M. Guinea, D. J. Smith, and A. Trampert,  
 Impact of Bi incorporation on the evolution of microstructure during growth of low-temperature  
 GaAs:Bi/Ga(As,Bi) layers,  
*J. Appl. Phys.* **126**, 085305, 13 pages (2019). DOI: 10.1063/1.5111532

## Facts & Figures – Publications

Luna, E., A. Trampert, J. Lu, T. Aoki, Y.-H. Zhang, M. R. McCartney, and D. J. Smith,  
Strategies for analyzing noncommon-atom heterovalent interfaces: The case of CdTe-on-InSb,  
*Adv. Mater. Interfaces* **7**, 1901658, 9 pages (2020), published online 17 December 2019.  
DOI: 10.1002/admi.201901658

Machado, D. H. O., A. Crespo-Poveda, A. S. Kuznetsov, K. Biermann, L. V. A. Scalvi, and P. V. Santos,  
Generation and propagation of superhigh-frequency bulk acoustic waves in GaAs,  
*Phys. Rev. Appl.* **12**, 044013, 14 pages (2019). DOI: 10.1103/PhysRevApplied.12.044013

Mahler, F., K. Reimann, M. Woerner, T. Elsaesser, C. Flytzanis, and K. Biermann,  
Impact of piezoelectric fields on coherent zone-folded phonons in GaAs/AlAs superlattices,  
*Phys. Rev. B* **100**, 121302(R), 6 pages (2019). DOI: 10.1103/PhysRevB.100.121302

Mahtab, M., R. Synowicki, V. Bahrami-Yekta, L. C. Bannow, S. W. Koch, R. B. Lewis, and T. Tiedje,  
Complex dielectric function of  $\text{GaAs}_{1-x}\text{Bi}_x$  as a function of Bi content,  
*Phys. Rev. Mater.* **3**, 054601, 11 pages (2019). DOI: 10.1103/PhysRevMaterials.3.054601

Mancini, L., M. Morassi, C. Sinito, O. Brandt, L. Geelhaar, H.-G. Song, Y.-H. Cho, N. Guan, A. Cavanna,  
J. Njeim, A. Madouri, C. Barbier, L. Largeau, A. Babichev, F. H. Julien, L. Travers, F. Oehler, N. Gogneau,  
J.-C. Harmand, and M. Tchernycheva,  
Optical properties of GaN nanowires grown on chemical vapor deposited-graphene,  
*Nanotechnol.* **30**, 214005, 11 pages (2019). DOI: 10.1088/1361-6528/ab0570

Michel, J., D. Splith, J. Rombach, A. Papadogianni, T. Berthold, S. Krischok, M. Grundmann,  
O. Bierwagen, H. von Wenckstern, and M. Himmerlich,  
Processing strategies for high-performance Schottky contacts on n-type oxide semiconductors:  
Insights from  $\text{In}_2\text{O}_3$ ,  
*ACS Appl. Mater. Interfaces* **11**, 27073–27087 (2019). DOI: 10.1021/acsami.9b06455

Nagata, T., O. Bierwagen, Z. Galazka, M. Imura, S. Ueda, Y. Yamashita, and T. Chikyow,  
Photoelectron spectroscopic study of electronic states and surface structure of an in situ cleaved  
 $\text{In}_2\text{O}_3$  (111) single crystal,  
*Jpn. J. Appl. Phys.* **58**, SDDG06, 5 pages (2019). DOI: 10.7567/1347-4065/ab0ff0

Nagata, T., O. Bierwagen, Z. Galazka, S. Ueda, M. Imura, Y. Yamashita, and T. Chikyow,  
Photoelectron spectroscopic study on electronic state and electrical properties of  $\text{SnO}_2$  single crystals,  
*Jpn. J. Appl. Phys.* **58**, 080903, 5 pages (2019). DOI: 10.7567/1347-4065/ab2c1e

Nakhaie, S., M. Heilmann, T. Krause, M. Hanke, and J. M. J. Lopes,  
Nucleation and growth of atomically thin hexagonal boron nitride on Ni/MgO(111) by molecular  
beam epitaxy,  
*J. Appl. Phys.* **125**, 115301, 14 pages (2019). DOI: 10.1063/1.5081806

Nicolai, L., Ž. Gačević, E. Calleja, and A. Trampert,  
Electron tomography of pencil-shaped  $\text{GaN}/(\text{In},\text{Ga})\text{N}$  core-shell nanowires,  
*Nanoscale Res. Lett.* **14**, 232, 10 pages (2019). DOI: 10.1186/s11671-019-3072-1

Niehle, M., J.-B. Rodriguez., L. Cerutti, E. Tournié, and A. Trampert,  
The interaction of extended defects as the origin of step bunching in epitaxial III–V layers on vicinal  
 $\text{Si}(001)$  substrates,  
*Phys. Status Solidi RRL* **13**, 1900290, 4 pages (2019). DOI: 10.1002/pssr.201900290

Oliva, M., G. Gao, E. Luna, L. Geelhaar, and R. B. Lewis,  
Axial  $\text{GaAs}/\text{Ga}(\text{As},\text{Bi})$  nanowire heterostructures,  
*Nanotechnol.* **30**, 425601, 6 pages (2019). DOI: 10.1088/1361-6528/ab3209

Pan, Y., S. Fölsch, Y.-C. Lin, B. Jariwala, J. A. Robinson, Y. Nie, K. Cho, and R. M. Feenstra,  
*WSe<sub>2</sub> homojunctions and quantum dots created by patterned hydrogenation of epitaxial graphene substrates*,  
*2D Mater.* **6**, 021001, 8 pages (2019). DOI: 10.1088/2053-1583/aaf58c

Patil, P. K., S. Shimomura, F. Ishikawa, E. Luna, and M. Yoshimoto,  
Strategic molecular beam epitaxial growth of GaAs/GaAsBi heterostructures and nanostructures,  
in *Bismuth-Containing Alloys and Nanostructures*, edited by S. Wang and P. Lu  
(Springer Singapore, 2019), pp. 59–96. DOI: 10.1007/978-981-13-8078-5\_4

Pham, V. D., K. Kanisawa, and S. Fölsch,  
Quantum rings engineered by atom manipulation,  
*Phys. Rev. Lett.* **123**, 066801, 5 pages (2019). DOI: 10.1103/PhysRevLett.123.066801

Ramsteiner, M., J. Feldl, and Z. Galazka,  
Signatures of free carriers in Raman spectra of cubic In<sub>2</sub>O<sub>3</sub>,  
*Semicond. Sci. Technol.* **35**, 015017, 5 pages (2020), published online Dec. 2<sup>nd</sup>, 2019.  
DOI: 10.1088/1361-6641/ab5615

Röben, B., X. Lü, K. Biermann, L. Schrottke, and H. T. Grahn,  
Terahertz quantum-cascade lasers for high-resolution spectroscopy of sharp absorption lines,  
*J. Appl. Phys.* **125**, 151613, 7 pages (2019). DOI: 10.1063/1.5079701

Samoylova, L., U. Boesenberg, A. Chumakov, V. M. Kaganer, I. Petrov, T. Roth, R. Rüffer, H. Sinn,  
S. Terentyev, and A. Madsen,  
Diffraction properties of a strongly bent diamond crystal used as a dispersive spectrometer  
for XFEL pulses,  
*J. Synchrotron Rad.* **26**, 1069–1072 (2019). DOI: 10.1107/S1600577519004880

Schroth, P., M. Al Humaidi, L. Feigl, J. Jakob, A. Al Hassan, A. Davtyan, H. Küpers, A. Tahraoui,  
L. Geelhaar, U. Pietsch, and T. Baumbach,  
Impact of the shadowing effect on the crystal structure of patterned self-catalyzed GaAs nanowires,  
*Nano Lett.* **19**, 4263–4271 (2019). DOI: 10.1021/acs.nanolett.9b00380

Schrottke, L., X. Lü, B. Röben, K. Biermann, T. Hagelschuer, M. Wienold, H.-W. Hübers, M. Hannemann,  
J. H. van Helden, J. Röpcke, and H. T. Grahn,  
High-performance GaAs/AlAs terahertz quantum-cascade lasers for spectroscopic applications,  
*IEEE Trans. Terahertz Sci. Technol.* **10**, 133–140 (2020), published online Dec. 6<sup>th</sup>, 2019.  
DOI: 10.1109/TTHZ.2019.2957456

Seddon, S. D., C. Benjamin, J. I. Bryant, C. W. Burrows, M. Walker, G. Matheson, J. Herranz,  
L. Geelhaar, and G. R. Bell,  
Work function of GaAs(*hkl*) and its modification using PEI: Mechanisms and substrate dependence,  
*Phys. Chem. Chem. Phys.* **21**, 24666–24673 (2019). DOI: 10.1039/c9cp04490f

Siekacz, M., P. Wolny, T. Ernst, E. Grzanka, G. Staszczak, T. Suski, A. Feduniewicz Żmuda, M. Sawicka, J. Moneta, M. Anikeeva, T. Schulz, M. Albrecht, and C. Skierbiszewski,  
Impact of the substrate lattice constant on the emission properties of InGaN/GaN short-period  
superlattices grown by plasma assisted MBE,  
*Superlattices Microstruct.* **133**, 106209, 6 pages (2019). DOI: 10.1016/j.spmi.2019.106209

Sikora, O., J. Kalt, M. Sternik, A. Ptok, P. T. Jochym, J. Łążewski, K. Parlinski, P. Piekarz, I. Sergueev,  
H.-C. Wille, J. Herfort, B. Jenichen, T. Baumbach, and S. Stankov,  
Ab initio and nuclear inelastic scattering studies of Fe<sub>3</sub>Si/GaAs heterostructures,  
*Phys. Rev. B* **99**, 134303, 13 pages (2019). DOI: 10.1103/PhysRevB.99.134303

## Facts & Figures – Publications

- Simion, C. E., F. Schipani, A. Papadogianni, A. Stanoiu, M. Budde, A. Oprea, U. Weimar, O. Bierwagen, and N. Barsan,  
Conductance model for single-crystalline/compact metal oxide gas-sensing layers in the non-degenerate limit: Example of epitaxial  $\text{SnO}_2$  (101),  
*ACS Sens.* **4**, 2420–2428 (2019). DOI: 10.1021/acssensors.9b01018
- Sinito, C., P. Corfdir, C. Pfüller, G. Gao, J. Bartolomé, S. Kölling, A. Rodil Doblado, U. Jahn, J. Lähnemann, T. Auzelle, J. K. Zettler, T. Flissikowski, P. Koenraad, H. T. Grahn, L. Geelhaar, S. Fernández-Garrido, and O. Brandt,  
Absence of quantum-confined Stark effect in GaN quantum disks embedded in (Al,Ga)N nanowires grown by molecular beam epitaxy,  
*Nano Lett.* **19**, 5938–5948 (2019). DOI: 10.1021/acs.nanolett.9b01521
- Sobanska, M., Z. R. Ztykiewicz, G. Calabrese, L. Geelhaar, and S. Fernández-Garrido,  
Comprehensive analysis of the self-assembled formation of GaN nanowires on amorphous  $\text{Al}_x\text{O}_y$ : *In situ* quadrupole mass spectrometry studies,  
*Nanotechnol.* **30**, 154002, 12 pages (2019). DOI: 10.1088/1361-6528/aafe17
- Takada, S., H. Edlbauer, H. V. Lepage, J. Wang, P.-A. Mortemousque, G. Georgiou, C. H. W. Barnes, C. J. B. Ford, M. Yuan, P. V. Santos, X. Waintal, A. Ludwig, A. D. Wieck, M. Urdampilleta, T. Meunier, and C. Bäuerle,  
Sound-driven single-electron transfer in a circuit of coupled quantum rails,  
*Nat. Commun.* **10**, 4557, 9 pages (2019). DOI: 10.1038/s41467-019-12514-w
- Takagaki, Y.,  
Commensurability and quantum interference magnetotransport oscillations in a two-dimensional electron gas sandwiched by superconductors,  
*J. Phys.: Condens. Matter* **31**, 485301, 8 pages (2019). DOI: 10.1088/1361-648X/ab3aa5
- Takagaki, Y., M. Ramsteiner, U. Jahn, B. Jenichen, and A. Trampert,  
Memristive resistive switch based on spontaneous barrier creation in metal-chalcogenide junctions,  
*J. Phys. D: Appl. Phys.* **52**, 385101, 7 pages (2019). DOI: 10.1088/1361-6463/ab2cbb
- Takagaki, Y., B. Jenichen, and O. Brandt,  
Semicohherent growth of single-crystal  $\beta\text{-In}_2\text{S}_3$  layers on InP(111) and InAs(111),  
*CrystEngComm* **21**, 5818–5823 (2019). DOI: 10.1039/c9ce01135h
- Terker, M., B. Jenichen, J. Herfort, and A. Trampert,  
*In situ* transmission electron microscopy of solid phase epitaxy of Ge on  $\text{Fe}_3\text{Si}$ ,  
*Semicond. Sci. Technol.* **34**, 124004, 6 pages (2019). DOI: 10.1088/1361-6641/ab4fad
- Tholen, H. M. G. A., J. S. Wildmann, A. Rastelli, R. Trotta, C. E. Pryor, E. Zallo, O. G. Schmidt, P. M. Koenraad, and A. Yu. Silov,  
Active tuning of the g-tensor in InGaAs/GaAs quantum dots via strain,  
*Phys. Rev. B* **99**, 195305, 8 pages (2019). DOI: 10.1103/PhysRevB.99.195305
- van Treeck, D., J. Ledig, G. Scholz, J. Lähnemann, M. Musolino, A. Tahraoui, O. Brandt, A. Waag, H. Riechert, and L. Geelhaar,  
Electroluminescence and current-voltage measurements of single-(In,Ga)N/GaN-nanowire light-emitting diodes in a nanowire ensemble,  
*Beilstein J. Nanotechnol.* **10**, 1177–1187 (2019). DOI: 10.3762/bjnano.10.117
- von Helden, L., L. Bogula, P.-E. Janolin, M. Hanke, T. Breuer, M. Schmidbauer, S. Ganschow, and J. Schwarzkopf,  
Huge impact of compressive strain on phase transition temperatures in epitaxial ferroelectric  $\text{K}_x\text{Na}_{1-x}\text{NbO}_3$  thin films,  
*Appl. Phys. Lett.* **114**, 232905, 5 pages (2019). DOI: 10.1063/1.5094405

**Ph. D. Theses**

Cheng, Zongzhe

"In-situ study of  $\text{Ga}_2\text{O}_3$  thermal expansion and epitaxy by synchrotron based x-ray diffraction and reflection high-energy electron diffraction"

Humboldt-Universität zu Berlin, August 2019

**Master Theses**

Sabelfeld, Alexander

Korrelative Raman- und KPFM-Untersuchungen zur ortsaufgelösten Bestimmung der Dotierung und Verspannung in epitaktischem Graphen

Technische Universität Berlin, January 2019

Pianetti, Andrea

Synthesis and characterization of 2D-Gallium Telluride

Università degli Studi di Roma "Tor Vergata", Italy, March 2019

Stramma, Alexander

Transport of exciton-polaritons in a structured  $(\text{Al},\text{Ga})\text{As}$  microcavity

Rheinisch-Westfälische Technische Hochschule Aachen, July 2019

**Students Working on their Master Thesis**

Góra, Michał

Humboldt-Universität zu Berlin

Graser, Karl

Humboldt-Universität zu Berlin

Nevkrytyh, Ekaterina

Technische Universität Berlin

Pires da Silva, Jorge Tiago

Instituto Superior Técnico, Lisboa, Portugal

Winkler, Daniel

Technische Universität Berlin

**Students Working on their Bachelor Thesis**

Oppermann, Lars

Humboldt-Universität zu Berlin

## Facts & Figures – Conferences organized by the Institute / Seminars of Visitors

### Conferences and Workshops organized by the Institute

#### **European Workshop on Molecular Beam Epitaxy – EuroMBE 2019**

February 17- 20, 2019

Henning Riechert, Paul-Drude-Institut für Festkörperferelektronik (PDI)

Workshop held at Arabella Brauneck Hotel Conference Center, Lenggries

#### **PDI Topical Workshop on 2D Materials Grown by MBE**

April 8-9, 2019

Marcelo Lopes, Paul-Drude-Institut für Festkörperferelektronik (PDI)

Workshop held at Paul-Drude-Institut für Festkörperferelektronik, Berlin

#### **Leibniz-Workshop on Knowledge-Transfer, "Voices from the other side"**

Mai 16, 2019

Carsten Hucho, Paul-Drude-Institut für Festkörperferelektronik (PDI)

Johannes Graupner, Leibniz-Institut für Gewässerökologie und Binnenfischerei (IGB)

Workshop held at Leibniz-Institut für Photonische Technologien (IPHT), Jena

#### **PDI Topical Workshop on Epitaxial III-Nitride Semiconductor Nanowires**

June 6-7, 2019

Thomas Auzelle, Paul-Drude-Institut für Festkörperferelektronik (PDI)

Lutz Geelhaar, Paul-Drude-Institut für Festkörperferelektronik (PDI)

Jonas Lähnemann, Paul-Drude-Institut für Festkörperferelektronik (PDI)

Workshop held at Weierstraß-Institut für Angewandte Analysis und Stochastik (WIAS), Berlin

#### **Leibniz-Workshop on Knowledge-Transfer, "Verhandeln"**

November 13, 2019

Carsten Hucho, Paul-Drude-Institut für Festkörperferelektronik (PDI)

Johannes Graupner, Leibniz-Institut für Gewässerökologie und Binnenfischerei (IGB)

Workshop held at Zoologisches Forschungsmuseum Alexander Koenig (ZFMK), Bonn

### Seminars of Visitors

21.01.2019

**Martin Hempel**, Fraunhofer-Institut für Zuverlässigkeit und Mikrointegration (IZM)

System Integration and Interconnection – New Approaches in High-Frequency Interconnects

28.01.2019

**Tzu-Kan Hsiao**, National Taiwan University

Single-photon emission from an acoustically-driven lateral light-emitting diode

04.02.2019

**Roger A. De Souza**, Rheinisch-Westfälische Technische Hochschule Aachen

Using transport studies to reveal the myriad of secrets of SrTiO<sub>3</sub>

22.02.2019

**Shumin Wang**, Laboratory of Terahertz Solid State Technology, Chinese Academy of Sciences

Shanghai, Institute of Microsystem and Information Technology Chinese Academy of Sciences

Progress on III-V-Bi alloys and light emitting devices

19.03.2019

**Arkady V. Krasheninnikov**, Helmholtz-Zentrum Dresden-Rossendorf, Germany

Defects and impurities in two-dimensional transition metal dichalcogenides

28.03.2019

**Minh Tuan Dau**, Institute for Nanoscience and Cryogenics, Research Laboratory of Spintronics and Technology, Alternative Energies and Atomic Energy Commission (CEA), Grenoble, France  
Conversion of spin-charge currents in epitaxial heterostructures

23.04.2019

**Oliver Dier**, Carl Zeiss SMT GmbH, Germany  
EUV lithography: optics enabling Moore's law / From epitaxial research to process architecture: skills and knowledge to succeed in industry

29.04.2019

**Luis Vicente Scalvi**, Universidade Estadual Paulista Júlio de Mesquita Filho, Brazil  
Photoluminescence of rare earth ion doping and interface related electrical transport properties of SnO<sub>2</sub> thin films based heterostructures

06.05.2019

**Darrell Schlom**, Cornell University, USA  
Progress toward Taming BaSnO<sub>3</sub>: Substrates, Films, and Transistors

20.05.2019

**Warren Jackson**, Xerox Palo Alto Research Center, USA  
Transition Metal Oxides and Resistive RAM Memory

03.06.2019

**Jens Martin**, Leibniz Institute for Crystal Growth, Berlin  
Technologies for novel hetero-structures: alternative growth methods and layer transfer

14.06.2019

**Vadim Khrapai**, Laboratory of Electron Kinetics Chernogolovka, Russia  
Topological protection of helical edge states as a quantum coherent phenomenon

20.06.2019

**Qirong Yao**, University of Twente, The Netherlands  
STM and STS study of 2D materials

21.06.2019

**Koji Ishibashi**, Designated National Research and Development Institute "RIKEN", Tokyo  
Superconductor/topological insulator Josephson Junctions – search for Majorana fermions

24.06.2019

**Hans-Werner Schumacher**, Physikalisch-Technische Bundesanstalt (PTB), Braunschweig, Germany  
Electrical quantum metrology for the revision of the SI system of units

10.07.2019

**Srini Krishnamurthy**, SRI International, Menlo Park, CA, USA  
Flat Optics — a review

29.07.2019

**Tomohiro Yamaguchi**, Kogakuin University, Japan  
Growth and characterization of nitrides by MBE and oxides by mist CVD

12.08.2019

**Luis Felipe Lastras-Martinez**, University of San Luis Potosi, Mexico  
Differential reflectance contrast technique in the near field limit: Application to graphene

## Facts & Figures – Seminars of Visitors

19.08.2019

**Yuval Gefen**, Weizmann Institute of Science, Israel

Interplay of heat conductance and electric currents at the edge: a fresh look at quantum Hall edges

02.09.2019

**Alexey Scherbakov**, Technical University of Dortmund, Germany

Strong magnon-phonon coupling at the nanoscale: visible effects of invisible modes

30.09.2019

**Alexander V. Kolobov**, Herzen University, Russia

First-principles study of ultra-thin films and superlattices: case examples of GaN and GeTe-Sb<sub>2</sub>Te<sub>3</sub>

04.11.2019

**Ingmar Swart**, Utrecht University, The Netherlands

Electronic quantum materials simulated with artificial model lattices

18.11.2019

**James Stotz**, Queen's University, Canada

Into the Deep: Scattering Surface Waves into the Bulk

25.11.2019

**Axel E. Bruchhausen**, Centro Atómico Bariloche & Instituto Balseiro, Argentina

Vibrational Dynamics in Transition Metal Dichalcogenide Membranes

02.12.2019

**Kris Bertness**, National Institute of Standards and Technology, USA

Metrology of GaN Nanostructures

10.12.2019

**Muhammad Y. Bashouti**, Ben-Gurion University of the Negev, Israel

Molecular surface Interactions: Science and applications

12.12.2019

**Madhu Thalakulam**, The Indian Institute of Science Education and Research, Thiruvananthapuram, India

1T MoS<sub>2</sub>: A 2D metal and superconductor

**Budget Summary**

<b>Fiscal year</b>	<b>2018</b>	<b>2019</b>
	k€	k€
<b>Revenues</b>		
Allocations	9,747.0	9,305.6
Earnings	18.0	21.2
<b>Sum</b>	<b>9,765.0</b>	<b>9,326.8</b>
<b>Expenditures</b>		
Staff	5,640.3	5,599.8
Administrative expenses	3,275.2	2,708.6
Equipment investment funds	849.5	1,018.4
<b>Sum</b>	<b>9,765.0</b>	<b>9,326.8</b>
<b>External funding through projects</b>		
Granted funds	5,063.0	2,643.2
Spent funds	1,387.5	1,599.7

## Facts & Figures – Summary of External Funding

### Summary of External Funding

Agency	Period	Title	Project leader
BMBF	01.12.2015 – 31.05.2019	Design principles in organic electronics: Heterogeneities in the volume and at phase boundaries – Charge and energy transfer processes at hybrid organic/inorganic semiconductor interfaces (LETOIG)	Dr. Oliver Brandt
BMBF	15.04.2018 – 31.01.2021	Monolithically integrated laser made from III-V nanowires for silicon photonics (MILAS)	Dr. Lutz Geelhaar
BMBF	01.06.2018 – 31.05.2021	InterPOL – Verbundprojekt: Polariton lattices: a solid-state platform for quantum simulations of correlated and topological states – Teilvorhaben: Development of polariton lattices with correlated and topological states for quantum simulation	Dr. Paulo V. Santos
DAAD	01.01.2018 – 31.12.2019	Study of the incorporation of Bi in GaSb for development of high performance lasers	Dr. Esperanza Luna
DAAD	01.01.2018 – 31.12.2019	Assessment of non-polar m-plane AlGaN surfaces, interfaces and heterostructures	Dr. Jonas Lähnemann
EFRE	01.08.2016 – 31.07.2020	Application laboratory electron tomography	Dr. Achim Trampert
DFG	01.07.2016 – 30.09.2020	Manipulation of single electrons and single excitons by surface acoustic waves	Dr. Paulo V. Santos
DFG	01.12.2015 – 31.12.2023	Quantum Hall based Aharonov-Bohm spectroscopy: electron-electron interaction in non-linear magneto-transport	PD Dr. Stefan Ludwig
DFG	01.05.2017 – 30.06.2021	Nonequilibrium phenomena and interactions in ultra-pure III-V nanowires	PD Dr. Stefan Ludwig
DFG	01.09.2017 – 29.02.2020	Manipulation and spectroscopy of quantum structures on semiconductor surfaces by cryogenic scanning tunneling microscopy	Dr. Stefan Fölsch
DFG	01.03.2018 – 28.02.2021	Coherent acousto-optical interactions in structured polariton microcavities	Dr. Alexander Kuznetsov
DFG	01.10.2018 – 30.09.2021	Coherent acousto-optical interactions in structured polariton microcavities	Dr. Paulo V. Santos
DFG	01.11.2018 – 31.10.2021	Controlling Electron-Phonon Interaction in Nanocircuits – Strong Coupling Regime	PD Dr. Stefan Ludwig
DFG	01.04.2019 – 31.03.2022	Controlling Electron-Phonon Interaction in Nanocircuits – Strong Coupling Regime	Dr. Paulo V. Santos
DFG	01.05.2019 – 30.04.2022	Far-infrared magneto-spectroscopy of novel semiconductor materials in megagauss magnetic fields using quantum-cascade lasers	Prof. Dr. Holger T. Grahn
ESA/ DLR	12.02.2019 – 11.02.2021	Frequency stabilization of a Quantum Cascade Laser for Supra-THz applications	Prof. Dr. Holger T. Grahn

<b>Agency</b>	<b>Period</b>	<b>Title</b>	<b>Project leader</b>
EU	01.06.2015 – 31.05.2019	SAWtrain – dynamic electromechanical control of semiconductor nanostructures by acoustic fields	Dr. Paulo V. Santos
EU	01.01.2019 – 31.12.2021	BeforeHand – Boosting Performance of Phase Change Devices by Hetero- and Nano-Structure Material Design	Dr. Raffaella Calarco
WGL (SAW)	01.07.2015 – 30.06.2019	Epitaxial phase change superlattices designed for the investigation of non-thermal switching	Dr. Raffaella Calarco
WGL (SAW)	01.04.2018 – 31.03.2021	Barium stannate based heterostructures for electronic applications (BaSTet)	Dr. Oliver Bierwagen
WGL (SAW)	01.06.2018 – 31.05.2021	Terahertz detection of atoms in plasma processes (TERAPLAS)	Prof. Dr. Holger T. Grahn
WGL (SAS)	01.07.2016 – 30.06.2020	Growth and fundamentals of oxides for electronic applications (GraFOx)	Dr. Oliver Bierwagen

## Facts & Figures – Visiting Scientists

### Visiting Scientists

Name	Institute	Period	Topic	Country
Dr. A. Bruchhausen	Centro Atómico Bariloche	22.11.2019–01.12.2019	Phonon-Polariton interactions in microcavities	Argentina
D. H. de Oliveira Machado	Universidade Estadual Paulista Jutio de Mesquita Filho, Sao Paulo	15.05.2018–14.05.2019	Piezoelectric excitation of GHz vibrations in GaAs-based structures	Brazil
G. Copetti	Universidade Federal do Rio Grande do Sul, Porto Allegre	03.08.2018–28.02.2019	Halogenation as a Route to Modification of Graphene's Properties	Brazil
T. Orestes Feijó	Universidade Federal do Rio Grande do Sul, Porto Allegre	17.09.2018–30.09.2019	Growth of van der Waals heterostructures by MBE for nanoelectronics	Brazil
Prof. Dr. J. A. H. Stotz	Dept of Physics, Engineering Physics, and Astronomy, Queen's University, Kingston, ON	02.08.2019–31.12.2019	Acoustic transport of indirect excitons	Canada
Dr. M. Karim Elsayed	Alexandria University, Al-Ibrahimiyyah, Alexandria	01.02.2019–31.07.2019	Single Photon Emitters in Large-Scale Hexagonal Boron Nitride Films for Scale Hexagonal Boron Nitride Films for Nanophotonic Applications	Egypt
M. Rio Calvo	Université de Montpellier-IES, Montpellier	10.07.2019–26.07.2019	Transmission electron microscopy of novel laser structures	France
Prof. Dr. U. Pietsch	Department of Physics, University of Siegen, Siegen	14.05.2018–30.09.2019	Röntgenbeugung an Nanostrukturen	Germany
Dr. Á. Caballero Lorenzo	Institut Kurz GmbH, Köln	01.06.2018–31.05.2020	Curved-channel magneto-rectification using (In,Ga)As/InP heterostructures	Germany
Dr. K. Ishibashi	Advanced Device Laboratory RIKEN, Wako, Saitama	19.06.2019–23.06.2019	Quantum Hybrid Systems for Information Processing	Japan
Dr. T. Yamaguchi	Kogakuin University, Hachioji-shi, Tokyo	23.07.2019–03.09.2019	Growth of semiconducting oxide thin films and group-III nitride nanowires	Japan

Name	Institute	Period	Topic	Country
Prof. Dr. L. F. Lastras-Martínez	Insituto de Investigacion en Comunicacion Optica (IICO), Universidad Autonoma de San Luis Potosi (UASLP), San Luis Potosí	22.07.2019– 21.08.2019	Optical anisotropy of semiconductor surfaces and nanostructures	Mexico
R. Ukropec	Universität Twente, Enschede	25.02.2019– 08.03.2019	Acoustic transport in silicon structures induced by GHz SAWs	Netherlands
Dr. Y. Zhao	Suzhou Institute of Nano-Tech and Nano-Bionics, Chinese Academy of Sciences, Suzhou	01.12.2018– 30.11.2019	Molecular beam epitaxy of (Al,Ga)N nanowires on graphene	P. R. China
Dr. K. Załęski	NanoBioMedical Centre Adam Mickiewicz University, Poznań, Poznań	17.06.2019– 12.07.2019	Deposition of Heusler alloys thin films on graphene substrates	Poland
A. Reszka	Institute of Physics, Polish Academy of Sciences, Warsaw	19.08.2019– 24.08.2019	Infrared cathodoluminescence spectroscopy on GaAs-InGaAs and ZnTe-CdSe core-shell NWs	Poland
Prof. Dr. K. Sabelfeld	Institute of Computational Mathematics and Mathematical Geophysics Russian Academy of Sciences, Novosibirsk	03.06.2019– 16.06.2019	Monte Carlo simulations of stationary and transient cathodoluminescence at threading dislocations in GaN	Russian Federation
Dr. A. Kolobov	Herzen University, St. Petersburg	26.09.2019– 01.10.2019	First-principles study of ultra-thin films and superlattices: case examples of GaN and GeTe-Sb <sub>2</sub> Te <sub>3</sub>	Russian Federation
R. Fandan	Universidad Politécnica de Madrid, Madrid	23.04.2019– 21.05.2019	Raman spectroscopy of graphene on piezoelectric substrates coupled to surface acoustic waves	Spain
Dr. S. Fernandez Garrido	Dpto. Física Aplicada, Universidad Autónoma de Madrid, Madrid	24.06.2019– 28.06.2019	Formation of group-III nitride nanowires	Spain

## Facts & Figures – Visiting Scientists

Name	Institute	Period	Topic	Country
A. Fernando Saavedra	ETSIT – Universidad Politecnica de Madrid, Madrid	01.08.2019– 31.10.2019	Electron tomography and microscopy of III-N based nanostructures	Spain
Dr. K. Shportko	Lashkaryov Institute of Semiconductor, National Academy of Science of Ukraine, Kyiv	04.03.2019– 08.03.2019	Chalcogenide-based phase-change alloys: optical properties and applications	Ukrainia
Dr. I. Brytavskyi	Interdepartmental Physico-technical Center of Odessa I. I. Mechnikov National University, Odessa	01.08.2019– 31.10.2019	Electrical and structural characterization of large-area h-BN / graphene van der Waals heterostructures for advanced 2D devices applications	Ukrainia
A. Rajput	University of Illinois, Urbana-Champaign, IL	20.05.2019– 01.08.2019	Electrical and optical analysis of LEDs based on GaAs nanowires	USA
Prof. Dr. S. Krishnamurthy	SRI International, Menlo Park CA	01.06.2019– 31.08.2019	Bright entangled photon source (BEPS) — quantum structures embedded in optical microcavities	USA
J. Wu	Bowdoin College, Brunswick, ME	26.06.2019– 17.07.2019	Mapping of high-frequency surface acoustic fields	USA
Prof. Dr. M. Msall	Bowdoin College, Brunswick, ME	17.06.2019– 31.07.2019	Mapping of high-frequency surface acoustic fields	USA
Prof. Dr. B. Peterson	University of Michigan, Ann Arbor, MI	01.09.2019– 31.12.2019	Contacts to and transport properties of $\text{Ga}_2\text{O}_3$	USA
Prof. Dr. S. W. Teitsworth	Physics Department, Duke University, Durham, NC	23.10.2019– 08.11.2019	Nonlinear Dynamics in Semiconductor Superlattices	USA
Dr. K. Bertness	National Institute of Standards and Technology, Gaithersburg, MD	25.11.2019– 06.12.2019	Growth, analysis, and applications of group-III nitride nanowires	USA
Prof. Dr. Y.-H. Zhang	Arizona State University, Tempe, AZ	04.12.2019– 04.01.2020	Integration of heterovalent semiconductor structures – Innovative Approaches for Structure Analysis –	USA

**Staff**

(December 31, 2019)

**Scientific staff:** including Ph. D. students (D) and externally funded personnel (P)

Auzelle, Thomas	Charge and energy transfer at hybrid organic/inorganic semiconductor interfaces
Ayuso Pérez, Irene (D, P)	Quantum transport in nanowires
Biermann, Klaus	Molecular beam epitaxy of GaAs-based advanced heterostructures
Bierwagen, Oliver	Molecular beam epitaxy of oxides
Brandt, Oliver	Group-III nitrides and semiconductor nanowires
Budde, Melanie (D, P)	Molecular beam epitaxy and doping of p-type semiconducting oxides
Cecchi, Stefano (P)	Group-IV-Te 2D materials and epitaxy of phase change materials
Crespo Poveda, Antonio (P)	Polariton lattices as a solid-state platform for quantum simulations of correlated and topological states
Czubak, Dietmar (D)	Spin transport in and vertical spin valve structure based on ferromagnet-semiconductor hybrid structures
Feldl, Johannes (D, P)	Optical spectroscopy of semiconducting oxides, in particular perovskites and sesquioxides
Flissikowski, Timur	Ultrafast dynamics of semiconductor structures
Fölsch, Stefan	Low-temperature scanning tunneling microscopy and spectroscopy
Freudenfeld, Jaan (D)	Interacting electronic nanostructures
Geelhaar, Lutz	Molecular beam epitaxy and semiconductor nanowires
Grahn, Holger	Optical and electrical properties of semiconductor nanostructures
Hanke, Michael	Synchrotron x-ray diffraction
Heilmann, Martin	Molecular beam epitaxy of graphene/h-BN van der Waals heterostructures
Helgers, Paul (D, P)	Acoustically modulated gigahertz single-photon sources using coupled quantum wires and dots in microcavities
Hellemann, Jan (D)	Electron-phonon interaction in nanostructures
Herfort, Jens	Ferromagnet-semiconductor heterostructures
Hernández Minguez, Alberto	Manipulation of optical and electronic properties of low-dimensional structures using surface acoustic waves
Herranz Zamorano, Jesús (P)	Devices based on group-III arsenide nanowires
Hoffmann, Georg (D, P)	Growth and doping of BaSnO <sub>3</sub> and LaInO <sub>3</sub>
Hucho, Carsten	Technology and transfer
Jenichen, Bernd	X-ray diffraction and electron microscopy

## Facts & Figures – Staff

Jordão Lopes, João Marcelo	Graphene and h-BN epitaxy
Kaganer, Vladimir	Theories of molecular-beam-epitaxial growth and x-ray scattering
Kurlov, Sergii (P)	Terahertz quantum-cascade lasers for far-infrared magneto spectroscopy in pulsed megagauss magnetic fields
Kuşdemir, Erdi (D, P)	Influence of Mg on the growth of (In,Ga)N/GaN short period superlattices
Kuznetsov, Alexander (P)	Microcavity exciton-polaritons in artificial potential landscapes
Lähnemann, Jonas	Spatially resolved optical spectroscopy and structural and chemical analysis of nanostructures
Lü, Xiang	Terahertz quantum-cascade lasers
Ludwig, Stefan	Quantum transport in nanoelectronic systems
Luna Garcia de la Infanta, Esperanza	Transmission electron microscopy of heterointerfaces
Mazzolini, Piero	Growth kinetics and doping of (Ga,Al) <sub>2</sub> O <sub>3</sub>
Müller, Philipp (P)	Electron-phonon coupling in lateral nanostructures based on two-dimensional electron gases
Nicolai, Lars (D, P)	Spectroscopic electron tomography and microscopy of nanomaterials
Niehle, Michael (P)	Electron tomography of semiconductor heterostructures
Oliva, Miriam (D)	Photoluminescence spectroscopy of ordered nanowire arrays
Papadogianni, Alexandra (D)	(In <sub>1-x</sub> Ga <sub>x</sub> ) <sub>2</sub> O <sub>3</sub> based gas sensors
Pham, Van Dong (P)	Atom manipulation on III-V semiconductors by low-temperature scanning tunneling microscopy
Ramsteiner, Manfred	Electronic, vibrational, and magnetic properties of semiconductors
Reis, Anna (D)	In.situ x-ray scattering study of surface and interface dynamics at growing crystalline layers
Riechert, Henning	Director
Röben, Benjamin (P)	Terahertz quantum-cascade-lasers for spectroscopic applications
Santos, Paulo	Acoustic, optic, and magnetic properties of nanostructures
Schrottke, Lutz	Quantum-cascade lasers and optical properties of heterostructures
Tahraoui, Abbes	Comprehensive semiconductor technology
Takagaki, Yukihiko	Electric properties of nanometer-scale materials
Terker, Markus (D)	In-situ transmission electron microscopy on semiconductor interfaces and defect structures
Trampert, Achim	Microstructure and electron microscopy
Yuan, Mingyun (P)	Manipulation of single excitons by surface acoustic waves
Zallo, Eugenio (P)	Group-III-Te 2D materials and deposition of phase change materials

**Non-Scientific Staff**

Anders, Walid	Technology
Arnhold, Kerstin	Finances/Purchasing
Baumann, René	Workshop
Behnke, Steffen	Technician
Bluhm, Anne-Kathrin	Technician
Ehrensack, Kerstin	Technician
Ferber, Thomas	Workshop
Hablizel, Kai (P)	European and National Grant Management
Hartung, Andreas	Human Resources and Travel Management
Heinitz, Sebastian	Electrician
Herrmann, Claudia	Technician
Holldack, Anja	Third Party Funding
Krauß, Sabine	Technician and Chairwoman Works Council
Litschauer, Maximilian (P)	Student Assistant
Matzeck, Christopher	Technician
Matzeck, Margarita (P)	Technician
Meister, Sebastian	Technology
Morgenroth, Katrin	Technician
Pakulat, Bernd	Head of IT and Data Protection Officer
Pfeiffer, Astrid	Technician
Pfeiffer, Jörg	Head of Workshop
Rauwerdink, Sander	Technology
Reischel, Mercedes	Transfer Management
Riedel, Angela	Technician
Schönherr, Hans-Peter	Technician
Seidel, Werner	Technology
Sieg, Michael	Workshop
Steffen, Doreen	Technician
Stemmler, Carsten	Technician
Suchilina, Ekaterina	Office Assistant
Timm, Anne Susanne	Library
Venohr, Thomas	Workshop
Wirsig, Arno	Technology
Wirt-Brunnckow, Andreas	IT



# Contact Kontakt

www.hochschu



## DIRECTORATE

### **Prof. Dr. Henning Riechert**

Director

phone: +49 30 20377-365

fax: +49 30 20377-201

riechert@pdi-berlin.de

### **Dr. Carsten Hucho**

Scientific-Administrative Coordinator

phone: +49 30 20377-234

hucho@pdi-berlin.de

### **Ekaterina Suchilina**

Office

phone: +49 30 20377-481

suchilina@pdi-berlin.de

## ADMINISTRATION

### **Kerstin Arnhold**

Purchasing/Finances

phone: +49 30 20377-358

fax: +49 30 20377-425

arnhold@pdi-berlin.de

### **Andreas Hartung**

Human Resources

phone: +49 30 20377-475

hartung@pdi-berlin.de

### **Anja Holldack**

Third-party funding

phone: +49 30 20377-352

holldack@pdi-berlin.de

## PUBLIC RELATIONS

### **Dr. Carsten Hucho**

phone: +49 30 20377-234

fax: +49 30 20377-515

hucho@pdi-berlin.de

## CHAIR OF WORK COUNCIL

### **Sabine Krauß**

phone: +49 30 20377-258

sabine.krauss@pdi-berlin.de

## SPEAKER OF SCIENTISTS

### **Dr. Oliver Bierwagen**

phone: +49 30 20377-491

bierwagen@pdi-berlin.de

## GENDER EQUALITY OFFICER

### **Kai Hablizel**

phone: +49 30 20377-342

fax: +49 30 20377-515

hablizel@pdi-berlin.de

## TRANSFER

### **Mercedes Reischel**

Technology Transfer Manager

phone: +49 30 20377-289

fax: +49 30 20377-515

reischel@pdi-berlin.de

## DEPARTMENTS

### **Dr. Lutz Geelhaar**

Head of Department Epitaxy  
phone: +49 30 20377-359  
fax: +49 30 20377-201  
[geelhaar@pdi-berlin.de](mailto:geelhaar@pdi-berlin.de)

### **Dr. Achim Trampert**

Head of Department Microstructure  
phone: +49 30 20377-280  
fax: +49 30 20377-201  
[trampert@pdi-berlin.de](mailto:trampert@pdi-berlin.de)

### **Prof. Dr. Holger T. Grahn**

Head of Department Semiconductor Spectroscopy  
phone: +49 30 20377-318  
fax: +49 30 20377-301  
[htgrahn@pdi-berlin.de](mailto:htgrahn@pdi-berlin.de)

### **Dr. Carsten Hucho**

Head of Department Technology and Transfer  
phone: +49 30 20377-234  
fax: +49 30 20377-515  
[hucho@pdi-berlin.de](mailto:hucho@pdi-berlin.de)





# Imprint

## Impressum

Paul-Drude-Institut für Festkörperelektronik,  
Leibniz-Institut im Forschungsverbund Berlin e.V.

Hausvogteiplatz 5-7  
10117 Berlin  
Germany

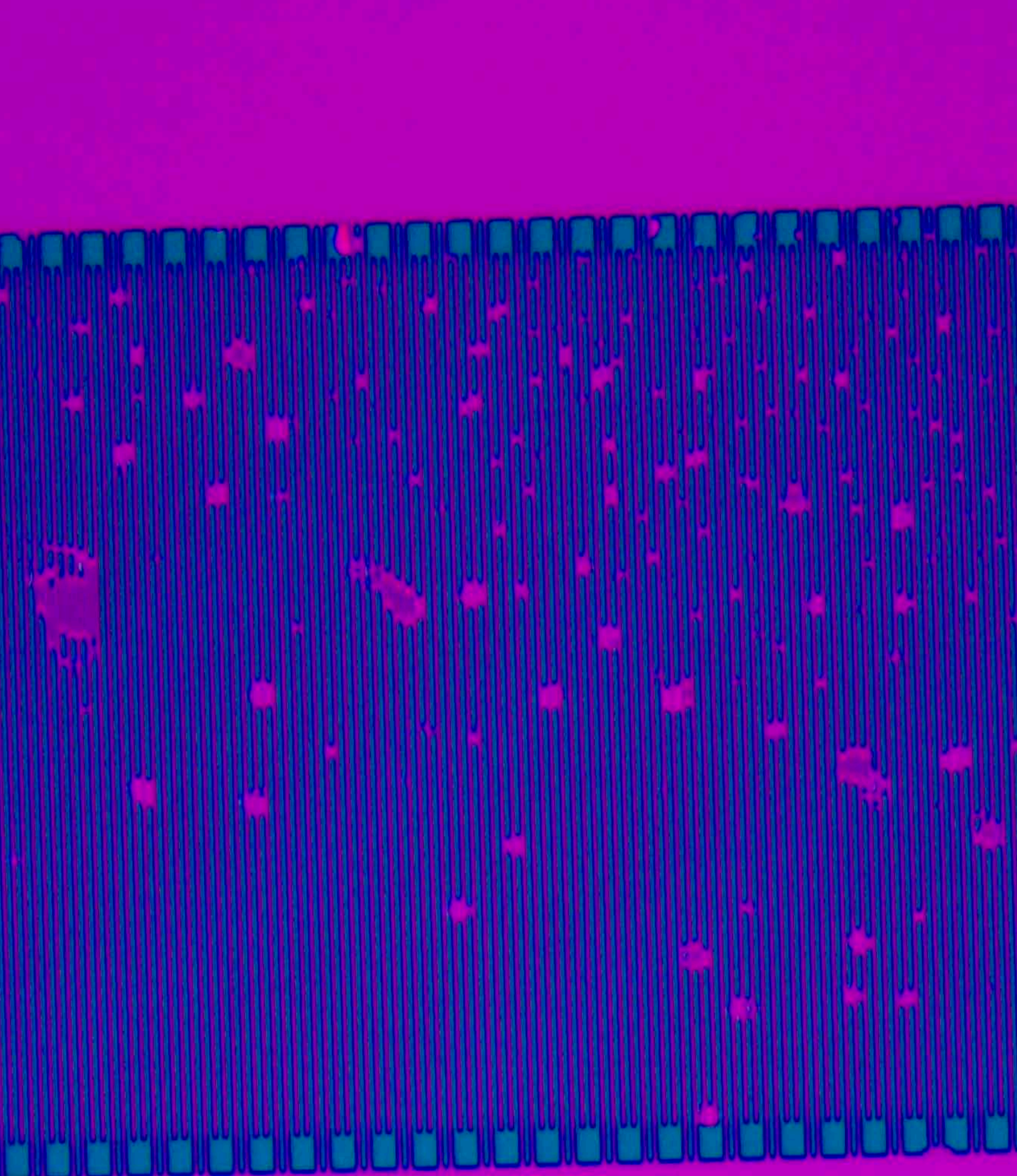
Tel. +49 30 20377-481  
Fax +49 30 20377-515  
[info@pdi-berlin.de](mailto:info@pdi-berlin.de)

PUBLISHED BY / HERAUSGEGEBEN VOM  
Paul-Drude-Institut für Festkörperelektronik, 2019

DESIGN / GESTALTUNG  
[unicom-berlin.de](http://unicom-berlin.de)

PHOTOS / FOTOS  
S. 4, Ekaterina Suchilina; S. 5, Anja Holldack; S. 8/9, Anja Holldack ;  
S 10/11, Jonas Lähnemann; S. 32/33 Jonas Lähnemann, S. 34 Sander Rauwerdink;  
S. 58/59 Sander Rauwerdink; S. 118/119 Sander Rauwerdink;  
S. 139 Frau Worzewski, FV; 144/145 Sander Rauwerdink;  
S. 166/167 Bernd Wannenmacher; S. 170/171 Andreas Hartung;  
S. 173 Sander Rauwerdink

[www.pdi-berlin.de](http://www.pdi-berlin.de)





Scientists and administrative staff experience phases of extreme stress at their workplace. The final stage of a dissertation, preparations for large conferences, or development of proposals for scholarship programs, leave little or no time for life outside the office or the lab. The employees' enormous personal engagement arises from their strong identification with the research they are involved in. While such identification can be very positive, leading to profound satisfaction with one's professional activity, it can also result in pressure and tensions in the family environment.

We at PDI place great importance on promoting work-life balance and support our employees in this respect through individual solutions. Our measures are continuously developed within an external audit process. On December 10, 2018 PDI was re-certified by berufundfamilie gGmbH for its engagement in pursuing a family-friendly human resources policy.

Alle Wissenschaftlerinnen und Wissenschaftler und die Wissenschaft unterstützenden Mitarbeiterinnen und Mitarbeiter kennen Phasen extremer zeitlicher Belastungen bei ihrer Arbeit. Während der Endphase einer Doktorarbeit, im Umfeld großer Tagungen oder in der Antragsphase für ein Stipendienprogramm ist oft kaum noch Platz für ein Leben außerhalb des Büros und Labors. Das enorme persönliche Engagement der Mitarbeiterinnen und Mitarbeiter speist sich aus der starken Identifikation mit der Forschung. Im positiven Fall bedeutet diese Identifikation große Zufriedenheit mit der beruflichen Tätigkeit – sie kann aber auch zu Belastungen und Einschränkungen im familiären Umfeld führen.

Wir legen am PDI großen Wert auf die Vereinbarkeit von Beruf und Familie und unterstützen unsere Mitarbeiterinnen und Mitarbeiter hierbei durch individuelle Maßnahmen. Im Rahmen eines externen Auditierungsprozesses werden unsere Maßnahmen weiterentwickelt. Das PDI wurde am 10. Dezember 2018 erneut für sein Engagement für eine familienbewusste Personalpolitik durch die berufundfamilie gGmbH zertifiziert.





Paul-Drude-Institut für Festkörperelektronik,  
Leibniz-Institut im Forschungsverbund Berlin e.V.

Hausvogteiplatz 5-7  
10117 Berlin  
Germany

[www.pdi-berlin.de](http://www.pdi-berlin.de)

